



Technische Universität München  
TUM School of Life Sciences

# Tracking fungal cultivations – Micro- and macromorphological evolution of filamentous fungal pellet cultivations revealed by 2D and 3D imaging and analysis

**Henri Maximilian Müller**

Vollständiger Abdruck der von der TUM School of Life Sciences der Technischen Universität München zur Erlangung eines Doktors der Ingenieurwissenschaften (Dr.-Ing.) genehmigten Dissertation.

**Vorsitz:** Prof. Dr. Johan Philipp Benz

**Prüfer der Dissertation:**

1. Prof. Dr.-Ing. Heiko Briesen
2. Prof. Dr. habil. Rainer Krull

Die Dissertation wurde am 16.10.2023 bei der Technischen Universität München eingereicht und durch die TUM School of Life Sciences am 19.03.2024 angenommen.



# Abstract

Filamentous fungi have outstanding skills in decomposition and biosynthesis. As cell factories, they produce enzymes, organic acids, antibiotics and other life-saving drugs on an industrial scale. By systematically improving these cell factories, fungal biotechnology can contribute significantly to 10 of 17 United Nations' sustainable development goals. In submerged bioprocesses, filamentous fungi develop various cellular morphologies, such as spherical pellets up to a few millimeters in size. This morphology influences to a large extent the productivity. Thus, morphology engineering strategies aim to optimize the growth of fungi in terms of process performance. However, in the absence of suitable morphometric analysis methods, a systematic understanding of the mode of action of such strategies on macro- and micromorphological development is often lacking, making targeted morphology engineering almost impossible. Current analytical methods do not allow for comprehensive micro- and macromorphological quantification of an entire fungal culture of a bioprocess.

In this publication-based dissertation, Article I summarizes the development of a universal law for predicting the diffusive mass transfer of nutrients inside fungal pellets depending on their morphology. Article II presents a high-throughput 2D image analysis based on stereomicroscopy that allows the macromorphological evolution of fungal cultivations to be tracked holistically, from single spores to spore agglomeration to final heterogeneous pellet populations. The image analysis of up to 1700 spore agglomerates and 1500 pellets per cultivation time allows the accurate quantification of the morphological development. Furthermore, synchrotron radiation-based  $\mu$ -computed tomography and the developed 3D image analysis is introduced in Article III, allowing to generate locally resolved micromorphological properties, including tip, branch, and pellet densities of 11,157 pellets from different cultivation time steps. From the time course of the data, the growth rate, apical growth velocity, and branching rate for pellets could be calculated for the first time. In addition, number density distributions calculated from the data can now be used to determine micromorphological population heterogeneities.

The micro- and macromorphological data from the methods developed will directly lead to a better understanding of the evolution of filamentous fungal morphologies, contributing to improved bioprocesses with higher productivity. In addition, based on the obtained data and the developed universal diffusion law, growth models can now be extended. This paves the way for the vision of general predictive modeling of fungal bioprocesses.

# Zusammenfassung

Filamentöse Pilze haben überragende Fähigkeiten in der Zersetzung und Biosynthese. Als Zellfabriken produzieren sie Enzyme, organische Säuren, Antibiotika und andere lebensrettende Medikamente im industriellen Maßstab. Durch die systematische Verbesserung dieser Zellfabriken kann die Pilz-Biotechnologie zu 10 von 17 Nachhaltigkeitszielen der Vereinten Nationen einen großen Beitrag leisten. In submersen Bioprozessen entwickeln filamentöse Schimmelpilze verschiedene zelluläre Morphologien, wie beispielsweise bis zu wenigen Millimetern große kugelige Pellets. Diese Morphologie beeinflusst die Produktivität stark. Morphologie-Engineering-Strategien zielen darauf ab, das Wachstum der Pilze im Hinblick auf die Prozessperformance zu optimieren. Mangels geeigneter morphometrischer Analysemethoden fehlt jedoch häufig ein systematisches Verständnis der Wirkungsweise solcher Strategien auf die makro- und mikromorphologische Entwicklung, was gezieltes Morphologie-Engineering nahezu unmöglich macht. Die derzeitigen Analysemethoden erlauben dabei keine umfassende mikro- und makromorphologische Quantifizierung der gesamten Pilzkultur eines Bioprozesses.

In dieser publikationsbasierten Dissertation fasst Artikel I die Entwicklung eines universellen Gesetzes zur Vorhersage des diffusiven Stofftransfers von Nährstoffen innerhalb von Pilzpellets in Abhängigkeit von deren Morphologie zusammen. Artikel II stellt eine 2D-Bildanalyse vor, die es ermöglicht die makromorphologische Entwicklung von Pilzkulturen ganzheitlich zu verfolgen, angefangen von einzelnen Sporen über Sporenagglomeration bis hin zu heterogenen Pelletpopulationen. Die Bildanalyse von bis zu 1700 Sporenagglomeraten und 1500 Pellets pro Kultivierungszeit ermöglicht dabei die genaue Quantifizierung der morphologischen Entwicklung. Des Weiteren wird in Artikel III die auf Synchrotronstrahlung basierte  $\mu$ -Computertomographie und 3D-Bildanalyse eingeführt, die es ermöglicht lokal aufgelöste mikromorphologische Eigenschaften einschließlich der Spitzen-, Verzweigungs- und Pelletdichte von 11.157 Pellets aus verschiedenen Kultivierungszeitpunkt zu erzeugen. Aus dem Zeitverlauf der Daten konnten erstmals die Wachstumsrate, die apikale Wachstumsgeschwindigkeit, und die Verzweigungsrate für Pellets berechnet werden. Darüber hinaus können aus den Daten errechnete Anzahldichteverteilungen genutzt werden, um nun mikromorphologische Populations-Heterogenitäten zu ermitteln.

Die mikro- und makromorphologischen Daten aus den entwickelten Methoden führen unmittelbar zu einem besseren Verständnis der Morphologieentwicklung filamentöser Pilze und werden so zu verbesserten Bioprozessen mit höherer Produktivität beitragen. Darüber hinaus können auf der Grundlage der gewonnenen Daten und des entwickelten universellen Diffusionsgesetzes, nun Wachstumsmodelle weiterentwickelt werden. Dies ebnet den Weg für die Vision einer allgemeinen prädiktiven Modellierung von Pilzbioprozessen.

# Danksagung

Zu Beginn möchte ich meinem Doktorvater Prof. Dr.-Ing. Heiko Briesen danken. Heiko hat als Leiter des Lehrstuhls für Systemverfahrenstechnik (SVT) die freie Entwicklung von Projekten und Ideen stets gefördert und war immer erreichbar für Diskussionen, ein gemeinsames Brainstorming, und andere fachliche sowie fachfremde Anliegen. Prof. Dr. habil. Rainer Krull und Prof. Dr.rer.nat. Philipp J. Benz danke ich sehr für die Durchführung meiner Doktorprüfung.

Des Weiteren möchte ich besonders den Kollegen des SVTs danken. Es war immer über-  
ragend mit euch am oder abseits des SVT zu arbeiten, Kaffee zu trinken, zu diskutieren, zu feiern und sich gegenseitig zu unterstützen. Vor allem Steve als Mitbegründer der Pilzfor-  
schung an unserem Lehrstuhl, Tiaan, Charlotte, Verena, Sebastian, Simon, Thomas, Michaela und Walter möchte ich für die vielen hilfreichen Diskussionen und Unterstützung im Zuge dieser Dissertation und bei Veröffentlichungen danken. Sebastian möchte ich zusätzlich für den gemeinsamen Aufbau und Durchführung der Vorlesung 3D Bildgebung danken.

Die DFG Schwerpunktprojekte 1934 DiSP Biotech und 2170 InterZell ermöglichten welt-  
klasse Kooperationen. Hier möchte ich allen Kooperationspartner/innen danken. Ein beson-  
ders großer Dank geht an Lars, Vera, Anna, Rainer Krull, Karin, Tolu, Philipp und Marcel.  
Außerhalb der Schwerpunktprojekte danke ich Ludwig für die Möglichkeit, dass ich an sei-  
nem Lehrstuhl Pilze kultivieren durfte. Tanja danke ich für die Einführung in die Welt der  
Pilz-Kompositmaterialien. Die Einblicke in eure Fachgebiete haben meinen Horizont erwei-  
tert, die Zusammenarbeit hat stets großen Spaß gemacht.

Den Pil(z)s und DESY Freunden Steve, Charlotte, Felix und Jörg möchte ich sehr für das  
Korrekturlesen meiner Arbeit danken. Jörg, vielen Dank, dass du mein Mentor warst und mir  
spannende Möglichkeiten der 3D Bildgebung und Verarbeitung aufgezeigt hast.

Danken möchte ich auch meinen Studenten/innen Diana, Lukas, Kilian, Domenic und Flo-  
rian. Die Betreuung eurer Arbeiten war für mich sehr förderlich, spaßig und lehrreich.

Zuletzt möchte ich von ganzem Herzen meiner Familie, sowie meinen Freunden/innen für  
die motivierenden Worte in der finalen Phase meiner Doktorarbeit und ihre Unterstützung  
über den gesamten Zeitraum danken. Mein Bruder hat mich motiviert an der TUM zu pro-  
movieren. Danke. Meiner Freundin Niko gilt der größte Dank, sie musste mich in der finalen  
Phase der Doktorarbeit aushalten. Ihr danke ich auch besonders für die grafische Unterstüt-  
zung bei Abbildungen.



# Contents

<b>1. Introduction</b>	<b>1</b>
<b>2. Theoretical background</b>	<b>4</b>
2.1. Fungal morphology during submerged cultivation . . . . .	4
2.2. Morphological development: from spores to heterogeneous pellet populations	4
2.2.1. Spores, spore agglomeration, and pellet formation . . . . .	5
2.2.2. Interplay between nutrient supply and productivity of pellets . . . . .	6
2.2.3. Fragmentation of pellets . . . . .	8
2.2.4. Heterogeneity of fungal cultivations . . . . .	9
2.3. Link between morphology engineering and growth processes . . . . .	11
2.4. High-throughput analysis techniques for fungal cultivations . . . . .	17
2.5. Modeling approaches . . . . .	19
<b>3. Problem definition</b>	<b>23</b>
<b>4. Methods for problem solving</b>	<b>25</b>
<b>5. Results</b>	<b>27</b>
5.1. Generalized morphology modeling of aggregating, filamentous microorganisms	27
5.2. From spores to fungal pellets: A new high-throughput image analysis high- lights the structural development of <i>Aspergillus niger</i> . . . . .	29
5.3. Synchrotron radiation-based micro-computed tomography for three-dimensional growth analysis of <i>Aspergillus niger</i> pellets . . . . .	31
<b>6. Discussion</b>	<b>33</b>
6.1. Opportunities: Analysis of spore agglomeration, macromorphological devel- opment, and heterogeneity . . . . .	33
6.2. Opportunities: Analysis of micromorphological development and heterogeneity	35
6.3. Possible improvements of the developed methods . . . . .	42
6.4. Analysis of nutrient transport and development of process control strategies .	44
6.5. Ready for predictive bioprocess modeling? . . . . .	46
<b>7. References</b>	<b>53</b>
<b>A. List of Publications</b>	<b>63</b>
<b>B. Published and peer-reviewed Articles II and III</b>	<b>66</b>



# 1. Introduction

The filamentous fungus *Aspergillus niger* enabled industrial biotechnology more than one hundred years ago (Cairns et al., 2018). The success story of commercial citric acid production, which began in 1919 using *A. niger* by the company Pfizer, is well known. Today, citric acid is still produced mainly with strains of this fungus and is a fast-growing, multi-billion Euro product used as a flavoring agent, preservative, antioxidant, acidifier, and chelating agent in foods and beverages, as well as in pharmaceutical, cosmetic, and cleaning applications (Cairns et al., 2018; Rokem, 2020). There are several other success stories with filamentous fungi as cell factories in established industrial bioprocesses, including the production of life-saving antibiotics such as penicillins as secondary metabolites of *Penicillium* species (Keller, 2019; van den Berg, 2011) or the production of enzymes such as glucoamylase and cellulase from *A. niger* and *Trichoderma reesei*, respectively (Bischof et al., 2016; Cairns et al., 2018; Ward, 2012). It is the lifestyle of filamentous fungi that makes them these efficient producers of a wide variety of products, such as drugs, enzymes, organic acids, or commodities for the pharmaceutical, food, feed, fuel, textile, and chemical industries. For their nutrition, filamentous fungi first produce large amounts of a variety of enzymes to break down polymeric substances, e.g., (hemi-)cellulose in organic waste, into monomers, such as glucose, and oligomers, which can then be used as carbon and energy source for fungal growth (Meyer et al., 2020; Wösten, 2019). In addition, filamentous fungi secrete primary metabolites, e.g., organic acids, and secondary metabolites, such as antibiotics, to dissolve soil minerals or inhibit the growth of other microorganisms (Liaud et al., 2014; Wösten, 2019). Based on this way of life - decomposing waste to produce valuable compounds and secure survival - fungal biotechnology has the potential to be a leading contributor to establish a future circular and sustainable economy (Meyer et al., 2020). Recently, fungal biotechnology has been predicted to significantly contribute to 10 of 17 United Nations' sustainable development goals (Meyer et al., 2020).

Industrial production is usually performed in bioreactors under agitated, aerobic, and submerged conditions (Cairns et al., 2018; Rokem, 2020). Under these cultivation conditions, filamentous fungi develop into different cellular morphologies that strongly influence the productivity of the bioprocess (Veiter et al., 2018). The established morphology is defined by the growth pattern of the curved and branched tubular filaments, called hyphae, that germinate from reproductive spores and constitute filamentous fungi (Papagianni, 2004). Fungal morphologies range from freely dispersed hyphae, over clumps, to dense spherical hyphal networks, called pellets (Figure 1). Each morphology state has its advantages and disadvantages.

In general, bioprocess performance is an interplay between the parameters morphology, broth rheology, as well as oxygen and nutrient supply (Wucherpfennig et al., 2010). However, the key balancing parameter that influences the other parameters mentioned is morphology. Therefore, multiple strategies have been developed to control the cellular morphology of filamentous fungi. These strategies range from varying the titer and hydrophobicity of the spore inoculum (Dynesen and Nielsen, 2003; Grimm et al., 2004; Papagianni and Mattey, 2006), to altering the environmental conditions in the bioreactor, i.e., the environome, including medium composition (el Enshasy et al., 1999; Liao et al., 2007), pH (Liu and Wu, 2012; Zhou et al., 2000), shear stress (El-Enshasy et al., 2006; Kelly et al., 2004; Lin et al., 2010), osmolality (Wucherpfennig et al., 2011), and addition of microparticles (Böl et al., 2021; Driouch et al., 2010; Kaup et al., 2008), to genetic modifications of the fungus (Cairns et al., 2019b; Fiedler et al., 2018; Meyer et al., 2021). However, in the absence of suitable morphometric analysis methods, the mode of action of such morphology engineering strategies is often unknown, making the transferability to different genera and strains of filamentous fungi as well as to different cultivation conditions almost impossible. Since productivity depends on oxygen and nutrient supply, which in turn depends on morphology, analysis of mass transfer within hyphal networks is a necessary prerequisite for targeted morphology engineering.

In this publication-based dissertation, Article I summarizes the development of a universal law for predicting the diffusive mass transport of oxygen and nutrients inside fungal pellets depending on their morphology. Article I has not yet been published, but since it is not subject to the peer-review procedure, it will be published as shown in Appendix C at SpringerNature in early 2024. The universal law was elaborated based on laboratory-scale X-ray micro-computed tomography ( $\mu$ -CT) and image analysis (Schmideder et al., 2019a), diffusion calculations through experimentally determined fungal pellets (Schmideder et al., 2019b), and Monte Carlo growth modeling to generate 3125 different hyphal networks in-silico, allowing the transfer to a universal law across genera and species (Schmideder et al., 2020). The developed universal law makes it now feasible to predict an optimized fungal pellet structure for bioprocess-adapted optimal oxygen and nutrient supply. However, a calculated optimized pellet structure must evolve during growth and, equally important, be maintained as long as possible during the bioprocess. To achieve this, the development of fungal cultivations during the process, with and without the influence of morphology engineering methods, must first be understood holistically at macro- and micromorphological levels. 2D image analysis is an established method for statistically representative macromorphological growth analysis of filamentous fungi. In addition, 3D imaging based on  $\mu$ -CT is the only method that can resolve a fungal pellet's whole non-destructed 3D structure. Subsequent 3D image analysis thereof is capable of locally detecting micromorphological parameters such as the amount of hyphal material, tips, and branching points (Schmideder et al., 2019a). However, both methods, based on 2D and 3D imaging, have drawbacks that limit the holistic analysis of fungal cultures over time. 2D imaging analysis lacks holistic tracking of all relevant growth processes, including spore agglomeration. Low sample throughput of 3D  $\mu$ -CT prevents micromorphological growth analysis of a statistically representative number of pellets for multiple time

points during the cultivation period. These methodological drawbacks are addressed in the peer-reviewed Article II and III, reprinted in Appendix B.

Article II presents a fast high-throughput method based on simple stereomicroscopy to holistically track the macromorphological evolution of fungal cultivations, starting from individual spores, through spore agglomeration, to final heterogeneous pellet populations. The image analysis pipeline developed allowed quantitative assessment of pelleted and dispersed fungal growth based on calculated size distributions, area fractions, and pellet concentrations for each of 44 cultivation time steps. In addition, Article III introduces synchrotron radiation-based micro-computed tomography to overcome the limitation of low sample throughput of lab scale  $\mu$ -CT. The new 3D image analysis pipeline thereof enabled the evaluation of locally resolved micromorphological properties of up to 579 pellets per cultivation time. The resulting time course of the data allowed computing the growth rate, apical growth velocity, and branching rate for pellets for the first time.

In future work, the experimental growth data obtained will be used to parameterize models for predicting the morphological development of fungal cultivations. Modeling approaches have the unique advantage of simulating filamentous fungal growth with the selective modification of individual growth and cultivation parameters while holding the others constant. This will make models indispensable for developing transferable targeted morphology engineering and process control strategies. However, due to knowledge gaps regarding the growth processes of filamentous fungal cultivations and missing growth parameters, predictive bioprocess modeling is not possible up to now. The presented methods within this dissertation will pave the way toward this vision.

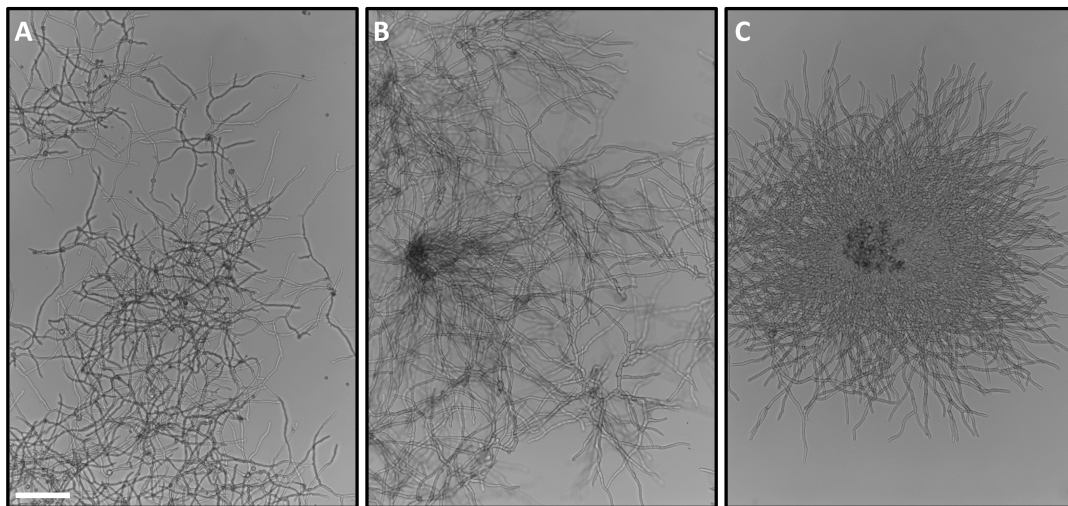


Figure 1: Cellular morphology states of filamentous fungi. A) Dispersed mycelia; B) Clump; C) Pellet. Scale bar: 100  $\mu$ m. (Meyer et al., 2021)

## **2. Theoretical background**

### **2.1. Fungal morphology during submerged cultivation**

During industrially-relevant submerged cultivation, filamentous fungi grow into different macro-morphologies defined by the growth pattern of the hyphae. Fungal hyphae can be freely distributed in the liquid medium, forming the morphology of dispersed mycelia, they can be loosely aggregated forming clumps, or they can grow as dense spherical networks with a diameter between a few hundred micrometers and some millimeters called pellets (Cairns et al., 2019b; Cox et al., 1998; Veiter et al., 2018). Each morphology has benefits and drawbacks. Rapid biomass accumulation can be achieved with dispersed mycelia. In contrast, cultivation broths with dispersed mycelia exhibit non-Newtonian fluid behavior and high viscosity, which requires high energy input for mixing (Wucherpfennig et al., 2010). In addition, the high viscosity limits convective oxygen and nutrient transport in industrial bioreactor runs with dispersed mycelia (Antecká et al., 2016; Wucherpfennig et al., 2010). Cultivations with fungal pellets as dominant morphological form show low viscosities (Krull et al., 2013). There is no consensus in the literature on whether the cultivation broth with pellets exhibits Newtonian or non-Newtonian behavior (Bliatsiou et al., 2020; Krull et al., 2013). However, a drawback of pellets is that the dense hyphal network restricts the diffusion-driven transport of nutrients and oxygen in the inner regions of the pellet, limiting pellet growth and growth-dependent production (Hille et al., 2009; Schmideder et al., 2019b; Veiter et al., 2020; Wittier et al., 1986). The morphology of clumps is only vaguely defined and less studied (Meyer et al., 2020). Clumps are often seen as intermediate between dispersed mycelia and pellets (Paul et al., 1999; Wucherpfennig et al., 2011), which can develop into pellets during cultivation (Veiter et al., 2018). Due to the rheological benefits of fungal pellets and the great potential for optimizing their productivity by exploring and altering their structure for enhanced oxygen and nutrient supply, the developed methods within this thesis focus on the analysis of fungal pellet populations.

### **2.2. Morphological development: from spores to heterogeneous pellet populations**

During the bioprocess, a filamentous fungal cultivation is in constant transformation. Starting from inoculation with spores, through spore agglomeration and growth of hyphae, to the establishment of a morphological form, to breakage events of the hyphae, heterogeneous

pellet populations arise. In the following, growth processes and their influence on pellet morphology are explained.

### 2.2.1. Spores, spore agglomeration, and pellet formation

Filamentous fungi form asexual spores called conidia to reproduce, spread, and survive in hostile environmental conditions (Baltussen et al., 2020). When the environment is favorable, conidia break their dormant state and germinate. Water, oxygen, and a degradable carbon source are usually needed to initiate germination (Lamarre et al., 2008; Osheroov and May, 2001). These requirements are given in industrial bioprocesses. After inoculation, germination begins with swelling of the conidia by water uptake, which can double their diameter (van Leeuwen et al., 2013). After isotropic swelling, cell polarity is established and a germ tube forms as the first hyphal element (Lamarre et al., 2008). Hyphae elongate at their tip by polar, i.e., directional, cell growth, which is maintained throughout filamentous fungal growth (Harris and Momany, 2004). During growth, hyphae can form new branches leading to new tips and branching points. A structured model of Paul and Thomas (1996) divided a hypha into growing apical regions, non-growing subapical regions, vacuolised hyphae, and metabolic inactive degenerated regions. Here, newly formed tips form new apical regions, whereby a septum separates non-growing regions at a certain distance from the apical tip. Increasing vacuolization in subapical regions may result in degenerated inactive hyphal regions.

Continuous branching and tip extension may result in a spherical hyphal network, i.e., a fungal pellet. Under nutrient- and oxygen-unlimited growth conditions unique to young and small mycelium (Section 2.2.2), branching and tip extension at a constant rate lead to an exponential increase in pellet biomass (Krull et al., 2010).

During germination in submerged conditions, spores may agglomerate so that a distinction is usually made between two types of pellet formation: (1) the coagulative type (representatives are *Aspergillus nidulans* and *A. niger*) and (2) the non-coagulative type (representative is *Rhizopus oryzae*) (Cairns et al., 2019b; Metz and Kossen, 1977; Veiter et al., 2018). In coagulative pellet formation (Figure 2, bottom row), the spores agglomerate during germination, and the hyphae arising from the spores of these agglomerates form the pelleted morphology (Metz and Kossen, 1977). In this case, spore agglomeration is crucial to the pellet structure. Electrostatic interactions, hydrophobicity of surface proteins, and salt-bridging between cell wall surface polysaccharides of spores affect spore agglomeration (Dynesen and Nielsen, 2003; Fontaine et al., 2010; Veiter et al., 2018; Zhang and Zhang, 2016). A spore agglomerate may consist of hundreds or thousands of spores (Fontaine et al., 2010; Metz and Kossen, 1977). A spore agglomerate that has formed a pellet and is located in the center of the pellet can also contain spores that have not formed germ tubes, as shown by El-Enshasy (2011) and Lyu et al. (2023). A pellet of the non-coagulative type can theoretically arise from one single spore (Figure 2, top row)). Here, a single spore germinates, and hyphal elongation and frequent branching can result in one pelleted hyphal network (Metz and Kossen, 1977). Depending on the cultivation parameters, e.g., titer of inoculum, medium composition, or agitation intensity, pellet formation can be affected, making it difficult to determine whether

a species belongs to one or the other pellet formation type (Grimm et al., 2005b; Nielsen et al., 1995; Veiter et al., 2018; Zhang and Zhang, 2016). This is also shown by the additional definition of a third type, the hyphal element agglomeration type (Veiter et al., 2018). This type was defined for *P. chrysogenum*, where dispersed mycelia from non-coagulating spores agglomerate, and depending on cultivation conditions, may form pellets (Nielsen et al., 1995).

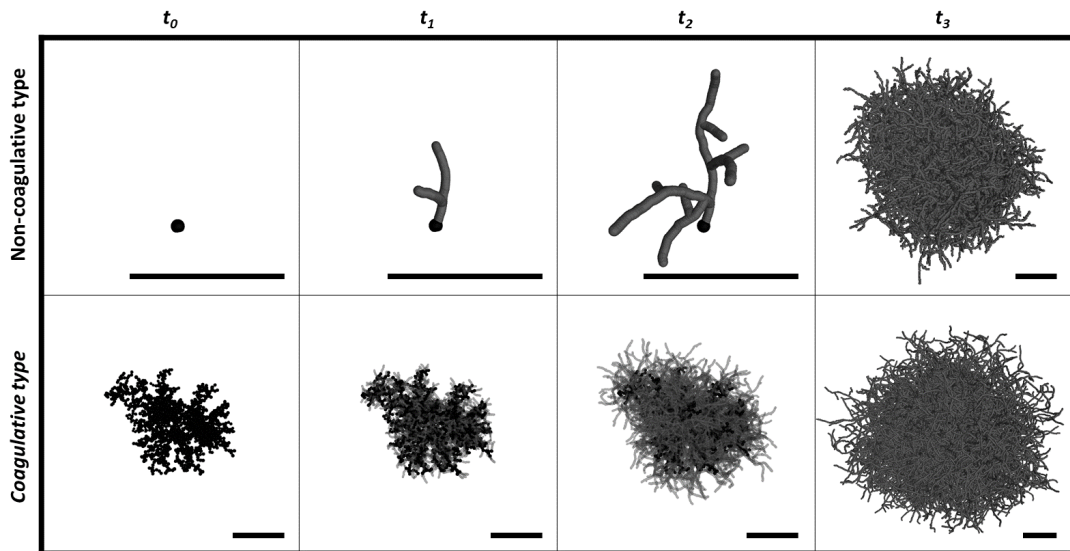


Figure 2: Development of pellets of the non-coagulative and coagulative type. Spores are marked black, whereas hyphae are grey. Three-dimensional morphologies were simulated with a Monte Carlo growth-model that is based on Celler et al. (2012). Scale bar: 100  $\mu\text{m}$ . With permission from Stefan Schmideder (Schmideder, 2022).

### 2.2.2. Interplay between nutrient supply and productivity of pellets

The development of a pellet cultivation is a multi-stage process. Fungal bioprocesses usually start with the inoculation of the medium with spores (Posch et al., 2013). After the pellet formation process, which can take up to 35 h for *P. chrysogenum* (Nielsen et al., 1995) and 24 h for *A. niger* (Papagianni and Mattey, 2006), the hyphae of pellets continue to grow by further uptake of nutrients, especially oxygen and carbons, from the medium. During rapid hyphal extension, secretion of proteins, including enzymes, is generally highest (Cairns et al., 2019b). Also, the production of organic acids, such as citric acid, coincides with specific active growth periods (Upton et al., 2017). However, nutrients must traverse through the pelleted hyphal network to supply internally producing pellet areas. In literature, it is often reported that the transport of nutrients inside pellets is mainly driven by diffusion (Cui et al., 1998b; King, 1998; Lejeune and Baron, 1997; Silva et al., 2001). In turbulent flow regimes, convection is assumed to have an enhanced influence in loose outer pellet regions as a second transport mechanism (Cronenberg et al., 1994; Hille et al., 2009). The oxygen concentration within a pellet can be determined experimentally using an oxygen microelectrode (Wittier et al., 1986). However, measuring oxygen transport under realistic flow conditions is challenging to reproduce since the pellet must be fixed for the measurement with an oxygen

microelectrode in a flow-through chamber (Cronenberg et al., 1994; Hille et al., 2005, 2009; Wittier et al., 1986). The theoretical background about the mainly relevant diffusion-driven transport inside pellets is described in Article I, "Diffusion computations within fungal pellets." As the pellet radius and density increase during pellet growth, substrate transfer through the hyphal network is increasingly hindered, resulting in substrate-limited areas in the center of pellets. It was experimentally shown that the concentration of nutrients decreases towards the center of pellets, and only an outer shell of the pellets with a thickness between 100 and 300  $\mu\text{m}$  is supplied (Cronenberg et al., 1994; Driouch et al., 2012; Hille et al., 2005, 2009; Wittier et al., 1986). In addition to the pellet size, the penetration depth of nutrients depends on the density of a pellet, i.e., the distribution of hyphal biomass inside a pellet, which is not homogeneous (Cronenberg et al., 1994; Hille et al., 2005, 2009; Schmideder et al., 2019b, 2020; Wittier et al., 1986). Thus, the locally resolved effective diffusion coefficients are required to calculate the diffusive mass transport inside pellets.

Substrate limitations within pellets cause the inactivation of cells and the end of growth-associated product formation in inactive pellet regions (Cairns et al., 2019b; Krull et al., 2013; Veiter et al., 2018). Driouch et al. (2012) demonstrated the production of glucoamylase of *A. niger* pellets based on a co-expression system with fluorescent GFP. Only hyphae in an outer pellet layer with a thickness of 200  $\mu\text{m}$  produced glucoamylase, and it was hypothesized that only the producing layer was sufficiently supplied with key nutrients, including oxygen and carbons. This hypothesis could not be verified since the oxygen or carbon concentration was not measured inside the pellets. Since oxygen limitation can lead to total inhibition of metabolite production in aerobic fungi and has been identified as the major limiting substrate (Gibbs et al., 2000; Veiter et al., 2018) multiple studies focus on the measurement of the oxygen concentration inside pellets (Hille et al., 2005, 2009; Wittier et al., 1986). In contrast, measurements of different nutrients are scarce. Cronenberg et al. (1994) analyzed the mass transport of glucose and oxygen inside pellets and demonstrated the interplay between metabolic activity and substrate limitation. At early cultivation stage, glucose penetrated *P. chrysogenum* pellets completely but was only consumed in the outer zone. Since oxygen was only present in the outer 200  $\mu\text{m}$  of the pellets, it was concluded that the absence of oxygen irreversibly inhibited the respiration of glucose in the center of the pellets. At later cultivation times, autolysis was assumed in central pellet regions. Bizukoje and Gonciarz (2015) measured the concentration of oxygen in *Aspergillus terreus* pellets and related the results to the production of the secondary metabolite and drug lovastatin. A higher lovastatin concentration was measured in the cultivation with smaller pellets, whereas the cultivation with larger pellets showed reduced production. The oxygen measurements unveiled that an increased percentage of the pellet area was penetrated with oxygen in the case of the smaller pellets compared to the larger ones. Since lovastatin production requires a carbon source that can only be utilized in the presence of oxygen, it was found that a significant increase in the concentration of the carbon source did not result in increased lovastatin production due to oxygen limitation. Besides products linked to active hyphal growth and sufficient nutrient supply, some products, such as penicillin, are produced in non-growing hyphal areas (Brakhage, 2013; Veiter et al.,

2018). Here it is conceivable that the limitation of specific substrates promotes the production of these substances (Cairns et al., 2019b).

This indicates that a detailed analysis of the nutrient transfer inside pellets is necessary to comprehensively understand production limitations during cultivation. Studies combining the experimental measurement of nutrients inside pellets and product formation are rare.

### **2.2.3. Fragmentation of pellets**

In addition to decreased production, a second effect caused by substrate limitation is the fragmentation of pellets. Pellet fragmentation can be divided into pellet breakup, e.g., the breakage of a pellet in two, and the abrasion of hyphal elements from loose outer pellet regions (Cui et al., 1997). Decreased binding forces between inactive cells lead to a loss of stability, and shear forces can more easily lead to pellet fragmentation, eventually resulting in a dispersed culture with unfavorable rheological behavior (Papagianni, 2004). Posch et al. (2012) observed a reduced pellet concentration after 15 h of *P. chrysogenum* pellet growth. Based on this observation, the authors hypothesized that oxygen transfer limitations within the center of the pellets cause cell death, resulting in loss of mechanical support and pellet breakup. Nielsen et al. (1995) performed a fed-batch cultivation which was inoculated with biomass consisting of 95% pellets. The pellet concentration decreased to the end of each growth period, so after 400 h, the main part of the biomass was present as dispersed mycelium and only 5% as pellets. It was proposed that substrate limitation in the center resulted in cell death, loss of stability, and, finally, the breakup of the pellets. However, no nutrient concentration analysis inside the pellets was performed. Besides pellet breakup, the abrasion of hyphal elements from the surface of the pellets was observed. Since the impact of shear forces upon pellets may increase with increasing pellet size, it was not possible to distinguish whether the pellets are fragmented due to increased size or to loss of stability due to substrate limitations. For dispersed mycelium of *A. niger*, it was shown that glucose limitation in the medium leads to autophagic processes to recycle carbon intracellularly (Nitsche et al., 2013, 2012). Autophagy is an intracellular degradation process whereby cytoplasmic proteins and organelles are transferred to vacuoles for recycling. Enhanced vacuolation during autophagy results in inactivity and fragmentation of the hyphae (Nitsche et al., 2013). Under limited glucose concentration, increased vacuolization and higher fragmentation of hyphal elements was observed for *A. niger* cultivations. Since less hyphal fragmentation occurred when cultivated under increased glucose concentration but under the same agitation conditions, it was found that increased vacuolated hyphae are more susceptible to fragmentation by shear forces (Papagianni et al., 1999). Also, during fed-batch cultivation of *P. chrysogenum*, nutrient limitation resulted in highly vacuolated hyphae and subsequent fragmentation due to shear forces (Paul et al., 1994). The last two publications mentioned showed increased vacuolation only for dispersed mycelium and clumps. Due to the complexity of pelleted hyphal networks, detailed studies of the hyphal degradation process inside pellets do not exist. However, several approaches based on staining agents (Bizukojc and Ledakowicz, 2010; de Bekker et al., 2011; El-Enshasy et al., 2006; Nieminen et al., 2013; Schrinner et al., 2020; Veiter and Herwig,

2019) and fluorescent protein co-expression systems (Driouch et al., 2012; Tegelaar et al., 2020) reveal metabolic inactive hyphae in central pellet regions and active shell-like outer hyphal regions. One commonly used staining agent to indicate dead hyphae is propidium iodide which penetrates cells with a defective membrane and binds to DNA, forming red fluorescent complexes which can be excited by fluorescence microscopy (Nieminen et al., 2013; Schrinner et al., 2020; Veiter and Herwig, 2019). Bizukoje and Ledakowicz (2010) stained *Aspergillus terreus* with lactophenol methyl blue and observed an increasingly inactive and fragmented central pellet region over cultivation time. Furthermore, the authors noted the abrasion of dead hyphal elements from the pellets, which appeared in the cultivation broth starting from 120 h of cultivation.

Pellet fragmentation generally depends on shear forces due to agitation and the physiological state, density, and size of pellets (Buffo et al., 2020; Cui et al., 1997). Even if the inactivation and fragmentation of hyphal fractions inside pellets due to process conditions cannot be clearly separated from the natural aging process of hyphae, i.e., apical areas transform into subapical and vacuolated areas, substrate limitation likely plays the most crucial role in this process. Since pellet fragmentation can lead to a dispersed cultivation with increased broth viscosity resulting in higher process costs for mixing power input, process control strategies must be found to maintain the pellet morphology during production. For increased production performance of penicillin with *P. chrysogenum* Posch and Herwig (2014) found to keep pellets small and viable by redirecting the metabolism from growth to maintenance and production. Here, a reduced growth rate could be achieved with a specific feeding strategy. However, such strategies require detailed knowledge about the nutrient transfer inside pellets depending on their current morphological state, e.g., local densities of the pellets, to predict growth limitation and pellet fragmentation.

#### **2.2.4. Heterogeneity of fungal cultivations**

In liquid-grown environments, filamentous fungi exhibit several heterogeneities, including the heterogeneous composition of a culture consisting of dispersed mycelia and pellets (Nielsen et al., 1995; Posch et al., 2012), the heterogeneous size of pellets (macromorphological heterogeneity) (Becker et al., 2011; Kurt et al., 2018), and the heterogeneous distribution of hyphal material, tips, and branches within pellets (micromorphological heterogeneity) (Hille et al., 2005; Schmideder et al., 2019a; Zacchetti et al., 2018). Heterogeneity also exists between individual hyphae and their compartments, which secrete different products (Bleichrodt et al., 2015; Nitsche et al., 2012; Zacchetti et al., 2018). For a comprehensive review of the multiscale heterogeneity phenomena of filamentous fungi and bacteria the author of this thesis refers to Zacchetti et al. (2018). In natural habitats of filamentous fungi, heterogeneity is a beneficial feature to survive under changing environmental conditions or to efficiently exploit further nutrients (Zacchetti et al., 2018). For example, hyphae and their compartments may be specialized for different tasks, such as exploring the environment to search for additional nutrients or secreting certain hydrolases to make nutrients available (Nitsche et al., 2012).

However, different hypotheses exist in the literature on whether heterogeneity is an advantage or a disadvantage for industrial bioprocesses.

On the one hand, heterogeneous pellet populations decrease the controllability and predictive capabilities of bioprocesses (Zacchetti et al., 2018). Usually, fungal bioprocesses are designed to produce only one product under defined environmental conditions. Thus, the fitness advantage resulting from heterogeneity in nature, e.g., different hyphae or hyphal compartments are specialized on different tasks or synthesize different products, is dispensable in ideal-mixed industrial bioreactor runs and might even reduce production yields (Nitsche et al., 2012). Becker et al. (2011) showed that *A. niger* cultures consisted of two different pellet populations, one with smaller diameters and another with larger diameters, which were evaluated based on the size distributions of the pellets. In addition to this size heterogeneity, the pellet population with larger diameters was found to express genes for glucoamylase and ferulic acid esterase to a lower level. Due to this heterogeneity in gene expression level, it was proposed that the protein production of *A. niger* can be improved by reducing the heterogeneity of the cultivation.

On the other hand, heterogeneity could possibly be beneficial to achieve fast biomass accumulation. Kurt et al. (2018) observed the development of *A. niger* cultures that were highly heterogeneous in size in a rocking motion bioreactor (RMB) compared to a stirred tank reactor (STR). A faster biomass accumulation was observed in the RMB cultivation, whereby it was hypothesized that the heterogeneity in size could be the driving factor for the maximized nutrient uptake and growth rate of the cultivation. The growth rate was lower when the cultivation was morphologically designed by adding talc microparticles to grow homogeneously as dispersed mycelia. However, this effect was possibly caused by a negative influence of the talc particles (Laible et al., 2021). Lyu et al. (2023) generated different sized *A. niger* pellet populations by influencing the spore agglomeration. It was found that smaller pellet populations secreted a larger variety and quantity of proteins compared to larger populations. However, some proteins were exclusively produced by small or large pellet populations. By co-culturing both populations, a synergistic increased cellulase activity was observed that could be useful by converting agricultural waste into bioplastic or biofuel within industrial bioprocesses (Lyu et al., 2023).

No matter whether heterogeneity within fungal cultivations is beneficial or not for industrial bioprocesses, the presented studies indicate that controlling heterogeneity enables further adjustments for improved bioprocess performance. Therefore, unveiling and understanding heterogeneity and its origin in fungal cultivations is desirable. To achieve this, large sample sizes from multiple time steps need to be analyzed to investigate size distributions of fungal cultivations that reveal micro- and macromorphological heterogeneity (Posch et al., 2012; Zacchetti et al., 2018). In addition, different growth processes influence the degree of cultivation heterogeneity. It is known that different concentrations of the spore inoculum (Papagianni and Mattey, 2006), genetically altered surface properties of spores (Dynesen and Nielsen, 2003), and process conditions such as pH (Colin et al., 2013) and agitation intensity of the medium (Grimm et al., 2005b) can lead to different spore agglomeration behavior and ultimately to

different sized pellets, dispersed mycelia, or altered ratio of dispersed to pelleted growth (Section 2.3). It was also shown that aggregation between young hyphae of filamentous bacteria is a crucial driver of population heterogeneity (Zacchetti et al., 2016). Furthermore, pellet fragmentation by pellet breakup and abrasion of hyphal elements leads to altered size distributions of pellets and an increasing amount of dispersed mycelium (Bizukojc and Ledakowicz, 2010; Nielsen et al., 1995). To conclude, the analysis of heterogeneity within fungal cultivations claims for high-throughput analysis methods to observe high amounts of morphological different samples. Section 2.4 presents existing high-throughput methods which are capable to analyze fungal heterogeneity. The following presents morphology engineering approaches that can be used to control heterogeneity in fungal cultivations.

### 2.3. Link between morphology engineering and growth processes

The term "morphology engineering" summarizes strategies that aim to precisely control the morphology of filamentous fungi within submerged cultivations (Krull et al., 2013). Since the morphology of filamentous fungi is one major key to increased productivity of submerged cultivated bioprocesses, several morphology engineering strategies exist. Most of them focus on the variation of cultivation conditions, including agitation, pH shifting of the medium, or the addition of microparticles. In addition, genes that affect or even control spore germination, hyphal growth, and, eventually, pellet formation can be predicted and genetically modified to alter macromorphology. However, the effects of morphology engineering strategies on filamentous fungal growth processes are largely unknown, limiting the targeted use of these strategies. Table 1 summarizes promising morphological engineering strategies, divided into process engineering and genetic strategies. Furthermore, their observed effect on morphology and the growth processes assumed to be affected mainly by the strategy are reported. Multiple review articles summarize additional studies about morphology engineering strategies (Böl et al., 2021; Krull et al., 2013; Veiter et al., 2018). Following Table 1, the morphology engineering strategies and their link to certain growth processes are described in detail.

**Spore concentration** The variation of the spore concentration at inoculation of the bioprocess results in altered macromorphologies of filamentous fungi of the coagulative and non-coagulative pellet formation type. Papagianni and Matthey (2006) observed a decreasing pellet size and the transition to disperse mycelia when raising the spore inoculum concentration from  $10^4$  to  $10^9$  spores/ml. An increased spore concentration was followed by a reduced dissolved oxygen level during hyphal growth, demonstrating the change of the environment inside the bioreactor and, thus, possibly the development of particular morphological forms during hyphal growth. Unfortunately, the authors did not investigate the spore agglomeration process, whereby no conclusions could be made between an altered spore agglomeration and developed morphology. Spore agglomeration of coagulative filamentous fungi and spore

concentration are necessarily interdependent, as shown by Grimm et al. (2004), who observed an increased agglomeration rate with increased spore concentration. Also Bizukojc and Ledakowicz (2010) observed an inversely proportional dependence between spore inoculum concentration and mean pellet diameter of *Aspergillus terreus* (coagulative pellet formation type) and an increased pellet concentration with increased spore concentration. Even pellets of the non-coagulative type such as *Rhizopus stolonifer* (synonym *Rhizopus nigricans*) decrease in size by increased spore concentration (Žnidaršič et al., 2000). A different behavior was observed for pellets of *P. chrysogenum* (hyphal element agglomeration type), where an increased spore concentration resulted in an increased agglomeration of hyphal elements and larger pellets (Nielsen et al., 1995).

**Type of inoculation** Lyu et al. (2023) inoculated the bioprocess with *A. niger* spores encapsulated in alginate, thereby prohibiting the agglomeration of spores. This inoculation strategy resulted in homogeneous small pellets with a diameter of around 285  $\mu\text{m}$ , whereas uncontrolled agglomerating spores formed pellets with a diameter of around 3,000  $\mu\text{m}$ . This study demonstrates how spore agglomeration controls the macromorphology and heterogeneity of fungal cultivations. The inoculation of the bioreactor with precultured pellets instead of spores can also improve the bioprocess performance (Wang et al., 2017).

**Agitation** The literature often states that an increased agitation intensity within stirred tank reactors (STR) results in smaller pellets (Veiter et al., 2018). For *Aspergillus awamori* pellets, enhanced mechanical forces at high stirrer speed resulted in pellet breakup and abrasion of hyphae and consequently smaller pellet diameters (Cui et al., 1997). The authors concluded that the fraction of dispersed mycelia in the cultivation broth is a function of the energy dissipation rate. In addition, the porosity of the pellets increased with decreasing stirring speed, indicating that agitation intensity also affects the internal structure of the pellets. Also *A. niger* grows in its dispersed form at high stirrer speeds, whereas low stirrer speeds can result in large pellets in low concentration (El-Enshasy et al., 2006). However, the effect of increased stirring intensity must be considered in combination with aeration intensity, making morphology engineering based on this strategy more complex. Lin et al. (2010) kept the volumetric power input into the bioreactor constant by varying either agitation or aeration intensity. At increased power input by aeration, *A. niger* pellets were smaller, and their concentration was higher. In contrast, at increased agitation intensity, pellets grew larger and formed a dense peripheral zone, possibly limiting oxygen and nutrients' mass transfer. This shows that not only the size but also the distribution of hyphal material within the pellets is affected by agitation, which in turn affects the mass transfer of oxygen and nutrients inside the pellets. In addition to stirring speed, stirrer type, or reactor geometry, also the reactor type can completely change the agitation of the cultivation broth and fungal morphology (Krull et al., 2013). Pellets can grow larger in a RMB and have a broader size distribution than in an STR (Kurt et al., 2018).

**pH shifting** By changing the medium properties, such as the variation of the pH or osmolality, the morphology can be influenced. Shifting the pH influences the spore agglomeration process by altering the spores' adhesion capacities (Colin et al., 2013). Here, an increase in the pH value from 2 to 8 resulted in the transition from dispersed mycelia to pellets with increasing diameters and a reduced number of pellets. The pH value has a major impact on the electrostatic and hydrophobic interactions between spores, which influence the agglomeration behavior of spores (Veiter et al., 2018).

**Salt-enhanced cultivation** Wucherpfennig et al. (2011) used sodium chloride to increase the osmolality of the medium. At elevated osmolality *A. niger* pellets were manipulated to grow smaller or as dispersed mycelia. The osmolality significantly impacted spore agglomeration and germination, whereby both processes were prolonged by elevated osmolality. When using the salt ammonium sulfate to increase osmolality, Tesche et al. (2019) increased the production of the pharmaceutically interesting peptide labyrinthopeptin A1 by the filamentous bacterium *Actinomadura namibiensis*. In addition, pellets with smaller Feret's diameter and increased circularity compared to the non-salt-supplemented control were obtained.

**Microparticle-enhanced cultivation (MPEC)** A recent and promising morphology engineering strategy is the addition of microparticles. Pellets are smaller and looser, or the filamentous fungus grows as dispersed mycelia at increased microparticle concentration in the cultivation broth (Driouch et al., 2012, 2010; Gonciarz and Bizukoje, 2014). The resulting small and loose pellet structures promote a sufficient oxygen mass transfer inside pellets (Gonciarz and Bizukoje, 2014). The commonly used microparticle types are talc, aluminum oxide, or titanate of sizes mostly below 50  $\mu\text{m}$  (Böl et al., 2021). The microparticles were added to the cultivation medium from inoculation with spores. In contrast, a later time of addition, e.g., after 12 or 18 h of cultivation, did not affect the macromorphology of the fungus (Driouch et al., 2010). The exact mode of action of microparticles on filamentous fungi and their morphology has yet to be understood (Laible et al., 2021). However, in the case of coagulative pellets, it is strongly assumed that the microparticles influence the spore agglomeration process (Driouch et al., 2012, 2010). Enforcing this hypothesis, the morphology of the fungal pellets, which were not of the coagulative pellet formation type, showed no decrease in size after the addition of microparticles (Kowalska et al., 2018).

**Genetics** Advances in genomics and transcriptomics technologies (Cairns et al., 2022; Carvalho et al., 2010; Kwon et al., 2019; Meyer et al., 2011; Schuetze and Meyer, 2017; Vanegas et al., 2019; Wanka et al., 2016) revealed potential gene candidates for optimizing fungal morphologies and made the generation of mutant strains in a high-throughput manner possible (Meyer et al., 2021). It has been estimated that around 2000 genes encode proteins that may participate in filamentous fungal growth and development (Cairns et al., 2019b). Aspects of genetic engineering strategies are summarized in two comprehensive reviews (Cairns et al., 2019b; Wang et al., 2020). More recent genetic engineering work is shortly summarized in the following.

By using a gene switch as a genetic tool (Wanka et al., 2016) within *A. niger*, the controlled expression of the gene *ap1D* of the endosomal transporter protein Ap1D generated hyphae of various lengths and branch phenotypes, which quantitatively correlated with various macromorphological features, such as pellet formation, diameter, and aspect ratio (Cairns et al., 2019a). Also, Fiedler et al. (2018) demonstrated the influence of a genetically modified branching frequency on the macromorphology of *A. niger* and reported a more compact macromorphology of the hyperbranching phenotype. It is often reported that proteins are secreted predominantly at the tips of filamentous fungi, and a high tip-to-biomass ratio may improve protein secretion. However, some studies did not correlate an elevated tip number with increased protein secretion (Cairns et al., 2019b). In addition to modifying the hyphal growth, the spore agglomeration process was modified by genetically changing the surface properties of spores (Dynesen and Nielsen, 2003; Miyazawa et al., 2019; Priegnitz et al., 2012). Fontaine et al. (2010) showed that the polysaccharide  $\alpha$ -1,3-glucan on the surface of swollen spores *Aspergillus fumigatus* plays an essential role for spore agglomeration. No spore agglomeration occurred when  $\alpha$ -1,3-glucans were degraded by adding  $\alpha$ -1,3-glucanase. Recently, Miyazawa et al. (2019) reported for *Aspergillus oryzae*, that genetic modification prevented biosynthesis of  $\alpha$ -1,3-glucan or galactosaminogalactan inhibits spore or hyphal aggregation, respectively, and thus pellet formation. In addition, when the biosynthesis of both cell wall surface polysaccharides was prevented in *A. oryzae*, optimized culture rheology and thus enhanced protein production was observed (Ichikawa et al., 2021).

The presented morphology engineering strategies show different ways to control filamentous fungal morphology. The strategies usually force the filamentous fungi to grow as small pellets or dispersed mycelia. Furthermore, they influence the different growth processes, with the spore agglomeration process being affected most. Here, it is essential to mention that growth processes are interdependent, e.g., increased spore concentration affects spore agglomeration and pellet growth due to reduced dissolved oxygen concentration. The same applies to the change in pH or stirrer speed and their influence on spore agglomeration and further growth processes. Therefore, when investigating morphology engineering methods, a holistic analysis starting from the spores is required to observe the main mechanisms of action. Furthermore, the impact of morphology engineering strategies on micromorphology is mainly unknown due to a lack of appropriate morphometric analysis methods. As a simple example, the increased productivity of a genetically engineered hyperbranching strain cannot be correlated with the number of tips (micromorphological property) if the number of tips cannot be determined for a statistically representative number of pellets. Therefore, there is a need for new morphometric analysis methods such as those presented in the results section.

Table 1.: Morphology engineering strategies, their effects, and the growth process assumed to be primarily affected. The pellet formation types are marked with (c) coagulative, (nc) non-coagulative, and hyphal element agglomeration type (ha).

Strategy	Organism	Effect/ Comment	Affected growth process	References
Spore concentration	<i>A. niger</i> (c)	Decreased pellet size to dispersed mycelia at increased concentration	Hyphal agglomeration, hyphal growth	Papagianni and Matthey (2006)
	<i>A. terreus</i> (c)	Decreased pellet size, increased pellet concentration at increased concentration	Spore agglomeration	Bizukoje and Ledakowicz (2010)
	<i>R. stolonifer</i> (nc)	—"	Pellet growth	Žnidarišič et al. (2000)
	<i>P. chrysogenum</i> (ha)	Increased pellet size at increased concentration	Hyphal agglomeration	Nielsen et al. (1995)
Type of inoculation	<i>A. niger</i> (c)	Encapsulation of spores compared to free spores resulted in small pellets	Spore agglomeration	Lyu et al. (2023)
Agitation	<i>A. niger</i> (c)	Inoculation with precultured pellets	Pellet growth	Wang et al. (2017)
	<i>A. awamori</i> (n/a)	Decreased pellet size and increased fraction of dispersed mycelia at increased agitation	Pellet fragmentation	Cui et al. (1997)
	<i>A. niger</i> (c)	—"	n/a	El-Enshasy et al. (2006)
	<i>A. niger</i> (c)	Depending on ratio between aeration and agitation intensity; decreased pellet size and increased pellet concentration at increased aeration and reduced agitation	Pellet growth	Lin et al. (2010)
	<i>A. niger</i> (c)	Larger pellets with heterogeneous size in RMB compared to STR	Pellet growth	Kurt et al. (2018)
pH shifting	<i>A. niger</i> (c)	Decreased pellet size to dispersed mycelia at decreased pH	Spore agglomeration	Colin et al. (2013)

Salt-enhanced cultivation (Osmolality)	<i>A. niger</i> (c) <i>A. nambibiensis</i> (n/a)	Decreased pellet size to dispersed mycelia at increased osmolality Decreased pellet size and increased circularity at increased osmolality	Spore agglomeration, germination Hyphal growth	Wucherpennig et al. (2011) Tesche et al. (2019)
Microparticle-enhanced cultivation (MPEC)	<i>A. niger</i> (c) <i>A. niger</i> (c) <i>A. niger</i> (c) <i>A. terreus</i> (c), <i>P. rubens</i> ( <i>ha</i> ), <i>C. globosum</i> ( <i>na</i> ), <i>M. racemosus</i> ( <i>nc</i> )	Decreased pellet size to dispersed mycelia with increased microparticle concentration —" —" Depending on organism: decreased pellet size ( <i>A. terreus</i> ), no effect on size ( <i>P. rubens</i> ), decreased pellet size ( <i>C. globosum</i> ), distinct cores ( <i>M. racemosus</i> ) with microparticles	Spore agglomeration Spore agglomeration Spore agglomeration ( <i>A. terreus</i> ), n/a ( <i>P. rubens</i> ), spore/hyphal agglomeration ( <i>C. globosum</i> ), n/a ( <i>M. racemosus</i> )	Driouch et al. (2010) Driouch et al. (2012) Gonciarz and Bizukojc (2014) Kowalska et al. (2018)
Genetics	<i>A. niger</i> (c) <i>A. niger</i> (c) <i>A. oryzae</i> (c) <i>A. oryzae</i> (c)	Smaller pellets and hyperbranched hyphae at low expression of <i>apID</i> gene Compact pellets of mutant hyperbranching strain Reduced pellet size or dispersed mycelia in knockout or double knockout mutants —"	Hyphal growth, pellet growth Hyphal growth, Pellet growth Spore agglomeration, hyphal agglomeration Spore agglomeration, hyphal agglomeration	Cairns et al. (2019a) Fiedler et al. (2018) Miyazawa et al. (2019) Ichikawa et al. (2021)

## 2.4. High-throughput analysis techniques for fungal cultivations

Schmideder (2022) elaborated a comprehensive list of quantitative morphological properties of filamentous fungi, which can be divided into micro- and macromorphological properties. Size (e.g., projected area, diameter), shape (e.g., circularity, aspect ratio), and compactness (e.g., solidity) refer to macromorphological properties. In contrast, the distribution of hyphal material, number of tips and branches, hyphal growth unit, or hyphal diameter refer to micromorphological properties. Furthermore, measurement techniques for the determination of these fungal properties are presented. To conclude, only a method based on  $\mu$ -computed tomography of freeze-dried fungal pellets and subsequent image analysis can reveal complex micromorphological properties of whole non-destructed pellets in 3D (Schmideder et al., 2019a). This method is summarized in Article I. However, the low sample throughput of the named method, resulting from long measurement times and a minor field of view at the required high resolution, limits its applicability for the representative analysis of complete fungal cultivations. For example, the micromorphological heterogeneity of fungal cultivations needs to be analyzed based on size distributions of micromorphological properties. For a *P. chrysogenum* cultivation, Posch et al. (2012) demonstrated that the diameter of 93 of 311 pellets must be measured to determine the actual average diameter  $\pm 10\%$  of the 311 pellets. However, to match the size distribution of the diameter from the 311 pellets, based on the Cramér-von-Mises (CvM) criterion (Anderson, 1962), analysis of at least 217 pellets would be required (Posch et al., 2012). Note that this required sample number was calculated for one specific fungal cultivation and depends on the characteristics of the cultivation's size distribution. For example, a more heterogeneous cultivation would require a larger sample size. The analysis of 200 pellets with the mentioned  $\mu$ -CT-based method (Schmideder et al., 2019a) would take about one month with uninterrupted measurement time. The following describes existing high-throughput analytical methods capable of detecting distributions of fungal properties. However, only macromorphological properties can be analyzed with the existing high-throughput methods. Moreover, the described methods can only quantify single growth processes and lack a holistic quantification of the cultivation development - from individual spores to pellets.

**Light microscopy** Light microscopy and corresponding image analysis are well established for offline analysis of filamentous fungi (Papagianni, 2014). In addition to morphological analysis of individual hyphal networks, hundreds of fungal pellets per time step can be imaged and automatically processed during image analysis to track the macromorphological evolution of fungal cultivations. The fraction of dispersed mycelia and pellets can be calculated, as well as size distributions of macromorphological properties of pellets, including shape factors, e.g., aspect ratio, circularity or solidity (Cairns et al., 2019a; Posch et al., 2012; Tesche and Krull, 2021; Willemse et al., 2018; Wucherpfennig et al., 2011). Posch et al. (2012) used an automated sample stage to record up to thousand highly resolved sub-

images of a microscope slide per sampling time. Image analysis of the generated sub-images discriminated dispersed mycelia, clumps, and pellets, whereby the pellet concentration and area fractions of the different fungal objects were calculated. Macromorphological properties such as area, solidity, pellet, and pellet core equivalent diameter were calculated for a few hundred pellets per sampling time to generate size distributions of these properties. Existing image analysis pipelines can also be adapted by the user to analyze different mycelial fragments and pellets of filamentous microorganisms (Willemsse et al., 2018). Based on pixel intensity values, Tesche et al. (2019) and Tesche and Krull (2021) discriminated dispersed mycelia and pellets on microscopic images. Since light microscopes are ubiquitous in laboratories, novel image analysis pipelines are relatively user-friendly and can compute multiple macromorphological properties of hundreds of pellets per time point, light microscopy-based image analysis will remain a standard tool for high-throughput analysis of filamentous fungal cultivations. However, the existing high-throughput microscopy-based image analysis misses capturing the complete growth process of filamentous fungi, e.g., by automatically switching from detecting spores and spore agglomerates to detecting dispersed mycelia or pellets without further user input.

**Focused beam reflectance measurement (FBRM)** was applied to follow the agglomeration of *A. niger* spores inline (Grimm et al., 2004, 2005b; Kelly et al., 2006). Based on the measured quantities of FBRM, the chord length and particle counts per second, the size of spore agglomerates over time, and the agglomeration rate were evaluated. Per time point, between 240 and 1000 particle counts per second with sizes close to zero and 500  $\mu\text{m}$  were recorded. Furthermore, the time-dependent data of FBRM were used to create a kinetic model of the spore agglomeration using population balance modeling (Lin et al., 2008). Besides, offline measurements of pellets were performed with FBRM (Pearson et al., 2003, 2004; Whelan et al., 2012). The evaluation of a high number of particles, which is also possible inline, is opposed by the fact that no shape descriptors can be determined with FBRM. The lack of shape descriptors makes the distinction between components of a cultivation broth, e.g., spore agglomerates, dispersed mycelia, pellets, or ingredients of the medium, uncertain if not impossible.

**Laser diffraction** Petersen et al. (2008) used the laser diffraction technique to generate the volumetric particle size distribution of the biomass of an *A. oryzae* cultivation. Based on the Fraunhofer diffraction theory, the detected intensities of the scattered laser beam by the particles are converted into the size distribution of the particles (Lin et al., 2010). Since the scattered light intensity depends on the volume of a particle, the particle's volume equivalent spherical diameter is calculated. An advantage of the technique is the high number of particles that can be measured within a short time, enabling, e.g., to calculate the size distributions of pellets at different agitation intensities (Lin et al., 2010) and after short time intervals during high-shear mixing to determine fragmentation rates (Quintanilla et al., 2018). Wucherpennig et al. (2011) used laser diffraction to track the spore agglomeration based on size distributions of spores/spore agglomerates at different osmolalities of the cultivation medium. Also advan-

tageously, similar to FBRM, pellets and spores are measured in their natural state directly in the liquid cultivation medium, which can also be done online within a bypass of the bioreactor (Rønneest et al., 2012; Wucherpfennig et al., 2011). However, shape factors of fungal pellets and the pellet concentration cannot be determined based on the laser diffraction technique (Lin et al., 2010; Petersen et al., 2008; Rønneest et al., 2012; Wucherpfennig et al., 2011).

**Flow cytometry** A recent review summarizes the technique of flow cytometry and its use for the analysis of fungal cultivations (Bleichrodt and Read, 2018). In short, similar to laser diffraction, particles are measured in a liquid medium within a flow cell, but only one particle passes through the laser beam at a time. In addition to the scattered light, the absorbed light by a particle can be emitted as fluorescence, which is also detected. Based on the recorded forward and side scatter signal, size distributions of pellets and hyphal agglomerates can be determined, as well as morphological shape descriptors for pellets, such as solidity or a novel compactness parameter, describing the pellet's periphery (Ehgartner et al., 2017). Ehgartner et al. (2016) used live/dead-staining and the recorded fluorescence signal to measure the amount of metabolic active *P. chrysogenum* spores. Furthermore, the swelling of the spores could be tracked. Based on flow cytometry and fluorescent staining, Veiter and Herwig (2019) presented an approach to determine the thickness of the metabolic active outer pellet layer for a high number of pellets. Due to the high number of measurable particles per time ( $\approx 1000/s$ ) (Bleichrodt and Read, 2018), the acquisition of shape properties (Ehgartner et al., 2017), and the emerging possibilities by exploiting the fluorescence signal (Ehgartner et al., 2016; Veiter and Herwig, 2019), flow cytometry is a promising high-throughput analysis method for fungal cultivations. However, flow cytometry is restricted by the size of the sampling tube, which can result in size-exclusion effects of large hyphal structures and the over-representation of small structures (Veiter and Herwig, 2019). Furthermore, Veiter and Herwig (2019) stated that a representative overview of morphology respecting all size classes is challenging. It should also be mentioned that, to the best of the author's knowledge, flow cytometry has never been used to analyze the process of spore agglomeration over time.

## 2.5. Modeling approaches

Modeling approaches offer the possibility to predict the course of fungal cultures under different growth and process conditions. Several models exist, aiming to predict the morphological development, biomass concentration, substrate uptake, and product formation of individual hyphal elements or pellets and entire filamentous fungal populations (Böl et al., 2021; Celler et al., 2012; Grimm et al., 2005a; King, 1998; Posch et al., 2013; Veiter et al., 2018). In general, a big advantage of all models compared to laboratory cultivation experiments is the repeatability of simulations under selective and defined changes of growth or cultivation model parameters, elucidating the underlying effects of morphological development. Furthermore, time-trajectories of in silico-grown individual pellets or complete cultivations under various parameters can be simulated quickly compared to in vivo experiments. Increasing computing

power makes it possible to simulate pellet structures within minutes (Schmideder et al., 2020). The different goals of modeling require different modeling scales. Schmideder (2022) categorized morphological modeling into 1) Microscopic approaches, 2) Continuum approaches, and 3) Population balance modeling (PBM) approaches. Microscopic and continuum models simulate individual pellets with morphological properties representative of the entire population or sub-populations within the cultivation. Continuum models focus on the transport mechanism inside the pellets, which are represented as a porous media. Morphological quantities are averaged, and their densities, such as the tip density, are given as functions of the pellet radius. Microscopic models, on the other hand, display the detailed three-dimensional micromorphological development of hyphae into pelleted hyphal networks computing the discrete positions of hyphal elements, including tips and branches. PBM approaches are used to simulate entire fungal populations and their interactions with each other. However, experimental micromorphological data from multiple samples per time point to calibrate these model types are missing, making rough assumptions within models necessary and the validation of the developed models impossible. According to the categorization of morphological modeling into 1) - 3), the characteristics of the different model types will be presented.

Microscopic models consider the outgrowth of a pellet from a single spore, hyphal extension, branching, and septation (Yang et al., 1992). Furthermore, Meyerhoff et al. (1995) added the diffusion-driven transport and consumption of growth-limiting substrates and the abrasion of hyphae due to shear forces to the microscopic modeling. To generate the pellet structure, Monte Carlo methods are applied to simulate hyphal branching, branching directions, and tip extension according to probability distributions of the required growth parameters such as the branching angle (Celler et al., 2012; Lejeune and Baron, 1997; Meyerhoff et al., 1995; Schmideder et al., 2020; Yang et al., 1992). In addition to input parameters such as the branching angle, growth direction, branch interval, or hyphal diameter, decisive for the result of the microscopic modeling is the number of spores from which the simulated pellets are formed (Schmideder et al., 2020). Based on the model of Celler et al. (2012), Schmideder et al. (2020) used microscopic Monte Carlo growth modeling to simulate 3125 different pellets under various growth parameters. In this study, pellets of the coagulative type could also be generated for the first time, as simulated spore agglomerates were used as the initial condition of hyphal growth compared to a single spore. The *in silico*-grown coagulative pellets visually resembled experimental pellets that were imaged based on  $\mu$ -CT. The details of the established modeling are summarized in Article I. Despite the microscopic Monte Carlo growth models' success, their validation remains an open task. The simulated 3D pellet structures and their obtained micromorphological data, such as the spatially resolved location and amount of hyphal material, tips, and branches, can be compared to the structure and data of a few individual pellets from  $\mu$ -CT measurements (Schmideder et al., 2020). However, morphological changes resulting from the abrasion of hyphae at the pellets' periphery or substrate limitations within the pellets occur during cultivation, necessitating multiple samples from multiple time points for observing such effects and model validation.

Already early continuum modeling approaches to predict the biomass of pellets included limited growth due to diffusion-driven transport limitations of substrates within pellets (Pirt, 1966). Here, the cube root relation assumed the increase of hyphal biomass only in a peripheral actively growing zone with a certain thickness. However, this model assumes a constant spatial distribution of hyphae within the pellet, whereas it was confirmed that the distribution of hyphae is heterogeneous (Hille et al., 2005; Lin et al., 2010; Priegnitz et al., 2012; Schmideder et al., 2019a). A more holistic continuum approach from Buschulte (1992) overcame this limitation and considered the micromorphological development, diffusive substrate transfer, and consumption inside a fungal pellet. Assuming spherical symmetry, coupled partial differential equations were solved to calculate the temporally resolved concentration of hyphae, tips, and substrates along the radial coordinate of the pellet within differentially sized spherical shells. In the model, calculated reduced diffusivity and consumption of oxygen and other substrates by the hyphal material resulted in substrate and growth limitation (Buschulte, 1992). This computational expensive approach was later simplified, whereby a fixed number of spherical shells was chosen to calculate the concentration of substrates (Meyerhoff et al., 1995). Continuum approaches are integrated in microscopic Monte Carlo modeling to compute the concentration of substrates, limiting the modeled hyphal growth inside pellets (Celler et al., 2012; Lejeune and Baron, 1997; Meyerhoff et al., 1995). The continuum model from Buschulte (1992) is still the most detailed one, although it included a wrong correlation between the structure and the diffusion for the calculation of the nutrient supply of hyphae (Schmideder et al., 2020). Continuum models for simulating pellets require parameters to describe hyphal growth, such as the maximal apical growth or branching rate (Buschulte, 1992; Celler et al., 2012; Lejeune and Baron, 1997; Meyerhoff et al., 1995). However, due to a lack of suitable morphometric analysis methods, these parameters can only be determined so far for dispersed growing young hyphae rather than for pellets. Furthermore, the evolution of micromorphological properties still needs to be validated, requiring time-resolved micromorphological properties as a function of the pellet radius.

Unlike microscopic and continuum models, PBM approaches simulate the morphological evolution of pellet populations of a whole bioreactor cultivation. Thus, the above discussed morphological heterogeneity (Section 2.2.4), which is affected by agglomeration, growth, pellet breakup, and generation of dispersed mycelia, calls for PBM describing the evolution of distributions of micromorphological properties over space and time (Ramkrishna, 2000). Based on PBM, the development of a characteristic micromorphological property, e.g., the overall pellet porosity or at a specific radial position within a pellet, could be predicted for classes of similar individuals. Here, the evolution of the entire population is described by a number density function  $f(y,t)$  over time  $t$  in which  $y$  is the characteristic property, e.g., the overall pellet porosity (King, 1998). Nielsen and Krabben (1995) established the first PBM of submerged cultivation. Their approach already included micromorphological properties within a bivariate PBM, where the average total length of hyphal elements and the average number of growing tips were predicted. However, their model did not include the growth of pellets. PBM was also used to predict the spore agglomeration, i.e., the evolution of the size

distribution of spore agglomerates over time (Lin et al., 2008). Despite the good agreement with experimental size distributions of spore agglomerates, this model included unjustified assumptions like constant aggregation/breakage kernels, which were independent of the spore agglomerates' size. PBM approaches were also used to understand the impact of morphology engineering methods on the overall cultivation morphology. Jüsten et al. (1997) simulated a *P. chrysogenum* cultivation at different agitation times. However, only the projected area (size) of hyphal structures was considered as characteristic variable. Later PBM approaches, such as the one of Liu et al. (2005), missed to include micromorphological information of pellets. So far, due to a lack of experimental micromorphological big data of pellet cultivations, no PBM takes the time-dependent evolution of the distribution of micromorphological pellet properties, e.g., the development of hyphal material within a pellet, into account. Still, a prerequisite for these approaches are analytical high-throughput methods, e.g., imaging tools, which provide the information necessary to determine macro- and micromorphological characteristics of a representative amount of pellets and dispersed mycelial structures during submerged cultivations. In combination with the substantial increase in computational power and significant advances in the numerical solution of multivariate population balance models (Briesen, 2009; Reinhold and Briesen, 2015; Rollié et al., 2009), PBM seems promising for simulating and analyzing filamentous fungal cultivation heterogeneity.

### 3. Problem definition

The theoretical background highlights that morphology is a crucial parameter for process performance, leading to various morphology engineering methods to control the fungal morphology. However, existing analytical methods reach their limits in analyzing the development of macro- and micromorphology in a representative and all-encompassing way. In addition, modeling of filamentous cultivations lacks experimental micromorphological data for calibration and validation. The following knowledge gaps were elaborated and addressed during this Ph.D. thesis.

**A simple method to holistically analyze the morphological development of an entire fungal cultivation, including spore agglomeration, dispersed mycelia, pellet growth/breakage, and cultivation heterogeneity, does not exist.** Morphology engineering strategies can influence the different growth processes during cultivation (Section 2.3). Thus, to understand the exact impact of these strategies, all growth processes, starting from spore agglomeration, need to be investigated. Furthermore, dispersed mycelia and a representative number of pellets must be analyzed to quantify macromorphological cultivation heterogeneity resulting from spore agglomeration and pellet breakage. Current high-throughput methods analyze either spore agglomeration or pellet development, whereby the analysis of an entire cultivation is only possible with further user input. A high-throughput method that can track spore agglomeration and automatically switches to the analysis of pellet growth would enable to observe whether a morphology engineering strategy influences the spore agglomeration, hyphal growth, or both. In addition, cultivation heterogeneity resulting from spore agglomeration or pellet breakage could be observed. Based on the gained experimental data, PBM approaches could be set up or extended, simulating the development of pellet cultivations, starting from spores.

**A method to track the 3D micromorphology of a statistically relevant number of fungal pellets in a reasonable measurement time does not exist.** The only experimental method that can resolve a fungal pellet's entire non-destructed 3D structure, enabling insights into the 3D micromorphology, is based on  $\mu$ -computed tomography ( $\mu$ -CT) of freeze-dried pellets. However, due to a small field of view and long measurement times at the required high local resolution, this method is not applicable to measure a few hundred pellets from multiple sampling times. For the investigation and quantification of micromorphological cultivation heterogeneity and its development, such high numbers of samples are necessary to be statistically representative. Additionally, modeling approaches simulating the development of pellets' micromorphology require number density distributions of micromorphological prop-

erties as a function of time for parameterization. Based on these distributions, e.g., the distribution of the total number of hyphal tips of each pellet, rate equations necessary within PBM approaches to describe the distributions' evolution over cultivation time can be estimated.

## 4. Methods for problem solving

To address the described shortcomings, the following methods were developed. A detailed description of all elaborated methods can be found in the included articles.

**Method to visualize several thousand filamentous fungal structures from multiple cultivation times in 2D.** Stereomicroscopy was applied to generate multiple 2D images of fungal structures from submerged cultivations at different growth phases. By adjusting the pixel size from 0.8  $\mu\text{m}$  to 4.1  $\mu\text{m}$ , individual spores with a diameter of a few micrometers and pellets of a few hundred micrometers could be imaged in high numbers within a short time. The stereomicroscope further enabled the visualization of dispersed mycelia and spore agglomerates in already-developed pellets.

**Method to visualize several thousand entire fungal pellets from multiple cultivation times in 3D.** By applying synchrotron radiation-based  $\mu$ -computed tomography (SR- $\mu$ -CT) at the Deutsches Elektronen-Synchrotron – DESY (Hamburg, Germany), the complete non-destructed 3D structure of several hundred fungal pellets at once could be captured in less than 10 minutes. The principle of SR- $\mu$ -CT is the same as laboratory-based  $\mu$ -CT. The significant difference is the source of X-ray radiation. At a synchrotron, electrons are accelerated to around 6 GeV (DESY) and kept on track by bending magnets in a 2.3-kilometer-long storage ring (DESY). At an insertion device along the storage ring, the electrons emit high-brilliant X-ray radiation, which is transferred to the imaging beamline. The brilliance quantifies the photons of a given wavelength and direction, which are concentrated on a spot per unit of time. The high photon flux/brilliance of synchrotron radiation enables a high signal-to-noise ratio during short exposure time per projection or, differently spoken, enables high-speed 3D imaging with high resolution. SR- $\mu$ -CT and newly developed sample holders allowed us to overcome the length scale difference between a culture sample consisting of several hundred pellets in a volume of about 40  $\text{mm}^3$  and the micromorphological structure of each pellet with hyphal diameters of about 3  $\mu\text{m}$ .

**Method to analyze two- and three-dimensional images of fungal structures automatically and in a high-throughput manner.** Image analysis was applied to segment filamentous fungal structures and quantify their macro- and micromorphology on the images generated by the abovementioned two methods. The 2D and 3D image processing algorithms were designed in a single software program (MATLAB, MathWorks) and run with little user input. In the case of the analysis of fungal objects on 2D images based on stereomicroscopy, the parameters required for segmentation must be predefined. Subsequently, the processing of

all images from multiple sampling times, regardless of whether individual spores, dispersed mycelia, or pellets are imaged, is automated. As a result of analysis, spore/spore agglomerate and pellet number concentrations, area fractions of fungal objects, including dispersed mycelia, and size distributions of spore agglomerates and pellets from different cultivation times were obtained. In addition, segmentation and quantification of spore agglomerates within already-developed pellets allowed to deduce a mechanism of pellet breakage.

The designed image analysis to segment and analyze individual 3D pellets from synchrotron measurements pipeline comprises the following steps: (1) The deletion of the sample holder on the whole 3D image and automatic segmentation into individual pellets, (2) the detection of spores within each pellet, (3) the quantification of the micromorphology including the local detection of tips, branching points, and hyphal material for each pellet. The determined high amounts of micromorphological data enable to compute number density distributions of micromorphological pellet properties and growth parameters. The data itself provide novel insights in the development of fungal pellets and allow further development and parameterization of individual pellet and population balance modeling.

## 5. Results

### 5.1. Article I: Generalized morphology modeling of aggregating, filamentous microorganisms (not published, not peer-reviewed)

Article I reviews the methods and results developed within the DFG priority program SPP 1934 DiSPBiotech. The methods presented in Article III build on these methods and findings. Article I has not yet been published, but since it is not subject to the peer-review procedure, it will be published as shown in Appendix C at SpringerNature in early 2024.

#### Summary

First, Article I reviews the development of 3D image analysis methods based on X-ray micro-computed tomography ( $\mu$ -CT) to determine the 3D micromorphology, including the 3D location of tips, branches, and hyphae of whole fungal pellets for the first time. Subsequently, it presents the development of a universal diffusion law. For this, representative cubic sub-volumes were extracted from the generated and processed 3D pellet images to perform diffusion computations through the 3D hyphal networks. By correlating the computed effective diffusion factors with the hyphal fraction/porosity of the sub-volumes, we proposed, until today, the first approach to link the pellets' 3D micromorphological hyphal structure with the diffusivity within pellets. This first correlation is based on five 3D-imaged *A. niger* pellets. Within the next step, diffusion computations with sub-volumes from 66 additional  $\mu$ -CT measured pellets of different industrial-relevant fungal species including *P. chrysogenum*, *R. stolonifer*, and *R. oryzae* were performed. Furthermore, diffusion computations through additional 3125 morphologically different fungal structures, generated in-silico based on Monte Carlo growth simulations, were conducted to cover the wide variety of fungal morphologies. On this database, a universal law that enables the prediction of the diffusive mass transport of nutrients, oxygen, and secreted metabolites within any filamentous fungal pellet was unveiled:

$$k_{eff} = (1 - c_h)^{1.76},$$

where  $k_{eff}$  is the effective diffusion factor that solely depends on the locally resolved hyphal fraction of fungal pellets  $c_h$ . The law is a basis for predicting the concentration of nutrients in fungal pellets based on continuum modeling. Thus, it contributes to the development of targeted morphology engineering and process control strategies resulting in enhanced productivity of bioprocesses.

## **Author contributions**

Henri Müller created the concept and wrote the report, edited and approved by co-authors Stefan Schmieder and Heiko Briesen. Heiko Briesen supervised the structure of the report.

Within the report, the studies Schmieder et al. (2019a), Schmieder et al. (2019b), and Schmieder et al. (2020) are summarized. As co-author within the study Schmieder et al. (2019b), Henri Müller developed a new sample preparation method for  $\mu$ -CT measurements, performed  $\mu$ -CT measurements, and image processing. Furthermore, Henri Müller conducted preliminary diffusion computations for the development of a universal diffusion law and proposed a first correlation between the hyphal fraction and the diffusivity. As the first co-author within the study Schmieder et al. (2020), Henri Müller performed  $\mu$ -CT measurements, image analysis, and developed an image processing algorithm to automatically segment multiple fungal pellets from laboratory scale  $\mu$ -CT measurements. Henri Müller created a video for the visualization of the 3D image analysis with VGstudio. In addition, Henri Müller wrote the image processing section within Schmieder et al. (2020).

Moreover, the studies presented in Article II (Müller et al., 2022) and Article III (Müller et al., 2023) within this dissertation are briefly summarized in the report. Heiko Briesen supervised all included studies within the report.

## 5.2. Article II: From spores to fungal pellets: A new high-throughput image analysis highlights the structural development of *Aspergillus niger* (Müller et al., 2022)

### Summary

Filamentous fungal pellet populations are usually very heterogeneous, which can be beneficial or detrimental to the performance of industrial bioprocesses. Population heterogeneity can be induced during submerged cultivation by spore agglomeration or pellet fragmentation. To quantify and analyze the extent and origin of heterogeneity, size distributions of morphological properties need to be calculated based on the observation of high numbers of fungal structures from different growth phases. As the dynamics underlying population heterogeneity are not yet fully understood, we developed a new high-throughput method based on easy-to-use stereomicroscopy and automated 2D image analysis to track both the spore agglomeration and the development of hyphal structures, i.e., pellets and dispersed mycelia. The designed 2D image analysis pipeline discriminated four object classes on the generated stereomicroscope images: (1) non-germinated spores and spore agglomerates, (2) spore cores which are the spore part of germinated spore agglomerates, (3) pellets, and (4) dispersed mycelia. The fungal objects were segmented based on their pixel intensity values of the different color channels from the RGB stereomicroscope images, whereby a watershed segmentation was used to separate attaching pellets. The area equivalent circular diameter and number concentration was calculated for each analyzed object and class (spores/ spore agglomerates, spore cores, pellets). The amount of dispersed mycelia was evaluated and compared to the other fungal object classes based on their area fractions. To demonstrate the potential of the developed image analysis, we harvested a hyperbranching strain of *Aspergillus niger* for 48 h and took samples from 44 time points during submerged cultivation. By calculating the concentrations and number density distributions of the area equivalent circular diameters of up to 1700 spore agglomerates and 1500 pellets per cultivation time, we could precisely track and quantify the development of pellets and population heterogeneity, starting from spore agglomeration. During cultivation, the amount of dispersed mycelia increased steadily. Furthermore, based on the detection and analysis of spore cores (spore agglomerates within already-developed pellets), we hypothesized that the pellets break at their spore core during nutrient limitation. The developed method can also be used to evaluate and understand the impact of morphology engineering methods, such as genetic approaches, on spore agglomeration and pellet growth. In addition, the gained high amounts of macromorphological data are adequate to set up a multivariate population balance model describing spore agglomeration and the transfer to heterogeneous pellet populations. The method was further used to validate the image analysis based on 3D imaging of several thousand pellets presented in Article III.

## **Author contributions**

Henri Müller, Lars Barthel, and Stefan Schmieder did the conception and design of the study. Henri Müller wrote the manuscript, which was edited and approved by all authors. Henri Müller, Heiko Briesen, and Stefan Schmieder interpreted the data. Heiko Briesen and Vera Meyer supervised the study. Lars Barthel, Tabea Schütze, Henri Müller, and Stefan Schmieder cultivated filamentous fungi. Lars Barthel developed the applied cultivation conditions. Henri Müller created the code for image analysis. Henri Müller performed the image and data processing and analyzed the results.

## **Copyrights**

Reprinted in Appendix B with permission from Müller et al. (2022), Copyright (2022) John Wiley and Sons.

### **5.3. Article III: Synchrotron radiation-based microcomputed tomography for three-dimensional growth analysis of *Aspergillus niger* pellets (Müller et al., 2023)**

#### **Summary**

Fungal morphology and process performance are closely related. Nevertheless, only a method based on  $\mu$ -computed tomography ( $\mu$ -CT) and subsequent 3D image analysis (Schmideder et al., 2019a) can quantify the detailed 3D micromorphology of non-destructed entire fungal pellets. However, the existing method resulted from laboratory  $\mu$ -CT measurements with very low sample throughput, whereby the image analysis was not designed to process and analyze high numbers of fungal pellets automatically. Thus, the micromorphological analysis of a statistically representative number of pellets necessary to quantify micromorphological heterogeneity, the impact of morphology engineering methods on pellet cultivations, and growth parameters or rate equations for population balance modeling was not possible. We overcame the low sample throughput by applying synchrotron radiation-based X-ray microtomography (SR- $\mu$ -CT) at the Deutsches Elektronen-Synchrotron (DESY) for fast 3D imaging and extended our developed image analysis to process several thousand pellets automatically. For SR- $\mu$ -CT measurements, we constructed a sample holder to ensure standardized measurements of freeze-dried fungal samples. The high photon flux of synchrotron radiation enabled the 3D imaging of up to 579 pellets within a sample holder in less than 10 minutes. The developed image analysis included the following steps: (1) The automatic segmentation into individual pellets from the sample holder containing multiple pellets, (2) the detection of spores within each pellet, which define the center of a pellet, and (3) the local detection of tips, branching points, and hyphal material for each pellet. A Gaussian mixture model further clustered the resulting data to determine artificial pellets, where the morphology was changed during sample preparation for SR- $\mu$ -CT measurements. The data of the remaining unbiased pellets were used to compute the locally resolved densities of spores, tips, branching points, and hyphal material. In addition, parameters such as the hyphal diameter, the total hyphal length, the average branch length, and the hyphal growth unit (HGU) of pellets were obtained. We analyzed pellet samples from 26 time points of a 48-hour *Aspergillus niger* cultivation. The time course of the calculated data allowed us to determine the growth rate, apical growth velocity, and branching rate for pellets, which to our knowledge, is the first time this has been done for entire fungal pellets. Furthermore, the number density distributions of the total hyphal volume for each pellet enabled tracking the growth and heterogeneity of pellets over time. Complementing modeling approaches, the obtained micromorphological data can serve to gain mechanistic insights into the development of fungal morphologies. In addition, the developed methodology will pave the way to predict the evolution of fungal morphologies as a function of genetic and environmental growth conditions applied during morphology engineering methods.

## **Author contributions**

Henri Müller did the conception and design of the study. Henri Müller and Charlotte Deffur wrote the manuscript by 95% and 5%, respectively. The manuscript was edited and approved by all authors. All authors interpreted the data. Heiko Briesen and Vera Meyer supervised the study. Lars Barthel, Henri Müller and Stefan Schmieder cultivated filamentous fungi and prepared pellets for microcomputed tomography (SR- $\mu$ -CT) measurements. Lars Barthel developed the applied cultivation conditions. Jörg Hammel, Henri Müller, Stefan Schmieder and Lars Barthel performed SR- $\mu$ -CT measurements of pellets. Jörg Hammel and Henri Müller reconstructed the image data. Henri Müller, Stefan Schmieder, Tiaan Friedrich and Lukas Mirlach created the code for image analysis. Charlotte Deffur created the code for modeling the growth parameters. Henri Müller and Tiaan Friedrich created the code for clustering the pellets with GMM. Henri Müller performed the image and data processing and analyzed the results.

## **Copyrights**

Reprinted in Appendix B with permission from Müller et al. (2023), Copyright (2023) John Wiley and Sons.

## 6. Discussion

The presented publications (Article II and III) describe high-throughput methods based on 2D and 3D imaging and analysis that can quantify pellet culture's micro- and macromorphological development. Thereby, the origin and extent of cultivation heterogeneity can be unveiled. Furthermore, by quantifying the morphological development program including spore agglomeration, the impact and mode of action of morphology engineering methods can be uncovered. The following will discuss opportunities, challenges, possible further adaptations, and use cases of the developed methods.

### 6.1. Opportunities: Analysis of spore agglomeration, macromorphological development, and heterogeneity

Only high-throughput morphometric analysis methods can quantify population heterogeneity by number density distributions determined from many data of macromorphological properties at different cultivation times (Section 2.4). Since different growth processes can influence heterogeneity, they must be analyzed equally to unveil the origin of cultivation heterogeneity. Furthermore, the various morphological forms of filamentous fungi - from spores to spore agglomerates to dispersed mycelia and pellets - need to be quantified over time (Section 2.1 and 2.2). However, the existing high-throughput methods only quantify specific growth phases. Some are designed to track the growth of pellets and dispersed mycelia when hyphal networks of a certain size have already formed (Section 2.4). Only a few publications present methods for the analysis of spore agglomeration (Grimm et al., 2004, 2005b; Lin et al., 2008). Wucherpennig et al. (2011) analyzed both spore agglomeration and pellet development but used different methods, i.e., laser diffraction and microscopy, with different data analysis methods.

Considering that no automated high-throughput method captures spore agglomeration and pellet development, including fragmentation, the quantification of spore agglomeration by size distributions of spore agglomerates is often wholly disregarded when investigating morphology engineering strategies. For example, multiple studies only focused on the size of already-formed pellets when modifying the morphology of coagulative-type pellets by changing the spore inoculum concentration (Papagianni and Matthey, 2006), the agitation and aeration intensity (Lin et al., 2010), the addition of microparticles (Driouch et al., 2012; Gonciarz and Bizukojc, 2014; Kowalska et al., 2018), and genetic modifications (Cairns et al., 2019a). Thus, the mechanisms of the morphology engineering strategies could not be clarified. The development of an increasing number of morphology engineering methods requires fast and

easy-to-use high-throughput analysis methods (Böl et al., 2021). The high-throughput method presented in Article II can track and quantify both spore agglomeration and pellet development in one continuous computational run requiring no further user input. Thus, the developed 2D image analysis tool is suitable for rapid and holistic heterogeneity and morphology engineering analysis. The results of an *A. niger* cultivation case study demonstrate the power of the tool.

In Article II, we quantified the spore agglomeration of *A. niger* by analyzing the area equivalent circular diameter of up to 66,300 spores and spore agglomerates per cultivation. Analysis of the size distribution at each sampling time during spore agglomeration showed that large spore agglomerates (>200  $\mu\text{m}$ ) broke up into smaller agglomerates at the onset of germination, with growing hyphae leading to the separation of loose connections between spore agglomerates. Contrary to Grimm et al. (2004), we did not observe a clear second aggregation step, where spores additionally aggregate after the start of germination for the analyzed hyperbranching strain *A. niger* MF22.4. This observation was supported by the spore/spore agglomerate concentrations and equivalent diameters, which showed only one strong decrease and increase during spore agglomeration, respectively. Spores that did not agglomerate and remained separated formed dispersed mycelia which constantly grew during cultivation, indicated by a constantly increasing area fraction of dispersed mycelia over cultivation time. The structure of the genetically engineered hyperbranching strain MF22.4 is denoted to have a more compact morphology compared to its parental strain (Fiedler et al., 2018), which is possibly the result of the absence of a second aggregation step and the development of a centrally embedded and compact spore core within the developed pellets. Unfortunately, the spore agglomeration of *A. niger* MF22.4 was not observed and compared to the parental strain (Fiedler et al., 2018). This example demonstrates that quantifying spore agglomeration, pellet development, and linking both processes can provide new insights in the mode of action of morphology engineering approaches. As another example, with the developed 2D image analysis method, it would be easy to follow spore agglomeration and subsequently pellet development at different spore inoculum concentrations. The quantification of the growth processes would clarify why mainly dispersed mycelia instead of pellets form at high spore concentrations (Papagianni and Mattey, 2006), possibly resulting from an altered spore agglomeration. Furthermore, spore agglomeration and pellet formation could be analyzed at different agitation intensities. Thus, it would be possible to differentiate if morphological different pellets or dispersed mycelia at different shear forces result from an altered spore agglomeration, pellet fragmentation (Section 2.2.3), or both.

In Article II, at the end of cultivation, we observed breakage of the pellets at the spore core due to nutrient starvation, which is supported by four quantified data sets based on the analysis of 1,200 pellets at the last sampling time: (1) The size distribution of pellets' equivalent diameters indicated a decrease/increase of larger/smaller pellets, respectively (Figure 3); (2) The pellet concentration increased; (3) The equivalent diameters of spore cores decreased; (4) The number of eccentric embedded spore cores increased, measured based on the Euclidean distance between the pellet and spore core centroid (Figure 4). In addition, the analyzed

concentration of the spore cores and pellets further unveiled that a pellet can have multiple spore cores, possibly arising from the agglomeration of young pellets. A reduction in the number of spore cores per pellet toward the end of cultivation indicates that pellets with, for example, two spore cores may break down into two pellets with one spore core each. This is supported by the number of spore cores, with 8% of the pellets having two or more spore cores after 12 hours, which decreased to 2% after 48 hours of cultivation. The overall wider distribution of the pellet equivalent diameters at the end of cultivation compared to early cultivation times confirm that the fragmentation of pellets is the main effect of the resulting cultivation heterogeneity.

The findings of the cultivation analyzed by 2D image analysis in Article II show that it is worthwhile to follow the spore agglomeration and link it to the morphological development. It should not be assumed that spore agglomeration of pellets classified as coagulative type always follows the same pattern since agglomeration depends not only on the organism/strain but also on environmental conditions (Papagianni and Matthey, 2006). Based on the developed 2D image analysis method, it is possible to categorize the pellet formation type for the organism and the given cultivation conditions. However, attention must be paid to the definition of morphological forms, e.g., the "pellet" morphology is not clearly defined in the literature. For example, Cox et al. (1998) defined the basic morphological structure of a pellet as follows: "The general structure of fungal pellets is a core of such densely packed hyphae surrounded to a greater or lesser extent by an annular or "hairy" region containing radially growing hyphae." Based on the calculation of spatially resolved hyphal densities within pellets in Article III, we have shown that the spore core of coagulative pellets is always the densest pellet region, not necessarily densely packed hyphae. In addition, in Article II, we found that a "pellet" can have multiple spore cores, which is a deviation from the definition of Cox et al. (1998). Due to existing known and unknown variations in pellet formation mechanisms, a precise definition of a fungal pellet is not currently possible. Therefore, definitions of morphological forms should always be considered when comparing results from different studies.

## **6.2. Opportunities: Analysis of micromorphological development and heterogeneity**

The micro-computed tomography ( $\mu$ -CT) based 3D imaging and analysis method of Schmideder et al. (2019a) was the first to quantify the 3D micromorphology of whole non-destructed filamentous fungal pellets. As a rough summary, Article III is an extensive update of this method to transfer the micromorphological analysis of a few individual pellets to the process scale, whereby it is possible to analyze a few hundred pellets from multiple sampling times of a bioprocess. In this way, the micromorphological properties of many pellets can be quantified over time, allowing the 3D micromorphological evolution of the entire pellet population to be followed in a statistically representative manner.

The update's development started with the design of a standardized sample holder for  $\mu$ -CT measurements, designed for simultaneous measurement of multiple freeze-dried pellet

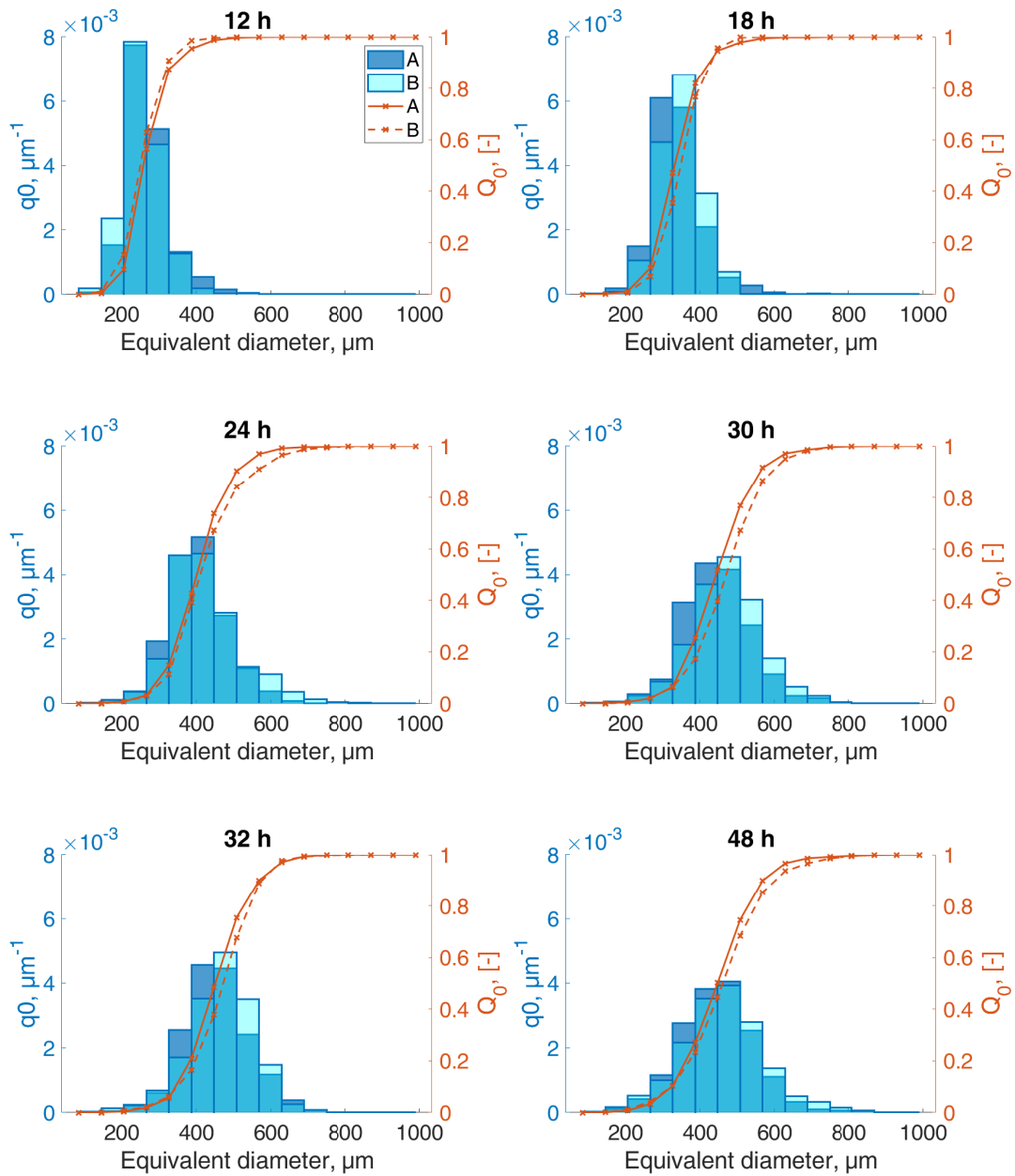


Figure 3: Normalized number-density-distribution  $q_0$  (left ordinate, blue) and cumulative size distributions  $Q_0$  (right ordinate, orange) as a function of the equivalent diameter of *Aspergillus niger* pellets at different sampling times for two replicated cultivation runs (A and B). To generate the distributions, the values of the equivalent diameters of pellets were divided into 15 equidistant size classes between the minimal and maximal equivalent diameter. The data were determined by the developed 2D image analysis based on stereomicroscopic images. (Adapted and reprinted with permission from Müller et al. (2022), Copyright (2022) John Wiley and Sons)

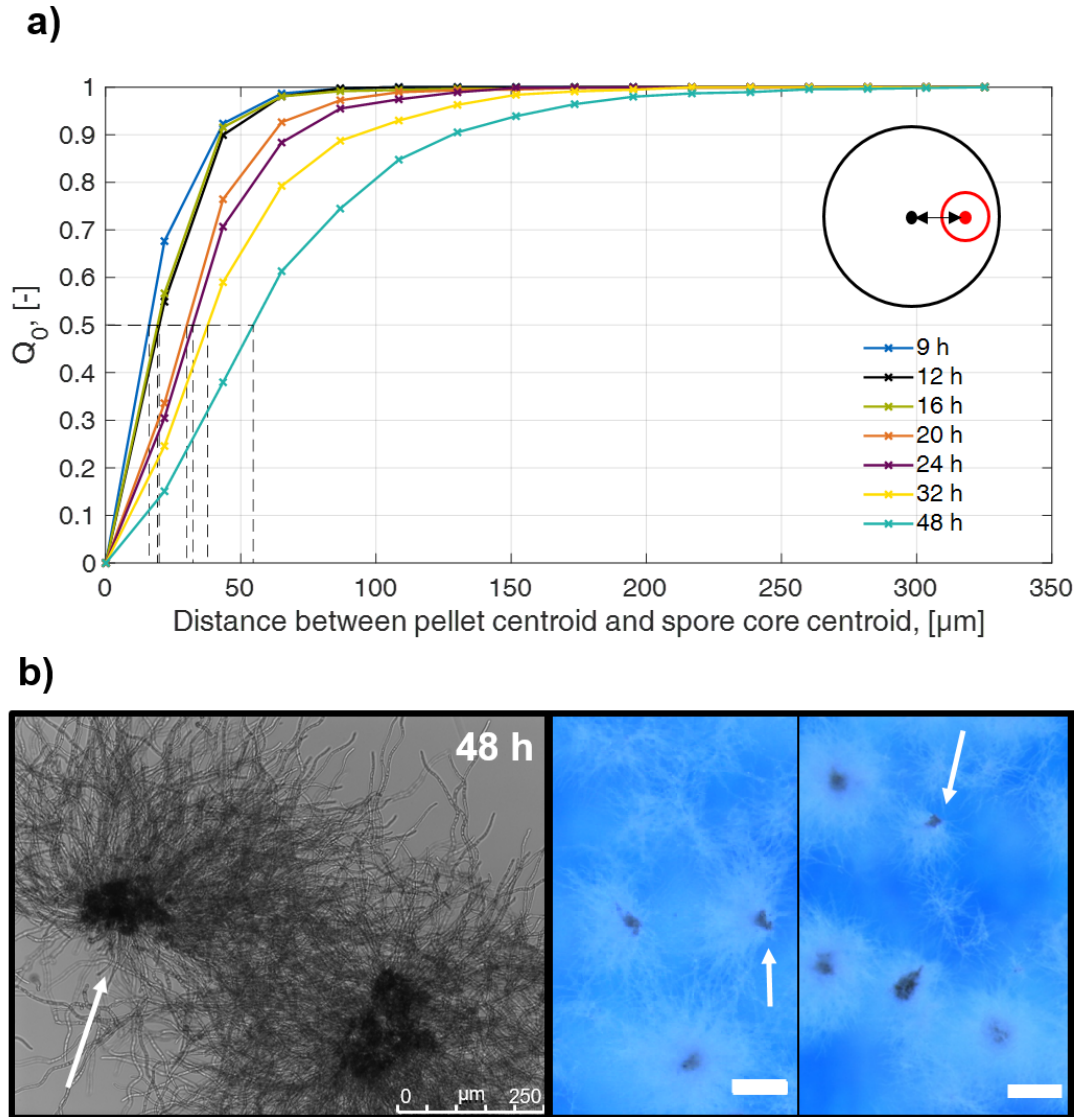


Figure 4: Analysis of pellet break-up. a) Cumulative distributions as a function of Euclidean distances between the centroid of the pellet and the centroid of the spore core at different sampling times of an *Aspergillus niger* cultivation run. The schematic drawing in the upper right corner depicts the distance between the pellet centroid (black dot) and the spore core centroid (red dot). The data were determined by the image analysis based on stereomicroscopic images. The dashed lines indicate the d50 values. b) Differential interference contrast image of broken *A. niger* pellet (left) and stereomicroscopic images showing broken pellets (right) at 48 h of the cultivation. Scale bar: 250  $\mu\text{m}$ . (Adapted and reprinted with permission from Müller et al. (2022), Copyright (2022) John Wiley and Sons)

samples and enabling rapid sample changes (Müller et al., 2020). In previous studies, individually selected pellet samples were fixed with an instant adhesive directly on a sample pin (Schmideder et al., 2019a). This error-prone and time-consuming work required a steady hand to transfer the most beautiful pellet (in most cases, the largest and most spherical) to the adhesive in a "cherry-picking" manner. The newly developed sample holder consisted of a Kapton<sup>®</sup> tube in which multiple pellets could be placed without fixation material and 3D imaged simultaneously with  $\mu$ -CT (Figure 5). Kapton<sup>®</sup> provides high X-ray transparency minimizing the influence on the X-ray beam spectrum and the final pixel intensity values of the imaged pellets (M. Antimonov et al., 2015). In addition, multiple pellets can be transferred to the sample holder at once since the pellets are loosely aggregated after freeze-drying and do not need to be separated compared to the previous method, thus, avoiding the "cherry-picking" of individual pellets (Figure 5a).

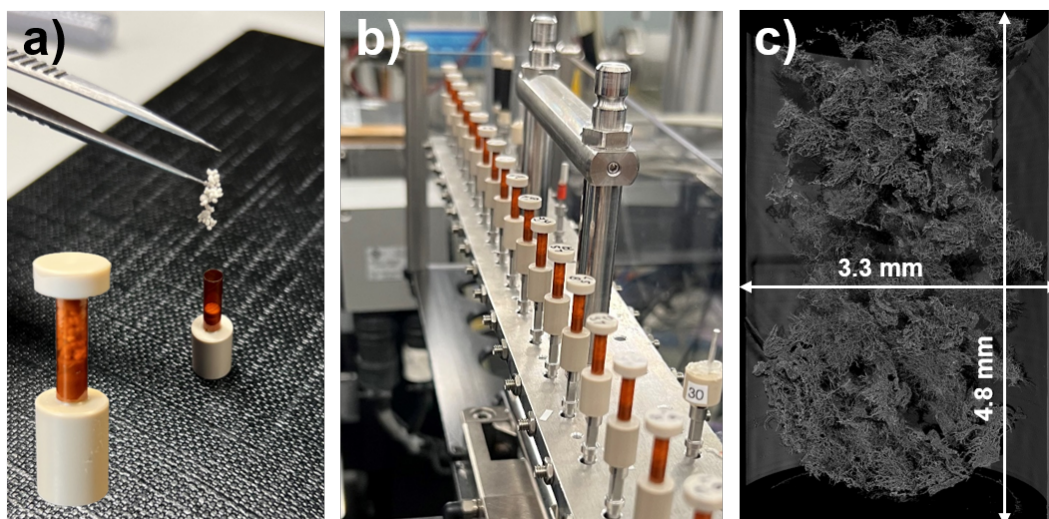


Figure 5: Standardized sample holder for SR- $\mu$ -CT measurements. a) Transfer of freeze-dried pellets into the sample holder. The sample holder consists of a Kapton<sup>®</sup> tube (orange), and PEEK base and cap (beige). b) Sample holders with freeze-dried pellets from different cultivation times at the microtomography beamline P05 of the Deutsches Elektronen-Synchrotron (DESY). c) SR- $\mu$ -CT with a voxel size of 1.28  $\mu$ m of freeze-dried pellets within a sample holder. The pellets on the 3D image were segmented into individual pellets based on the developed 3D image processing. (Adapted and reprinted with permission from Müller et al. (2023), Copyright (2023) John Wiley and Sons)

Furthermore, a 3D image analysis pipeline was developed to perform the segmentation of individual pellets from the developed sample holder and the entire cluster of measured pellets touching each other. Based on the segmented individual pellets, morphological pellet data was calculated. In our previous studies, different software was used to segment the pellets and perform the image analysis of the individual pellets (Schmideder et al., 2019a,b). The novel 3D image analysis pipeline in Article III performs the segmentation of pellets, analysis, and data processing in one software program (MATLAB, MathWorks), thus, enabling fast sample evaluation with almost no user input.

Since laboratory-scale  $\mu$ -CT offers a small field of view and needs long measurement times at the required high resolution to resolve hyphae with diameters of about 3  $\mu\text{m}$  (Schmideder et al., 2019a), which limits the total sample throughput, we applied for beamtime at the German Electron Synchrotron (DESY, Hamburg) for fast synchrotron radiation-based X-ray micro-computed tomography (SR- $\mu$ -CT). The accepted beamtime of 46 h enabled the 3D imaging and analysis of two entire *A. niger* pellet cultivations (Article III). During this study, 4.85 Terabyte of 3D image data resulting from 26 sampling times for each cultivation and 19,940 pellets were generated and processed. The analysis of 19,940 similar-sized pellets with a laboratory-scale  $\mu$ -CT (XCT-1600HR; Matrix Technologies, Feldkirchen, Germany) would take 128 days with the simultaneous measurement of a maximum of 26 pellets, which was proved to work in a previous study, and a required measuring time of 4 hours (Müller et al., 2020). Thus, a whole pellet cultivation analysis at multiple cultivation times would not be feasible with a laboratory-scale  $\mu$ -CT. Based on the developed sample holder and the short measurement times of SR- $\mu$ -CT, up to 579 pellets of one cultivation time could be 3D imaged simultaneously in less than 10 minutes. The advanced 3D image analysis enabled efficient automatic segmentation of the imaged pellets. Based on the image analysis of the segmented individual pellets, the following global morphological properties, taking the complete pellet structure into account, were determined for each pellet: volume equivalent spherical diameter of the pellet and the spore core, total number of tips, branching points and spores, total hyphal length, hyphal growth unit, average branch length, total volume of hyphae, average diameter of hyphae, and circularity of pellets. In addition, the following micromorphological properties were locally resolved: pellet density, i.e., the hyphal fraction, tip, and branching point density.

The novel methodology (Article III) offers the possibility to determine pellet-specific and time-dependent growth parameters such as the branching rate or apical growth velocity. Until now, this was not possible since a method that allows in-vitro 3D micromorphological analysis of the same non-destructed and metabolic active fungal pellet at multiple cultivation times does not exist. Existing methods that automatically track the micromorphological development of metabolically active mycelium over time only analyze the development of dispersed mycelium or young hyphae growing out of individual spores (Barry et al., 2015; Brunk et al., 2018; de Ulzurrun et al., 2019; Sachs et al., 2019; Sánchez-Orellana et al., 2019). However, the micromorphological evolution of a complex 3D hyphal network of a pellet cannot be analyzed on a plane with 2D images (Schmideder, 2022). Therefore, an approach based on analyzing a statistically representative number of pellets per cultivation time must have been adopted to account for cultivation heterogeneity and determine representative growth parameters. Such an approach is the developed SR- $\mu$ -CT-based high-throughput 3D image analysis (Article III).

In Article III, based on the determined total number of tips and total hyphal length over time, we calculated a branching rate of  $0.00042 \mu\text{m}^{-1}\text{h}^{-1}$  and apical growth velocity, also known as apical extension rate, of  $9.3 \mu\text{m h}^{-1}$  during the exponential pellet growth phase after 9 h to 22 h, based on 15 cultivation time points and a total number of 7885 processed pellets.

Furthermore, based on the calculated hyphal volume of each pellet from 3D image analysis, a growth rate of  $0.09 \text{ h}^{-1}$  was calculated within the exponential growth phase. Such growth parameters were determined for the first time for complex pellet structures. Comparable experimentally determined parameters for the apical extension rate result from the evaluation of young dispersed hyphae growing mainly on solid substrate (King, 1998). In addition, growth parameters strongly depend on the applied cultivation conditions. On solid agar, Trinci (1974) measured a strongly varying hyphal extension rate for *Aspergillus nidulans* between  $33$  and  $80 \mu\text{m h}^{-1}$  starting from germination of a single spore until  $12 \text{ h}$  of hyphal growth. In liquid medium, an apical extension rate of hyphal elements between  $20$  and  $38 \mu\text{m h}^{-1}$  was determined for *A. niger* at different glucose concentrations (Muller et al., 2000; Spohr et al., 1998). For *P. chrysogenum*, Nielsen and Krabben (1995) calculated an apical extension rate of around  $8 \mu\text{m h}^{-1}$  within submerged cultivation. Due to missing data, the calculated branching rate could not be compared with values from the literature. The growth rate is usually determined by the biomass dry weight of the complete culture, including dispersed mycelia (Kurt et al., 2018; Kwon et al., 2013; Müller et al., 2022; Nielsen et al., 1995; Nielsen and Krabben, 1995; Posch et al., 2012). Thereby, for a hyperbranching *A. niger* strain, a growth rate of  $0.24 \text{ h}^{-1}$  was determined (Kwon et al., 2013). For *A. niger* pellet cultivations with and without the addition of microparticles and in different reactor types (rocking motion and stirred tank bioreactor), growth rates between  $0.11$  and  $0.24 \text{ h}^{-1}$  based on the biomass dry weight of a culture sample were calculated. Since dispersed mycelia generally grow at a higher growth rate than pellets (Kurt et al., 2018; Papagianni and Matthey, 2006; Veiter et al., 2018), the difference between the growth rate of  $0.09 \text{ h}^{-1}$  determined in Article III and higher values from the literature, which are based on the total culture biomass including dispersed mycelia, can be explained.

Since in Article III, the same *A. niger* cultivations were analyzed as in Article II, we were able to compare time-dependent macromorphological pellet data from 2D image analysis (Article II) with data calculated by the 3D image analysis (Article III). Figure 3 in Article III, compares the calculated mean area/volume equivalent circular/spherical diameters of pellets and spore cores from 2D and 3D image analysis. The higher standard deviations after  $31 \text{ h}$ ,  $32 \text{ h}$ , and  $48 \text{ h}$  of the volume equivalent spherical diameter (3D data) may result from an insufficient number of sampled pellets for the cultivation heterogeneity, which was shown to increase after later sampling times (Article II). However, the overall good agreement between 2D and 3D data emphasizes a proper segmentation and detection of pellets and spores by the 3D image analysis. Based on 2D and 3D image data, a similar constant growth velocity of the equivalent diameter of pellets of  $13.14 \mu\text{m h}^{-1}$  (2D) and  $14.06 \mu\text{m h}^{-1}$  (3D) was calculated, respectively. Since hyphae extend in a tortuous manner, the increase of the mean equivalent pellet radius, which was calculated to be  $7.03 \mu\text{m h}^{-1}$ , is in good accordance with the calculated apical growth velocity of hyphae of  $9.3 \mu\text{m h}^{-1}$ . The ratio between the growth velocity of the equivalent radius and the apical growth velocity is used in continuum models to model the increase of the pellet radius during hyphal growth (Buschulte, 1992; King, 1998). However, this model parameter has not been determined yet for pellets and was calculated to be

0.76 (Article III). In the continuum growth model of Buschulte (1992), a value of 0.8 was assumed.

Also, the volume equivalent spherical diameters of spore cores from 3D data confirm the trend of the 2D data (Figure 3 in Article III). However, based on the 2D data alone, we assumed that the area equivalent circular diameter would increase after 9 to 24 h, due to the growth of hyphae within the spore core. However, by detecting individual spores within pellets based on the 3D image analysis, we observed that the mean number of spores per pellet increased from 767 after 9 h to 1233 after 24 h. This indicates that non-germinated spores within pellets still swell, as more spores can be detected by 3D image analysis due to their enlargement over time. This example demonstrates that in-depth 3D analysis provides more detailed insights and can further elucidate the growth phenomena of filamentous fungi. By dissection pellets, also Lyu et al. (2023) observed non-germinated spores within pellets. The authors of this study found that large pellets with non-germinated spores in their core are more resistant to heat and oxidative stress than small pellets. Here, the hyphae protected the non-germinated spores within pellets. It was further shown that non-germinated spores within pellets are viable (Lyu et al., 2023), as also indicated by the ongoing swelling of non-germinated spores within pellets (Article III). This possibly evolutionary-induced fitness advantage could be used in bioprocesses. Since we found that pellets are very likely to break at their spore core (Article II), which is also confirmed by the decreasing spore number within pellets at later cultivation time points based on the 3D image analysis, it is quite conceivable that forced breaking of the pellets by shear stress exposes non-germinated spores to the medium and thereby promotes re-growth of the pellets, prolonging the production phase. Even if this thesis is speculative, it demonstrates that detailed 3D and holistic 2D cultivation analysis, including spore agglomeration, may promote the development of new process control strategies.

Number density distributions of pellet properties are essential to observe cultivation heterogeneity (Posch et al., 2012; Zacchetti et al., 2018). The developed method (Article III) now allows to identify the micromorphological cultivation heterogeneity. The number density distributions of the hyphal volume of each pellet at different cultivation times are shown in Figure 8 of Article III. The increase in the width of the distributions at later cultivation times confirms an increase in pellet heterogeneity, which was also observed in Article II. The hyphal volume for each of a few hundred pellets per cultivation time has never been determined before. This makes it now feasible to estimate the growth rates for the individual size classes within a pellet cultivation. These growth rates, depending on a characteristic pellet property, are necessary within population balance modeling to predict the development of the biomass of the pellet culture. In addition to the total hyphal volume, micromorphological properties such as the total number of tips, branches, spores, or the hyphal fraction at a specific radial position within a pellet could be determined for many pellet samples per cultivation time and used to generate distributions to study micromorphological heterogeneity between pellets or determine growth rates of individual subpopulations. Furthermore, the effect of morphology engineering methods on different pellet size classes can be analyzed. For example, the influ-

ence of shear stress at different stirring speeds on the pellets' tip and branching point number, or pellet density, can be shown as a function of their size. It is assumed that large pellets are subjected to higher shear forces (Section 2.2.3). In addition to global micromorphological parameters (total number of tips or branching points), the 3D image analysis enables calculating densities, such as the hyphal density (hyphal fraction) within a pellet, locally resolved over the radius for each pellet. Thus, pellets from different agitated and aerated bioreactor runs could be divided into size classes, whereby the distribution of the hyphal density within pellets from a specific size class can be analyzed. Lin et al. (2010) observed the development of dense peripheral pellet regions at different agitation and aeration rates based on a few individual slices of pellets sliced manually by a microtome. With the methodology of Article III, such studies could be extended to multiple time steps and a statistically representative number of non-sliced, i.e., non-destructed, pellets. Additionally, the locally resolved density of tips and branches could be observed. More advanced, based on the determined locally resolved hyphal material and the developed universal diffusion law for filamentous fungi, described in Article I, it is possible to compute the diffusive mass transport of nutrients inside each 3D imaged and processed pellet from different cultivation times.

### 6.3. Possible improvements of the developed methods

The application of the presented high-throughput stereomicroscope-based 2D image analysis (Article II) and SR- $\mu$ -CT-based 3D image analysis (Article III) has resulted in ideas to improve and enable a broader application of the developed methods.

**Improvement of 2D imaging and analysis** In the turn of the detection of individually dispersed spores during the spore agglomeration on the generated stereomicroscope images (Article II), we observed that the highest possible magnification of the applied stereomicroscope is at the lower level for the detection of individually dispersed spores of the *A. niger* MF22.4 strain. As reported in Article II, the spore concentration after inoculation determined with the 2D image analysis differs from the original concentration by a factor of 10 ( $3.2 \cdot 10^5$  vs.  $2.5 \cdot 10^6$  spores/ml) due to a low detection efficiency of individual spores in out of focus image regions. Since the diameter of spores from different genera and strains vary a lot, e.g., *Aspergillus niger* MF22.4: 4-7.6  $\mu\text{m}$  (Müller et al., 2022), *Penicillium* species: 2-8  $\mu\text{m}$ , a higher adaptable magnification of the used stereomicroscope would improve the detection of individual spores from different fungi. Novel stereomicroscopes and optics enable a broader magnification range, which is also continuously adjustable, at a comparable field of view for the given magnification compared to the applied stereomicroscope (Schnitzler and Zimmer, 2008). In addition to the size of spores, also the melanin (from Greek μέλας "black ") content can vary depending on the strain and cultivation conditions (Wargenau et al., 2011), which can result in a low contrast and detection efficiency of individual spores. Image filtering during image analysis can enhance the pixel intensity gradient between background and spore boundaries, which is also done in dissolved air flotation to detect transparent microbub-

bles (Schmieder et al., 2022), and thus, improve the segmentation of individually dispersed spores.

**Improvement of sampling for SR- $\mu$ -CT based 3D imaging and data processing** After 3D imaging and analyzing 19,940 potential pellet objects, a Gaussian mixture model (GMM) algorithm, which is a type of machine learning algorithm (Bishop, 2009), was used to perform a soft clustering of the segmented pellet objects in "artificial" pellets, damaged during the sample preparation for SR- $\mu$ -CT, and "regular" pellets, which have normally formed during the bioprocess (Article III). Only those pellet objects clustered as "regular" pellets were considered for further analysis. 44 % or 8,783 of the 19,940 potential pellet objects were clustered as artifacts, which is a high percentage. Improving the pellet sample preparation procedure, which includes freezing, freeze-drying, and transfer to the  $\mu$ -CT sample holder, would reduce the number of artificially changed pellets. Especially the transfer of the freeze-dried pellets from the reaction tube into the sample holder for SR- $\mu$ -CT measurements provides risks of sample damage. It is possible to omit the transfer process altogether if the liquid culture sample is transferred directly to the sample holder, frozen and freeze-dried. This would reduce the mechanical impact on the pellets and possible damage. However, the volume of a representative liquid culture sample before freezing and freeze-drying must fit into the sample holder, which is designed to match the field of view during  $\mu$ -CT imaging. For freeze-drying of *A. niger* pellets, 1000 mm<sup>3</sup> of liquid sample volume was taken per cultivation time step, whereas the sample holder had a volume of only about 50 mm<sup>3</sup> (Article III). Please note that the pellets must be deep-frozen while floating in the liquid medium to preserve their natural state. By using a larger camera in the SR- $\mu$ -CT measurements, it would be possible to double the field of view at a similar required voxel size and thus also use a larger sample holder. However, it should be noted that doubling the field of view in the x-y-z direction would increase the memory requirement for a 3D image by a factor of 8 (current memory usage (Article III): 93.3 GB/image), making 3D image analysis and data handling difficult and time-consuming. In addition to the improvement of the pellet preparation to minimize artificial sample damage, another approach would be to improve the image and data processing.

As reported in article III, the entire raw 3D image was split into two equally sized sub-images during image processing to reduce computational effort and allow segmentation of the pellets. However, pellets can also be cropped during this processing step. This could already be prevented by further improving the segmentation algorithm in terms of computational effort and using a larger random access memory (RAM), eliminating the need to split the entire raw 3D image into sub-images. Furthermore, the GMM soft clustering provides the opportunity to cluster the pellet objects in more classes than two ("artificial" and "regular pellets"). Therefore, pellet objects could be divided into "broken", "agglomerated", and "regular" pellets enabling a more detailed analysis of whether breakage or agglomeration of pellets results from sample preparation, including freeze-drying or from the bioprocess. For this, the right features, such as aspect ratio or pellet density (Article III), have to be found to

enable precise clustering into the different classes. First attempts to achieve this failed since the selected features did not correlate with specific pellet structures, such as agglomerated or broken pellets.

If only "regular" pellets are analyzed, one could assume that the observation of possible population heterogeneity is lost. However, in the case of the previously analyzed *A. niger* cultivation (Article III), the number density distributions of the equivalent pellet diameter from 2D analysis (Figure 3) and of the total hyphal volume of pellets from 3D analysis (Figure 8 in Article III), both indicate an increasing population heterogeneity towards 48 h. In addition, 2D and 3D image analysis determined a decreasing mean equivalent diameter of the spore cores after 48 h (Figure 3 in Article III), which was additionally confirmed by a reduced number of detected spores per pellet (Article III). This indicates that an increasing population heterogeneity can also be determined by the 3D image analysis after soft clustering by the GMM that classifies only very "unusual" pellets as artifacts. However, it must be mentioned that the cluster result of the GMM depends on the input data. If very heterogeneous cultivation is to be analyzed, it is more likely that the GMM will misclassify "artificial" pellets as "regular" pellets and vice versa.

#### **6.4. Analysis of nutrient transport and development of process control strategies**

Article I summarizes the development of the universal diffusion law for filamentous fungi. The law correlates the local hyphal fractions/porosities of a pellet with the local effective diffusion factors. It thus enables the calculation of diffusive mass transport of nutrients into the interior of pellets based on partial differential diffusion equations (Buschulte, 1992; Celler et al., 2012; King, 1998). The solution of the diffusive mass transfer equation in pellets makes it now possible to calculate the concentration profile of nutrients, including oxygen, inside pellets with continuum modeling approaches (Buschulte, 1992; Celler et al., 2012; King, 1998). In addition to the diffusive transport, the consumption of nutrients for maintenance and growth metabolism must be calculated within these models. For this, micromorphological properties such as the local hyphal fractions and the tip densities as a function of the pellet radius are needed (Figure 7 in Article III). The additionally required nutrient consumption rates for growth and maintenance and the constants for Michaelis-Menten kinetics can be found in the literature. Based on data from the developed 3D image analysis, studies to calculate the oxygen concentration profile, including experimental validation, are currently underway in cooperation with the Krull lab at TU Braunschweig.

All required locally resolved micromorphological data (tip and hyphal densities) to calculate concentration profiles can now be obtained for a statistically representative number of pellets from multiple cultivation times (Article III). The universal diffusion law and continuum modeling can then be used to determine nutrient concentration profiles for pellets of a given size class based on their representative micromorphological properties. This approach would enable observing at which cultivation time the inner regions of pellets from

different size classes run into nutrient starvation. Based on the gained knowledge, process control strategies could be developed. For example, Posch and Herwig (2014) proposed a specific feeding strategy for redirecting the metabolism from growth to maintenance and production to keep *P. chrysogenum* pellets small and viable for prolonged penicillin production. Micromorphological properties from *P. chrysogenum* pellets at different time points during cultivation could now be elaborated from 3D image analysis and used for modeling the concentration profiles for each pellet at the applied cultivation conditions. At a time during the bioprocess where the penicillin production increases or peaks, the concentration profiles of, e.g., oxygen, being the prime limiting substrate for the metabolism of filamentous fungi, and glucose, which was shown to strongly influence penicillin production (Brakhage, 2013; Brakhage et al., 2004), could be analyzed. Based on the result, e.g., glucose or/and oxygen limitation in central pellet parts, which possibly promote penicillin production (Cairns et al., 2019b), a specific feeding strategy for those substrates could be developed to limit the growth rate and maintain the pellet morphology to keep the production high. Contrary to penicillin, where the production peaks during phases of low or no cultivation growth, a different strategy must be used for biomass/growth-associated products like enzymes or citric acid (Cairns et al., 2019b; Upton et al., 2017). For citric acid production, small and compact pellets are preferred to ensure the nutrient supply of the entire pellet biomass and keep the bioreactor's viscosity low (Papagianni, 2004; Sun et al., 2018). Based on micromorphological properties and simulated nutrient concentration profiles of pellets in a bioprocess, the time at which nutrient limitation occurs inside pellets could be determined. Thereupon a stirring strategy could be developed that includes increased stirring to break up the pellets and reduce their size to restore nutrients to the entire pellet, followed by reduced stirring to continue growth without breaking. Furthermore, morphology engineering strategies, including the addition of microparticles, increased osmolality, or genetic modification (Section 2.3), can be used to force the pellets to reach an optimal production-related size at a given cultivation time point based on their determined nutrient concentration profile.

In addition to developing process control strategies, biological phenomena such as hyphal degradation could be revealed based on the determined locally resolved micromorphological data (Figure 7 in Article III). Here, a reduced hyphal fraction in the center of a pellet combined with the observed nutrient starvation based on simulated nutrient concentration profiles would indicate hyphal lysis. Hyphal cell lysis due to substrate limitation or aging within fungal pellets is often hypothesized in the literature (Bizukoje and Gonciarz, 2015; Bizukoje and Ledakowicz, 2010; Krull et al., 2010). 3D imaging and analysis of several complete pellets from late cultivation periods when the pellets are nutrient deficient will facilitate determining if, when, and under what conditions cell lysis occurs. The gained knowledge can be used to parameterize the lysis rate used in continuum and microscopic models to predict hyphal degradation (King, 1998; Meyerhoff et al., 1995).

## 6.5. Ready for predictive bioprocess modeling?

The morphology of filamentous fungi that evolves and constantly transforms during the bioprocess strongly impacts productivity (Veiter et al., 2018). To enable the rational optimization of the bioprocess performance, two prerequisites must be fulfilled: (1) The micro- and macromorphological evolution of the entire fungal cultivation need to be analyzed holistically with a statistically representative number of samples, starting from individual spores, through spore agglomeration, to final heterogeneous pellet populations. (2) The nutrient supply of fungal pellets as a function of their micromorphology needs to be quantified and linked to product titers during the bioprocess. Only then can the mode of action of morphology engineering approaches be understood, and targeted bioprocess control strategies can be systematically developed. Article II and III provide new methods to generate novel statistically representative macro- and micromorphological data of fungal cultivations over time. Furthermore, based on the findings presented in Article I, the nutrient concentrations within fungal pellets can be calculated. Altogether, the methods developed during this Ph.D. thesis enable new model-based opportunities for targeted optimization of bioprocesses. These opportunities can culminate in general model-based predictability and optimization of bioprocesses. Figure 6 demonstrates the arising opportunities.

For now, only the **blue and gray paths** in Figure 6 need to be followed, which demonstrate the opportunities resulting from the direct use of the experimental data from the developed 2D and 3D imaging and analysis (Article II and III) for model parameterization/validation and culture analysis. The gray paths indicate the required laboratory work and culture evaluation. The words in bold denote the steps in Figure 6. Starting from a **pilot cultivation** (lower left corner), for example, modified by morphology engineering strategies, such as the cultivation of a genetically modified hyperbranched filamentous fungal strain (Fiedler et al., 2018; Kwon et al., 2013), the developed **3D and 2D high-throughput imaging and analysis** methods are used for in-depth cultivation analysis starting from the inoculation with spores. The macro- and micromorphological data collected from the image analysis can be stored in a **database**. From the holistic high-throughput 2D image analysis (Article II), macromorphological data for each sampled cultivation time can be generated, including:

- The equivalent diameter of each spore/spore agglomerate, spore core, and pellet
- The concentration of spores/spore agglomerates, spore cores, and pellets
- The area fractions of spores/spore agglomerates, spore cores, pellets, and dispersed mycelia
- The number density distributions of spores/spore agglomerates, spore cores, and pellets as a function of their, e.g., equivalent diameter

From the high-throughput 3D image analysis (Article III), the following detailed micro- and macromorphological data for each sampled cultivation time can be generated including:

- The equivalent diameter of each pellet and spore core
- The total hyphal volume of each pellet

- The average hyphal diameter of each pellet
- The total hyphal length of each pellet
- The total number of tips and branches of each pellet
- The total number of spores within each pellet
- The hyphal growth unit (Trinci, 1974), and average branch length (Müller et al., 2023) of each pellet
- Locally resolved hyphal fraction, tip, and branching point densities over the radius of each pellet
- The number density distributions of spore cores and pellets as a function of their, e.g., total hyphal volume

In addition to these generated data for the used strain and cultivation conditions, parameters calculated from them, such as apical growth rate, branching rate, or growth rate, are collected in the **database**. The **database** can be directly used to understand the mode of action of **morphology engineering strategies** (Section 2.3) and **development/optimization of process control strategies**. For example, an enhanced number of tips and tip density of the hyperbranching strain compared to pellets of the parental strain can now be determined. Also, the influence of genetic modifications on spore agglomeration can be analyzed. For example, Sun et al. (2018) knocked down genes of a chitin synthase and obtained high citric acid-producing, small, and compact pellets, as well as reduced content of dispersed mycelia compared to the control strain. The underlying effects of the morphology transformation were not revealed. However, the development of spores and, thus, possibly spore agglomeration are influenced by chitin synthesis (Müller et al., 2002), which could be observed by the developed 2D image analysis (Article II). In addition, different agitation intensities and their influence on spore agglomeration (Article II) and pellet micromorphology (Article III) can be analyzed (Section 2.3).

Based on the novel micro- and macromorphological data in the **database**, **microscopic growth models** (Section 2.5) can be parameterized/validated. Within stochastic microscopic growth models of Yang et al. (1992), Meyerhoff et al. (1995), Lejeune and Baron (1997), Celler et al. (2012), and Schmieder et al. (2020) input parameters such as the apical growth velocity, the growth rate, branching rate/branch interval, hyphal diameter, and the number of spores from which the simulated pellets were formed are needed. Based on the developed 3D imaging, those data can now be obtained for entire pellet populations at different time steps. In future works, the 3D image processing can be extended to compute the branching angles and growth directions required for modeling based on the voxel skeleton, i.e., the centerline of binarized pellets. Furthermore, since pellets can have multiple spore cores, as observed in Article II, preliminary work to simulate the growth of individual pellets from more than one spore core based on microscopic growth modeling succeeded (Deffur et al., 2023).

Since the developed methods are able to analyze a high number of samples of multiple cultivation time steps, it is possible to use the obtained experimental micro- and macromorphological data to calculate number density distributions and deduce the required growth rates for **population balance modeling (PBM)** (Section 2.5), simulating the spore agglomer-

ation (Lin et al., 2008) and development of an entire usually heterogeneous fungal cultivation (King, 1998; Nielsen and Krabben, 1995). Here, PBM simulating the evolution of the size distribution of pellets (Edelstein and Hadar, 1983; Tough et al., 1995) and spore agglomerates (Lin et al., 2008) as well as the amount of dispersed mycelia (Jüsten et al., 1997) during cultivation can be established from the obtained macromorphological data of 2D image analysis (Article II). In addition, multivariate PBM can be developed based on SR- $\mu$ -CT measurements and 3D image analysis (Article III) to simulate the evolution of several micromorphological properties such as the number of tips, pellet porosity, or total hyphal volume of each pellet population. The developed PBM from the experimental morphological data will improve the knowledge of cultivation heterogeneities resulting from spore agglomeration, pellet growth, and breakage. Thus, new **process control strategies can be developed or optimized**.

Based on the developed **universal diffusion law** (Article I) and the **database**, containing the local hyphal fractions of pellets from different time steps, the diffusive mass transport of nutrients within each pellet can be solved. Furthermore, within the framework of **continuum modeling** (Section 2.5) based on partial differential diffusion-reaction equations (Buschulte, 1992; Celler et al., 2012; King, 1998), the evolution of nutrient concentration profiles within fungal pellets over the cultivation time can be determined. In addition to solving the diffusion term based on the universal diffusion law, the reaction term must also be solved. For this, the required micromorphological data over time, e.g., number of tips and total hyphal length, can in turn be derived from the **database/3D image analysis** (Article III). The **consumption rates** for the reaction term can be derived **from literature or experiments** (top, right corner) based on microelectrode measurements to obtain, e.g., the oxygen concentration within metabolic active and inactive pellets (Hille et al., 2009). A **comparison** of the computed nutrient concentration profiles within multiple pellets **with the experimentally determined product titer** of the sampled cultivation times enables to determine whether the bioprocess production increases/decreases when substrate-limited regions within a representative number of pellets evolve. Especially for the production of secondary metabolites such as penicillin, the optimal morphology is unclear (Cairns et al., 2019b). For penicillin, it is assumed that a nutrient limitation within pellets can induce the production (Cairns et al., 2019b). The knowledge gained from the comparison can be used to **develop or optimize the applied process control strategy based on morphology engineering**. In the case of the exemplary pilot cultivation of the hyperbranched strain, a fictitious result of such a comparison could be as follows: Indeed, a determined increased number of tips per pellet increases product titers, but only in the early growth phase. Determined increased densities of the hyperbranched pellets create substrate-limited pellet areas early on, shortening the optimal production period and overall product titers. Thus, the applied genetic modification needs to be optimized or combined with a further morphology engineering strategy.

The direct use of the data from 2D and 3D image analysis itself or for modeling enables the in-depth analysis and optimization of one cultivation under the given environome. Given the myriad possible combinations of fungal species and strains, cultivation conditions, and morphology engineering methods, predictive and transferable bioprocess modeling would

boost the development of targeted morphology engineering and process control strategies. To evaluate the current possibilities for predictive bioprocess modeling, only the **orange and gray paths** in Figure 6 need to be followed.

**Simulation studies** (top, middle) of **microscopic growth modeling** by the variation of reasonable growth parameters in a specific range of experimentally determined data can be used to extend the micro- and macromorphological **database** by in-silico generated pellet structures (Schmideder et al., 2020). The diffusion-reaction equations of the **continuum modeling** are linked with stochastic **microscopic growth modeling** to simulate the development of the microscopic pellet structure as a function of the nutrient concentration (Buschulte, 1992; Celler et al., 2012; Lejeune and Baron, 1997; Meyerhoff et al., 1995). However, the existing models missed to include well-founded correlations between the structure and the diffusivity for the computation of the nutrient supply. This limitation can be overcome by using the developed **universal diffusion law** (Article I). In addition, the abrasion of hyphae of the pellet's peripheral regions can be included in the **microscopic modeling** (Cui et al., 1998a; Meyerhoff et al., 1995). The simulated pellet structures within the **database** can directly be evaluated based on the computed **nutrient concentration profiles** from **continuum modeling** and the experimentally gained knowledge, whether nutrient limitation promotes or inhibits production (**Comparison with experimentally determined product titer**). A pellet structure within the database that allows the required nutrient concentration profile can then be selected for optimal production (Schmideder et al., 2020). Using **morphology engineering approaches**, **process control strategies** can be **developed** to achieve and maintain the desired morphology as long as possible during the bioprocess. If the **product titer** (yellow box) of the **pilot cultivation** is sufficient, **scale-up for industrial production** can be initiated.

Growth rates determined from **microscopic growth modeling** of individual simulated pellets representing a pellet (sub-)population can be included in the **database** and used to simulate the population's development over time within **PBM**. In addition, based on computed nutrient concentration profiles from **continuum modeling**, oxygen-limited/inactive and oxygen-supplied/active pellet regions and thereof, the actively growing/producing biomass, substrate consumption, and production of the bioprocess can be predicted within the **PBM**. **Simulation studies of the PBM**, including the targeted variation of spore/pellet agglomeration and breakage kernels, will deepen the mechanistic understanding of induced cultivation heterogeneity that can limit or enhance bioprocess performance (Section 2.2.4). For example, within an experimental cultivation Lyu et al. (2023) prevented the spore agglomeration and observed small highly productive pellets compared to pellets resulting from spore agglomeration. A reduced spore agglomeration kernel within PBM could predict this morphological evolution of pellets. Furthermore, the variation of the breakage kernel allows the prediction of the morphology of pellet populations under low and high shear stress conditions resulting from different bioreactor types (Kurt et al., 2018) or agitation intensities (Lin et al., 2010). These simulation studies of PBM will result in the **development/optimization of process control strategies** using **morphology engineering**.

The generated time-dependent micro- and macromorphological data from the developed 2D and 3D analysis and imaging can now provide all morphological data required for the proposed multi-scale modeling approach, predicting the evolution of individual pellets on the microscopic scale that can be abstracted on the process/bioreactor-scale to predict the overall development of the cultivation based on PBM. Concluding, the modeling concepts are already there. Now, the tools that have been developed during this thesis (Article II - III) enable to parameterize these concepts. Thus, the vision of predictive bioprocess modeling is getting a big step closer. In addition, the direct analysis of the holistic macro- and micromorphological data from the methods developed will contribute to targeted morphological engineering and optimized process control strategies for enhanced bioprocess productivity.

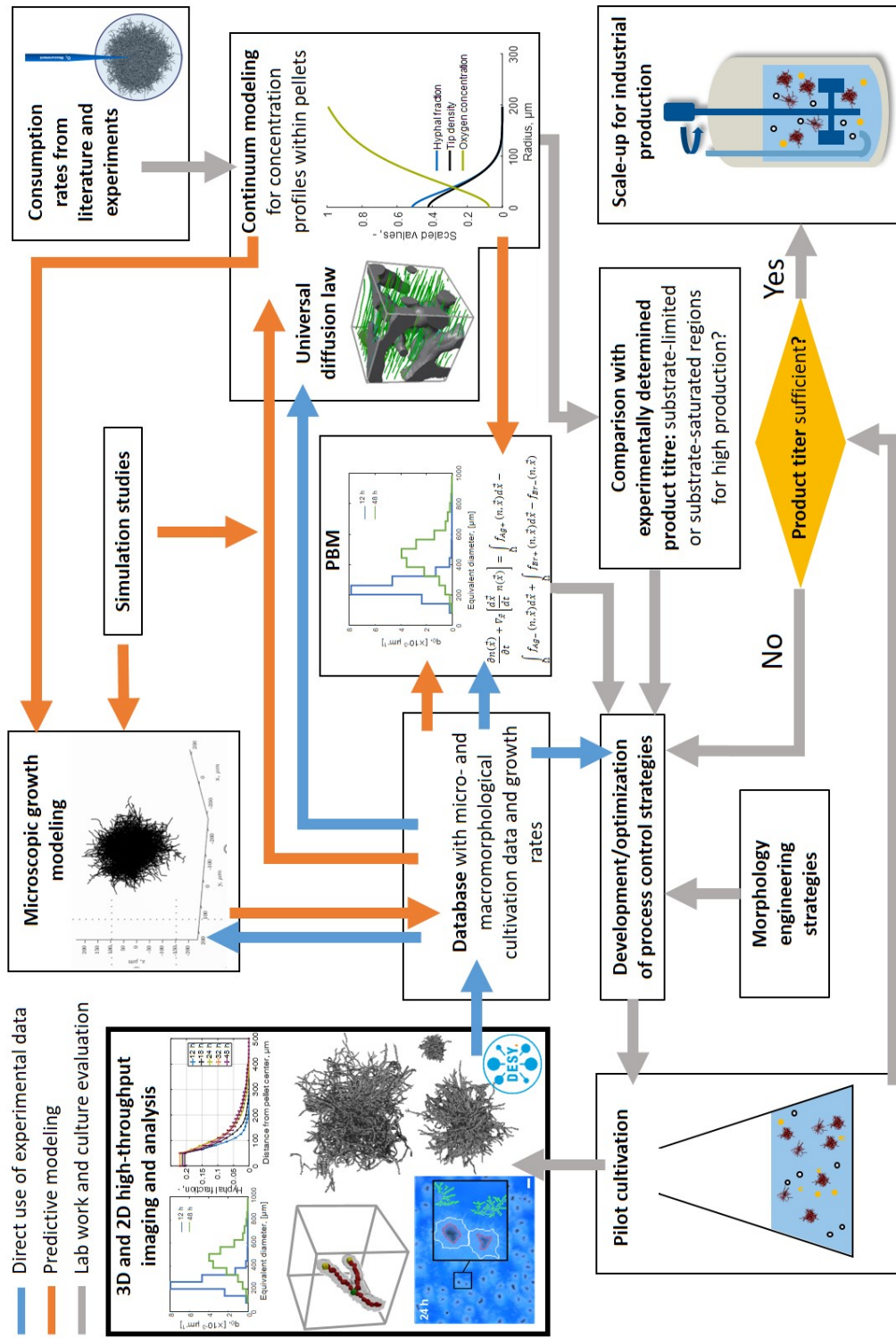


Figure 6: Development of novel process control strategies based on 3D and 2D high-throughput imaging and multi-scale modeling.



## 7. References

- Anderson, T. W. (1962). On the distribution of the two-sample cramér-von mises criterion. *The Annals of Mathematical Statistics*, 33(3):1148–1159.
- Antecka, A., Bizukojc, M., and Ledakowicz, S. (2016). Modern morphological engineering techniques for improving productivity of filamentous fungi in submerged cultures. *World journal of microbiology & biotechnology*, 32(12):193.
- Baltussen, T. J. H., Zoll, J., Verweij, P. E., and Melchers, W. J. G. (2020). Molecular mechanisms of conidial germination in aspergillus spp. *Microbiology and molecular biology reviews : MMBR*, 84(1).
- Barry, D. J., Williams, G. A., and Chan, C. (2015). Automated analysis of filamentous microbial morphology with anamorf. *Biotechnology Progress*, 31(3):849–852.
- Becker, J., Wieser, C., Fell, S., and Steiner, K. (2011). A multi-scale approach to material modeling of fuel cell diffusion media. *International Journal of Heat and Mass Transfer*, 54(7-8):1360–1368.
- Bischof, R. H., Ramoni, J., and Seiboth, B. (2016). Cellulases and beyond: the first 70 years of the enzyme producer trichoderma reesei. *Microbial cell factories*, 15(1):106.
- Bishop, C. M. (2009). *Pattern recognition and machine learning*. Information science and statistics. Springer, New York, NY, corrected at 8th printing 2009 edition.
- Bizukojc, M. and Gonciarz, J. (2015). Influence of oxygen on lovastatin biosynthesis by aspergillus terreus atcc 20542 quantitatively studied on the level of individual pellets. *Bioprocess and biosystems engineering*, 38(7):1251–1266.
- Bizukojc, M. and Ledakowicz, S. (2010). The morphological and physiological evolution of aspergillus terreus mycelium in the submerged culture and its relation to the formation of secondary metabolites. *World Journal of Microbiology and Biotechnology*, 26(1):41–54.
- Bleichrodt, R.-J. and Read, N. D. (2018). Flow cytometry and facs applied to filamentous fungi. *Fungal Biology Reviews*.
- Bleichrodt, R.-J., Vinck, A., Read, N. D., and Wösten, H. A. (2015). Selective transport between heterogeneous hyphal compartments via the plasma membrane lining septal walls of aspergillus niger. *Fungal Genetics and Biology*, 82:193–200.
- Bliatsiou, C., Schrinner, K., Waldherr, P., Tesche, S., Böhm, L., Kraume, M., and Krull, R. (2020). Rheological characteristics of filamentous cultivation broths and suitable model fluids. *Biochemical Engineering Journal*, 163:107746.
- Böl, M., Schrinner, K., Tesche, S., and Krull, R. (2021). Challenges of influencing cellular morphology by morphology engineering techniques and mechanical induced stress on filamentous pellet systems-a critical review. *Engineering in Life Sciences*, 21(3-4):51–67.
- Brakhage, A. A. (2013). Regulation of fungal secondary metabolism. *Nature reviews. Microbiology*, 11(1):21–32.
- Brakhage, A. A., Spröte, P., Al-Abdallah, Q., Gehrke, A., Plattner, H., and Tüncher, A. (2004). Regulation of penicillin biosynthesis in filamentous fungi. *Advances in biochemical engineering/biotechnology*, 88:45–90.

- Briesen, H. (2009). Two-dimensional population balance modeling for shape dependent crystal attrition. *Chemical Engineering Science*, 64(4):661–672.
- Brunk, M., Sputh, S., Doose, S., van de Linde, S., and Terpitz, U. (2018). Hyphatracker: An imagej toolbox for time-resolved analysis of spore germination in filamentous fungi. *Scientific reports*, 8(1):605.
- Buffo, M. M., Esperança, M. N., Farinas, C. S., and Badino, A. C. (2020). Relation between pellet fragmentation kinetics and cellulolytic enzymes production by aspergillus niger in conventional bioreactor with different impellers. *Enzyme and Microbial Technology*, 139:109587.
- Buschulte, T. C. (1992). *Mathematische Modellbildung und Simulation von Zellwachstum, Stofftransport und Stoffwechsel in Pellets aus Streptomyces (PhD thesis)*. Stuttgart, Germany: Fakultät Verfahrenstechnik der Universität Stuttgart.
- Cairns, T. C., Feurstein, C., Zheng, X., Zheng, P., Sun, J., and Meyer, V. (2019a). A quantitative image analysis pipeline for the characterization of filamentous fungal morphologies as a tool to uncover targets for morphology engineering: a case study using apld in aspergillus niger. *Biotechnology for biofuels*, 12:149.
- Cairns, T. C., Nai, C., and Meyer, V. (2018). How a fungus shapes biotechnology: 100 years of aspergillus niger research. *Fungal biology and biotechnology*, 5:13.
- Cairns, T. C., Zheng, X., Feurstein, C., Zheng, P., Sun, J., and Meyer, V. (2022). A library of aspergillus niger chassis strains for morphology engineering connects strain fitness and filamentous growth with submerged macromorphology. *Frontiers in bioengineering and biotechnology*, 9.
- Cairns, T. C., Zheng, X., Zheng, P., Sun, J., and Meyer, V. (2019b). Moulding the mould: understanding and reprogramming filamentous fungal growth and morphogenesis for next generation cell factories. *Biotechnology for biofuels*, 12:77.
- Carvalho, N. D. S. P., Arentshorst, M., Jin Kwon, M., Meyer, V., and Ram, A. F. J. (2010). Expanding the ku70 toolbox for filamentous fungi: establishment of complementation vectors and recipient strains for advanced gene analyses. *Applied Microbiology and Biotechnology*, 87(4):1463–1473.
- Celler, K., Picioreanu, C., van Loosdrecht, Mark C. M., and van Wezel, G. P. (2012). Structured morphological modeling as a framework for rational strain design of streptomyces species. *Antonie van Leeuwenhoek International Journal of General and Molecular Microbiology*, 102(3, SI):409–423.
- Colin, V., Baigori, M., and Pera, L. (2013). Tailoring fungal morphology of aspergillus niger mya 135 by altering the hyphal morphology and the conidia adhesion capacity: biotechnological applications. *AMB Express*, 3.
- Cox, P. W., Paul, G. C., and Thomas, C. R. (1998). Image analysis of the morphology of filamentous microorganisms. *Microbiology-UK*, 144(4):817–827.
- Cronenberg, C. C. H., Ottengraf, S. P. P., Heuvel, J. C., Pottel, F., Ziele, D., Schgerl, K., and Bellgardt, K. H. (1994). Influence of age and structure of penicillium chrysogenum pellets on the internal concentration profiles. *Bioprocess Engineering*, 10(5-6):209–216.
- Cui, Y. Q., Okkerse, W. J., van der Lans, R., and Luyben, K. (1998a). Modeling and measurements of fungal growth and morphology in submerged fermentations. *Biotechnology and Bioengineering*, 60(2):216–229.
- Cui, Y. Q., van der Lans, R., and Luyben, K. (1998b). Effects of dissolved oxygen tension and mechanical forces on fungal morphology in submerged fermentation. *Biotechnology and Bioengineering*, 57(4):409–419.
- Cui, Y. Q., vanderLans, R., and Luyben, K. (1997). Effect of agitation intensities on fungal morphology of submerged fermentation. *Biotechnology and Bioengineering*, 55(5):715–726.

- de Bekker, C., van Veluw, G. J., Vinck, A., Wiebenga, L. A., and Wösten, H. A. B. (2011). Heterogeneity of aspergillus niger microcolonies in liquid shaken cultures. *Applied and environmental microbiology*, 77(4):1263–1267.
- de Ulzurrun, G. V.-D., Huang, T.-Y., Chang, C.-W., Lin, H.-C., and Hsueh, Y.-P. (2019). Fungal feature tracker (fft): A tool for quantitatively characterizing the morphology and growth of filamentous fungi. *bioRxiv*.
- Deffur, C., Schmideder, S., Müller, H., Kaur, G., Dinius, A., Krull, R., and Briesen, H. (2023). Understanding the interplay of fungal morphology development and oxygen supply: A multiscale model approach. *ECFG 2023 (Innsbruck)*, Poster Presentation.
- Driouch, H., Haensch, R., Wucherpfennig, T., Krull, R., and Wittmann, C. (2012). Improved enzyme production by bio-pellets of aspergillus niger: Targeted morphology engineering using titanate microparticles. *Biotechnology and Bioengineering*, 109(2):462–471.
- Driouch, H., Sommer, B., and Wittmann, C. (2010). Morphology engineering of aspergillus niger for improved enzyme production. *Biotechnology and Bioengineering*, 105(6):1058–1068.
- Dynesen, J. and Nielsen, J. (2003). Surface hydrophobicity of aspergillus nidulans conidiospores and its role in pellet formation. *Biotechnology Progress*, 19(3):1049–1052.
- Edelstein, L. and Hadar, Y. (1983). A model for pellet size distributions in submerged mycelial cultures. *Journal of Theoretical Biology*, 105(3):427–452.
- Ehgartner, D., Herwig, C., and Fricke, J. (2017). Morphological analysis of the filamentous fungus penicillium chrysogenum using flow cytometry-the fast alternative to microscopic image analysis. *Applied Microbiology and Biotechnology*, 101(20):7675–7688.
- Ehgartner, D., Herwig, C., and Neutsch, L. (2016). At-line determination of spore inoculum quality in penicillium chrysogenum bioprocesses. *Applied Microbiology and Biotechnology*, 100(12):5363–5373.
- el Enshasy, H., Hellmuth, K., and Rinas, U. (1999). Fungal morphology in submerged cultures and its relation to glucose oxidase excretion by recombinant aspergillus niger. *Applied Biochemistry and Biotechnology*, 81(1):1–11.
- El-Enshasy, H., Kleine, J., and Rinas, U. (2006). Agitation effects on morphology and protein productive fractions of filamentous and pelleted growth forms of recombinant aspergillus niger. *Process Biochemistry*, 41(10):2103–2112.
- El-Enshasy, H. A. (2011). Filamentous fungal cultures – process characteristics, products, and applications. In Yang, S.-T., editor, *Bioprocessing for Value-Added Products from Renewable Resources*, pages 225–261. Elsevier Science, Burlington.
- Fiedler, M. R. M., Barthel, L., Kubisch, C., Nai, C., and Meyer, V. (2018). Construction of an improved aspergillus niger platform for enhanced glucoamylase secretion. *Microbial cell factories*, 17(1):95.
- Fontaine, T., Beauvais, A., Loussert, C., Thevenard, B., Fulgsang, C. C., Ohno, N., Clavaud, C., Prevost, M.-C., and Latgé, J.-P. (2010). Cell wall alpha 1-3glucans induce the aggregation of germinating conidia of aspergillus fumigatus. *Fungal genetics and biology : FG & B*, 47(8):707–712.
- Gibbs, P. A., Seviour, R. J., and Schmid, F. (2000). Growth of filamentous fungi in submerged culture: Problems and possible solutions. *Critical Reviews in Biotechnology*, 20(1):17–48.
- Gonciarz, J. and Bizukojc, M. (2014). Adding talc microparticles to aspergillus terreus atcc 20542 preculture decreases fungal pellet size and improves lovastatin production. *Engineering in Life Sciences*, 14(2):190–200.

- Grimm, L. H., Kelly, S., Hengstler, J., Gobel, A., Krull, R., and Hempel, D. C. (2004). Kinetic studies on the aggregation of aspergillus niger conidia. *Biotechnology and Bioengineering*, 87(2):213–218.
- Grimm, L. H., Kelly, S., Krull, R., and Hempel, D. C. (2005a). Morphology and productivity of filamentous fungi. *Applied Microbiology and Biotechnology*, 69(4):375.
- Grimm, L. H., Kelly, S., Völkerding, I. I., Krull, R., and Hempel, D. C. (2005b). Influence of mechanical stress and surface interaction on the aggregation of aspergillus niger conidia. *Biotechnology and Bioengineering*, 92(7):879–888.
- Harris, S. D. and Momany, M. (2004). Polarity in filamentous fungi: moving beyond the yeast paradigm. *Fungal Genetics and Biology*, 41(4):391–400.
- Hille, A., Neu, T. R., Hempel, D. C., and Horn, H. (2005). Oxygen profiles and biomass distribution in biopellets of aspergillus niger. *Biotechnology and Bioengineering*, 92(5):614–623.
- Hille, A., Neu, T. R., Hempel, D. C., and Horn, H. (2009). Effective diffusivities and mass fluxes in fungal biopellets. *Biotechnology and Bioengineering*, 103(6):1202–1213.
- Ichikawa, H., Miyazawa, K., Komeiji, K., Susukida, S., Zhang, S., Muto, K., Orita, R., Takeuchi, A., Kamachi, Y., Hitosugi, M., Yoshimi, A., Shintani, T., Kato, Y., and Abe, K. (2021). Improved recombinant protein production in aspergillus oryzae lacking both alpha-1,3-glucan and galactosaminogalactan in batch culture with a lab-scale bioreactor. *Journal of bioscience and bioengineering*.
- Jüsten, P., Paul, G. C., Nienow, A. W., and Thomas, C. R. (1997). A mathematical model for agitation-induced fragmentation of penicillium chrysogenum. *Bioprocess Engineering*, 18(1):7–16.
- Kaup, J.-A., Ehrich, K., Pescheck, M., and Schrader, J. (2008). Microparticle-enhanced cultivation of filamentous microorganisms: Increased chloroperoxidase formation by caldariomyces fumago as an example. *Biotechnology and Bioengineering*, 99(3):491–498.
- Keller, N. P. (2019). Fungal secondary metabolism: regulation, function and drug discovery. *Nature reviews. Microbiology*, 17(3):167–180.
- Kelly, S., Grimm, L. H., Hengstler, J., Schultheis, E., Krull, R., and Hempel, D. C. (2004). Agitation effects on submerged growth and product formation of aspergillus niger. *Bioprocess and Biosystems Engineering*, 26(5):315–323.
- Kelly, S., Grimm, L. H., Jonas, R., Hempel, D. C., and Krull, R. (2006). Investigations of the morphogenesis of filamentous microorganisms. *Engineering in Life Sciences*, 6(5):475–480.
- King, R. (1998). Mathematical modelling of the morphology of streptomyces species: Relation between morphology and process performances. In Schügerl, K., editor, *Relation Between Morphology and Process Performances*, pages 95–124. Springer Berlin Heidelberg, Berlin, Heidelberg.
- Kowalska, A., Boruta, T., and Bizukojc, M. (2018). Morphological evolution of various fungal species in the presence and absence of aluminum oxide microparticles: Comparative and quantitative insights into microparticle-enhanced cultivation (mpec). *Microbiologyopen*, 7(5).
- Krull, R., Cordes, C., Horn, H., Kampen, I., Kwade, A., Neu, T. R., and Nörtemann, B. (2010). Morphology of filamentous fungi: Linking cellular biology to process engineering using aspergillus niger. In Wittmann, C. and Krull, R., editors, *Biosystems Engineering II: Linking Cellular Networks and Bioprocesses*, pages 1–21. Springer Berlin Heidelberg, Berlin, Heidelberg.
- Krull, R., Wucherpfennig, T., Esfandabadi, M. E., Walisko, R., Melzer, G., Hempel, D. C., Kampen, I., Kwade, A., and Wittmann, C. (2013). Characterization and control of fungal morphology for improved production performance in biotechnology. *Journal of Biotechnology*, 163(2):112–123.

- Kurt, T., Marbà-Ardébol, A.-M., Turan, Z., Neubauer, P., Junne, S., and Meyer, V. (2018). Rocking aspergillus: morphology-controlled cultivation of aspergillus niger in a wave-mixed bioreactor for the production of secondary metabolites. *Microbial cell factories*, 17(1):128.
- Kwon, M. J., Nitsche, B. M., Arentshorst, M., Jorgensen, T. R., Ram, A. F. J., and Meyer, V. (2013). The transcriptomic signature of racA activation and inactivation provides new insights into the morphogenetic network of aspergillus niger. *PLoS one*, 8(7).
- Kwon, M. J., Schütze, T., Spohner, S., Haefner, S., and Meyer, V. (2019). Practical guidance for the implementation of the crispr genome editing tool in filamentous fungi. *Fungal Biology and Biotechnology*, 6:15.
- Laible, A. R., Dinius, A., Schrader, M., Krull, R., Kwade, A., Briesen, H., and Schmideder, S. (2021). Effects and interactions of metal oxides in microparticle-enhanced cultivation of filamentous fungi and bacteria. *Engineering in Life Sciences*.
- Lamarre, C., Sokol, S., Debeaupuis, J.-P., Henry, C., Lacroix, C., Glaser, P., Coppée, J.-Y., François, J.-M., and Latgé, J.-P. (2008). Transcriptomic analysis of the exit from dormancy of aspergillus fumigatus conidia. *BMC genomics*, 9:417.
- Lejeune, R. and Baron, G. V. (1997). Simulation of growth of a filamentous fungus in 3 dimensions. *Biotechnology and Bioengineering*, 53(2):139–150.
- Liao, W., Liu, Y., and Chen, S. (2007). Studying pellet formation of a filamentous fungus rhizopus oryzae to enhance organic acid production. *Applied Biochemistry and Biotechnology*, 137(1):689–701.
- Liaud, N., Giniés, C., Navarro, D., Fabre, N., Crapart, S., Gimbert, I. H., Levasseur, A., Raouche, S., and Sigoillot, J.-C. (2014). Exploring fungal biodiversity: organic acid production by 66 strains of filamentous fungi. *Fungal Biology and Biotechnology*, 1(1).
- Lin, P.-J., Grimm, L. H., Wulkow, M., Hempel, D. C., and Krull, R. (2008). Population balance modeling of the conidial aggregation of aspergillus niger. *Biotechnology and Bioengineering*, 99(2):341–350.
- Lin, P.-J., Scholz, A., and Krull, R. (2010). Effect of volumetric power input by aeration and agitation on pellet morphology and product formation of aspergillus niger. *Biochemical Engineering Journal*, 49(2):213–220.
- Liu, G., Xing, M., and Han, Q. (2005). A population-based morphologically structured model for hyphal growth and product formation in streptomycin fermentation. *World Journal of Microbiology and Biotechnology*, 21(8-9):1329–1338.
- Liu, Y.-S. and Wu, J.-Y. (2012). Effects of tween 80 and pH on mycelial pellets and exopolysaccharide production in liquid culture of a medicinal fungus. *Journal of industrial microbiology & biotechnology*, 39(4):623–628.
- Lyu, J., Tegelaar, M., Post, H., Moran Torres, J., Torchia, C., Altelaar, A. F. M., Bleichrodt, R.-J., de Cock, H., Lugones, L. G., and Wösten, H. A. B. (2023). Heterogeneity in spore aggregation and germination results in different sized, cooperative microcolonies in an aspergillus niger culture. *mBio*, 14(1):e0087022.
- M. Antimonov, A. Khounsary, S. Weigand, J. Rix, D. Keane, J. J. Grudzinski, A. Johnson, Z. Zhou, and W. Jansma (2015). Large-area kapton x-ray windows. pages 62–71. SPIE.
- Metz, B. and Kossen, N. W. F. (1977). The growth of molds in the form of pellets—a literature review. *Biotechnology and Bioengineering*, 19(6):781–799.
- Meyer, V., Basenko, E. Y., Benz, J. P., Braus, G. H., Caddick, M. X., Csukai, M., de Vries, R. P., Endy, D., Frisvad, J. C., Gunde-Cimerman, N., Haarmann, T., Hadar, Y., Hansen, K., Johnson, R. I., Keller, N. P., Kraševc, N., Mortensen, U. H., Perez, R., Ram, A. F. J., Record, E., Ross, P., Shapaval, V., Steiniger, C., van den Brink, H., van Munster, J., Yarden, O., and Wösten, H. A. B. (2020). Growing a circular economy with fungal biotechnology: a white paper. *Fungal Biology and Biotechnology*, 7(1):5.

- Meyer, V., Cairns, T., Barthel, L., King, R., Kunz, P., Schmideder, S., Müller, H., Briesen, H., Dinius, A., and Krull, R. (2021). Understanding and controlling filamentous growth of fungal cell factories: novel tools and opportunities for targeted morphology engineering. *Fungal Biology and Biotechnology*, 8(1):8.
- Meyer, V., Wanka, F., van Gent, J., Arentshorst, M., van den Hondel, C. A. M. J. J., and Ram, A. F. J. (2011). Fungal gene expression on demand: an inducible, tunable, and metabolism-independent expression system for *aspergillus niger*. *Applied and environmental microbiology*, 77(9):2975–2983.
- Meyerhoff, J., Tiller, V., and Bellgardt, K.-H. (1995). Two mathematical models for the development of a single microbial pellet. *Bioprocess Engineering*, 12(6):305–313.
- Miyazawa, K., Yoshimi, A., Sano, M., Tabata, F., Sugahara, A., Kasahara, S., Koizumi, A., Yano, S., Nakajima, T., and Abe, K. (2019). Both galactosaminogalactan and alpha-1,3-glucan contribute to aggregation of *aspergillus oryzae* hyphae in liquid culture. *Frontiers in Microbiology*, 10.
- Müller, C., McIntyre, M., Hansen, K., and Nielsen, J. (2002). Metabolic engineering of the morphology of *aspergillus oryzae* by altering chitin synthesis. *Applied and environmental microbiology*, 68(4):1827–1836.
- Muller, C., Spohr, A. B., and Nielsen, J. (2000). Role of substrate concentration in mitosis and hyphal extension of *aspergillus*. *Biotechnology and Bioengineering*, 67(4):390–397.
- Müller, H., Barthel, L., Schmideder, S., Schütze, T., Meyer, V., and Briesen, H. (2022). From spores to fungal pellets: A new high-throughput image analysis highlights the structural development of *aspergillus niger*. *Biotechnology and Bioengineering*, 119(8):2182–2195.
- Müller, H., Deffur, C., Schmideder, S., Barthel, L., Friedrich, T., Mirlach, L., Hammel, J. U., Meyer, V., and Briesen, H. (2023). Synchrotron radiation-based microcomputed tomography for three-dimensional growth analysis of *aspergillus niger* pellets. *Biotechnology and Bioengineering*.
- Müller, H., Schmideder, S., Barthel, L., Niessen, L., Meyer, V., and Briesen, H. (2020). Optimized x-ray micro-computed tomography and 3d volumetric image processing of filamentous fungal pellets. *Chemie Ingenieur Technik*, 92(9):1201.
- Nielsen, J., Johansen, C. L., Jacobsen, M., Krabben, P., and Villadsen, J. (1995). Pellet formation and fragmentation in submerged cultures of *penicillium chrysogenum* and its relation to penicillin production. *Biotechnology Progress*, 11(1):93–98.
- Nielsen, J. and Krabben, P. (1995). Hyphal growth and fragmentation of *penicillium chrysogenum* in submerged cultures. *Biotechnology and Bioengineering*, 46(6):588–598.
- Nieminen, L., Webb, S., Smith, M. C. M., and Hoskisson, P. A. (2013). A flexible mathematical model platform for studying branching networks: Experimentally validated using the model actinomycete, *streptomyces coelicolor*. *PLoS one*, 8(2).
- Nitsche, B. M., Burggraaf-van Welzen, A.-M., Lamers, G., Meyer, V., and Ram, A. F. J. (2013). Autophagy promotes survival in aging submerged cultures of the filamentous fungus *aspergillus niger*. *Applied Microbiology and Biotechnology*, 97(18):8205–8218.
- Nitsche, B. M., Jørgensen, T. R., Akeroyd, M., Meyer, V., and Ram, A. F. J. (2012). The carbon starvation response of *aspergillus niger* during submerged cultivation: insights from the transcriptome and secretome. *BMC genomics*, 13:380.
- Oshero, N. and May, G. S. (2001). The molecular mechanisms of conidial germination. *FEMS Microbiology Letters*, 199(2):153–160.
- Packer, H. L. and Thomas, C. R. (1990). Morphological measurements on filamentous microorganisms by fully automatic image analysis. *Biotechnology and Bioengineering*, 35(9):870–881.

- Papagianni, M. (2004). Fungal morphology and metabolite production in submerged mycelial processes. *Biotechnology Advances*, 22(3):189–259.
- Papagianni, M. (2014). Characterization of fungal morphology using digital image analysis techniques. *Journal of Microbial & Biochemical Technology*, 06(04).
- Papagianni, M. and Matthey, M. (2006). Morphological development of *aspergillus niger* in submerged citric acid fermentation as a function of the spore inoculum level. application of neural network and cluster analysis for characterization of mycelial morphology. *Microbial cell factories*, 5:3.
- Papagianni, M., Matthey, M., and Kristiansen, B. (1999). Hyphal vacuolation and fragmentation in batch and fed-batch culture of *aspergillus niger* and its relation to citric acid production. *Process Biochemistry*, 35(3):359–366.
- Paul, G., Priede, M., and Thomas, C. (1999). Relationship between morphology and citric acid production in submerged *aspergillus niger* fermentations. *Biochemical Engineering Journal*, 3(2):121–129.
- Paul, G. C., Kent, C. A., and Thomas, C. R. (1994). Hyphal vacuolation and fragmentation in *penicillium chrysogenum*. *Biotechnology and Bioengineering*, 44(5):655–660.
- Paul, G. C. and Thomas, C. R. (1996). A structured model for hyphal differentiation and penicillin production using *penicillium chrysogenum*. *Biotechnology and Bioengineering*, 51(5):558–572.
- Pearson, A. P., Glennon, B., and Kieran, P. M. (2003). Comparison of morphological characteristics of *streptomyces natalensis* by image analysis and focused beam reflectance measurement. *Biotechnology Progress*, 19(4):1342–1347.
- Pearson, A. P., Glennon, B., and Kieran, P. M. (2004). Monitoring of cell growth using the focused beam reflectance method. *Journal of Chemical Technology & Biotechnology*, 79(10):1142–1147.
- Petersen, N., Stocks, S., and Gernaey, K. V. (2008). Multivariate models for prediction of rheological characteristics of filamentous fermentation broth from the size distribution. *Biotechnology and Bioengineering*, 100(1):61–71.
- Pirt (1966). A theory of the mode of growth of fungi in the form of pellets in submerged culture. *Proceedings of the Royal Society of London B: Biological Sciences*, 166(1004):369–373.
- Posch, A. E. and Herwig, C. (2014). Physiological description of multivariate interdependencies between process parameters, morphology and physiology during fed-batch penicillin production. *Biotechnology Progress*, 30(3):689–699.
- Posch, A. E., Herwig, C., and Spadiut, O. (2013). Science-based bioprocess design for filamentous fungi. *Trends in Biotechnology*, 31(1):37–44.
- Posch, A. E., Spadiut, O., and Herwig, C. (2012). A novel method for fast and statistically verified morphological characterization of filamentous fungi. *Fungal Genetics and Biology*, 49(7):499–510.
- Priegnitz, B.-E., Wargenau, A., Brandt, U., Rohde, M., Dietrich, S., Kwade, A., Krull, R., and Fleissner, A. (2012). The role of initial spore adhesion in pellet and biofilm formation in *aspergillus niger*. *Fungal genetics and biology : FG & B*, 49(1):30–38.
- Quintanilla, D., Chelius, C., Iambamrung, S., Nelson, S., Thomas, D., Gernaey, K. V., and Marten, M. R. (2018). A fast and simple method to estimate relative, hyphal tensile-strength of filamentous fungi used to assess the effect of autophagy. *Biotechnology and Bioengineering*, 115(3):597–605.
- Ramkrishna, D. (2000). *Population Balances: Theory and Applications to Particulate Systems in Engineering*. Elsevier.

- Reinhold, A. and Briesen, H. (2015). High dimensional population balances for the growth of faceted crystals: Combining monte carlo integral estimates and the method of characteristics. *Chemical Engineering Science*, 127:220–229.
- Rokem, J. S. (2020). Tca cycle organic acids produced by filamentous fungi: The building blocks of the future. In Nevalainen, H., editor, *Grand Challenges in Fungal Biotechnology*, Grand Challenges in Biology and Biotechnology Ser, pages 439–476. Springer International Publishing AG, Cham.
- Rollié, S., Briesen, H., and Sundmacher, K. (2009). Discrete bivariate population balance modelling of heteroaggregation processes. *Journal of Colloid and Interface Science*, 336(2):551–564.
- Rønnest, N. P., Stocks, S. M., Lantz, A. E., and Gernaey, K. V. (2012). Comparison of laser diffraction and image analysis for measurement of streptomyces coelicolor cell clumps and pellets. *Biotechnology letters*, 34(8):1465–1473.
- Sachs, C. C., Koepff, J., Wiechert, W., Grünberger, A., and Nöh, K. (2019). mycelyso - high-throughput analysis of streptomyces mycelium live cell imaging data. *BMC bioinformatics*, 20(1):452.
- Sánchez-Orellana, G., Casas-Flores, S., and Gutiérrez-Medina, B. (2019). Automated, continuous video microscopy tracking of hyphal growth. *Fungal Genetics and Biology*, 123:25–32.
- Schmideder, S. (2022). *Following fungal features - micromorphology and diffusivity of filamentous fungal pellets revealed by three-dimensional imaging and simulation*. Universitätsbibliothek der TU München, München.
- Schmideder, S., Barthel, L., Friedrich, T., Thalhammer, M., Kovačević, T., Niessen, L., Meyer, V., and Briesen, H. (2019a). An x-ray microtomography-based method for detailed analysis of the three-dimensional morphology of fungal pellets. *Biotechnology and Bioengineering*, 116(6):1355–1365.
- Schmideder, S., Barthel, L., Müller, H., Meyer, V., and Briesen, H. (2019b). From three-dimensional morphology to effective diffusivity in filamentous fungal pellets. *Biotechnology and Bioengineering*, 116(12):3360–3371.
- Schmideder, S., Müller, H., Barthel, L., Friedrich, T., Niessen, L., Meyer, V., and Briesen, H. (2020). Universal law for diffusive mass transport through mycelial networks. *Biotechnology and Bioengineering*, 118(2):930–943.
- Schmideder, S., Thurin, L., Kaur, G., and Briesen, H. (2022). Inline imaging reveals evolution of the size distribution and the concentration of microbubbles in dissolved air flotation. *Water research*, 224:119027.
- Schnitzler, H. and Zimmer, K.-P. (2008). Advances in stereomicroscopy. In Mazuray, L., Wartmann, R., Wood, A., Tissot, J.-L., and Raynor, J. M., editors, *Optical Design and Engineering III*, SPIE Proceedings, page 71000P. SPIE.
- Schrinner, K., Veiter, L., Schmideder, S., Doppler, P., Schrader, M., Münch, N., Althof, K., Kwade, A., Briesen, H., Herwig, C., and Krull, R. (2020). Morphological and physiological characterization of filamentous *lentzea aerocolonigenes*: Comparison of biopellets by microscopy and flow cytometry. *PLoS one*, 15(6):e0234125.
- Schuetze, T. and Meyer, V. (2017). Polycistronic gene expression in *aspergillus niger*. *Microbial Cell Factories*, 16(1):1–8.
- Silva, E. M. E., Gutierrez, G. F., Dendooven, L., Hugo, J. I., and Ochoa-Tapia, J. A. (2001). A method to evaluate the isothermal effectiveness factor for dynamic oxygen into mycelial pellets in submerged cultures. *Biotechnology Progress*, 17(1):95–103.
- Spohr, A., Dam-Mikkelsen, C., Carlsen, M., Nielsen, J., and Villadsen, J. (1998). On-line study of fungal morphology during submerged growth in a small flow-through cell. *Biotechnology and Bioengineering*, 58(5):541–553.

- Sun, X., Wu, H., Zhao, G., Li, Z., Wu, X., Liu, H., and Zheng, Z. (2018). Morphological regulation of *aspergillus niger* to improve citric acid production by *chsc* gene silencing. *Bioprocess and biosystems engineering*, 41(7):1029–1038.
- Tegelaar, M., Aerts, D., Teertstra, W. R., and Wösten, H. A. B. (2020). Spatial induction of genes encoding secreted proteins in micro-colonies of *aspergillus niger*. *Scientific Reports*, 10(1):1536.
- Tesche, S. and Krull, R. (2021). An image analysis method to quantify heterogeneous filamentous biomass based on pixel intensity values – interrelation of macro- and micro-morphology in *actinomadura namibiensis*. *Biochemical Engineering Journal*, 166:107865.
- Tesche, S., Rösemeyer-Scheumann, R., Lohr, J., Hanke, R., Büchs, J., and Krull, R. (2019). Salt-enhanced cultivation as a morphology engineering tool for filamentous actinomycetes: Increased production of labyrinthopeptin A in *actinomadura namibiensis*. *Engineering in Life Sciences*, 19(11):781–794.
- Tough, A. J., Pulham, J., and Prosser, J. I. (1995). A mathematical model for the growth of mycelial pellet populations. *Biotechnology and Bioengineering*, 46(6):561–572.
- Trinci, A. P. (1974). A study of the kinetics of hyphal extension and branch initiation of fungal mycelia. *Journal of General Microbiology*, 81(1):225–236.
- Upton, D. J., McQueen-Mason, S. J., and Wood, A. J. (2017). An accurate description of *aspergillus niger* organic acid batch fermentation through dynamic metabolic modelling. *Biotechnology for biofuels*, 10:258.
- van den Berg, M. A. (2011). Impact of the *penicillium chrysogenum* genome on industrial production of metabolites. *Applied Microbiology and Biotechnology*, 92(1):45–53.
- van Leeuwen, M. R., Krijgsheld, P., Bleichrodt, R., Menke, H., Stam, H., Stark, J., Wösten, H. A. B., and Dijksterhuis, J. (2013). Germination of conidia of *aspergillus niger* is accompanied by major changes in rna profiles. *Studies in mycology*, 74(1):59–70.
- Vanegas, K. G., Jarczynska, Z. D., Strucko, T., and Mortensen, U. H. (2019). Cpf1 enables fast and efficient genome editing in *aspergilli*. *Fungal biology and biotechnology*, 6:6.
- Veiter, L. and Herwig, C. (2019). The filamentous fungus *penicillium chrysogenum* analysed via flow cytometry—a fast and statistically sound insight into morphology and viability. *Applied Microbiology and Biotechnology*, 103(16):6725–6735.
- Veiter, L., Kubicek, M., Hutter, H., Pittenauer, E., Herwig, C., and Slouka, C. (2020). Study of metabolism and identification of productive regions in filamentous fungi via spatially resolved time-of-flight secondary ion mass spectrometry. *Analytical and bioanalytical chemistry*, 412(9):2081–2088.
- Veiter, L., Rajamanickam, V., and Herwig, C. (2018). The filamentous fungal pellet-relationship between morphology and productivity. *Applied Microbiology and Biotechnology*, 102(7):2997–3006.
- Wang, B., Chen, J., Li, H., Sun, F., Li, Y., and Shi, G. (2017). Pellet-dispersion strategy to simplify the seed cultivation of *aspergillus niger* and optimize citric acid production. *Bioprocess and biosystems engineering*, 40(1):45–53.
- Wang, Q., Zhong, C., and Xiao, H. (2020). Genetic engineering of filamentous fungi for efficient protein expression and secretion. *Frontiers in bioengineering and biotechnology*, 8:293.
- Wanka, F., Cairns, T., Boecker, S., Berens, C., Happel, A., Zheng, X., Sun, J., Krappmann, S., and Meyer, V. (2016). Tet-on, or tet-off, that is the question: Advanced conditional gene expression in *aspergillus*. *Fungal genetics and biology : FG & B*, 89:72–83.

- Ward, O. P. (2012). Production of recombinant proteins by filamentous fungi. *Biotechnology Advances*, 30(5):1119–1139.
- Wargenau, A., Fleißner, A., Bolten, C. J., Rohde, M., Kampen, I., and Kwade, A. (2011). On the origin of the electrostatic surface potential of *aspergillus niger* spores in acidic environments. *Research in Microbiology*, 162(10):1011–1017.
- Whelan, J., Murphy, E., Pearson, A., Jeffers, P., Kieran, P., McDonnell, S., Raposo, S., Lima-Costa, M. E., and Glennon, B. (2012). Use of focussed beam reflectance measurement (fbrm) for monitoring changes in biomass concentration. *Bioprocess and biosystems engineering*, 35(6):963–975.
- Willemse, J., Büke, F., van Dissel, D., Grevink, S., Claessen, D., and van Wezel, G. P. (2018). Sparticle, an algorithm for the analysis of filamentous microorganisms in submerged cultures. *Antonie van Leeuwenhoek*, 111(2):171–182.
- Wittier, R., Baumgartl, H., Lübbers, D. W., and Schügerl, K. (1986). Investigations of oxygen transfer into penicillium chrysogenum pellets by microprobe measurements. *Biotechnology and Bioengineering*, 28(7):1024–1036.
- Wösten, H. A. B. (2019). Filamentous fungi for the production of enzymes, chemicals and materials. *Current opinion in biotechnology*, 59:65–70.
- Wucherpennig, T., Hestler, T., and Krull, R. (2011). Morphology engineering–osmolality and its effect on *aspergillus niger* morphology and productivity. *Microbial cell factories*, 10:58.
- Wucherpennig, T., Kiep, K. A., Driouch, H., Wittmann, C., and Krull, R. (2010). Morphology and rheology in filamentous cultivations. *Advances in applied microbiology*, 72:89–136.
- Yang, H., King, R., Reichl, U., and Gilles, E. D. (1992). Mathematical model for apical growth, septation, and branching of mycelial microorganisms. *Biotechnology and Bioengineering*, 39(1):49–58.
- Zacchetti, B., Willemse, J., Recter, B., van Dissel, D., van Wezel, G. P., Wösten, H. A. B., and Claessen, D. (2016). Aggregation of germlings is a major contributing factor towards mycelial heterogeneity of streptomyces. *Scientific reports*, 6:27045.
- Zacchetti, B., Wösten, H. A. B., and Claessen, D. (2018). Multiscale heterogeneity in filamentous microbes. *Biotechnology Advances*, 36(8):2138–2149.
- Zhang, J. and Zhang, J. (2016). The filamentous fungal pellet and forces driving its formation. *Critical Reviews in Biotechnology*, 36(6):1066–1077.
- Zhou, Y., Du, J., and Tsao, G. T. (2000). Mycelial pellet formation by *rhizopus oryzae* atcc 20344. *Applied Biochemistry and Biotechnology*, 84(1):779–789.
- Žnidaršič, P., Komel, R., and Pavko, A. (2000). Influence of some environmental factors on *rhizopus nigricans* submerged growth in the form of pellets. *World Journal of Microbiology and Biotechnology*, 16(7):589–593.

# A. List of Publications

## Peer-Reviewed Publications

**Henri Müller**, Charlotte Deffur, Stefan Schmieder, Lars Barthel, Tiaan Friedrich, Lukas Mirlach, Jörg U. Hammel, Vera Meyer, Heiko Briesen, 2023, Synchrotron radiation-based microcomputed tomography for three-dimensional growth analysis of *Aspergillus niger* pellets. *Biotechnology and Bioengineering*, <https://doi.org/10.1002/bit.28506>.

**Henri Müller**, Lars Barthel, Stefan Schmieder, Tabea Schütze, Vera Meyer, Heiko Briesen, 2022, From spores to fungal pellets: A new high-throughput image analysis highlights the structural development of *Aspergillus niger*. *Biotechnology and Bioengineering*, 119(8): 2182–2195. <https://doi.org/10.1002/bit.28124>

Stefan Schmieder, **Henri Müller**, Lars Barthel, Tiaan Friedrich, Ludwig Niessen, Vera Meyer, and Heiko Briesen, 2021, Universal law for diffusive mass transport through mycelial networks. *Biotechnology and Bioengineering*, 118(2):930–943. <https://doi.org/10.1002/bit.27622>

Vera Meyer, Timothy Cairns, Lars Barthel, Rudibert King, Philipp Kunz, Stefan Schmieder, **Henri Müller**, Heiko Briesen, Anna Dinius, Rainer Krull, 2021, Understanding and controlling filamentous growth of fungal cell factories: novel tools and opportunities for targeted morphology engineering. *Fungal Biology and Biotechnology*, 8(1): 8. <https://doi.org/10.1186/s40694-021-00115-6>

Stefan Schmieder, Lars Barthel, **Henri Müller**, Vera Meyer, and Heiko Briesen, 2019, From three-dimensional morphology to effective diffusivity in filamentous fungal pellets. *Biotechnology and Bioengineering*, 116(12): 3360–3371. <https://doi.org/10.1002/bit.27166>

## Not Peer-Reviewed Publication

**Henri Müller**, Stefan Schmieder, Heiko Briesen, unpublished, Generalized morphology modeling of aggregating, filamentous microorganisms. *Springer Nature*, to be published.

## Oral Presentations

**Henri Müller**, Stefan Schmieder, Lars Barthel, Jörg U. Hammel, Tiaan Friedrich, Vera Meyer, Heiko Briesen, 2021, Inside mycelium – synchrotron radiation and image processing to unveil the time-resolved three-dimensional growth of filamentous fungal

pellets. 13th European Congress of Chemical Engineering and 6th European Congress of Applied Biotechnology, Keynote Presentation, Online.

**Henri Müller**, Charlotte Deffur, Stefan Schmideder, Lars Barthel, Tiaan Friedrich, Jörg U. Hammel, Vera Meyer, Heiko Briesen, 2023, 3D growth analysis of filamentous fungal pellets at the PETRA III imaging beamline P05. DESY Photon Science Users' Meeting 2023, Hamburg, Deutschland.

Charlotte Deffur, Stefan Schmideder, **Henri Müller**, Gumeet Kaur, Anna Dinius, Rainer Krull, Heiko Briesen, 2023, Multiscale modeling of the interplay of fungal morphology development and oxygen supply. 14th European Congress of Chemical Engineering and 7th European Congress of Applied Biotechnology, Berlin, Germany.

Karin Engelbert, Tolue Kheirkhah, **Henri Müller**, Charlotte Deffur, Stefan Junne, Heiko Briesen, Peter Neubauer, Vera Meyer, 2023, Controlling macromorphologies of *Aspergillus niger* during high and low shear stress bioreactor cultivation. 16th European Conference on Fungal Genetics, Innsbruck, Austria.

Lars Barthel, Stefan Schmideder, **Henri Müller**, Heiko Briesen, Vera Meyer, 2022, Quantifying fungal pellets during submerged cultivation: from 3D X-ray microtomography imaging to diffusive mass transport. 31st Fungal Genetics Conference, Asilomar, USA.

Heiko Briesen, Stefan Schmideder, **Henri Müller**, 2020, Morphological characterization and modeling of filamentous fungi. 4th Indo-German Workshop on Advances in Materials, Reaction & Separation Processes, Berlin, Germany.

Stefan Schmideder, Lars Barthel, **Henri Müller**, Vera Meyer, and Heiko Briesen, 2020, On the three-dimensional morphology and substrate-diffusion in filamentous fungal pellets. 15th European Conference on Fungal Genetics (ECFG15), Rome, Italy.

Stefan Schmideder, Lars Barthel, **Henri Müller**, Vera Meyer, and Heiko Briesen, 2020, From macro- to micro-morphological properties of filamentous fungal pellets. ProcessNet Jahrestagung und DECHEMA-Jahrestagung der Biotechnologen 2020, Web-Konferenz.

## Poster Presentations

**Henri Müller**, Stefan Schmideder, Lars Barthel, Charlotte Deffur, Jörg U. Hammel, Vera Meyer, Heiko Briesen, 2023, Synchrotron radiation-based micro-computed tomography for three-dimensional growth analysis of *Aspergillus niger* pellets. 16th European Conference on Fungal Genetics, Innsbruck, Austria.

**Henri Müller**, Jörg U. Hammel, Heiko Briesen, 2023, Inside mycelium – synchrotron radiation and image processing to unveil the three-dimensional growth of filamentous fungal pellets. DESY Photon Science Users' Meeting 2023, Hamburg, Deutschland.

**Henri Müller**, Stefan Schmieder, Lars Barthel, Ludwig Niessen, Vera Meyer, and Heiko Briesen, 2020, Optimized X-ray microcomputed tomography and 3D volumetric image processing of filamentous fungal pellets. ProcessNet Jahrestagung und DECHEMA-Jahrestagung der Biotechnologen 2020, Online.

Fangxing Zhang, **Henri Müller**, Jörg U. Hammel, Bertram Schmidt, Vera Meyer, Heiko Briesen, 2023, Three-dimensional structure analysis of biodegradable composite material based on fungal filaments and hemp substrate. 14th European Congress of Chemical Engineering and 7th European Congress of Applied Biotechnology, Berlin, Germany.

Karin Engelbert, Tolue Kheirkhah, **Henri Müller**, Charlotte Deffur, Stefan Junne, Heiko Briesen, Peter Neubauer, Vera Meyer, 2023, Controlling macromorphologies of *Aspergillus niger* during high and low shear stress bioreactor cultivation. 16th European Conference on Fungal Genetics, Innsbruck, Austria.

Lars Barthel, Sven Duda, **Henri Müller**, Heiko Briesen, Vera Meyer, 2023, Systems and 3D imaging approaches to understand the *Aspergillus niger* chitin synthase gene repertoire. 16th European Conference on Fungal Genetics, Innsbruck, Austria.

Karin Engelbert, **Henri Müller**, Jörg U. Hammel, Heiko Briesen, Vera Meyer, 2023, The development of pellet populations during submerged cultivation of *Aspergillus niger*. 16th European Conference on Fungal Genetics, Innsbruck, Austria.

Charlotte Deffur, Stefan Schmieder, **Henri Müller**, Gumeet Kaur, Anna Dinius, Rainer Krull, Heiko Briesen, 2023, Understanding the interplay of fungal morphology development and oxygen supply: A multiscale model approach. 16th European Conference on Fungal Genetics, Innsbruck, Austria.

Lars Barthel, Stefan Schmieder, **Henri Müller**, Heiko Briesen, Vera Meyer, 2022, Quantifying fungal pellets during submerged cultivation: from 3D X-ray microtomography imaging to diffusive mass transport. 31st Fungal Genetics Conference, Asilomar, USA.

## **B. Published and peer-reviewed Articles II and III**

## **Article II**

## ARTICLE

# From spores to fungal pellets: A new high-throughput image analysis highlights the structural development of *Aspergillus niger*

Henri Müller<sup>1</sup>  | Lars Barthel<sup>2</sup>  | Stefan Schmideder<sup>1</sup>  | Tabea Schütze<sup>2</sup>  | Vera Meyer<sup>2</sup>  | Heiko Briesen<sup>1</sup> 

<sup>1</sup>Department of Process Systems Engineering, School of Life Sciences Weihenstephan, Technical University of Munich, Freising, Germany

<sup>2</sup>Department of Applied and Molecular Microbiology, Institute of Biotechnology, Technische Universität Berlin, Berlin, Germany

## Correspondence

Vera Meyer, Department of Applied and Molecular Microbiology, Technische Universität Berlin, Straße des 17. Juni 135, 10623 Berlin, Germany.  
Email: [vera.meyer@tu-berlin.de](mailto:vera.meyer@tu-berlin.de)

Heiko Briesen, Department of Process Systems Engineering, Technical University of Munich, Gregor-Mendel-Str. 4, 85354 Freising, Germany.  
Email: [heiko.briesen@tum.de](mailto:heiko.briesen@tum.de)

## Funding information

Deutsche Forschungsgemeinschaft, Grant/Award Numbers: 315305620, 315384307, 427889137

## Abstract

Many filamentous fungi are exploited as cell factories in biotechnology. Cultivated under industrially relevant submerged conditions, filamentous fungi can adopt different macromorphologies ranging from dispersed mycelia over loose clumps to pellets. Central to the development of a pellet morphology is the agglomeration of spores after inoculation followed by spore germination and outgrowth into a pellet population, which is usually very heterogeneous. As the dynamics underlying population heterogeneity is not yet fully understood, we present here a new high-throughput image analysis pipeline based on stereomicroscopy to comprehensively assess the developmental program starting from germination up to pellet formation. To demonstrate the potential of this pipeline, we used data from 44 sampling times harvested during a 48 h submerged batch cultivation of the fungal cell factory *Aspergillus niger*. The analysis of up to 1700 spore agglomerates and 1500 pellets per sampling time allowed the precise tracking of the morphological development of the overall culture. The data gained were used to calculate size distributions and area fractions of spores, spore agglomerates, spore agglomerates within pellets, pellets, and dispersed mycelia. This approach eventually enables the quantification of culture heterogeneities and pellet breakage.

## KEYWORDS

*Aspergillus niger*, image analysis, morphology development, pellet growth, spore agglomeration/ aggregation

## 1 | INTRODUCTION

The birth of industrial biotechnology dates back to the start of citric acid production using the filamentous fungus *Aspergillus niger* more than 100 years ago. Ever since, filamentous fungi played an important role in many industrial processes and are nowadays of central importance to establish a future circular economy (Cairns et al., 2018;

V. Meyer et al., 2020). Filamentous fungi are used as cell factories for a diverse range of products, for example, drugs, enzymes, organic acids, or commodities for the pharma, feed, food, fuel, textile, and chemical industries (V. Meyer et al., 2020). During submerged cultivation, spores and hyphae from filamentous fungi develop into different macromorphologies ranging from dispersed mycelium to pellets. Contrary to dispersed mycelia (freely dispersed hyphae) and

This is an open access article under the terms of the Creative Commons Attribution-NonCommercial License, which permits use, distribution and reproduction in any medium, provided the original work is properly cited and is not used for commercial purposes.

© 2022 The Authors. *Biotechnology and Bioengineering* published by Wiley Periodicals LLC.

clumps (loose agglomerates of hyphae), fungal pellets are dense spherical hyphal networks with a diameter between a few hundred micrometers and some millimeters (Cairns et al., 2019; Cox et al., 1998). The developed macromorphological structure of fungal production strains greatly influences the productivity of the bioprocess (Tegelaar et al., 2020; Veiter et al., 2018). Higher viscosity and a non-Newtonian behavior characterize the cultivation processes of dispersed mycelia compared to pellets. Therefore, less energy is required to mix a cultivation of pellets and hence lower shear stress is applied. Furthermore, homogeneous mass transfer of substrates and especially oxygen into the medium and from the bulk phase to the pellets is favorably enhanced (Gibbs et al., 2000). However, the diffusivity of oxygen inside fungal pellets depends on the hyphal density (Schmideder et al., 2019, 2020). Dense hyphal structures can result in oxygen-limited regions in the center of fungal pellets, resulting in growth limitation and reduced growth-associated product formation (Driouch et al., 2010; Hille et al., 2009). Posch et al. (2012) observed a diffusion-limiting compactness after 15 h of pelleted growth of *Penicillium chrysogenum*. Different strategies have thus been developed to increase the productivity of bioprocesses by altering fungal macromorphologies. Most of them focus on the variation of the cultivation conditions, including medium composition, pH and osmolality of the medium, spore inoculum concentration, viability/vitality of the inoculum, bioreactor geometry, shear stress, aeration rate, temperature, and the addition of microparticles to name but a few (Böl et al., 2021; Driouch et al., 2010; Kaup et al., 2008; Laible et al., 2021; Papagianni, 2004; Wucherpfennig et al., 2010, 2011). Genetic factors and intracellular processes that affect or even control spore germination, hyphal growth, and eventually pellet formation can be grouped into cytoskeletal networks, exocytosis, endocytosis, cell membrane, and cell wall biogenesis. They jointly define hyphal growth and hyphal surface properties, and thus contribute to the development of macromorphologies (for recent reviews, see Cairns et al., 2019; Commer & Shaw, 2020; Miyazawa et al., 2020). Remarkably, systems biology data and gene coexpression networks nowadays allow the prediction and modification of genes to be important for fungal macromorphological developments (Cairns et al., 2019; Fiedler, Cairns, et al., 2018).

In general, pellet formation can be classified into either coagulative or noncoagulative processes (Veiter et al., 2018). During coagulative pellet formation (representatives are *A. niger*, *Aspergillus nidulans*, or *Penicillium oxalicum*), spores agglomerate after inoculation due to electrostatic and salt bridging between cell wall surface polysaccharides and due to hydrophobicity of spore surface proteins (Dynesen & Nielsen, 2003; Pascual et al., 2000; Zhang & Zhang, 2016). During noncoagulative pellet formation (one representative is *Rhizopus oryzae*), single spores form single pellets, that is, spores remain dispersed during germination, but hyphae can agglomerate at later growth phases (Zhang & Zhang, 2016). Notably, the macromorphological development of some fungi follows both the coagulative and noncoagulative processes (a representative is *Penicillium chrysogenum*). Coagulative spore types are also able to form noncoagulative pellets when environmental conditions change, for example, pH increase of the medium (Veiter et al., 2018).

Recently, it was shown that macromorphologies of *A. niger* considerably differed when cultivated in two different bioreactor types (stirred-tank reactor, waved-mixed reactor), although identical medium compositions, feeding schemes, temperature, and pH control were applied (Kurt et al., 2018). Reduced shear stress under wave-mixed conditions provoked the formation of *A. niger* pellets, which were very heterogeneous in size. It was hypothesized that these very heterogeneous pellet populations ensured faster biomass accumulation when compared to stirred-tank cultivations, where homogeneously dispersed mycelia were predominantly formed by *A. niger* (Kurt et al., 2018). Importantly, the mycelial heterogeneity phenomenon is not restricted to filamentous fungi but is also observed in filamentous bacteria including *Streptomyces*, some of which are also well-established cell factories for drug and antibiotics production (Nepal & Wang, 2019). Here, it was shown that heterogeneity is also influenced by germling aggregation in *Streptomyces* spp. (Zacchetti et al., 2016).

Hence, only a deeper and holistic understanding of the interactions as well as interdependencies of process conditions, genetic conditions, and population heterogeneities will pave the way for the rational morphology engineering of filamentous fungi in the future. One central prerequisite to achieve this is the availability of image analysis pipelines that allow the qualitative and quantitative description of different processes including spore agglomeration, pellet formation, pellet growth, pellet breakage events, and to access the extent of population heterogeneity. In particular, the holistic description of the pellet formation processes is of great importance, for example, it is difficult to quantify the influence of different cultivation conditions on the fungi just by analyzing the final fungal morphological state without considering a possibly changed spore agglomeration, which is the first step and one driving factor for the initial formation of pellets.

Existing high-throughput methods to study the structural development of filamentous fungi cultivations, including focused beam reflectance measurement and image analysis, track either the spore agglomeration or the macromorphological pellet development during growth (Cairns et al., 2019; Grimm et al., 2004; Willemse et al., 2018). To the best of our best knowledge, flow cytometry, which can be used for fungal pellet analysis (Bekker et al., 2011; Ehgartner et al., 2017; Schrinner et al., 2020; Tegelaar et al., 2020; Veiter & Herwig, 2019), has never been used to analyze the spore agglomeration and the morphological development of pellets within one cultivation.

In the present study, we aim to track the evolution of pellets and dispersed mycelia in the coagulative-type industrially exploited fungus *A. niger* starting from spore inoculation. To observe and evaluate spore agglomeration, pellet formation, pellet growth, and population heterogeneities, we designed a new fast high-throughput image analysis pipeline based on stereomicroscopic images from culture samples. In doing so, we were able to analyze 2500 fungal objects (spores/spore agglomerates, spore agglomerates within pellets, pellets) on average per sample during cultivation and were able to calculate the size distributions of the detected objects. We

complemented the size distributions by area fractions of the fungal objects including dispersed mycelia to enable complete characterization of the whole cultivation.

## 2 | MATERIALS AND METHODS

### 2.1 | Strain and inoculum preparation

We utilized the hyperbranching *A. niger*  $\Delta$ racA strain MF22.4 (Fiedler, Barthel, et al., 2018; Kwon et al., 2013). Conidiospores of MF22.4 were obtained from agar plate cultures by using standard procedures for filamentous fungi (Bennet & Lasure, 1991). Ten milliliters of physiological salt solution (PS) were carefully added on top of the well-sporulated plate culture. Subsequently, a cotton stick was used to spread the PS over the plate, while simultaneously using it to scrub the spores from the mycelium. Spores were then filtrated and stored in PS for 17 h at 4°C until inoculation. The PS solution was prepared with 8.9 g/L sodium chloride.

### 2.2 | Media, cultivation, and sampling

Five-liter Erlenmeyer flasks and 1 L complete medium (V. Meyer et al., 2010) with 9 g/L glucose were used for the submerged cultivation of *A. niger*. The shake flasks were inoculated with  $2.5 \times 10^6$  spores/ml. *Aspergillus niger* MF22.4 was cultivated for 48 h at 30°C with a rotational speed of 90 RPM in an Infors HT Multitron Standard shaker (Infors AG). The cultivation was performed in duplicate (flasks A and B).

Samples were taken every 30 min for the first 10 h and every hour for the next 22 h. The last sample was taken after 48 h of cultivation, resulting in a total number of 44 sampling times. At each sampling time, stereo and differential interference contrast (DIC) microscopy were performed. The biomass concentration was determined every hour from the sampling time 6 h on. The glucose concentration was determined every second hour.

### 2.3 | Stereomicroscopy

The main imaging, that is, the method to acquire thousands of fungal objects, was performed with a Leica S8APO stereomicroscope (Leica Microsystems GmbH) connected to a Leica MC120 HD camera (Leica Microsystems GmbH). For image capture, 3 ml of culture volume were carefully pipetted into a Petri dish (Sarstedt AG & Co. KG) with 85 mm inside diameter using a 10 ml serological pipette (Sarstedt AG & Co. KG) and diluted with distilled H<sub>2</sub>O until the bottom of the Petri dish was just completely filled with liquid. Care was taken to ensure that there was not too much water in the Petri dish to avoid overlapping of pellets. Further, the Petri dish was gently swirled to separate loosely attached pellets from each other. Subsequently, the Petri dish was put on a blue cardboard with a rectangular grid in the

measurement area of the stereomicroscope (Supporting Information: Figure S1). As the blue cardboard enhanced the contrast, it facilitated the subsequent image analysis. One image per 13 × 11 mm rectangle and at least 24 images per sampling time were taken by carefully sliding the blue cardboard template together with the Petri dish from rectangle to rectangle while preventing the pellets from moving to avoid double image capture of the same sample area. In total, about 1300 images were taken for each cultivation flask. To depict all structural changes of *A. niger* MF22.4 during submerged cultivation and to bridge the length scale between single spores in the range of a few micrometers and pellets in the range of a few hundred micrometers, the magnification of the stereo microscope was adjusted at certain sampling times. Supporting Information: Table S1 summarizes the isotropic pixel size, the field of view, and sampling times when the magnification was changed. The stereomicroscopic images were saved in an 8-bit RGB JPEG file format.

### 2.4 | DIC microscopy

To image a few fungal objects per sampling time with higher magnification, a Leica DM 5000 CS (Leica Microsystems GmbH) DIC microscope was used. Per sampling time, 15  $\mu$ l of culture volume were transferred on a microscope slide and covered with a cover glass. Twenty to 40 images per sampling time with 100- and 400-fold magnification resulting in pixel sizes of 0.651 and 0.163  $\mu$ m, respectively, were taken. The DIC high-resolution images were used to validate the results of our newly developed image analysis pipeline, which is based on the stereomicroscope images.

The stereomicroscopic images were saved in an 8-bit RGB JPEG file format. The stereomicroscopic and DIC images of all sampling times for flasks A and B can be downloaded via the provided link: <https://doi.org/10.14459/2021mp1634565>

### 2.5 | Determination of the biomass

After taking stereomicroscopic images, the sample was completely transferred into a preweighted Falcon tube and was washed twice with distilled H<sub>2</sub>O. The tube was centrifuged after every washing step for 5 min at 10,300 RPM and the supernatant was withdrawn. After 10 h of cultivation, sedimentation replaced the centrifugation steps. The washed biomass within the Falcon tubes was freeze-dried and the dry weight of the biomass was subsequently measured.

### 2.6 | Determination of glucose concentration in the supernatant

Samples for the determination of glucose concentration were taken every second hour. For that, 1 ml of culture volume was centrifuged and 250  $\mu$ l of the supernatant was instantly frozen in liquid nitrogen and stored at -80°C for the subsequent measurement of glucose

concentration. After completing the cultivation, all samples were measured in duplicate using the Glucose GOP/PAP Liquicolor kit (mti-diagnostics GmbH) following the manufacturer's manual.

## 2.7 | Automated image analysis and data processing

MATLAB (version R2020b; MathWorks) was used to develop a fully automated image analysis pipeline (Figure 1). We discriminated four fungal object classes on the 8-bit stereomicroscopic RGB images. The four object classes are marked on the zoomed sections of the stereomicroscopic images in Figure 2a: (1) nongerminated spores and spore agglomerates (Figure 2a, orange), (2) spore cores comprised of the spore part of germinated spore agglomerates (Figure 2a, red), (3) total pellets composed of spore agglomerate and mycelia (Figure 2a, white), (4) and dispersed mycelia (Figure 2a, green). For better readability, the four classes will be referred to as spores/spore agglomerates, spore cores, pellets, and dispersed mycelia, respectively. Figure 1 shows a flowchart giving an overview of key sections of the developed spore/spore agglomerate, spore core, and pellet segmentation pipeline. In the following, the image analysis steps will be described in detail referring to the subimages labeled a–l in this

visual overview. Images are represented by matrices of intensity values of different color channels. Thus, if matrix operations are performed during image processing, the expression will be used equivalently to the image itself.

## 2.8 | Segmentation of spores, spore agglomerates, and hyphae of pellets

To binarize spores, spore agglomerates, and spore cores into foreground objects, we used two different threshold methods, that is, the adaptive threshold method and the global threshold method. The adaptive threshold method (Bradley & Roth, 2007) was used for the first 3 h of cultivation to binarize spores and spore agglomerates into foreground objects. The global threshold method, used for images taken after 3 h of cultivation time, was used to binarize spores/spore agglomerates, and spore cores into foreground objects.

For the adaptive threshold method, the 8-bit RGB image was converted into a grayscale image and the function *adaptthresh* (MathWorks) with a sensitivity value of 0.5 was utilized to calculate an adaptive threshold matrix. After thresholding the grayscale image, the black and white values of the binarized image were inverted to obtain the spores and spore agglomerates as foreground objects. An

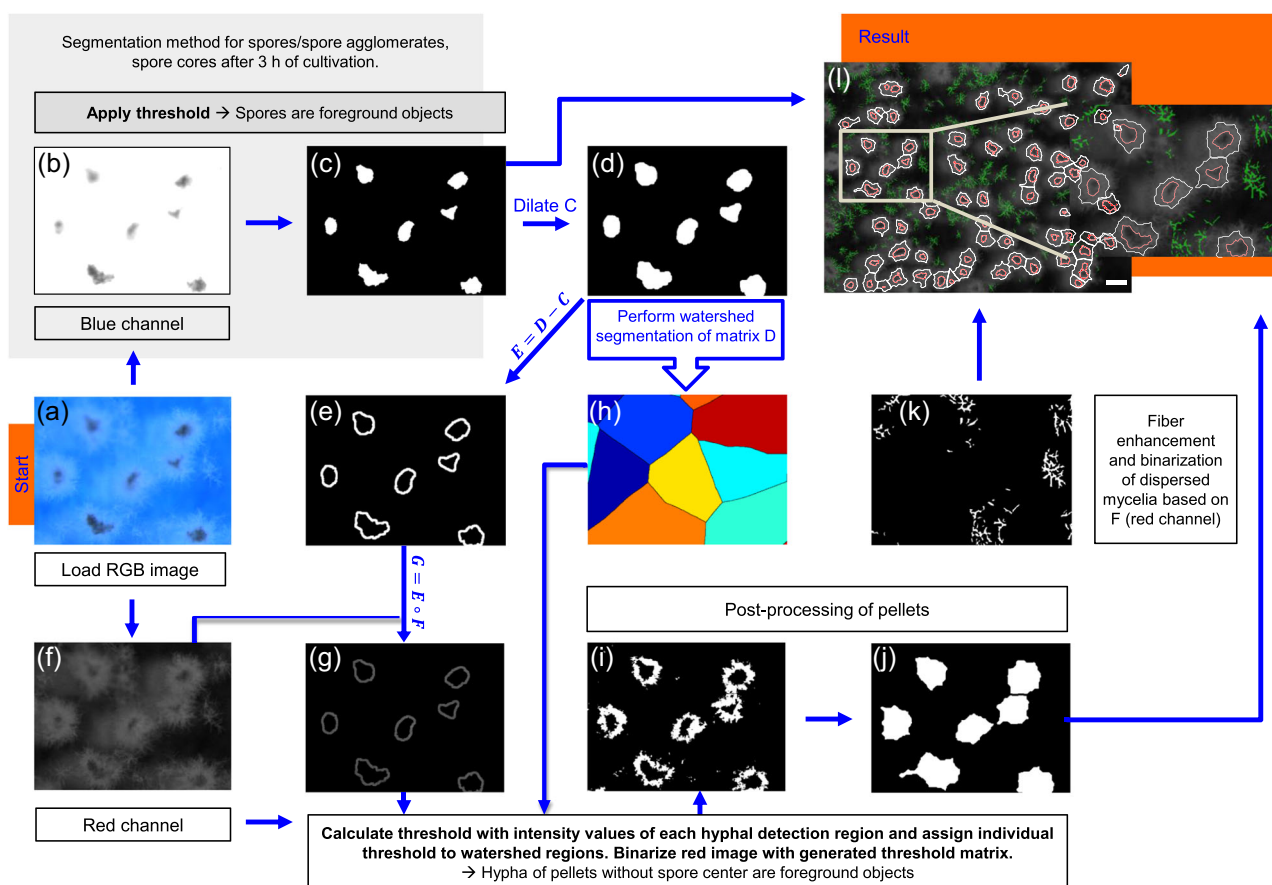


**FIGURE 1** Overview of the automated image analysis and data processing resulting in segmentation of spore cores (red), pellets (white), and dispersed mycelium (green) on image I. Images a–k represent a zoomed section of the image I. The scale bar of image I represents a length of 500 μm.

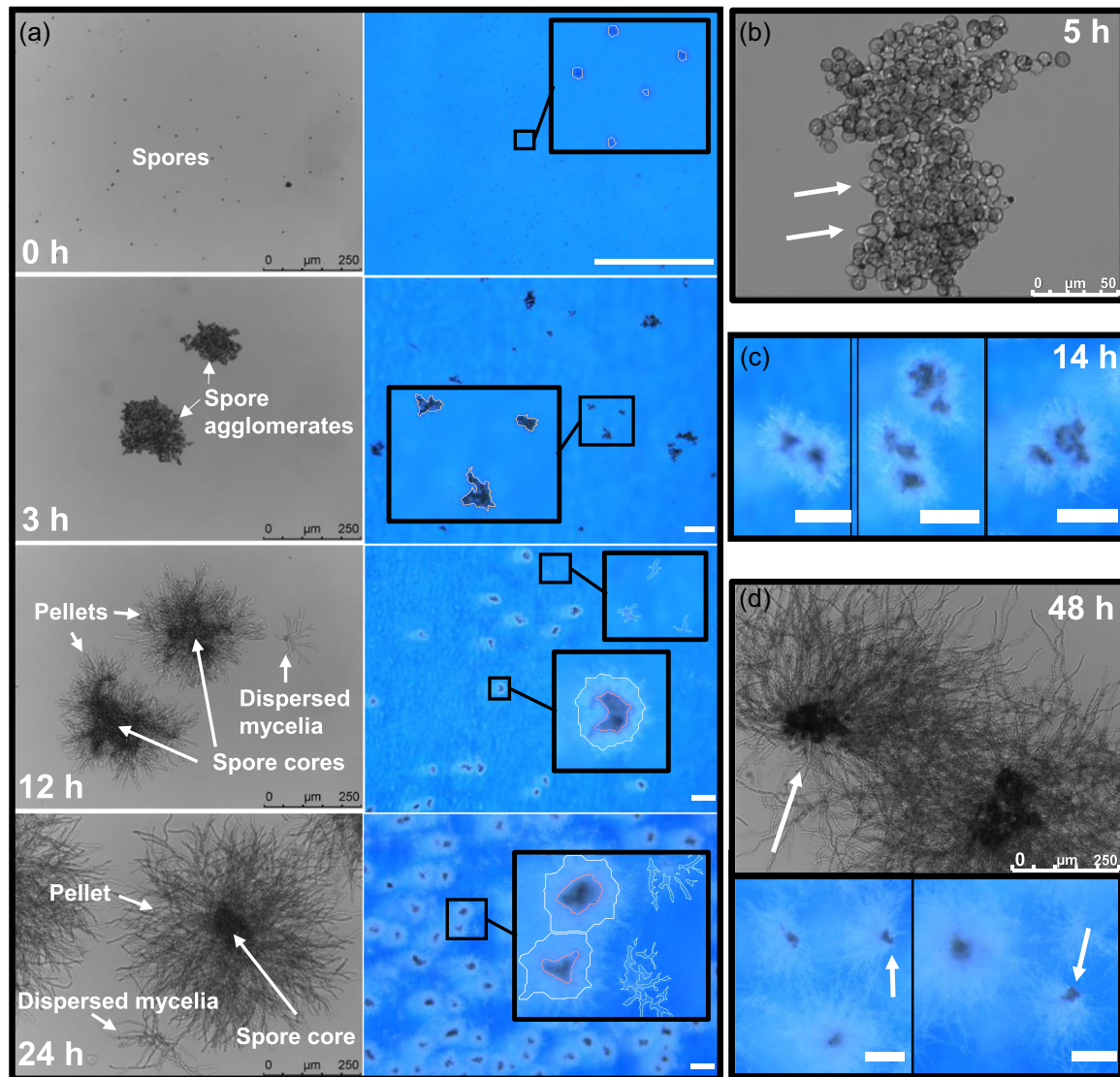


**FIGURE 2** Differential interference contrast (DIC) images (grayscale images) and stereomicroscopic images (RGB images) at different cultivation times showing important steps and observations during pellet growth. (a) DIC (left) and stereomicroscopic images (right) with marked spores, spore agglomerates, spore cores, pellets, and dispersed mycelia. The fungal objects to be recognized by the image analysis are indicated on the DIC images (left). The stereomicroscopic images (right) show the fungal objects marked by the image analysis including spores/spore agglomerates (orange) at 0 and 3 h, pellets (white), spore cores (red), and dispersed mycelia (green) at 12 and 24 h of cultivation. The scale bars on the stereomicroscopic images (right) represent a length of 500  $\mu\text{m}$ . (b) DIC image of a spore agglomerate with germinating spores (white arrows) at 5 h of cultivation. (c) Stereomicroscopic images of pellets with multiple spore cores at 14 h of cultivation; the scale bar represents a length of 250  $\mu\text{m}$ . (d) DIC and stereomicroscopic images of broken pellets (white arrows) at 48 h of cultivation; the scale bar represents a length of 250  $\mu\text{m}$ .

illustration of this threshold method can be found in Supporting Information: Figure S2.

For the second segmentation method, the blue channel (Figure 1, subimage b) of the RGB image stack (Figure 1, subimage a) was used for the global threshold method. Blue channel intensity values smaller than 255 were identified as spores and binarized into foreground objects (Figure 1, subimage c). Note that a blue cardboard was used as background for the imaging. In contrast to the black spores, the transparent hyphae of pellets had no blue channel intensity values smaller than 255.

Based on the ongoing agglomeration, the spore agglomerates increased in size. So that a sufficient number of developed spore agglomerates could still be depicted, the magnification was reduced. The change in magnification from a pixel size of 0.82–1.63  $\mu\text{m}$  was chosen to coincide with the switch of the two spore segmentation methods. Spores, spore agglomerates, and spore cores were reliably analyzed with the second spore segmentation method, even in blurred regions. Note that by further using an adaptive threshold, spore cores within pellets would not be sufficiently detected, but the adaptive threshold method showed better performance for the

detection of single spores at early sampling times. However, the initial spore concentration (sampling time 0 h) determined with the image analysis based on stereomicroscopic images differs from the original concentration by a factor of 10 ( $3.2 \times 10^5$  vs.  $2.5 \times 10^6$  spores/ml) due to a low detection efficiency of single spores in out of focus image regions. Spore agglomerates and spore cores were almost completely detected by the image analysis, which was verified by carefully checking the analyzed stereomicroscope images by visual inspection. Due to the limited spatial resolution, binarized spores and spore agglomerates smaller than an area of 9 pixels were deleted to prevent the false detection of small impurities within the medium and image noise as foreground objects.

Hyphae of pellets were segmented on the red channel image (Figure 1, subimage f). In Figure 1, subimage f, it can be seen that the hyphae have the highest gray intensity values and show a good contrast compared to the background. The general strategy to segment the hyphae is to identify the potential regions of hyphae around each spore agglomerate first and then threshold the red channel intensities within these regions to binarize hyphae into foreground objects. This procedure of calculating a region-dependent threshold enables the detection of hyphae even in blurred image regions. Further, the detection of pellets starts automatically when the red channel intensity values around spore agglomerates reach a certain level, which was adjusted to the intensity values of grown hyphae.

To generate the potential detection regions for hyphae around each spore agglomerate, we dilated the identified spore agglomerates (MATLAB function "imdilate") with a disk-shaped structured element of radius 7 pixels (Figure 1, subimage d) and subtracted the original nondilated spore agglomerate (Figure 1, subimage c), resulting in the ring-shaped binary hyphae detection region (Figure 1, subimage e). By element-wise multiplication of matrix  $E$  (Figure 1, subimage e) with the original red channel matrix  $F$  (Figure 1, subimage f), the intensity values of the red channel image for each hyphae detection region were obtained (Figure 1, subimage g). The red channel intensity values in subimage g were used to calculate a region-specific threshold  $T_r$  for each region around a spore agglomerate. The thickness of the hyphae detection region was chosen to be 7 pixels, as enough red channel intensity values should be used to calculate a representative threshold to binarize all pellets' hyphae into foreground objects. A larger thickness would hinder the detection of short hyphae of young pellets, as pixel intensity values of the background would also be included in the threshold calculation for the short hyphae. Equation (1) was used,

$$T_r = \bar{x}_r - S_r, \quad (1)$$

where  $\bar{x}_r$  is the arithmetic mean of the red channel intensity values within a hyphae detection region and  $S_r$  is the standard deviation of those intensity values, to calculate the threshold for each region around a spore agglomerate. The regions were defined by performing a watershed segmentation (F. Meyer, 1994) of the Euclidean distance-transformed (Maurer et al., 2003) matrix  $D$  (dilated spore agglomerates, Figure 1, subimage d). The threshold values calculated with Equation (1) were assigned to their matching watershed regions

(Figure 1, subimage h), which are defined by the computed watershed lines (Figure 1, subimage h). With this method, a threshold matrix with different thresholds per watershed region was generated, which was used to binarize hyphae on the red channel image into foreground objects (Figure 1, subimage i). The computation of the threshold matrix for the detection of hyphal objects starts from the first sampling times. Regions with calculated threshold values smaller than a red channel intensity value of 60 were set to infinity. Consequently, binarization of pixels into foreground pixels is not possible within those particular threshold regions. Only if the threshold value is greater or equal to 60 will the binarization of pixels into foreground pixels become possible. Although there is some unavoidable arbitrariness involved, the intensity value of 60 was chosen by carefully checking the images and histograms of the images, from which it was concluded that hyphae have significant higher red channel intensity values than 60. After the binarization, the hyphae of pellets were postprocessed.

## 2.9 | Postprocessing of pellets and detection of spore cores and dispersed mycelia

The postprocessing of the binarized hyphal foreground objects (Figure 1, subimage i) comprises a closing, filling, and image opening step. Thereby, pellet objects were obtained that need to pass a control mechanism to be ultimately recognized as a pellet. To close (MATLAB function "imclose") the fractured hyphal objects (Figure 1, subimage i), a disk-shaped structured element of a radius of 15 pixel was used. To fill the remaining holes in the closed hyphal objects, *imfill* (Matlab function) was used. Thin and elongated protruding structures were removed from the closed and filled hyphal structures by an opening (MATLAB function "imopen") operation with a disk-shaped structured element having a radius of 4 pixels. The resulting matrix was multiplied element-wise with the complement of the binarized watershed line to separate the generated pellet object candidates, grown together during the closing operation. In the last postprocessing step, pellet objects with an equivalent diameter smaller than  $25 \mu\text{m}$  were deleted. In a final control step, it was checked if a pellet object was at least connected to one spore agglomerate with an equivalent diameter of  $25 \mu\text{m}$  or higher. If not, the object was not identified as a pellet, but had the possibility to be identified as dispersed mycelia. Subimage j in Figure 1 shows the postprocessed binarized pellets. Detected spore agglomerates, which are connected to a pellet, are labeled as spore cores. Figure 1, subimage l displays the original red channel image with marked borders of spore cores (red) and pellets (white).

To identify dispersed mycelia, a vessel enhancement filter (Frangi et al., 1998) was applied to the original red channel image. Since the filter enhances elongated structures and the hyphae of dispersed mycelia are only loosely agglomerated, the vessel enhancement filter (MATLAB function "fibermetric") was capable to increase the intensity values of hyphae belonging to dispersed mycelia. The filtered image was binarized by setting a threshold, which was

calculated with Otsu's method (Otsu, 1979). The result was a binarized image with freely dispersed hyphae as foreground objects (Figure 1, subimage k). Since hyphae of the fluffy outer parts of pellets were also binarized into foreground objects, the calculated pellet objects were deleted from the binarized dispersed mycelia image. A final closing of the dispersed mycelia foreground objects with a square of edge length 3 pixels was performed to connect and smoothen fractured hypha. In Figure 1, subimage l, the binarized image with dispersed mycelia as foreground objects is overlaid in green about the red channel image.

Note that the given image (Figure 1, subimage l) is a sample after 24 h cultivation time. Thus, spores/spore agglomerates without surrounding mycelia are no longer present. Further, dispersed mycelia, spores/spore agglomerates, and pellets touching the image borders were deleted (MATLAB function "imclearborder").

## 2.10 | Data processing

The four fungal object classes comprising spores/spore agglomerates, spore cores, pellets, and dispersed mycelia were differentiated and analyzed separately on the binarized images. The number of fungal objects and the area-equivalent circular diameter of each object were computed for the class of spores/spore agglomerates, spore cores, and pellets. The area fraction was calculated for all object classes, including dispersed mycelia.

To obtain the analyzed/imaged sample volume for each sampling time, the area fraction under investigation of the Petri dish was multiplied by the original sample volume of 3 ml. The number of analyzed fungal objects on the images per Petri dish was then divided by the analyzed sample volume to obtain the concentration of spore/spore agglomerates, spore cores, and pellets.

To create the cumulative size distributions  $Q_0(d) = \int_0^d q_0(d') dd'$  of spores/spore agglomerates, spore cores, and pellets per sampling time, the values of the area-equivalent circular diameter  $d, d'$  were divided into 15 equidistant size classes between the minimal and maximal fungal object diameter.  $q_0$  is the normalized number density distribution. While  $d$  is the argument of the cumulative distribution function,  $d'$  is the integration variable. To assess the change in the distributions over the cultivation time, the same grid of the size data for all sampling times was applied. Since objects touching the image border were deleted, a bias would be introduced in the size distributions as large objects are more likely to touch the image border than smaller ones. Thereby, the proportion of large objects would be underestimated in comparison to smaller objects. To consider this bias, the correction factor

$$CF_{\text{class}} = \frac{h_{\text{image}} \times w_{\text{image}}}{(h_{\text{image}} - d_{\text{class\_mid}}) \times (w_{\text{image}} - d_{\text{class\_mid}})} \quad (2)$$

was introduced for each class, where  $h_{\text{image}}$  and  $w_{\text{image}}$  indicate the image height and width. The correction factor increases with the size of  $d_{\text{class\_mid}}$ , which is the diameter of the midpoint per class. The introduced correction factor is based on the "adjusted count"

method, which is described in Russ (2016).  $CF_{\text{class}}$  was multiplied with each class of the number density distributions  $q_0(d)$ .

In addition, box-and-whisker plots were used to describe the distributions of the equivalent diameter of spores/spore agglomerates during cultivation. The whiskers and the outliers of the box-and-whisker plots were calculated by 1.5 times the interquartile range.

The area fraction of each object class was calculated by the ratio between the sum of object areas within the class and the total area of all captured images per sampling time.

To evaluate the locations of spore cores within pellets and to observe asymmetric positions of the spore cores relating to the pellet center, we calculated the Euclidean distance between the coordinates of the centroid of a pellet and the centroid of its spore core. This calculation was performed for pellets containing only one spore core. The obtained data were used to calculate cumulative distributions of the Euclidean distances at different sampling times.

## 3 | RESULTS AND DISCUSSION

In this study, we demonstrate the potential of a newly developed image analysis pipeline (Figure 1) to investigate the morphological development of a filamentous fungal culture into pellets and dispersed mycelia and to describe population heterogeneities. Exemplarily, we present data for duplicate *A. niger* batch cultivations performed in shake flasks for 48 h. Examples of DIC and stereomicroscopic images at all sampling times for cultivation flask A are shown in Supporting Information: Figure S3. With the developed image analysis pipeline (see Figure 1 and Section 2), we were able to analyze both spore agglomeration and growth of *A. niger* pellets during submerged cultivation. At 44 sampling times, about 42,700 spores/spore agglomerates, 35,500 spore cores, and 33,000 pellets were analyzed in total for culture flask A, and 66,300, 34,000, and 31,500, respectively, for the duplicate culture flask B. The lowest numbers of analyzed objects per class and sampling time were 600 for flask A and 400 for flask B, respectively.

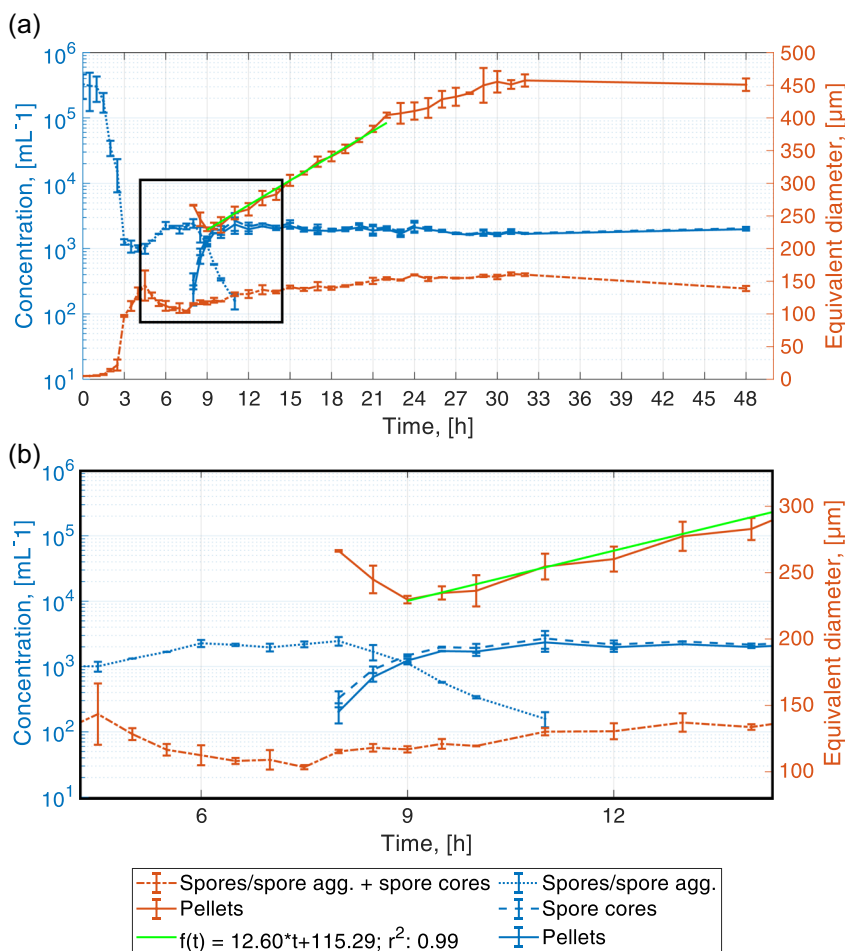
### 3.1 | Overall cultural development

Figure 3 provides an overview focusing on spore agglomeration and pellet growth with calculated mean concentrations (left ordinate) and mean equivalent diameters of the fungal objects (right ordinate) per cultivation flask over time (abscissa). Small standard deviations between both duplicates demonstrate high reproducibility of the cultivation method and the developed image analysis pipeline. As depicted in Figure 3a, spore concentration decreases starting from 1 until 4.5 h and the equivalent diameter of spores/spore agglomerates increases. This indicates that spore agglomeration already starts after 1 h, forming spore agglomerates with a mean equivalent diameter of about 140  $\mu\text{m}$  at 4.5 h. This observation agrees with the qualitative analysis of the DIC images. Selected examples of DIC and stereomicroscope images for all sampling times for flask A can be found in the Supporting Information: Figure S3. Exemplary spore agglomerates at 3 h are shown in Figure 2a. Surprisingly,

from 4.5 h on, spore/spore agglomerate concentrations increase and spore agglomerate equivalent diameters decrease, indicating breakage of spore agglomerates possibly due to the start of germination (Figure 3a). Figure 2b shows germinating spores of a spore agglomerate at 5 h. After 6 h, the concentration of spores/spore agglomerates remains almost constant until the first pellets become detected at 8 h (Figure 3b). The first pellets are detected at a sampling time of 8 h and not from the start of germination at 5 h, as a certain length of hyphae is needed to calculate a pellet specific threshold with the method described in the image analysis section (see Section 2). Consequently, the concentration of spore agglomerates decreases only from 8 h and not at earlier sampling times, which might be expected from a biological point of view. At 8 h, the difference between the mean equivalent diameter of pellets (266  $\mu\text{m}$ ) and spore agglomerates (115  $\mu\text{m}$ ) is about 150  $\mu\text{m}$  (Figure 3b), due to the thickness of the hyphal layer around the spore agglomerates needed for pellet detection. Further, pellets with large spore agglomerates are detected first in comparison to smaller pellets, resulting in an over-estimation of the mean value for the whole population. At 9 h, the growth of hyphae enables the detection of smaller pellets as well, resulting in an increased pellet concentration and a decreased mean equivalent pellet diameter of 228  $\mu\text{m}$ . At 12 h, all spore agglomerates grew into spore cores within pellets. The concentration of spore cores of pellets after 12 h is nearly similar to the spore agglomerate concentration after 6 h (Figure 3b). Therefore, we calculated the mean number of spores per

pellet with the ratio of the initial spore concentration in the medium of  $2.5 \times 10^6$  spores/ml and the concentration of pellets at 12 h (1975 pellets/ml), resulting in about 1265 spores per pellet, assuming that all spores have agglomerated and all spore agglomerates have built a pellet. Notably, the concentration of spore cores is slightly higher than the concentration of pellets (Figure 3b), as pellets can contain multiple spore cores as shown in Figure 2c. At 12 h, a pellet contains an average of about 1.1 spore cores. From 9 to 22 h, a constant growth rate of 12.6  $\mu\text{m}/\text{h}$  of the pellet mean equivalent diameter was calculated with a simple linear regression model with a coefficient of determination of 0.99 (Figure 3a).

Figure 4 shows the development of the mean glucose and biomass concentration for flasks A and B (right ordinate) and the area fraction of the fungal structures (left ordinate), which is the sum of the area fractions of nongerminated spores/spore agglomerates, pellets (including spore cores), and dispersed mycelia. The development of the area fraction of the fungal structures shows the same trend as the development of the determined biomass concentration per sampling time, except for the values at 30 and 31 h. We strongly assume measurement errors for the biomass concentrations at the sampling times of 30 and 31 h. The glucose concentration constantly decreases from 10 to 32 h and behaves as expected, inversely proportional to the area fraction of the fungal structures and the accumulated biomass. The slower increase in biomass and the area fraction between 32 and 48 h indicates the end of the exponential growth phase due to glucose limitation.



**FIGURE 3** Overview on spore agglomeration and pellet growth with calculated mean number concentrations and mean equivalent diameters of spores/spore agglomerates, spore cores, and pellets per sampling time. (a) The graphs were calculated with the data obtained by the image analysis of the stereo microscope images. The shown data of number concentrations (left ordinate) and equivalent diameters (right ordinate) are mean values, calculated with the mean of flasks A and B. Spores/spore agglomerates (spore agg.) indicate ungerminated spores and spore agglomerates. Spore cores are detected spore agglomerates within pellets. The error bars indicate the standard deviation between the mean of flasks A and B. The function  $f(t)$  was calculated by a linear regression model. The slope of 12.60  $\mu\text{m}/\text{h}$  indicates the growth velocity of the pellet equivalent diameter from 9 to 22 h. (b) Zoomed section of the rectangle in (a).

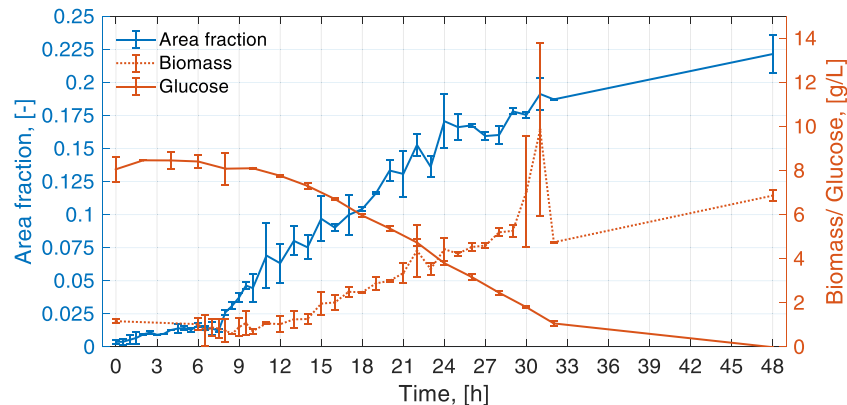


**FIGURE 4** Total area fractions of the fungal structures (left ordinate, blue) as well as biomass and glucose concentration (right ordinate, orange) for all 44 sampling times. The total area fraction of the fungal structures is the sum of the area fractions of spores, spore agglomerates, pellets (including spore cores), and dispersed mycelia. The data of the area fractions were determined by the image analysis based on stereomicroscopic images. The depicted area fractions are mean values, calculated with the total area fractions for flasks A and B. The error bars indicate the standard deviation between flasks A and B. The orange gridlines and the right ordinate show the mean biomass (dotted line) and glucose (solid line) concentration in the medium of flasks A and B per sampling time.

Figure 5 displays the area fractions of all fungal objects. The area fraction of dispersed mycelia constantly increases from 7.5 to 32 h and shows reduced growth from 32 h. Due to the loose structure of dispersed mycelia, we assume that nutrient and oxygen transfer limitation from the medium bulk phase to the hyphae is a minor factor, but that glucose limitation is the main reason for the growth limitation of dispersed mycelia. The slower increase of the area fraction of pellets starts already from 24 h. In addition, the area fraction (Figure 5) and the equivalent diameter (Figure 3a) of spore cores do not increase anymore from 24 h.

Assuming that the growth of hyphae within spore cores enlarges the spore core, growth limitations due to transfer hindrance of nutrients and oxygen through the dense hyphal pellet structure could be a reason for the stagnating area fraction of spore cores. At 24 h, a pellet mean equivalent diameter of 410  $\mu\text{m}$  can be observed (Figure 3a). Driouch et al. (2012) and Hille et al. (2009) proposed a critical diameter of 400  $\mu\text{m}$  at which oxygen transfer limitations can occur within *A. niger* pellets. Here, it must be mentioned that a critical diameter for oxygen transfer limitations depends on the hyphal density within a pellet (Schmideder et al., 2019, 2020).

The area fraction of spores and spore agglomerates slightly increases until 6 h (Figure 5). The isotropic swelling of spores results in higher area fraction values of spores and spore agglomerates, as the diameter of *Aspergillus* spores increases twofold or more before germination (Van Leeuwen et al., 2013). Further, spore agglomerates, which are built by the agglomeration between spore agglomerates, enclose hollow regions resulting in an overestimation of the area fraction of spore agglomerates.

### 3.2 | Spore agglomeration

The high amount of analyzed fungal objects per sampling time made it possible to calculate size distributions. To represent the evolution

of the distributed size of spores/spore agglomerates, spore cores, and pellets throughout cultivation, we used the cumulative size distribution  $Q_0(d)$ . Figure 6 exemplarily depicts the time evolution of  $Q_0(d)$  of spores/spore agglomerates and spore cores for flask A. The distribution evolution for flask B can be found in Supporting Information: Figure S4. The boxplots in Figure 7 summarize the distributions of all equivalent diameters of spores/spore agglomerates and spore cores per sampling time for flask A. The boxplots per sampling time for flask B can be found in the Supporting Information: Figure S5.

In Figure 6, it can be observed that the  $d_{90}$  value at 0 h of the cumulative size distribution is about 6.6  $\mu\text{m}$ , which means that 90% of all analyzed spores of flask A at 0 h (start of cultivation) have an equivalent diameter less or equal to about 6.6  $\mu\text{m}$ . This indicates that the spores are individually dispersed. Manually measured diameters of 37 single spores on the DIC images at 0 h range between 4 and 7.6  $\mu\text{m}$  with a mean of 5.3  $\mu\text{m}$  and a standard deviation of 0.6  $\mu\text{m}$ . At 2 h, the equivalent diameter of 90% of spores and spore agglomerates is shifted to less or equal to about 28  $\mu\text{m}$  ( $d_{90}$  value). Large spore agglomerates already reach a size of about 190  $\mu\text{m}$ . The shift of the distributions from a convex to a concave curvature at 3 h shows the increase of the equivalent diameter for all size classes and the rise of the spore agglomeration. The cumulative size distributions at 4.5 h indicate a  $d_{90}$  value of spore agglomerates of 253  $\mu\text{m}$ . Larger agglomerates may form by agglomeration of already formed agglomerates. The comparison of the distributions of 4.5 and 6 h suggests that such large spore agglomerates (>200  $\mu\text{m}$ ) at 4.5 h break into smaller spore agglomerates at 6 h, as growing hyphae due to the start of germination between 4.5 and 6 h lead to the mechanical separation of loose connections between spore agglomerates. At 6 h, the  $d_{90}$  value decreases to about 220  $\mu\text{m}$ . At 8 h, the first pellets and thus spore cores are detected. The cumulative size distribution (Figure 6) and the boxplot (Figure 7) at 8 h indicate that 50% of the

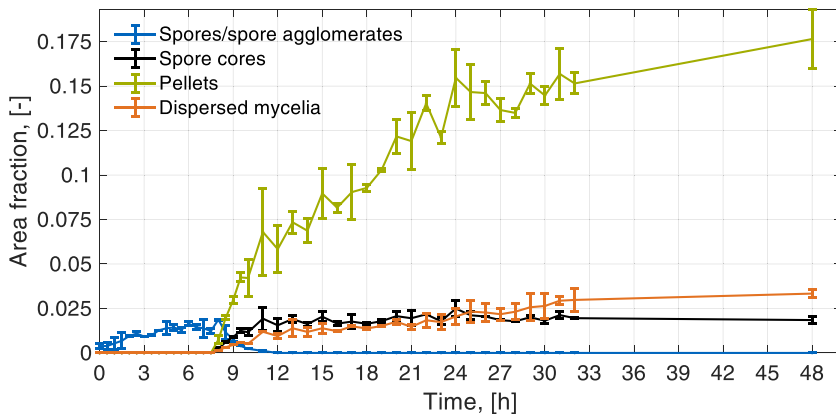


**FIGURE 5** Mean area fractions for fungal objects per sampling time. The mean area fractions are calculated with the area fractions for flasks A and B. The error bars indicate the standard deviation between flasks A and B. The data of the area fractions were determined by the image analysis based on stereomicroscopic images. Spore cores are detected spore agglomerates within pellets.

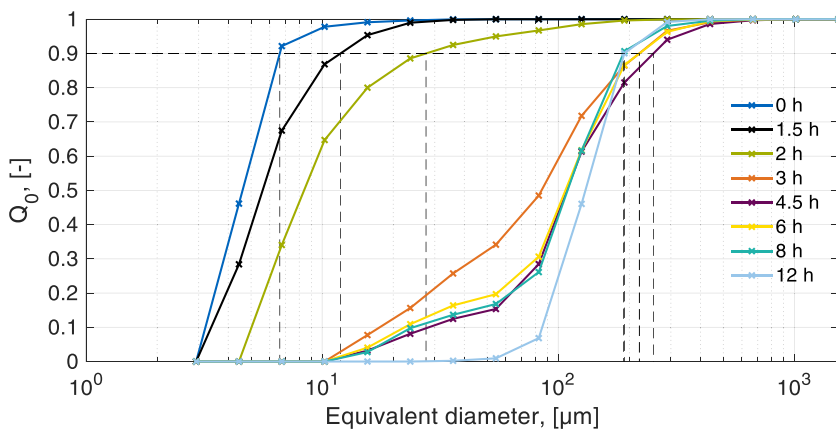


**FIGURE 6** Cumulative size distributions  $Q_0(d)$  of equivalent diameters of spores, spore agglomerates, and spore cores of flask A at different sampling times. The data were determined by the image analysis based on stereomicroscopic images. The dashed lines indicate the  $d_{90}$  values.

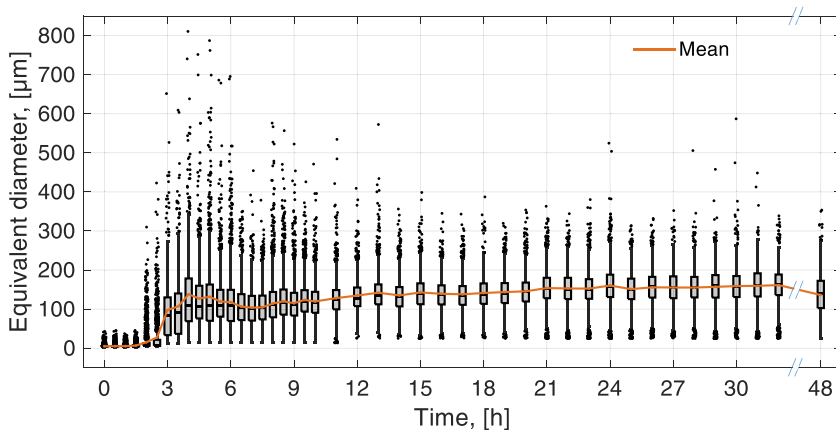


**FIGURE 7** Boxplots of equivalent diameters of spores, spore agglomerates, and spore cores per sampling time for flask A. Black lines within the boxes mark the median. The outliers are indicated by scattered black dots. The orange graph shows the mean equivalent diameter of all detected spores, spore agglomerates, and spore cores per sampling time. The data were determined by the image analysis based on stereomicroscopic images.

equivalent diameters of spore agglomerates and spore cores range between 70 and 140  $\mu\text{m}$ . The cumulative size distribution at 12 h, when no spore agglomerates without hyphae are detected anymore, shows an increase in the equivalent diameter of spore cores (Figure 6). As stated above, this observation possibly goes along with the growth of hyphae in the center of spore cores, resulting in an increased equivalent diameter of detected spore cores. The boxplots in Figure 7 furthermore indicate that the highest heterogeneity can be observed during the first 9 h after inoculation. Also, it demonstrates that the spore core equivalent diameters further increase between 12 and 24 h due to the shift of the boxes,

representing the middle 50% of the data, to larger equivalent diameters. The median and the mean increase from about 130  $\mu\text{m}$  at 12 h to 160  $\mu\text{m}$  at 24 h. From 24 to 32 h, that is, when glucose becomes limited, the increase of the spore cores stagnates and 50% of the equivalent diameters remain constant between 130 and 190  $\mu\text{m}$ . It has previously been shown that glucose limitation, and thus the onset of starvation, leads to autophagic processes in *A. niger* to recycle carbon intracellularly (Nitsche et al., 2012, 2013). Compared to 32 h, the distribution of 48 h shows a decrease in the equivalent diameters of spore cores. At 48 h, 50% of equivalent diameters range between 100 and 170  $\mu\text{m}$ . The median and the mean

decrease to about 135  $\mu\text{m}$ . Due to the decreased equivalent diameters and the increased concentration of spore cores at 48 h compared to 32 h in Figure 3a, we assume pellet breakage at the spore core. We will further discuss this hypothesis by taking the cumulative size distributions  $Q_0(d)$  of the pellet equivalent diameters into account.

### 3.3 | Pellet growth and breakage

The growth and structural development of pellets within the cultivation can be tracked with the cumulative size distributions  $Q_0(d)$  of the equivalent diameter of pellets per sampling time. Figure 8 displays the cumulative size distributions  $Q_0(d)$  of flask A. The normalized number density distributions  $q_0(d)$  of flask A at different sampling times are shown in the Supporting Information: Figure S6. In addition, the cumulative size distributions  $Q_0(d)$  and the normalized number density distributions  $q_0(d)$  of flask B can be found in the Supporting Information: Figures S7 and S8. Further, the boxplots of equivalent diameters of pellets per sampling time can be found in the Supporting Information: Figures S9 and S10. The shift of the cumulative distributions of flask A (Figure 8) and flask B (Figure S7) to larger diameters until the sampling time of 32 h indicates the growth of pellets of all size classes. From sampling times from 24 until 48 h, the cumulative size distributions of flasks A and B become wider, showing an increase in the heterogeneity of the pellet size probably due to breakage and agglomeration events of hyphal structures. This can also be seen in the normalized number density distributions  $q_0(d)$  of flasks A and B in the Supporting Information: Figures S6 and S8. By comparing the sampling times at 32 and 48 h, the size distribution of flask A at 48 h shows a larger number of pellets within the equivalent diameter range from about 200 and 390  $\mu\text{m}$  and a lower number of pellets with an equivalent diameter between 390 and 510  $\mu\text{m}$  (Figure 8 and Supporting Information: Figure S6). Supporting Information: Figures S7 and S8 show a similar observation for flask B. Figure 3a also shows a decrease in the pellet mean equivalent diameter and an increase in the pellet concentration from 32 to 48 h. Note that a pellet can break into two new pellets, which are detected by the image analysis, leading to an increased pellet number concentration. Although the mean equivalent diameter of pellets in Figure 3a stagnates from 30 h or even slightly

decreases from 32 h, the area fraction of pellets in Figure 5 further increases between 32 and 48 h. These observations lead to the hypothesis that pellets grow to a certain size until increasing shear forces act upon them. Also, inactive cells due to oxygen and glucose limitations in central parts result in weaker bonding forces between the cells and finally in pellet break up (Figure 2d). Glucose limitation and eventually starvation are explained by dramatic transcriptomic changes, as about 7000 out of the 14,000 genes of *A. niger* become differentially expressed in the postexponential growth phase compared to the exponential growth phase (Nitsche et al., 2012). Among those are genes encoding for secreted hydrolytic enzymes including chitinases, glucanases, proteases, and phospholipases that remodel (and supposedly weaken) the cell surface of *A. niger*. Pellet fragmentation leading to increased population heterogeneity can also be induced by a change of the carbon source from glucose to maltose (Tegelaar et al., 2020). This could potentially be caused by a short period of carbon limitation. Posch et al. (2012) assumed pellet breakage due to oxygen transfer limitation to the pellet core at area-equivalent circular diameters between 350 and 400  $\mu\text{m}$ . Hille et al. (2009) stated that above a critical pellet diameter of about 400  $\mu\text{m}$ , diffusion limitation in the pellet core of *A. niger* occurs. Driouch et al. (2012) verified this critical radius with the use of a green fluorescent protein producing *A. niger* strain. In Figure 8, the  $d_{50}$  value of the cumulative size distribution at 24 h of flask A shows that 50% of the analyzed pellets have equivalent diameters larger than a diameter of 400  $\mu\text{m}$ . At 32 h, the  $d_{50}$  value even increases to about 450  $\mu\text{m}$ , leading to the assumption of oxygen and nutrient limitation followed by pellet breakage at the pellet center within 48 h of cultivation.

As already mentioned, Figures 3a and 7 show a smaller mean equivalent diameter of spore cores at 48 h compared to 32 h. These observations lead to the hypothesis that pellet breakage occurs at the spore core of a pellet, which is normally located in the center of a pellet. Figure 2d shows a DIC image of a pellet, which has broken at its spore core and two exemplary stereomicroscopic images with broken pellets at 48 h of cultivation. Buffo et al. (2020) observed the breakage of pellets into large pellet fragments with sizes between 200 and 500  $\mu\text{m}$  during *A. niger* bioreactor cultivations. Pictures in their publication show these fragments breaking out of central pellet parts.

To statistically strengthen the hypothesis that breakage through the central parts of the pellets occur, we used the distance between the

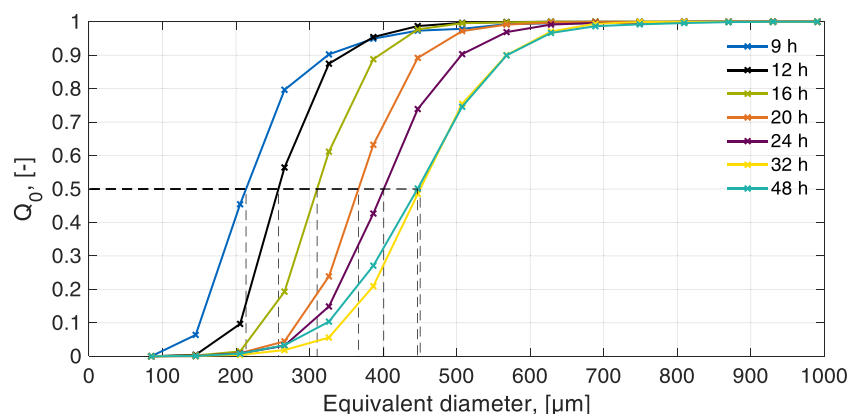


**FIGURE 8** Cumulative size distributions  $Q_0(d)$  of the equivalent diameters of pellets at different sampling times for flask A. The data were determined by the image analysis based on stereomicroscopic images. The dashed lines indicate the  $d_{50}$  values.

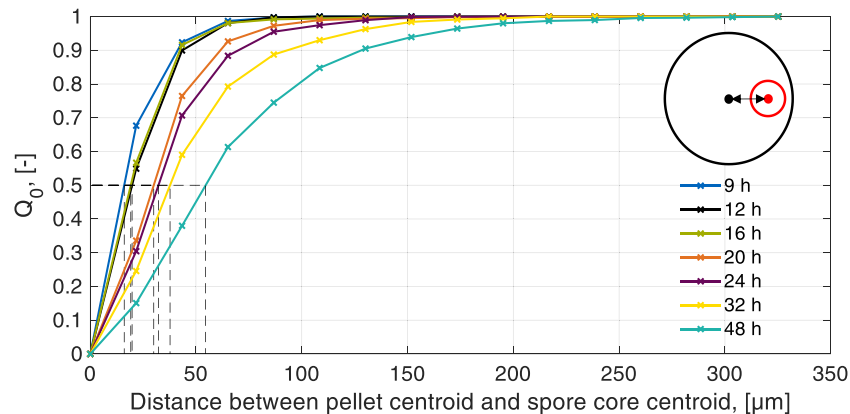


**FIGURE 9** Cumulative distribution of Euclidean distances between the centroid of the pellet and the centroid of the spore core at different sampling times for flask A. The schematic drawing in the upper right corner depicts the distance between the pellet centroid (black dot) and the spore core centroid (red dot). The data were determined by the image analysis based on stereomicroscopic images. The dashed lines indicate the  $d_{50}$  values. The distances were calculated for pellets containing one spore core.

centroid of the pellet and the centroid of the pellets' spore core as a measure of the eccentricity. Such measure is directly linked to the asymmetry of a pellet and increasing asymmetry should be expected if central breakage of pellets occurs. Figure 9 shows the cumulative distribution of the distance between the centroid of the pellet and the centroid of the pellets' spore core for all pellets per sampling time for flask A. The same graph for flask B can be found in the Supporting Information: Figure S11. Note that we calculated the distance between the centroids for pellets that contain only one spore core. However, starting from sampling time 12 h, over 91% of the pellets per sampling time of flasks A and B contained only one spore core. A "perfect" spherical pellet with a spherical spore core in the pellet center would have a distance of zero. The increase of the  $d_{50}$  values indicates an increasing asymmetry of the position of the spore cores within pellets. Reasons for this observation could be the agglomeration of dispersed mycelia and pellets, or breakage of hyphae due to shear forces and asymmetric growth of the pellet. Since almost no increase of the equivalent diameters of pellets starting from about  $390\ \mu\text{m}$  can be observed between 32 and 48 h in Figure 8 and Supporting Information: Figure S7, we assume that breakage of pellets results in the increased centroid distances between 32 and 48 h in Figure 9. Therefore, the increase of the centroid distance between 32 and 48 h provides additional evidence of pellet breakage at its spore core since the spore core is no longer in the middle of a pellet due to the breakage.

## 4 | CONCLUSION

The present study describes a new high-throughput image analysis pipeline based on stereomicroscopic images. The new method has a considerable advantage over already existing tools in that it can track both the spore agglomeration and the structural development of pellets during growth. This added value in comparison to other image analysis tools, for example, SPARTICLE by Willemse et al. (2018), is realized by detecting multiple fungal object classes at ones without additional user

input. Within a stereomicroscopic image, spores/spore agglomerates, pellets, spore cores, which are spore agglomerates within pellets, and dispersed mycelia can be segmented and analyzed. Our image analysis is computationally undemanding. Thus, the developed algorithm can analyze 30 images that only contain spores within one minute with a standard desktop PC (AMD Ryzen 7 2700 Eight-Core Processor; 3.4 GHz); 30 images that also show pellets can be calculated within 4 min. The image capturing of 30 images including the sampling could be performed within 10 min. Regarding the short image capturing and processing time, the new method can provide information and conclusions about the development during cultivation.

The proposed method can quantify the morphological evolution during the cultivation of filamentous fungal pellets. Starting from the inoculum, the spore agglomeration, transitioning to hyphal growth, and the macromorphological development of pellets as well as the amount of dispersed mycelia can be tracked. Thus, our method enables one to study the influence of cultivation conditions, including, for example, medium composition, inoculum concentration, pH, temperature, agitation, aeration, or microparticles as well as the impact of genetic modifications on the spore agglomeration but also on the pellet morphology during cultivation. Based on *A. niger* cultivations of 48 h, we demonstrated the potential of the developed image analysis. With the calculated spore and spore agglomerate size distributions of different time steps during cultivation, we could observe the breakage of large spore agglomerates ( $>200\ \mu\text{m}$ ) into smaller ones from the beginning of germination. Based on the quantification of spore cores, the size distributions of pellets, together with the area fractions, and physiological data (glucose consumption, and biomass formation), a hypothesis about pellet breakage at the spore core has been corroborated as a consequence of mass transfer limitations in the interior of pellets. A wider pellet size distribution at the end of the cultivation run, possibly caused by pellet breakage, indicated an increased cultural heterogeneity. Summarizing, the combination of high-throughput, tracking of both spore agglomeration and pellet development, as well as the automated detection of spores,

spore agglomerates, spore cores, and pellets at different sampling times within one computation run, renders the proposed image analysis a valuable tool for studying the morphological development of filamentous fungal pellets during cultivation.

## ACKNOWLEDGMENTS

The authors thank Nadine Münch and Florian Edenhofner for preliminary studies on image analysis and data processing. We also wish to thank Ali Khajehesamedini and Tiaan Friedrich for helpful and fruitful discussions. The authors thank the Deutsche Forschungsgemeinschaft for financial support for this study within the SPP 1934 DiSPBiotech—315384307 and 315305620 and SPP2170 InterZell—427889137. Open access funding was enabled and organized by Projekt DEAL.

## CONFLICTS OF INTEREST

The authors declare no conflicts of interest.

## DATA AVAILABILITY STATEMENT

The data that support the findings of this study are available from the corresponding author upon reasonable request. Data and image analysis scripts are available for readers upon request.

## ORCID

Henri Müller  <http://orcid.org/0000-0002-4831-0003>

Lars Barthel  <http://orcid.org/0000-0001-8951-5614>

Stefan Schmideder  <http://orcid.org/0000-0003-4328-9724>

Tabea Schütze  <http://orcid.org/0000-0001-7630-3794>

Vera Meyer  <http://orcid.org/0000-0002-2298-2258>

Heiko Briesen  <http://orcid.org/0000-0001-7725-5907>

## REFERENCES

- Bekker, C., de van Veluw, G. J., Vinck, A., Wiebenga, L. A., & Wösten, H. A. B. (2011). Heterogeneity of *Aspergillus niger* microcolonies in liquid shaken cultures. *Applied and Environmental Microbiology*, 77(4), 1263–1267. <https://doi.org/10.1128/AEM.02134-10>
- Bennet, J. W., & Lasure, L. L. (1991). *More gene manipulations in fungi*. Academic Press
- Böl, M., Schrinner, K., Tesche, S., & Krull, R. (2021). Challenges of influencing cellular morphology by morphology engineering techniques and mechanical induced stress on filamentous pellet systems—A critical review. *Engineering in Life Sciences*, 21(3–4), 51–67. <https://doi.org/10.1002/elsc.202000060>
- Bradley, D., & Roth, G. (2007). Adaptive thresholding using the integral image. *Journal of Graphics Tools*, 12(2), 13–21. <https://doi.org/10.1080/2151237X.2007.10129236>
- Buffo, M. M., Esperança, M. N., Farinas, C. S., & Badino, A. C. (2020). Relation between pellet fragmentation kinetics and cellulolytic enzymes production by *Aspergillus niger* in conventional bioreactor with different impellers. *Enzyme and Microbial Technology*, 139, 109587. <https://doi.org/10.1016/j.enzmictec.2020.109587>
- Cairns, T. C., Feurstein, C., Zheng, X., Zheng, P., Sun, J., & Meyer, V. (2019). A quantitative image analysis pipeline for the characterization of filamentous fungal morphologies as a tool to uncover targets for morphology engineering: A case study using apID in *Aspergillus niger*. *Biotechnology for Biofuels*, 12, 149. <https://doi.org/10.1186/s13068-019-1473-0>
- Cairns, T. C., Nai, C., & Meyer, V. (2018). How a fungus shapes biotechnology: 100 years of *Aspergillus niger* research. *Fungal Biology and Biotechnology*, 5, 13. <https://doi.org/10.1186/s40694-018-0054-5>
- Cairns, T. C., Zheng, X., Zheng, P., Sun, J., & Meyer, V. (2019). Moulding the mould: Understanding and reprogramming filamentous fungal growth and morphogenesis for next generation cell factories. *Biotechnology for Biofuels*, 12, 77. <https://doi.org/10.1186/s13068-019-1400-4>
- Commer, B., & Shaw, B. D. (2020). Current views on endocytosis in filamentous fungi. *Mycology*, 12(1), 1–9. <https://doi.org/10.1080/21501203.2020.1741471>
- Cox, P. W., Paul, G. C., & Thomas, C. R. (1998). Image analysis of the morphology of filamentous micro-organisms. *Microbiology*, 144(4), 817–827.
- Driouch, H., Haensch, R., Wucherpfennig, T., Krull, R., & Wittmann, C. (2012). Improved enzyme production by bio-pellets of *Aspergillus niger*: Targeted morphology engineering using titanate microparticles. *Biotechnology and Bioengineering*, 109(2), 462–471.
- Driouch, H., Sommer, B., & Wittmann, C. (2010). Morphology engineering of *Aspergillus niger* for improved enzyme production. *Biotechnology and Bioengineering*, 105(6), 1058–1068.
- Dynesen, J., & Nielsen, J. (2003). Surface hydrophobicity of *Aspergillus nidulans* conidiospores and its role in pellet formation. *Biotechnology Progress*, 19(3), 1049–1052. <https://doi.org/10.1021/bp0340032>
- Ehgartner, D., Herwig, C., & Fricke, J. (2017). Morphological analysis of the filamentous fungus *Penicillium chrysogenum* using flow cytometry—The fast alternative to microscopic image analysis. *Applied Microbiology and Biotechnology*, 101(20), 7675–7688.
- Fiedler, M. R. M., Barthel, L., Kubisch, C., Nai, C., & Meyer, V. (2018). Construction of an improved *Aspergillus niger* platform for enhanced glucoamylase secretion. *Microbial Cell Factories*, 17, 17.
- Fiedler, M. R. M., Cairns, T. C., Koch, O., Kubisch, C., & Meyer, V. (2018). Conditional expression of the small GTPase ArfA impacts secretion, morphology, growth, and actin ring position in *Aspergillus niger*. *Frontiers in Microbiology*, 9, 878. <https://doi.org/10.3389/fmicb.2018.00878>
- Frangi, A. F., Niessen, W. J., Vincken, K. L., & Viergever, M. A. (1998). Multiscale vessel enhancement filtering. In W. M. Wells, A. Colchester, & S. Delp (Eds.), *Lecture notes in computer science: Vol. 1496. Medical Image Computing and Computer-Assisted Intervention—MICCAI'98: First International Conference Cambridge, MA, USA, October 11–13, 1998 Proceedings* (pp. 130–137). Springer. <https://doi.org/10.1007/BFb0056195>
- Gibbs, P. A., Seviour, R. J., & Schmid, F. (2000). Growth of filamentous fungi in submerged culture: Problems and possible solutions. *Critical Reviews in Biotechnology*, 20(1), 17–48.
- Grimm, L. H., Kelly, S., Hengstler, J., Gobel, A., Krull, R., & Hempel, D. C. (2004). Kinetic studies on the aggregation of *Aspergillus niger* conidia. *Biotechnology and Bioengineering*, 87(2), 213–218.
- Hille, A., Neu, T. R., Hempel, D. C., & Horn, H. (2009). Effective diffusivities and mass fluxes in fungal biopellets. *Biotechnology and Bioengineering*, 103(6), 1202–1213.
- Kaup, J.-A., Ehrich, K., Pescheck, M., & Schrader, J. (2008). Microparticle-enhanced cultivation of filamentous microorganisms: Increased chloroperoxidase formation by *Caldariomyces fumago* as an example. *Biotechnology and Bioengineering*, 99(3), 491–498.
- Kurt, T., Marbà-Ardébol, A.-M., Turan, Z., Neubauer, P., Junne, S., & Meyer, V. (2018). Rocking *Aspergillus*: Morphology-controlled cultivation of *Aspergillus niger* in a wave-mixed bioreactor for the production of secondary metabolites. *Microbial Cell Factories*, 17(1), 128. <https://doi.org/10.1186/s12934-018-0975-y>
- Kwon, M. J., Nitsche, B. M., Arentshorst, M., Jorgensen, T. R., Ram, A. F. J., & Meyer, V. (2013). The transcriptomic signature of RacA activation and inactivation provides new insights into the morphogenetic network of *Aspergillus niger*. *PLoS One*, 8(7), 68946.

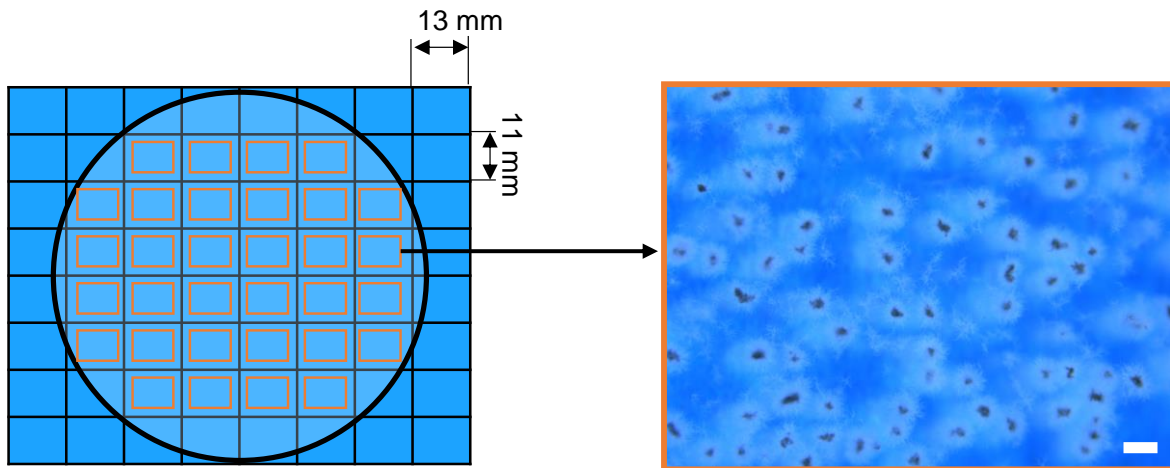
- Laible, A. R., Dinius, A., Schrader, M., Krull, R., Kwade, A., Briesen, H., & Schmideder, S. (2021). Effects and interactions of metal oxides in nanoparticle-enhanced cultivation of filamentous fungi and bacteria. *Engineering in Life Sciences*. Advance online publication. <https://doi.org/10.1002/elsc.202100075>
- Maurer, C. R., Qi, R., & Raghavan, V. (2003). A linear time algorithm for computing exact Euclidean distance transforms of binary images in arbitrary dimensions. *IEEE Transactions on Pattern Analysis and Machine Intelligence*, 25(2), 265–270. <https://doi.org/10.1109/TPAMI.2003.1177156>
- Meyer, F. (1994). Topographic distance and watershed lines. *Signal Processing*, 38(1), 113–125. [https://doi.org/10.1016/0165-1684\(94\)90060-4](https://doi.org/10.1016/0165-1684(94)90060-4)
- Meyer, V., Basenko, E. Y., Benz, J. P., Braus, G. H., Caddick, M. X., Csukai, M., de Vries, R. P., Endy, D., Frisvad, J. C., Gunde-Cimerman, N., Haarmann, T., Hadar, Y., Hansen, K., Johnson, R. I., Keller, N. P., Kraševac, N., Mortensen, U. H., Perez, R., Ram, A., ... Wösten, H. (2020). Growing a circular economy with fungal biotechnology: A white paper. *Fungal Biology and Biotechnology*, 7(1), 5. <https://doi.org/10.1186/s40694-020-00095-z>
- Meyer, V., Ram, A. F. J., & Punt, P. J. (2010). Genetics, genetic manipulation, and approaches to strain improvement of filamentous fungi. In R. H. Baltz, J. E. Davies, & A. L. Demain (Eds.), *Manual of industrial microbiology and biotechnology* (3rd ed., pp. 318–329). ASM Press. <https://doi.org/10.1128/9781555816827.ch22>
- Miyazawa, K., Yoshimi, A., & Abe, K. (2020). The mechanisms of hyphal pellet formation mediated by polysaccharides,  $\alpha$ -1,3-glucan and galactosaminogalactan, in *Aspergillus* species. *Fungal Biology and Biotechnology*, 7(1), 10. <https://doi.org/10.1186/s40694-020-00101-4>
- Nepal, K. K., & Wang, G. (2019). Streptomycetes: Surrogate hosts for the genetic manipulation of biosynthetic gene clusters and production of natural products. *Biotechnology Advances*, 37(1), 1–20. <https://doi.org/10.1016/j.biotechadv.2018.10.003>
- Nitsche, B. M., Burggraaf-van Welzen, A.-M., Lamers, G., Meyer, V., & Ram, A. F. J. (2013). Autophagy promotes survival in aging submerged cultures of the filamentous fungus *Aspergillus niger*. *Applied Microbiology and Biotechnology*, 97(18), 8205–8218. <https://doi.org/10.1007/s00253-013-4971-1>
- Nitsche, B. M., Jørgensen, T. R., Akeroyd, M., Meyer, V., & Ram, A. F. J. (2012). The carbon starvation response of *Aspergillus niger* during submerged cultivation: Insights from the transcriptome and secretome. *BMC Genomics*, 13, 380. <https://doi.org/10.1186/1471-2164-13-380>
- Otsu, N. (1979). A threshold selection method from gray-level histograms. *Systems, Man and Cybernetics, IEEE Transactions on*, 9, 62–66.
- Papagianni, M. (2004). Fungal morphology and metabolite production in submerged mycelial processes. *Biotechnology Advances*, 22(3), 189–259.
- Pascual, S., Cal, A., de Magan, N., & Melgarejo, P. (2000). Surface hydrophobicity, viability and efficacy in biological control of *Penicillium oxalicum* spores produced in aerial and submerged culture. *Journal of Applied Microbiology*, 89(5), 847–853. <https://doi.org/10.1046/j.1365-2672.2000.01189.x>
- Posch, A. E., Spadiut, O., & Herwig, C. (2012). A novel method for fast and statistically verified morphological characterization of filamentous fungi. *Fungal Genetics and Biology*, 49(7), 499–510.
- Russ, J. (2016). *The image processing handbook* (7th ed.). CRC Press. <https://doi.org/10.1201/b18983>
- Schmideder, S., Barthel, L., Müller, H., Meyer, V., & Briesen, H. (2019). From three-dimensional morphology to effective diffusivity in filamentous fungal pellets. *Biotechnology and Bioengineering*, 116(12), 3360–3371. <https://doi.org/10.1002/bit.27166>
- Schmideder, S., Müller, H., Barthel, L., Friedrich, T., Niessen, L., Meyer, V., & Briesen, H. (2020). Universal law for diffusive mass transport through mycelial networks. *Biotechnology and Bioengineering*, 118(2), 930–943. <https://doi.org/10.1002/bit.27622>
- Schrinner, K., Veiter, L., Schmideder, S., Doppler, P., Schrader, M., Münch, N., Althof, K., Kwade, A., Briesen, H., Herwig, C., & Krull, R. (2020). Morphological and physiological characterization of filamentous *Lentzea aerocolonigenes*: Comparison of biopellets by microscopy and flow cytometry. *PLoS One*, 15(6), e0234125. <https://doi.org/10.1371/journal.pone.0234125>
- Tegelaar, M., Aerts, D., Teertstra, W. R., & Wösten, H. A. B. (2020). Spatial induction of genes encoding secreted proteins in micro-colonies of *Aspergillus niger*. *Scientific Reports*, 10(1), 1536. <https://doi.org/10.1038/s41598-020-58535-0>
- Van Leeuwen, M. R., Krijgsheld, P., Bleichrodt, R., Menke, H., Stam, H., Stark, J., Wösten, H. A., & Dijksterhuis, J. (2013). Germination of conidia of *Aspergillus niger* is accompanied by major changes in RNA profiles. *Studies in Mycology*, 74(1), 59–70. <https://doi.org/10.3114/sim0009>
- Veiter, L., & Herwig, C. (2019). The filamentous fungus *Penicillium chrysogenum* analysed via flow cytometry—A fast and statistically sound insight into morphology and viability. *Applied Microbiology and Biotechnology*, 103(16), 6725–6735. <https://doi.org/10.1007/s00253-019-09943-4>
- Veiter, L., Rajamanickam, V., & Herwig, C. (2018). The filamentous fungal pellet—Relationship between morphology and productivity. *Applied Microbiology and Biotechnology*, 102(7), 2997–3006.
- Willemse, J., Büke, F., van Dissel, D., Grevink, S., Claessen, D., & van Wezel, G. P. (2018). Sparticle, an algorithm for the analysis of filamentous microorganisms in submerged cultures. *Antonie Van Leeuwenhoek*, 111(2), 171–182. <https://doi.org/10.1007/s10482-017-0939-y>
- Wucherpfeffennig, T., Hestler, T., & Krull, R. (2011). Morphology engineering—Osmolality and its effect on *Aspergillus niger* morphology and productivity. *Microbial Cell Factories*, 10, 58. <https://doi.org/10.1186/1475-2859-10-58>
- Wucherpfeffennig, T., Kiep, K. A., Driouch, H., Wittmann, C., & Krull, R. (2010). Morphology and rheology in filamentous cultivations. In A. I. Laskin, S. Sariaslani, & G. M. Gadd (Eds.), *Advances in applied microbiology* (Vol. 72, pp. 89–136). Elsevier Academic Press Inc.
- Zacchetti, B., Willemse, J., Recter, B., van Dissel, D., van Wezel, G. P., Wösten, H. A. B., & Claessen, D. (2016). Aggregation of germlings is a major contributing factor towards mycelial heterogeneity of *Streptomyces*. *Scientific Reports*, 6, 27045. <https://doi.org/10.1038/srep27045>
- Zhang, J., & Zhang, J. (2016). The filamentous fungal pellet and forces driving its formation. *Critical Reviews in Biotechnology*, 36(6), 1066–1077.

## SUPPORTING INFORMATION

Additional supporting information can be found online in the Supporting Information section at the end of this article.

**How to cite this article:** Müller, H., Barthel, L., Schmideder, S., Schütze, T., Meyer, V., & Briesen, H. (2022). From spores to fungal pellets: A new high-throughput image analysis highlights the structural development of *Aspergillus niger*. *Biotechnology and Bioengineering*, 1–14. <https://doi.org/10.1002/bit.28124>

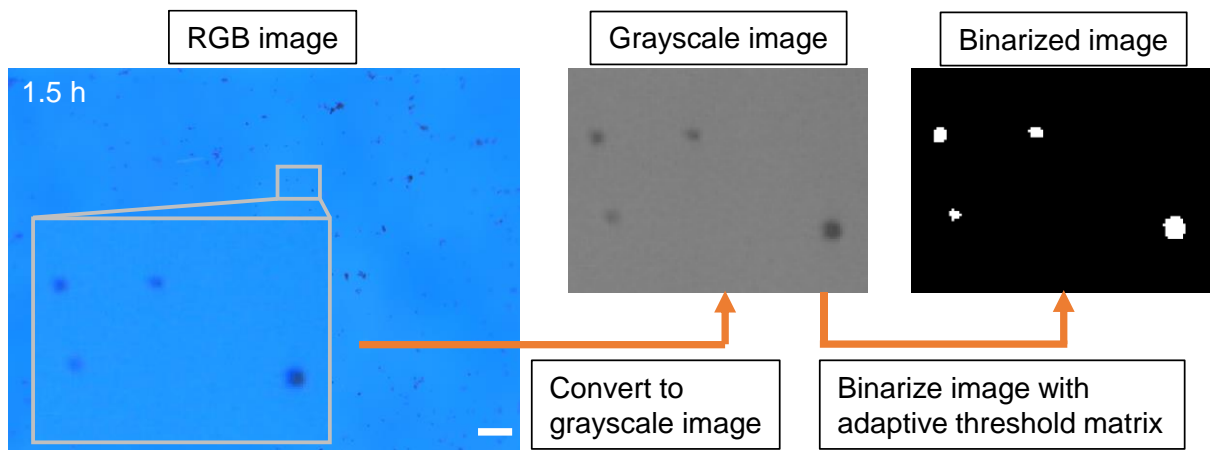
1 **Supplementary Figures**



2

3 **Figure S1: Drawing of the image capturing.**

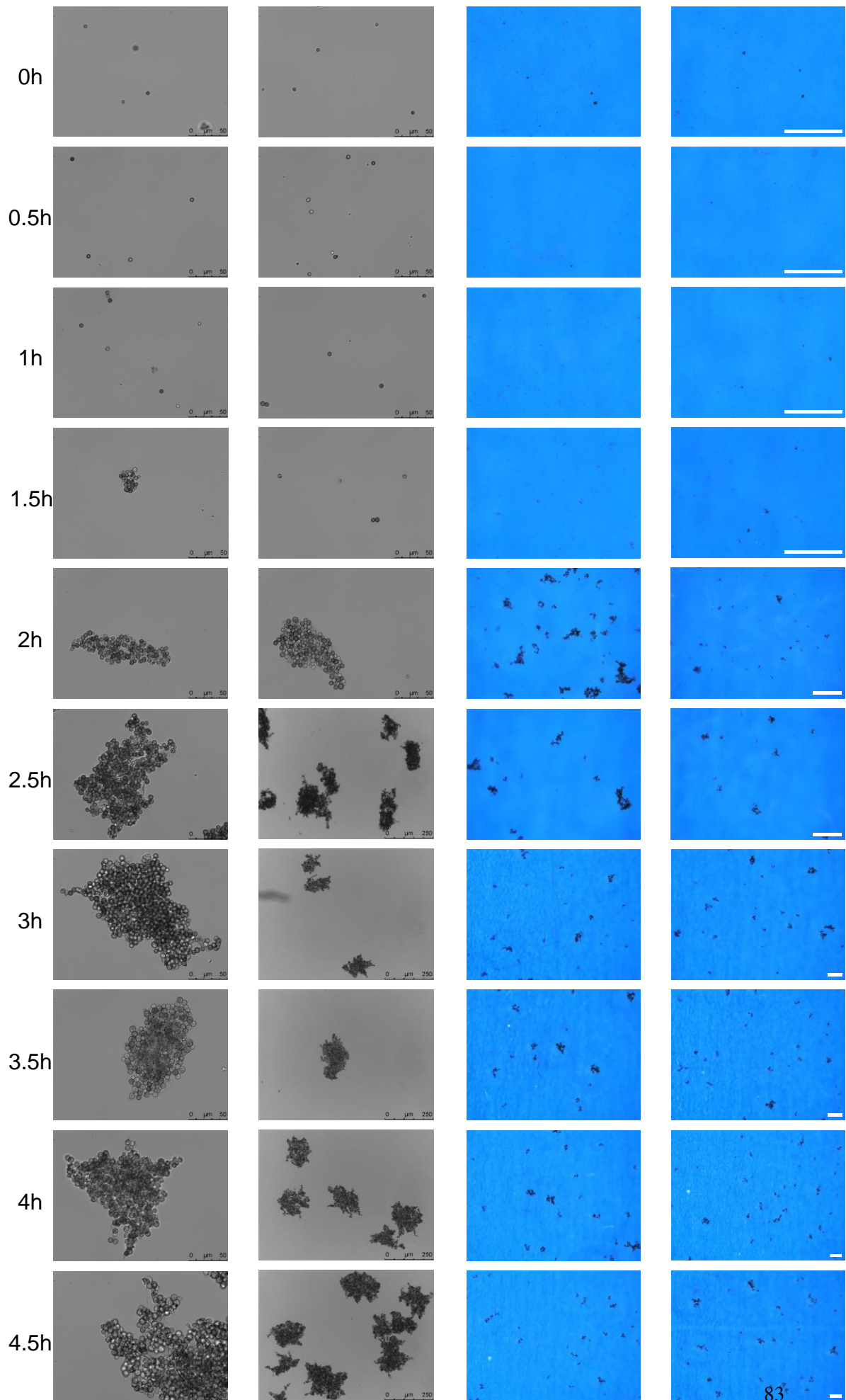
4 The Petri dish (black circle) with a culture sample was placed on a blue cardboard with a rectangular  
5 grid. One image per 13 × 11 mm rectangle was taken by sliding the blue cardboard template together  
6 with the Petri dish from rectangle to rectangle within the field of view of the stereomicroscope. The  
7 scale bar represents a length of 500 μm.

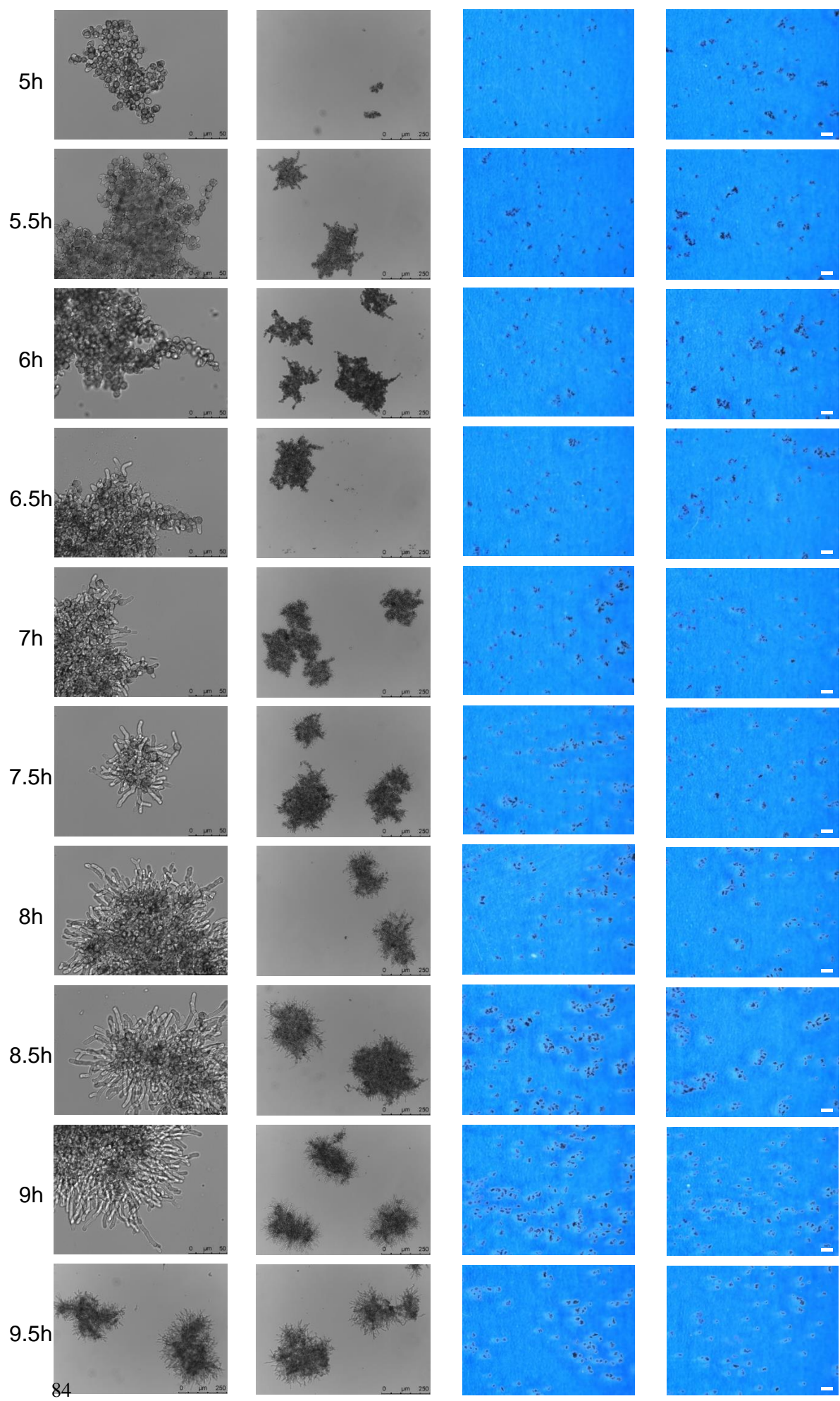


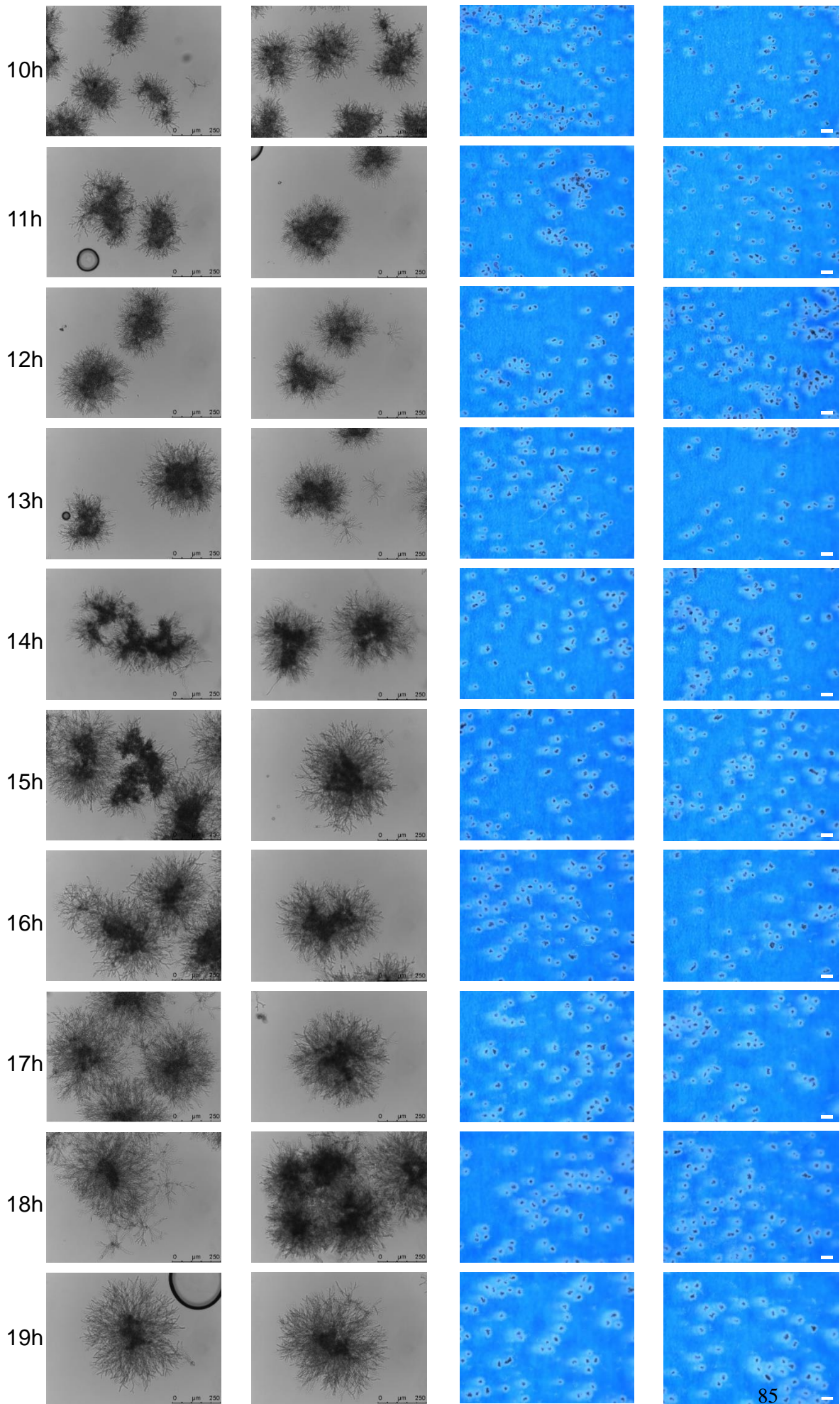
8

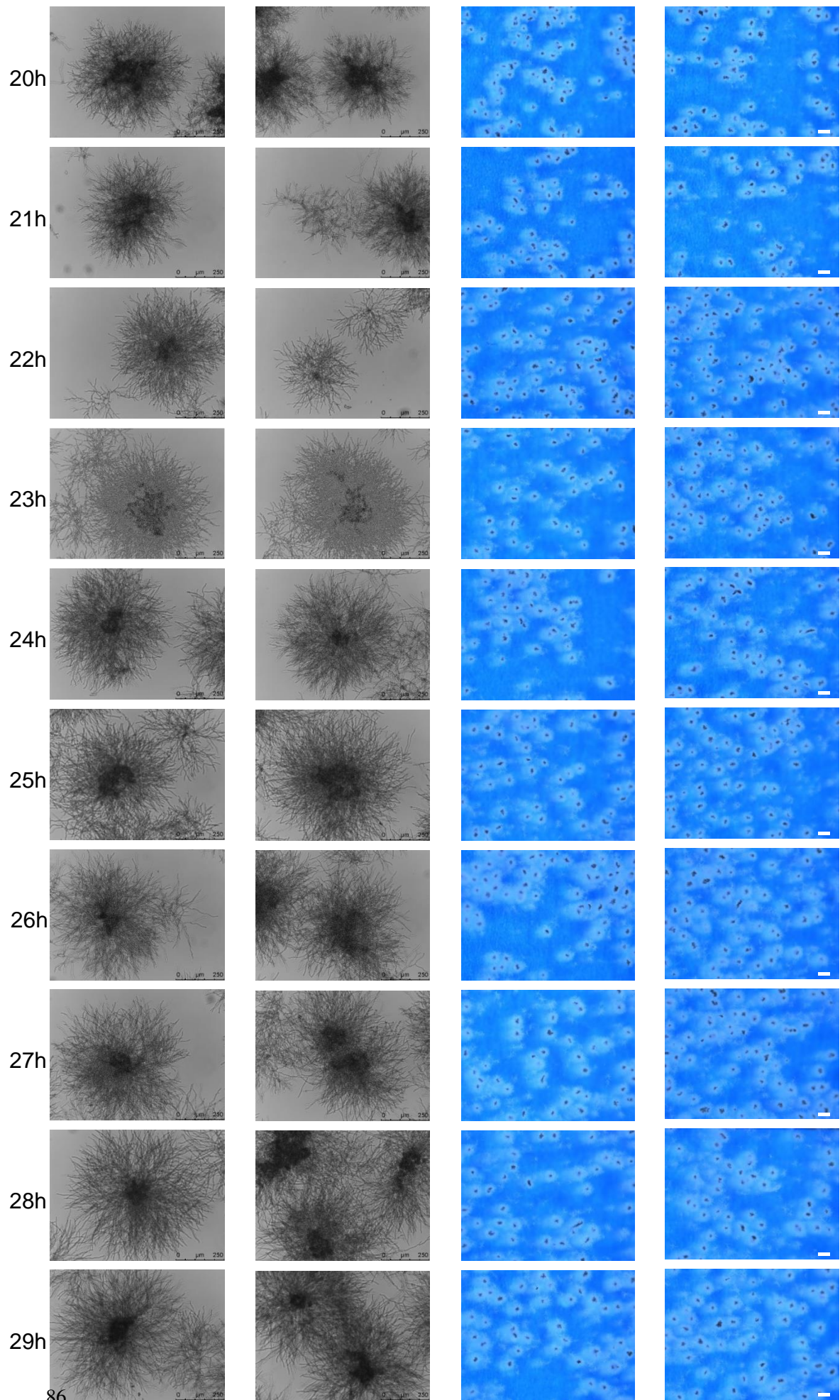
9 **Figure S2: Representation of the threshold method used for the first 3 h of cultivation to binarize**  
10 **spores and spore agglomerates on the stereomicroscopic images into foreground objects.**

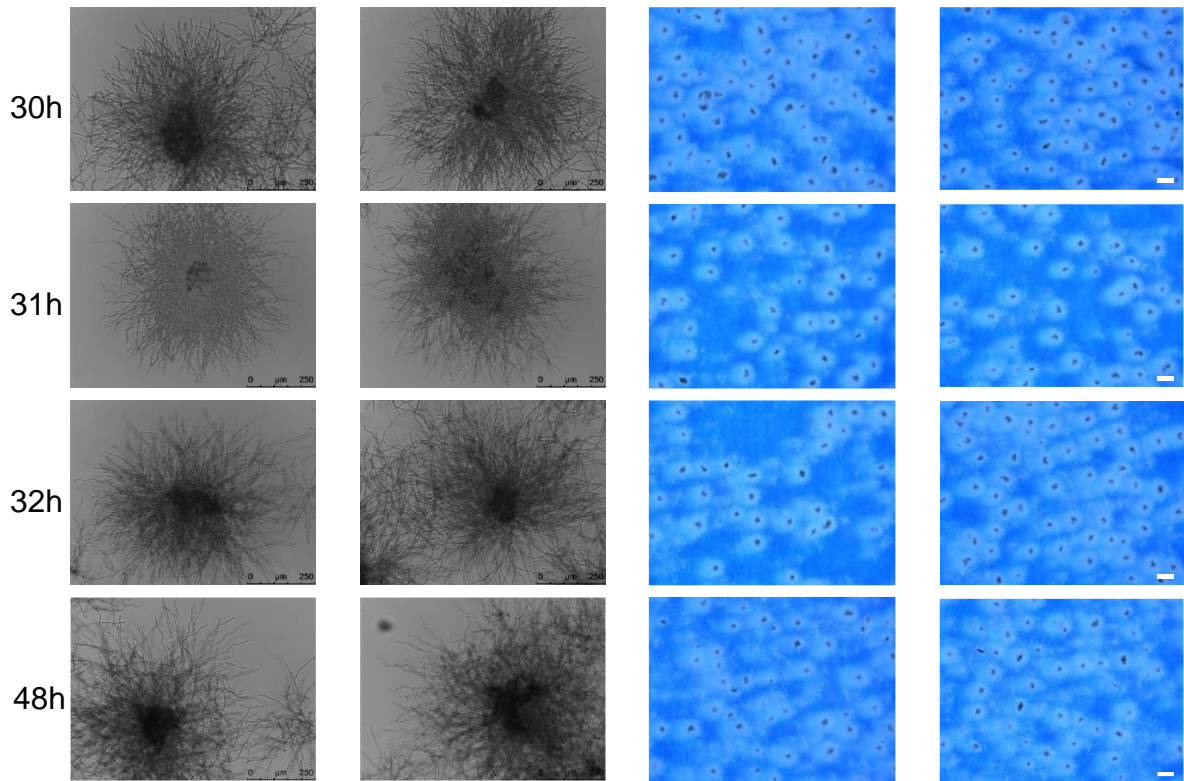
11 The stereomicroscopic RGB image shows spores/ spore agglomerates at 1.5 h of cultivation time. The  
12 scale bar on the stereomicroscopic image represents a size of 100 μm. For better visibility, a zoomed  
13 section of the RGB image is shown and the image processing is visualized on that section.







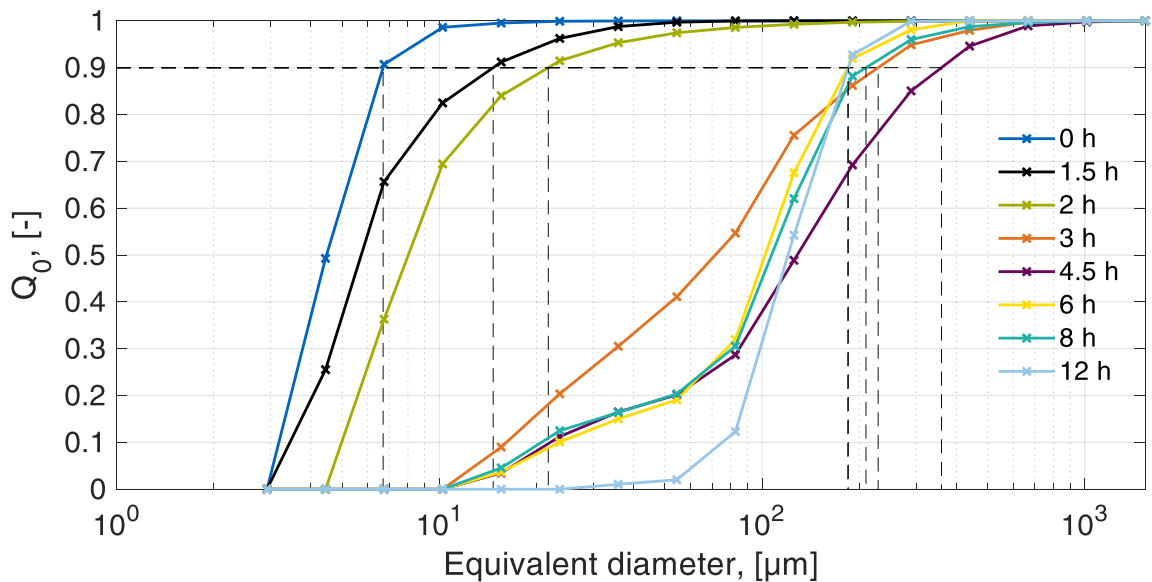




18

19 **Figure S3: Selected examples of differential interference contrast images (DIC) (left two rows)**  
 20 **and stereomicroscopic images (right two rows) at all sampling times of cultivation flask A.**

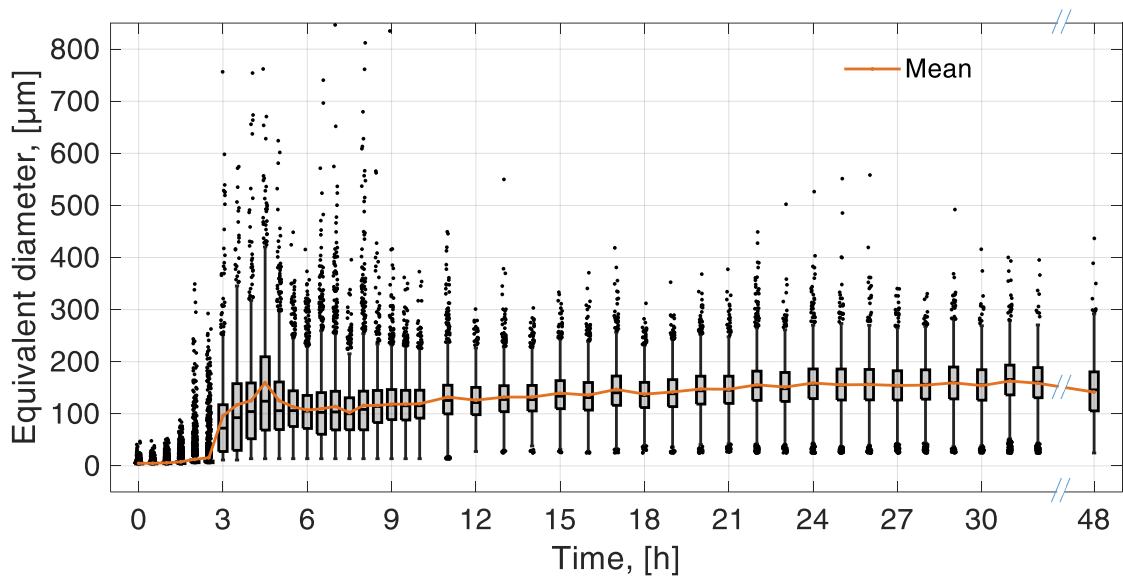
21 The scale bars on the stereomicroscopic images represent a length of 500  $\mu\text{m}$ .



22

23 **Figure S4: Cumulative size distributions  $Q_0(d)$  of equivalent diameters of spores, spore**  
 24 **agglomerates and spore cores of flask B at different sampling times.**

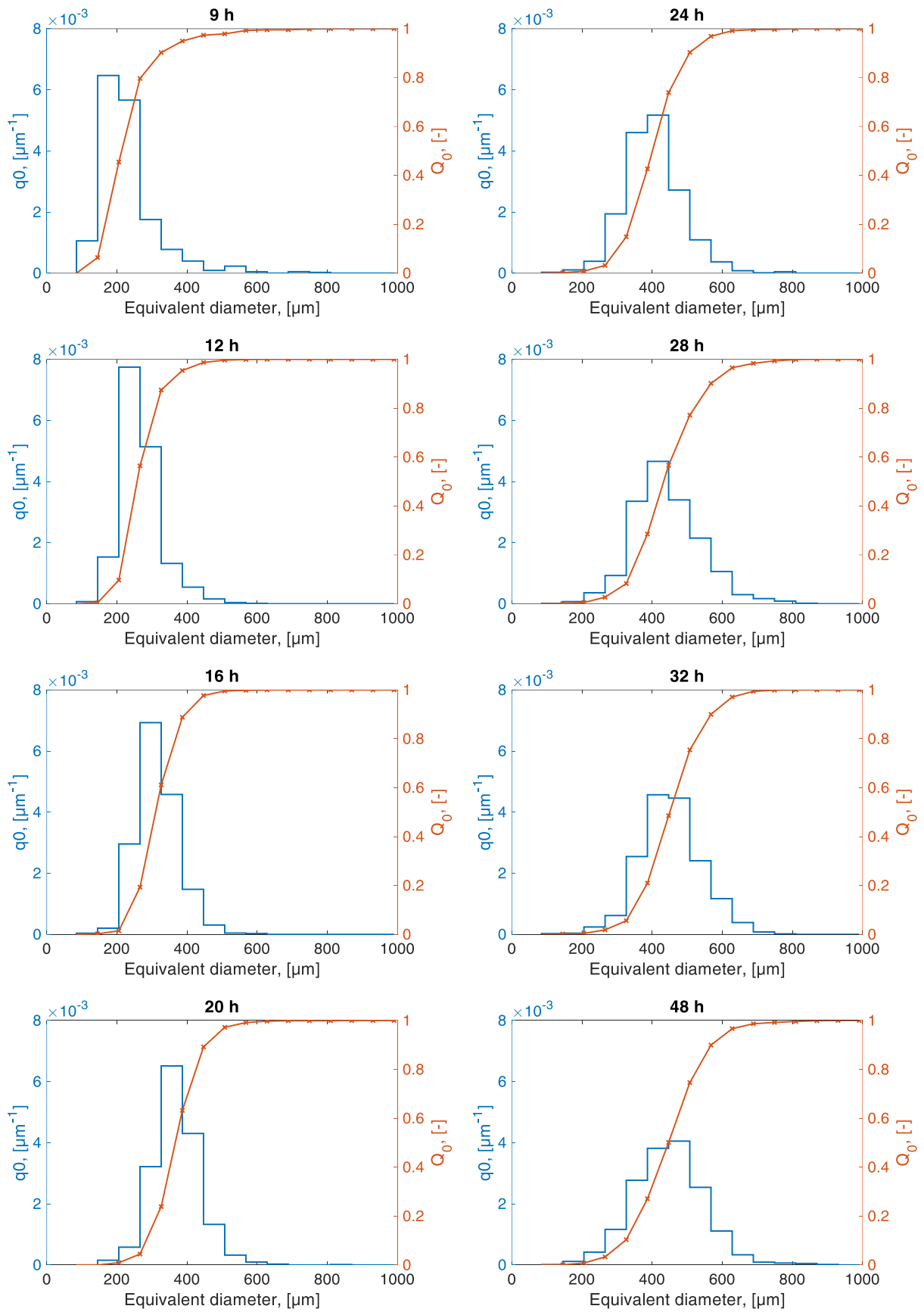
25 The data were determined by the image analysis based on stereomicroscopic images. The dashed lines  
26 indicate the  $d_{90}$  values.



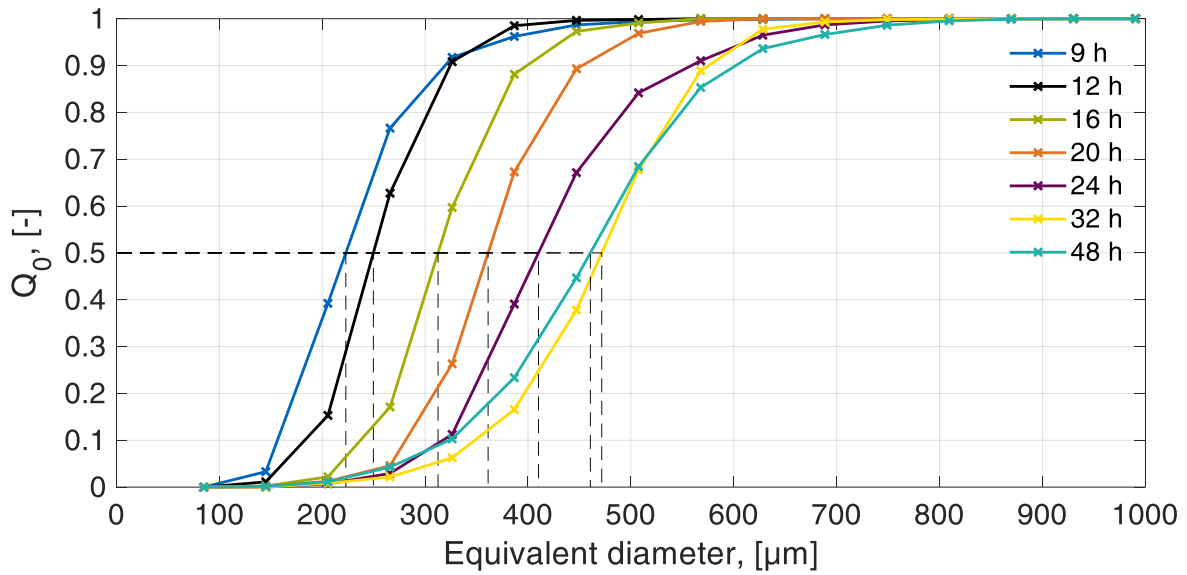
27

28 **Figure S5: Boxplots of equivalent diameters of spores, spore agglomerates, and spore cores per**  
29 **sampling time for flask B.**

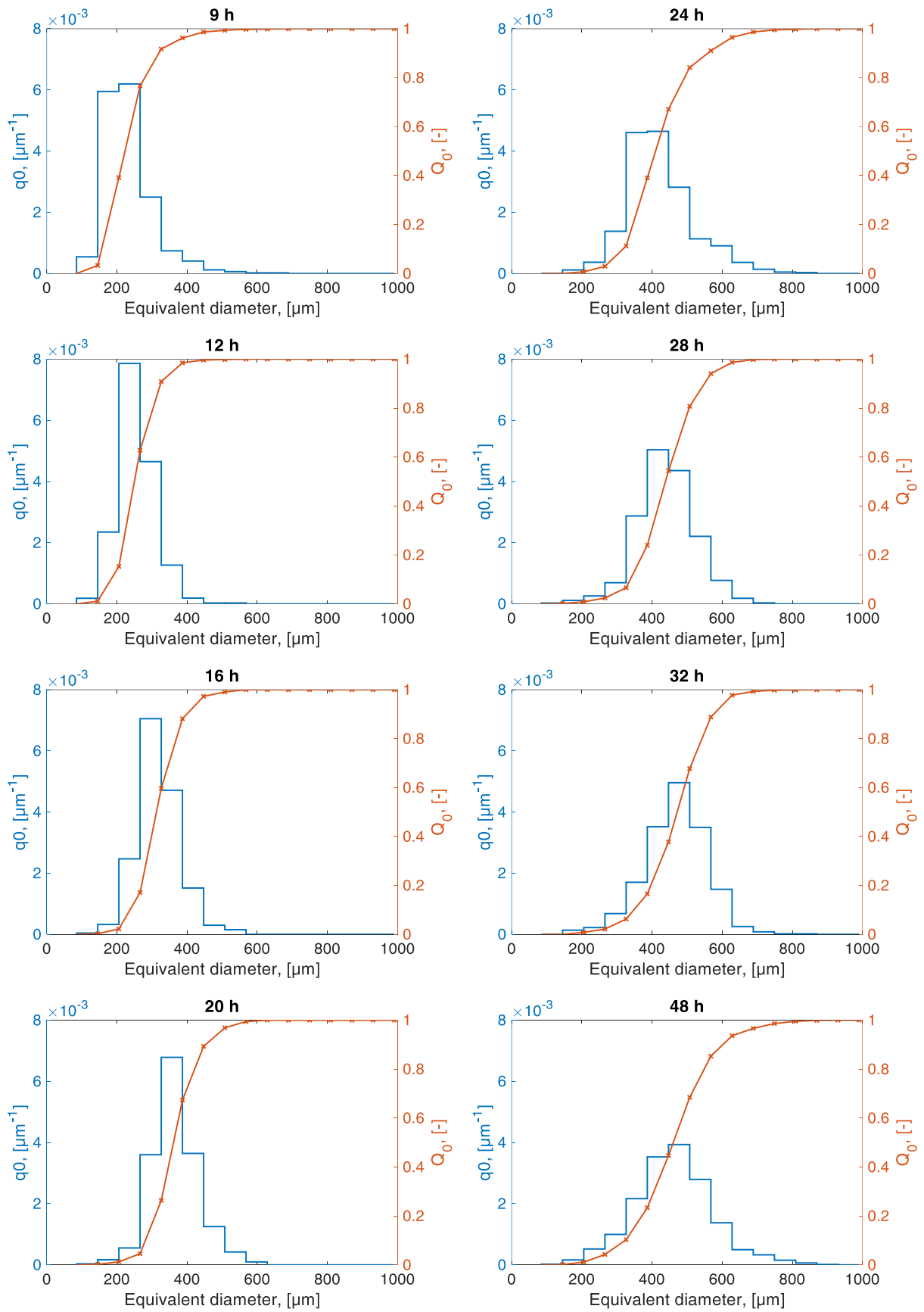
30 Black lines within the boxes mark the median. The outliers are indicated by scattered black dots. The  
31 orange graph shows the mean equivalent diameter of all detected spores, spore agglomerates, and spore  
32 cores per sampling time. The data were determined by the image analysis based on stereomicroscopic  
33 images.



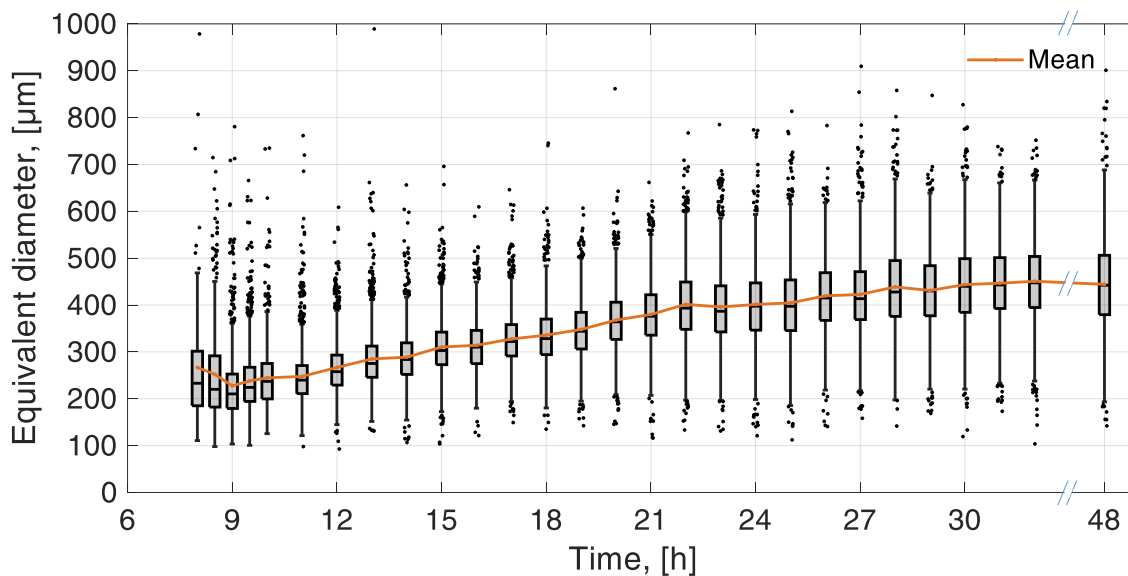
35 **Figure S6: Number-density-distribution  $q_0(d)$  of the equivalent diameters of pellets at different**  
 36 **sampling times for flask A.**  
 37 The data were determined by the image analysis based on stereomicroscopic images.



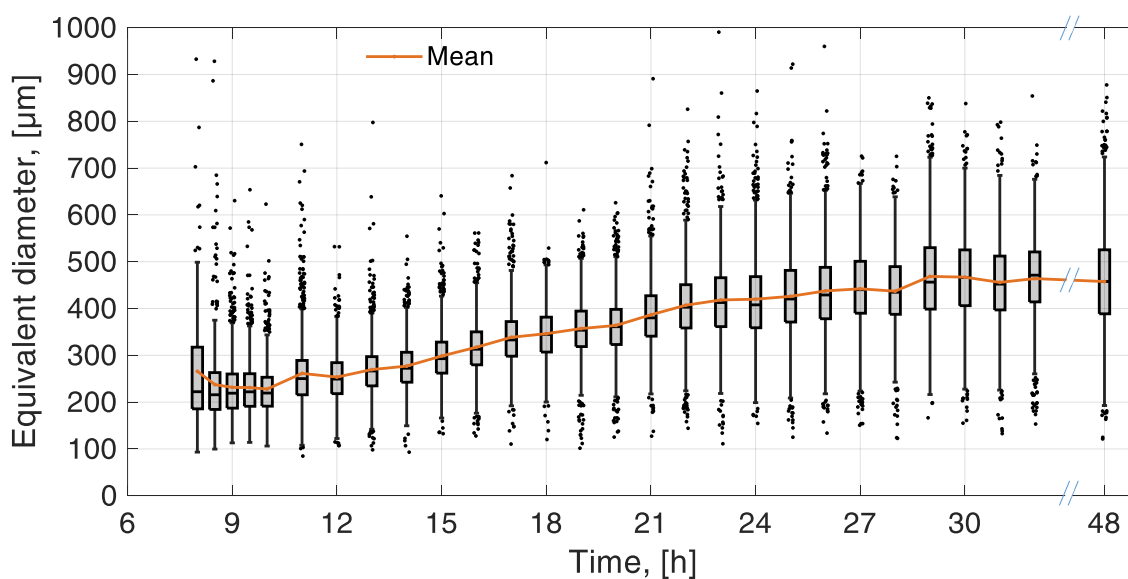
38  
 39 **Figure S7: Cumulative size distributions  $Q_0(d)$  of the equivalent diameters of pellets at different**  
 40 **sampling times for flask B.**  
 41 The data were determined by the image analysis based on stereomicroscopic images. The dashed lines  
 42 indicate the  $d_{50}$  values.



44 **Figure S8: Number-density-distribution  $q_0(d)$  of the equivalent diameters of pellets at different**  
45 **sampling times for flask B.**  
46 The data were determined by the image analysis based on stereomicroscopic images.

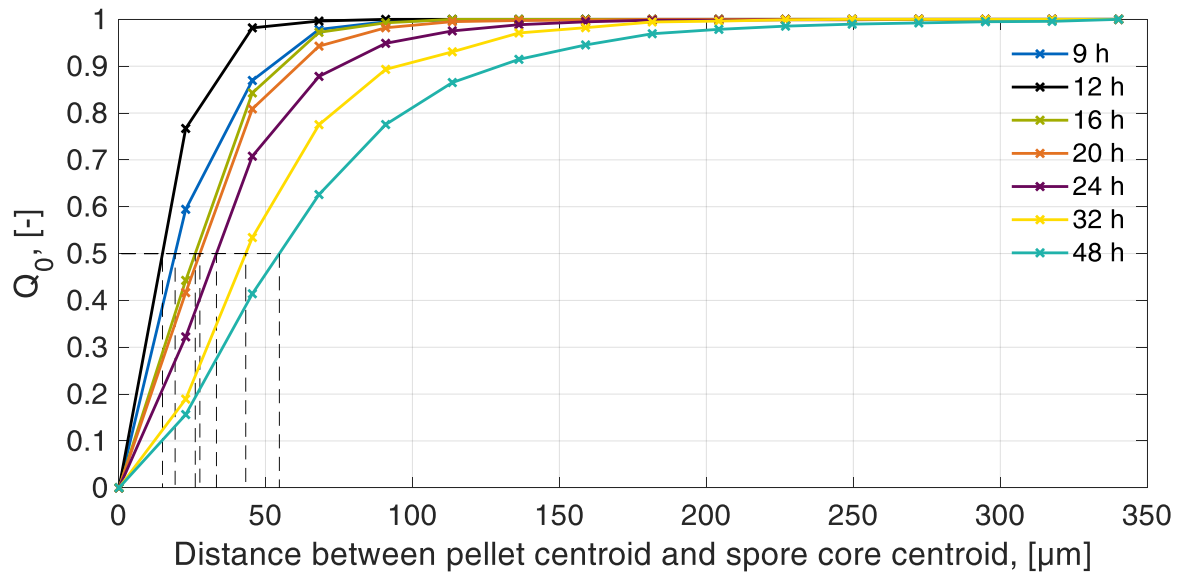


47  
48 **Figure S9: Boxplots of equivalent diameters of pellets per sampling time for flask A.**  
49 Black lines within the boxes mark the median. The outliers are indicated by scattered black dots. The  
50 orange gridline shows the mean equivalent diameter of all detected pellets per sampling time. The data  
51 were determined by the image analysis based on stereomicroscopic images.



52  
53 **Figure S10: Boxplots of equivalent diameters of pellets per sampling time for flask B**

54 Black lines within the boxes mark the median. The outliers are indicated by scattered black dots. The  
55 orange gridline shows the mean equivalent diameter of all detected pellets per sampling time. The data  
56 were determined by the image analysis based on stereomicroscopic images.



57

58 **Figure S11: Cumulative distribution of Euclidean distances between the centroid of the pellet and**  
59 **the centroid of the spore core at different sampling times for flask B.**

60 The data were determined by the image analysis based on stereomicroscopic images. The dashed lines  
61 indicate the  $d_{50}$  values. The distances were calculated for pellets containing one spore core.

1 **Supplementary Tables**

2 **Table S1: Pixel size and field of view during sampling.**

3 Based on the ongoing agglomeration, the spore agglomerates increased in size. To still depict a  
4 sufficient number of developed spore agglomerates, the magnification was reduced at certain sampling  
5 times. The table summarizes the resulting pixel size and field of view during sampling.

<b>Sample point, [h]</b>	<b>Pixel size, [<math>\mu\text{m}</math>]</b>	<b>Field of view, [mm]</b>
0 – 1.5	0.82	$1.49 \times 1.12$
2 – 2.5	1.63	$2.97 \times 2.22$
3 – 3.5	3.33	$6.07 \times 4.55$
4 – 48	4.08	$7.44 \times 5.58$

6

## **Article III**

# Synchrotron radiation-based microcomputed tomography for three-dimensional growth analysis of *Aspergillus niger* pellets

Henri Müller<sup>1</sup>  | Charlotte Deffur<sup>1</sup>  | Stefan Schmideder<sup>1</sup>  | Lars Barthel<sup>2</sup>  |  
Tiaan Friedrich<sup>1</sup>  | Lukas Mirlach<sup>1</sup>  | Jörg U. Hammel<sup>3</sup>  | Vera Meyer<sup>2</sup>  |  
Heiko Briesen<sup>1</sup> 

<sup>1</sup>School of Life Sciences Weihenstephan, Chair of Process Systems Engineering, Technical University of Munich, Freising, Germany

<sup>2</sup>Chair of Applied and Molecular Microbiology, Institute of Biotechnology, Technische Universität Berlin, Berlin, Germany

<sup>3</sup>Helmholtz-Zentrum hereon, Institute of Materials Physics, Geesthacht, Germany

## Correspondence

Heiko Briesen, Chair of Process Systems Engineering, Technical University of Munich, Gregor-Mendel-Str. 4, 85354 Freising, Germany.  
Email: [heiko.briesen@tum.de](mailto:heiko.briesen@tum.de)

## Funding information

Deutsche Forschungsgemeinschaft; Deutsches Elektronen-Synchrotron; Helmholtz Association; Projekt DEAL; SPP2170 InterZell-427889137; SPP 1934 DiSPBiotech-315384307 and 315305620

## Abstract

Filamentous fungi produce a wide range of relevant biotechnological compounds. The close relationship between fungal morphology and productivity has led to a variety of analytical methods to quantify their macromorphology. Nevertheless, only a  $\mu$ -computed tomography ( $\mu$ -CT) based method allows a detailed analysis of the 3D micromorphology of fungal pellets. However, the low sample throughput of a laboratory  $\mu$ -CT limits the tracking of the micromorphological evolution of a statistically representative number of submerged cultivated fungal pellets over time. To meet this challenge, we applied synchrotron radiation-based X-ray microtomography at the Deutsches Elektronen-Synchrotron [German Electron Synchrotron Research Center], resulting in 19,940 3D analyzed individual fungal pellets that were obtained from 26 sampling points during a 48 h *Aspergillus niger* submerged batch cultivation. For each of the pellets, we were able to determine micromorphological properties such as number and density of spores, tips, branching points, and hyphae. The computed data allowed us to monitor the growth of submerged cultivated fungal pellets in highly resolved 3D for the first time. The generated morphological database from synchrotron measurements can be used to understand, describe, and model the growth of filamentous fungal cultivations.

## KEYWORDS

3D image analysis, *Aspergillus niger*, computed tomography, filamentous fungi, morphology, pellet growth

## 1 | INTRODUCTION

Filamentous fungi are an indispensable part of industrial biotechnology. During submerged cultivation in bioreactors with a volume of several hundred cubic meters, these cell factories produce chemicals, enzymes, organic acids, antibiotics, and other drugs

(Cairns et al., 2018; Fütting et al., 2021; Meyer et al., 2020; Ward, 2012; Wösten, 2019).

The morphology of filamentous fungi is closely linked to the productivity (Cairns, Zheng, et al., 2019; Lyu et al., 2023; Tegelaar et al., 2020; Veiter et al., 2018). Their macromorphologies, which they adopt during submerged cultivation, range from non-aggregated

This is an open access article under the terms of the Creative Commons Attribution-NonCommercial License, which permits use, distribution and reproduction in any medium, provided the original work is properly cited and is not used for commercial purposes.

© 2023 The Authors. *Biotechnology and Bioengineering* published by Wiley Periodicals LLC.

hyphae called dispersed mycelia to loosely aggregated clumps of hyphae, to densely packed spherical hyphal networks called pellets (Papagianni, 2004; Veiter et al., 2018). Titer, vitality, and hydrophobicity of the spore inoculum, cultivation conditions, and the genetic background all influence the morphology that finally develops (Papagianni, 2004; Wucherpennig et al., 2010; Zhang & Zhang, 2016). The bioprocess can be positively and negatively influenced by the developed (Ehgartner et al., 2017). Dispersed mycelia grow rapidly, but cause a non-Newtonian behavior and a high viscosity of the cultivation broth, which in turn lowers the oxygen transfer rate. On the other hand, cultivations with pellets mostly show a Newtonian fluid behavior with low viscosity, but the dense hyphal structures limit nutrient and oxygen supply to inner parts of the pellet, reducing growth and growth-associated product formation (Cairns, Zheng, et al., 2019; Hille et al., 2009; Veiter et al., 2020; Wittier et al., 1986).

Since filamentous morphology is a key parameter for the effectiveness of fungal bioprocesses, a thorough understanding of the growth of the hyphal structures and the development of the morphology is crucial. Hyphal networks of fungal pellets are large and complex. Furthermore, their inner 3D structures, for example, the spatial distribution of hyphal material and tips, affect their productivity. Therefore, classical light microscopy is insufficient to study the complete and inner pellet morphology in 3D. The only method that can resolve the complete non-destructed 3D structure of a fungal pellet bases on  $\mu$ -computed tomography ( $\mu$ -CT) of freeze-dried pellets and subsequent 3D image analysis to locally detect the amount of hyphal material, tips, and branching points—the micro-morphology of a pellet (Schmideder, Barthel, Friedrich, et al., 2019). However, a small field of view and long measurement times at the required high local resolution massively reduce the sample throughput. On the contrary, high heterogeneities between fungal pellets during cultivation make it necessary to measure the morphology of a few hundred pellets in each cultivation time step to be statistically representative.

Up to now,  $\mu$ -CT measurements of hundreds of pellets for multiple cultivation times cannot be efficiently achieved with lab-scale computer tomography. We have overcome this limitation in this study by harnessing  $\mu$ -CT based on synchrotron X-ray radiation at the Deutsches Elektronen-Synchrotron-DESY (Hamburg, Germany). The high photon flux and large field of view of synchrotron radiation enables the generation of 3D images of up to 579 pellets in less than 10 min. Furthermore, we updated our previously developed image acquisition and analysis methods (Schmideder, Barthel, Friedrich, et al., 2019) by the development of a standardized sample holder, the automatic segmentation of pellets, the detection of spores within pellets—the spore core of a pellet, and the automatic analysis of micromorphological properties in a single programming language (MATLAB, version 2020b). Since 2D image analysis tools of microscopic images enable a high sample throughput and are the state of the art for following the macromorphological development of fungal pellets, for example, size and shape of filamentous fungi (Cairns, Feurstein, et al., 2019;

Müller et al., 2022; Posch et al., 2012; Willemse et al., 2018), we compared 2D data of the same *Aspergillus niger* cultivations in Müller et al. (2022) with the data generated from the synchrotron measurements.

Based on  $\mu$ -CT measurements and growth simulations, we previously presented a universal law to correlate the 3D structure and diffusive mass transport of oxygen and nutrients through hyphal networks (Schmideder, Barthel, Müller, et al., 2019; Schmideder et al., 2020). In combination with statistically representative 3D data from synchrotron measurements, it is now possible to model the growth and substrate availability during filamentous fungal cultivations. Complementing modeling, this pure 3D growth data will lead to a holistic understanding of the morphological evolution of fungal pellets.

## 2 | MATERIALS AND METHODS

### 2.1 | Cultivation, sampling, and preparation of pellets

In this study, we analyzed samples from the same cultivations of the hyperbranching *A. niger*  $\Delta$ racA strain MF22.4 (Fiedler et al., 2018; Kwon et al., 2013), which were already used for our development of a 2D high-throughput image analysis pipeline (Müller et al., 2022). Thereby, two 5 L Erlenmeyer flasks with 1 L complete medium, based on a minimal medium described in Meyer et al. (2010) supplemented with 1% (w/v) yeast extract and 0.5% (w/v) casamino acids, were inoculated with  $2.5 \cdot 10^6$  spores/mL. For a detailed description of the inoculum preparation, we refer to Müller et al. (2022). The replicated cultivations (flask A and B) were performed for 48 h at 30°C with a rotational speed of 90 RPM in an Infors HT Multitron Standard shaker (Infors AG).

For  $\mu$ -CT measurements, pellet samples were taken after 9 h, 9.5 h, and every hour from 10 h until 32 h. The last sample was taken after 48 h of cultivation, resulting in a total number of 26 sampling times. At every sampling time, 1 mL of culture volume with *A. niger* pellets was carefully pipetted into a 1.5 mL reaction tube (Sarstedt AG & Co. KG) using a 10 mL serological pipette (Sarstedt AG & Co. KG). To generate freeze dried fungal pellet samples, we followed our previously developed protocol (Schmideder, Barthel, Friedrich, et al., 2019). Thereby, the culture sample was washed three times with sterile deionized water and deep frozen in liquid nitrogen while pellets were floating in water. Subsequently, the samples were freeze dried, resulting in one reaction tube with multiple freeze dried pellets per sampling time. Within the study of Schmideder, Barthel, Friedrich, et al. (2019), we showed that freeze-drying preserves fungal morphology. For synchrotron radiation-based microcomputed tomography (SR- $\mu$ -CT) measurements, the freeze-dried fungal pellets were carefully transferred into sample holders (Figure 1a) for each sampling time. These newly developed and standardized sample holders consist of a polyether ether ketone (PEEK) base, a hollow Kapton<sup>®</sup> tube with inside diameter of 3.2 mm, and a PEEK cap.

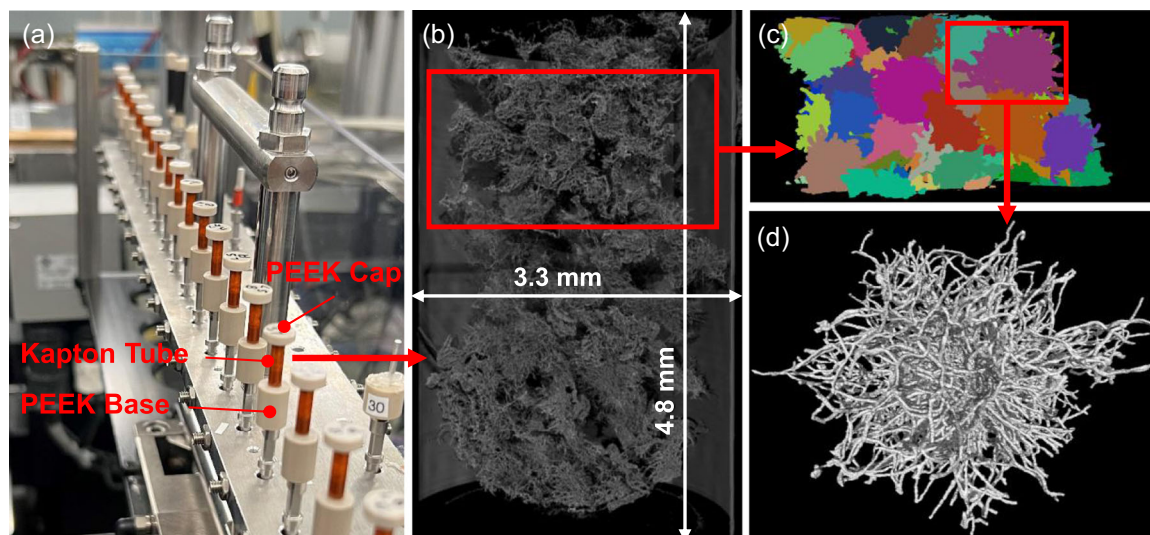


**FIGURE 1** Sample preparation, microtomography, and image processing. (a) Sample holders with freeze dried pellets from different cultivation times at the microtomography beamline P05. (b) Synchrotron radiation based X-ray microtomography with a voxel size of  $1.28 \mu\text{m}$ . (c) By the marker-controlled watershed segmentation labeled pellets. (d) Segmented and binarized pellet with an equivalent diameter of  $557 \mu\text{m}$ .

Kapton<sup>®</sup> and PEEK provide high X-ray transparency and resistance (Antimonov et al., 2015; Kurtz, 2012).

## 2.2 | Synchrotron $\mu$ -CT

SR- $\mu$ -CT of *A. niger* pellets was achieved with the Imaging Beamline P05 (Greving et al., 2014; Haibel et al., 2010; Wilde et al., 2016) operated by the Helmholtz-Zentrum hereon at the PETRA III storage ring (Deutsches Elektronen-Synchrotron–DESY). For each measurement, the sample holder containing the pellets of the corresponding sampling time was placed on a sample pin that fits in the sample rotation stage. The rotation axis of the sample holder was adjusted once to the center of the field of view and adopted for all further measurements. Imaging was performed with a photon energy of 18 keV with 30 ms exposure time per projection. For each tomographic scan, 2401 projections equally spaced between  $0^\circ$  and  $180^\circ$  were recorded using a 20 MP CMOS camera system with an effective pixel size of  $0.64 \mu\text{m}$  and a field of view of  $3.32 \times 2.46 \text{ mm}$  (Lytaev et al., 2014). The sample detector distance was set to 100 mm. We performed two scans for each sample to increase the field of view in vertical direction. The volumes were reconstructed with twofold binning based on the filtered back projection algorithm, which was implemented in a custom reconstruction pipeline (Moosmann et al., 2014) based on MATLAB (MathWorks) and the Astra Toolbox (Van Aarle et al., 2015, 2016; Palenstijn et al., 2011). The reconstructed bottom and upper volumes of a sample were stitched together with an overlap of 120 slices by a custom stitching algorithm based on MATLAB. The resulting sample volume has a size of  $2595 \times 2595 \times 3718$  voxels with a binned voxel size of  $1.28 \mu\text{m}$  (Figure 1b). The 3D images were saved as image stacks with floating point numbers resulting in a size of 93.3 GB for each image. Since we

measured 26 sampling times for each cultivation flask, we generated 4.85 TB of 3D image data for analysis.

## 2.3 | Image processing

Our developed image processing pipeline was completely established in MATLAB (Version 2020b) and can be divided into three parts: (1) The automatic segmentation into individual pellets from the total sample volume consisting of multiple pellets (Figure 1b–d). (2) The detection of spores within each pellet, which define the center of a pellet. (3) The local detection of tips, branching points, and hyphal material for each pellet.

Part (3) is based on the previously developed image analysis methods described in Schmideder, Barthel, Friedrich, et al. (2019). To unify and automate image processing, some of the code was reprogrammed into MATLAB, which is now the only platform used for the analysis. This allowed the automatic processing of 19,940 pellet objects at once. The newly developed image processing steps are described in more detail below.

### 2.3.1 | Pellet segmentation

The total sample volume with multiple pellets was divided into two equal size subvolumes along the rotation axis to reduce computational effort. The slices of a subvolume were converted to a 16-bit gray level image. The gray level image represents pellets, parts of the sample holder and air. The sample holder base was removed by determining the gray value gradient in vertical z-direction between the transition of the PEEK base and air. Slices before the gradient depicting the PEEK base were deleted. The remaining gray level

image including pellets, and the sample holder Kapton<sup>®</sup> tube was binarized by setting a gray value threshold, which was calculated with Otsu's method (Otsu, 1979). Subsequently, the binarized tube was removed based on a normalized cross-correlation (Haralick & Shapiro, 1992; Lewis, 1995). Thereby, the position and tilt of a cylindrical template that corresponded to the internal volume of the Kapton<sup>®</sup> tube was calculated. By masking the binarized subvolume with the cylindrical template, a binary image depicting only pellets as foreground objects was obtained. To label and segment the pellets into individual ones, a marker-controlled watershed segmentation (Meyer, 1994) was performed. For this method, closed pellet spheres were generated by dilating the pellets with a spherical structured element and filling remaining holes in the dilated pellets (Schmideder et al., 2020). Subsequently, a distance transformation was performed on the complemented binary image with closed pellet spheres, resulting in a distance image with the Euclidean distances of each voxel of closed pellet spheres to the closest background voxel. To calculate separate markers representing the inner part of each closed pellet sphere, voxels that had a Euclidean distance greater than 18 voxels from the background on the resulting distance image were binarized into foreground markers. For each marker, a complete pellet sphere was labeled by the watershed segmentation (Figure 1c). By masking all voxels on the original gray level subvolume with zero except a corresponding labeled pellet sphere, a gray level image was obtained representing only a single pellet. The resulting 16-bit gray level images representing only one single pellet were cropped according to pellet size (Schmideder et al., 2020). Other than the deletion of the sample holder base, the same segmentation procedure was repeated for the second subvolume. The PEEK cap was not in the field of view of the second SR- $\mu$ -CT scan.

### 2.3.2 | Detection of spores

The gray level images of single pellets were directly used for the detection of spores in the center of pellets. Spores appear as bright spherical shells with low gray values in their centers. To enhance the isolated low gray values inside of spores, bottom-hat filtering (MATLAB function "imbothat") was performed using a spherical structured element with a diameter of 5 voxels. The radius choice of the structuring element aimed to completely cover the low gray values inside of the potential spores. The gray values of the resulting bottom-hat filtered image, in which the formerly low gray values in the center of spores are now bright gray values, were scaled to the interval [0–1] and binarized with a fixed threshold of 0.3. This guaranteed that only high gray values that represented potential spore objects were binarized into the foreground. Since potential spores are only detected based on the low gray values inside of the bright spherical shells of spores, large objects with a volume of at least 30 voxels were deleted. Afterwards, clustering of the remaining spore objects was performed as another control mechanism for spore detection. Thereby, the centroid of each spore object was calculated and clustered with the dbscan algorithm (Ester et al., 1996). The

number of neighboring spore centroids was set to 10 within a search radius of 15  $\mu\text{m}$ . Since spores are densely agglomerated within pellets, the choice of cluster parameters was based on a relatively small radius and high minimum number of neighbors. Identified clusters with the highest number of spores and those with at least 100 spores were finally recognized together as spore agglomerate within the pellet—the spore core of the pellet. The yellow dots within pellets in Figure 2, middle row, mark the centroids of the detected spores. Afterwards, the mass center of the clustered spore centroids (Figure 2, bottom row, red dot) and the volume of the spore core based on the convex hull (MATLAB function "convhull") was calculated. The obtained center of mass of the spore core defined the pellet center (Figure 2, bottom row, red dot).

### 2.3.3 | Determination of local hyphal fractions, tips, and branching point densities

To differentiate between the hyphae of a pellet and the background, the cropped gray level images were binarized by setting a gray value threshold that was calculated using Otsu's method (Otsu, 1979). After binarization, connected objects smaller than 5000  $\mu\text{m}^3$  were deleted to eliminate small impurities among the hyphae. Figure 2, top row, shows segmented and binarized pellets after 16, 24, and 32 h. The local detection of tips and branching points based on the skeleton of the binarized 3D pellet image is described by Schmideder, Barthel, Friedrich, et al. (2019).

The hyphal fraction is defined as the ratio between the volume of hyphae within a representatively sized pellet section and the total volume of the pellet section (Schmideder, Barthel, Müller, et al., 2019). A similar definition applies to the number density of tips and branching points, that is, the number of tips or branching points divided by the representative total volume. To characterize the number densities of tips, branching points and the hyphal fractions of a pellet radially along its distance from the pellet center, these micromorphological features were analyzed in shells of the pellet (Figure 2, bottom row left). The width of shells was set to 15  $\mu\text{m}$  and the inner sphere had a radius of 50  $\mu\text{m}$ . The geometric center of the shells is defined by the center of mass of the spore core. Since the spore core can be embedded eccentrically in the pellet, the shells were constrained by the convex hull of the pellet. Otherwise, for example, the hyphal fractions along the distance from the pellet center would be strongly underestimated if the spore core is located at the outer edge of a pellet. To compute the constrained volume of the shell, the intersection between the convex hull and the corresponding shell was calculated (Jacobson & Panozzo, 2018) as shown in Figure 2, bottom row right. To avoid that the hyphal fraction is determined in intersections that have a very small volume, the minimum intersection volume was set to at least 10% of the corresponding total spherical shell. Finally, the hyphal fraction for each shell was calculated by the ratio between the hyphal volume within an intersection and the total volume of the intersection. The number density of tips and branching points along the distance from the pellet center was calculated accordingly.

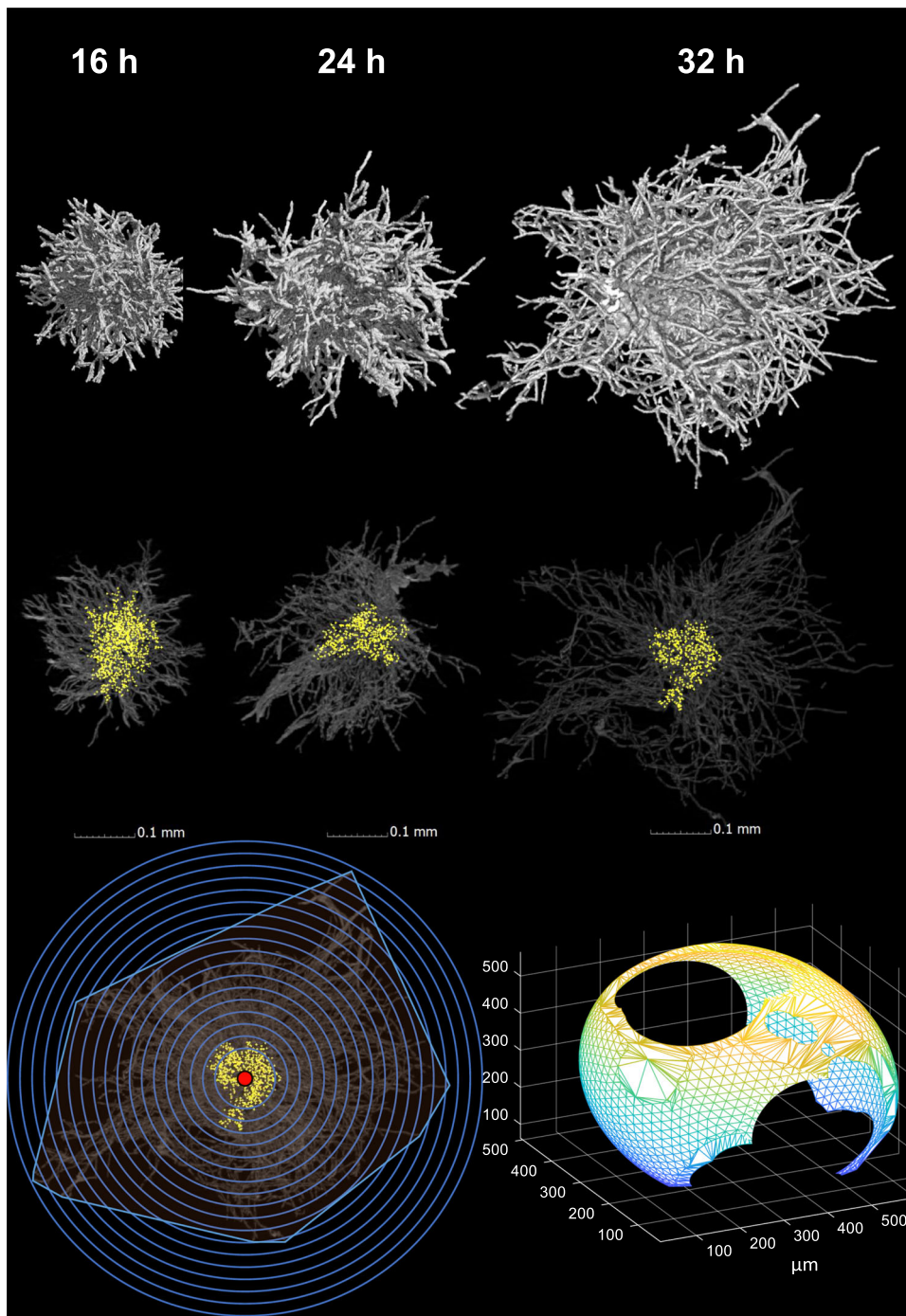


**FIGURE 2** Segmented *Aspergillus niger* pellets from different sampling times and detected spores defining the growth center of a pellet. Top row: Segmented and binarized *A. niger* pellets from 3D image processing based on SR- $\mu$ -CT after 16, 24, and 32 h of cultivation. The pellets shown were clustered as regular pellets. Middle row: Detected spore centroids (yellow dots) based on bottom-hat filtering of the 16-bit gray level pellet images. Bottom row left: Spherical shells (blue) centered on the growth center (red dot) of the pellet. The growth center is calculated as the mass center of the detected spore centroids (yellow dots). The outer spherical shells form intersections with the convex hull of the pellet (light blue). Bottom row right: Calculated 3D intersection between the convex hull and a corresponding spherical shell. The hyphal fraction, tip, and branching point densities as a function of the distance from the growth center are analyzed in the spherical shells or intersections. SR- $\mu$ -CT, synchrotron radiation-based microcomputed tomography.

### 2.3.4 | Determination of global morphology features

Global morphology features are those that are calculated based on the complete pellet structure. The volume equivalent spherical diameter of a pellet and the spore core were calculated using the volume of the convex hull of the pellet and the spore core, respectively, as  $d = \sqrt[3]{\frac{6 \cdot V_{\text{ConvHull}}}{\pi}}$ . The total number of tips, branching points, and spores for each pellet were determined by summing up the corresponding segmented objects for each pellet. Furthermore, the total volume of hyphae for each pellet  $V_{\text{Hyphae}}$  was calculated by counting all foreground voxels of the binarized pellet and multiplying it with the volume per voxel (Schmideder, Barthel, Friedrich, et al., 2019).

To calculate the average diameter of the hyphae  $d_{\text{Hyphae}}$  for each pellet, we performed an Euclidean distance transformation (MATLAB function "bwdist") (Maurer et al., 2003) of the complemented binarized pellet image. In addition, we computed the skeleton (MATLAB function "bwskel") (Kerschnitzki et al., 2013; Lee et al., 1994) of the binarized pellet image. By masking all voxels of the distance image with zero except for those representing the skeleton of the pellet, we obtained the regional radii of hyphae. Based on the regional hyphal radii, we calculated the arithmetic mean of the hyphal diameter  $d_{\text{Hyphae}}$ . Using the total volume of hyphae  $V_{\text{Hyphae}}$  and the average diameter of hyphae  $d_{\text{Hyphae}}$ , the total hyphal length  $L_{\text{Hyphae}}$  for each pellet was calculated as  $L_{\text{Hyphae}} = \frac{4 \cdot V_{\text{Hyphae}}}{\pi \cdot d_{\text{Hyphae}}^2}$ .

The average branch length of pellets, which is the average length between two branching points or a branching point and a tip, was estimated as  $\frac{L_{\text{Hyphae}}}{\text{Total number of tips} + \text{Total number of branching points}}$ . Furthermore, the hyphal growth unit (HGU) of pellets was calculated by  $\frac{L_{\text{Hyphae}}}{\text{Total number of tips}}$  as originally defined by Caldwell and Trinci (1973). A video illustrating important image processing steps can be found on YouTube. The video was created using  $\mu$ -CT scans of *Rhizopus stolonifer* pellets performed with a lab-scale  $\mu$ -CT system.

## 2.4 | Data processing

### 2.4.1 | Preprocessing of pellet data by Gaussian mixture modeling (GMM) clustering

Various artifacts can occur during sample preparation for SR- $\mu$ -CT measurements and segmentation of the pellets during image processing. Components in the medium can adhere to freeze dried pellets or be entrapped between the sampled pellets. Furthermore, pellet samples may become entangled during freeze drying and cannot be properly separated by image analysis. In addition, breakage can occur during the transfer to the sample holder. During image processing, pellets can be cropped when dividing the total sample volume into two subvolumes. Therefore, different control mechanisms were established to filter potential pellet objects into artifacts and regular pellets.

First of all, potential pellet objects with volume equivalent spherical diameters smaller than 100  $\mu\text{m}$  and larger than 1000  $\mu\text{m}$

were considered to be artifacts and were not considered for further data analysis. This can be justified by the 2D image analysis of the cultivations (Müller et al., 2022), where no pellets outside of this size range could be identified after 9–48 h of cultivation. Furthermore, pellet objects with no detected spore cores were disregarded, since they were considered impurities or dispersed mycelia. In addition to these hard cut-off parameters, a soft clustering was performed using GMM (Bishop, 2009) with two classes, artifacts and regular pellets. Therefore, three morphological features for each pellet resulting from 19,940 segmented pellet objects from flask A and B were used for model creation. The three features are visualized in a sketch in Supporting Information: Figure S1a: (1) the calculated hyphal fraction within the inner sphere with a radius of 50  $\mu\text{m}$  centered around the center of mass of the spore core. For example, entangled pellets have a lower hyphal fraction in their inner sphere (Supporting Information: Figure S1b). (2) The volume ratio between the convex hull of a pellet object and the volume of the circumscribed sphere of a pellet object centered on the center of mass of the spore core. For example, damaged and cropped pellets have an eccentricity where the spore core is not centered in the pellet, resulting in a smaller volume ratio compared to whole pellets (Supporting Information: Figure S1c,d). (3) The axis ratio of the shortest and longest major axis of a pellet object. For example, pellets cropped due to image processing obtain a smaller axis ratio (Supporting Information: Figure S1d).

Since all features had a seemingly log-normal distribution, they were logarithmized to obtain a more stable clustering result. Furthermore, the features were standardized (MATLAB function "zscore") to have a mean of zero and standard deviation of one. For the sake of stability, 10 replicates of the model were built with the one with the highest log likelihood as the final model. Finally, all pellets of the corresponding features were classified against the chosen model by calculating the largest posterior probability (Bishop, 2009).

Only potential pellet objects classified as regular pellets were used for the determination of growth parameters and 3D growth analysis.

### 2.4.2 | Determination of growth parameters

For fitting the growth parameters with the experimental 3D image data and biomass, we used the exponential growth phase of the culture, which was identified to be after 9–22 h in Müller et al. (2022).

The exponential growth of biomass ( $X$ ) and hyphal volume of pellets ( $V$ ) was formulated as  $X = X_0 \cdot e^{\mu_X \cdot t}$  and  $V = V_0 \cdot e^{\mu_V \cdot t}$ , respectively. The initial value of the biomass  $X_0$  and the hyphal volume  $V_0$  in the exponential equations were estimated as unknown variables at the same time with the growth parameters  $\mu_X$  and  $\mu_V$ . Based on a model proposed from Schuhmann and Bergter (1976), which was later used by Buschulte (1992) to describe the exponential growth in the early cultivation phase, we obtained the mean apical growth

velocity  $\alpha$  in  $\mu\text{m}$  per hour per tip and branching rate  $\beta$  in number of tips per  $\mu\text{m}$  per hour from the experimental image analysis data. Thus, we fitted  $\alpha$  and  $\beta$  by simultaneously solving the proposed ordinary differential equations  $\frac{dL}{dt} = \alpha \cdot N(t)$  and  $\frac{dN}{dt} = \beta \cdot L(t)$ . Here,  $N(t)$  is the total number of tips and  $L(t)$  is the total hyphal length of a pellet depending on time  $t$ . The MATLAB solver ODE45 was used for integration of the simple system of first order differential equations. The parameter estimation was done by minimizing the sum of square errors of  $X$ ,  $V$  separately, and  $N$  and  $L$  combined over the recorded times using the iterative trust-region method (MATLAB function "lsqnonlin"). The 95% confidence intervals (CI) were computed using a nonlinear least squares method (MATLAB function "nlparci") and the Jacobian matrix on the found solution.

### 3 | RESULTS AND DISCUSSION

In this study, we demonstrate the potential of SR- $\mu$ -CT measurements and subsequent 3D image analysis to investigate the morphological development of filamentous pellets. As a first case study, a replicated submerged cultivation (flask A and B) of *A. niger* MF22.4 was investigated in detail. This strain is characterized by the deletion of the Rho GTPase RacA, causing an approximately 30% increase in branching without altering the growth rate in submerged cultivation. Furthermore, its potential use as a platform strain for enhanced glucoamylase production was demonstrated, making it promising for industrial applications (Fiedler et al., 2018; Kwon et al., 2013). Table 1 summarizes the number of pellets for each cultivation time originating from flask A and B, which were finally clustered as regular pellets and used for 3D growth analysis. Regular pellets have a volume equivalent spherical diameter between 100 and 1000  $\mu\text{m}$  and own a spore core (Material and Methods Section 2.4.1). In addition, due to soft GMM clustering, regular pellets obtain a calculated hyphal fraction near the center of mass of the spore core (Feature 1) in the range of 0.12–0.35, a volume ratio between the convex hull and the volume of the circumscribed sphere

(Feature 2) in the range of 0.25–0.59, and an axis ratio in the range of 0.39–0.93 (Feature 3).

Since fungal parameters describing 3D pellet growth are rarely found in literature for method evaluation, the section starts with a comparison between 2D and 3D image analysis of the identical cultivation. Afterwards, global and local morphology parameters for each cultivation time will be presented. The section closes with a critical evaluation of the developed methodology.

#### 3.1 | Comparison between results of 2D and 3D image analysis and spore detection

Figure 3 shows a direct comparison of the calculated mean area/volume equivalent circular/spherical diameters of pellets and spore cores from cultivation flask A and B over time using 2D and 3D image data, respectively. The 2D data were replicated here from Müller et al. (2022).

After 9 h, the calculated 2D and 3D mean area/volume equivalent circular/spherical diameter is 230 and 195  $\mu\text{m}$ , respectively. Until 12 h, the volume-based (3D) mean equivalent diameters and their standard deviations are below the area-based (2D) data. These differences may be caused by the nonspherical shape of young pellets resembling the shape of their fractured spore cores. Based on the 3D volume data, we calculated a mean axis ratio between the minor and major axes per pellet of 0.58 after 9 h which increased to 0.64 after 13 h (Supporting Information: Figure S3). When measuring equivalent diameters of nonspherical objects with their projections, which is the case when calculating an area-based circular equivalent diameter, a difference is usually found between area- and volume-based equivalent diameters. After 32 h, a higher 3D mean equivalent diameter of 513  $\mu\text{m}$  can be observed compared to 450  $\mu\text{m}$  (2D). Here, the 2D image analysis is unable to detect individual protruding hyphae from pellets that are more common after later cultivation times, possibly due to substrate limitations. For example, denser pellets with short and highly branched hyphae are formed under higher dissolved oxygen tensions (Cui et al., 1998; Wongwicharn

**TABLE 1** Analyzed number of pellets for each flask and cultivation time.

Time (h)	9	9.5	10	11	12	13	14	15	16	17	18	19	20
Flask A	52	63	80	96	491	208	579	237	278	437	525	546	241
Flask B	64	163	128	29	202	140	206	3	387	298	464	299	383
Total	116	226	208	125	693	348	785	240	665	735	989	845	624
Time (h)	21	22	23	24	25	26	27	28	29	30	31	32	48
Flask A	420	292	265	180	208	223	96	65	151	127	128	107	77
Flask B	355	219	255	154	166	222	233	140	128	112	66	101	68
Total	775	511	520	334	374	445	329	205	279	239	194	208	145

Note: The numbers indicate the number of SR- $\mu$ -CT analyzed pellets clustered as regular pellets by the applied Gaussian mixture model. Abbreviation: SR- $\mu$ -CT, synchrotron radiation-based microcomputed tomography.

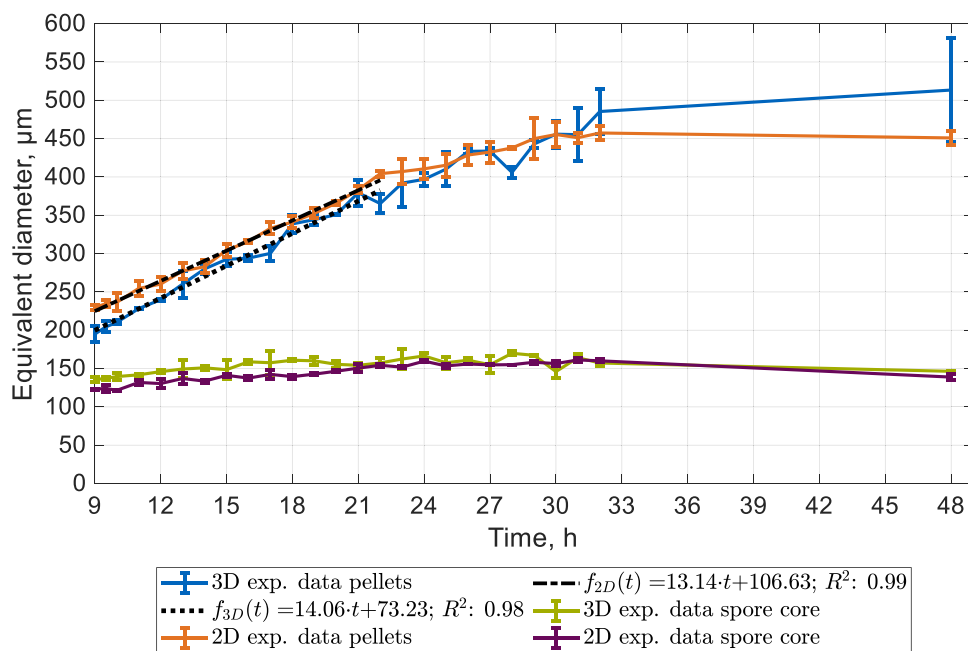


**FIGURE 3** Comparison of the calculated mean equivalent diameters of pellets and spore cores as a function of cultivation time using 2D and 3D image data. The 2D data were taken from Müller et al. (2022). The graphs for 3D data were calculated with the data obtained by the 3D image analysis of the SR- $\mu$ -CT images. The shown data of equivalent diameters are mean values, calculated with the mean of flasks A and B. Spore cores are detected spore agglomerates within pellets. The error bars indicate the standard deviation between the mean of flasks A and B. The functions  $f_{3D}(t)$  and  $f_{2D}(t)$  were calculated by linear regression models. The slope of the calculated functions ( $14.06 \mu\text{m h}^{-1}$  3D and  $13.14 \mu\text{m h}^{-1}$  2D) indicate the growth velocity of the pellet equivalent diameter after 9–22 h. SR- $\mu$ -CT, synchrotron radiation-based microcomputed tomography.

et al., 1999). Accordingly, we calculated a higher HGU and average branch length starting after 21 h (see following Section). Furthermore, the convex hull used to calculate the 3D volume-based equivalent diameter is placed around the outermost tips of a pellet resulting in a higher equivalent diameter in contrast to the 2D image analysis. The standard deviations between the means of the replicated flasks A and B are in the range of the ones from the 2D image analysis and demonstrate high reproducibility of the sampling method for 3D imaging and the developed 3D image analysis pipeline. Higher standard deviations are observed after 31, 32, and 48 h, which may be due to an insufficient number of sampled pellets for the increasing heterogeneity of the cultivation after later sampling times (Müller et al., 2022). In addition to the small deviations of the mean equivalent diameters from 2D and 3D image data, a similar constant growth velocity of  $13.14 \mu\text{m h}^{-1}$  (2D) and  $14.06 \mu\text{m h}^{-1}$  (3D) of the pellet mean equivalent diameter was calculated with a simple linear regression model (Figure 3). Please note that in Müller et al. (2022), a constant growth velocity of  $12.6 \mu\text{m h}^{-1}$  is reported, compared to the growth velocity of  $13.14 \mu\text{m h}^{-1}$  used in this contribution. The reason for this is that for the assessment of the growth velocity reported in Müller et al. (2022), only the results from flask A have been used. Revisiting our previous results, we decided to use the data from both (flask A and B) for determination of an averaged growth velocity. Figure 3 also shows the mean equivalent diameter of the identified spore cores in the pellets for each cultivation time. The same trend and

similar values of the 2D and 3D data can also be observed here. After 9 h, a 3D volume-based mean equivalent diameter of  $136 \mu\text{m}$  was calculated compared to  $123 \mu\text{m}$  based on the 2D data. After 24 h, the mean equivalent diameters increased to  $166 \mu\text{m}$  (3D) and  $159 \mu\text{m}$  (2D). In Müller et al. (2022), we assumed that growth of hyphae within spore cores enlarges the spore cores, however, the number of detected spores for each pellet also increases (Figure 4). The boxplots in Figure 4 show the number of spores for each pellet for all analyzed pellets (flasks A and B) and the mean number of spores per pellet. After 9 h, a mean number of 767 spores and after 24 h, 1233 spores per pellet could be detected. This increase suggests that non-germinated spores within spore cores still swell, since more spores can be detected by the 3D image analysis due to their enlargement. Thus, the growth of hyphae not necessarily enlarges the spore core (Müller et al., 2022), but there is an ongoing swelling of non-germinated spores within the spore core. Non-germinated spores within pellets are also reported by El-Enshasy (2011) and Lyu et al. (2023). With the exception of the early and final cultivation times, a relatively constant number of spores per pellet was identified, for example, after 12–32 h, indicating high reproducibility of spore detection. In Müller et al. (2022), approximately 1265 spores per pellet were calculated, assuming that all spores had agglomerated and all spore agglomerates had built a pellet. In this study, we were able to identify a mean of 1038 spores per pellet, calculated with 11,157 analyzed regular pellets.

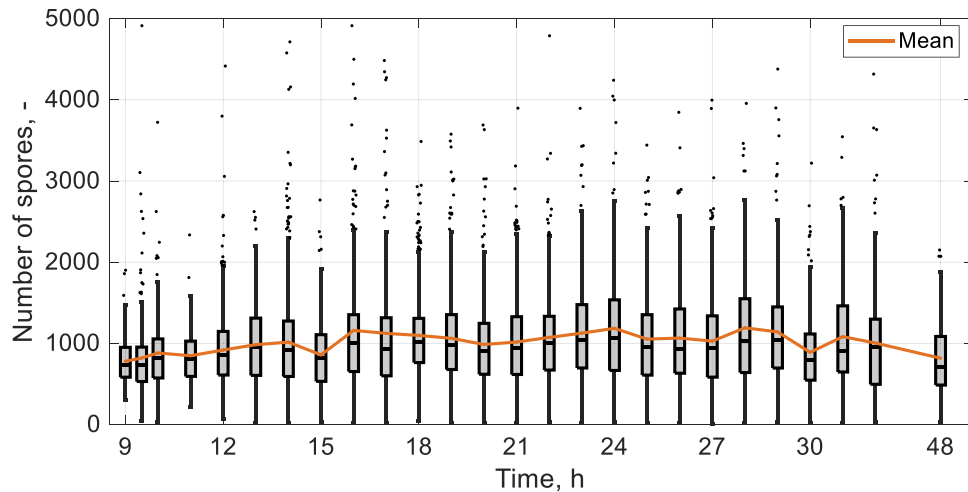
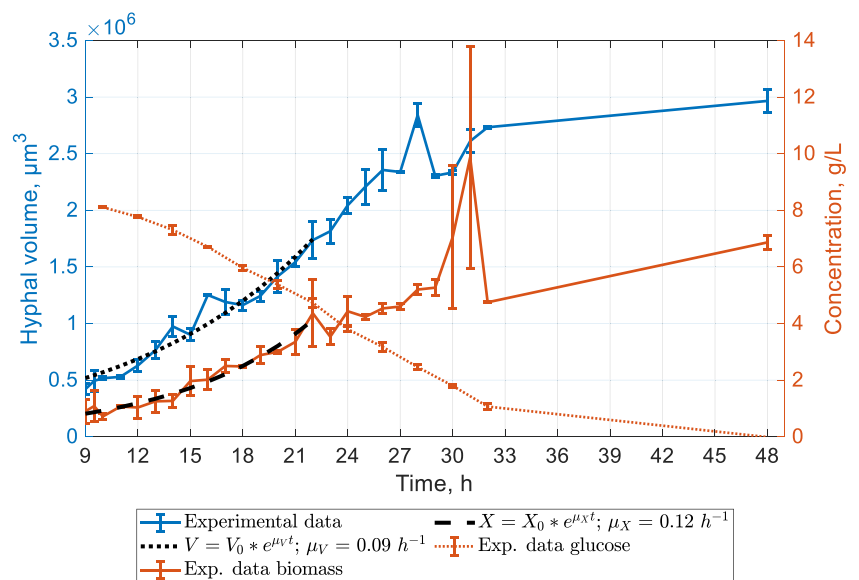


**FIGURE 4** Boxplots representing the number of spores of pellets for each cultivation time for all analyzed pellets from flasks A and B. Black lines within the boxes mark the median. The outliers are indicated by scattered black dots. The whiskers and the outliers were calculated by 1.5 times the interquartile range. The orange graph shows the mean number of spores of pellets for each cultivation time. The data were determined by the 3D image analysis based on  $\mu$ CT images.  $\mu$ CT, microcomputed tomography.

**FIGURE 5** Mean hyphal volume of pellets (left ordinate, blue) as well as biomass and glucose concentration (right ordinate, orange) as a function of cultivation time. The mean hyphal volumes of pellets were calculated with the mean hyphal volumes of flasks A and B. The error bars indicate the standard deviations between flasks A and B. The hyphal volumes were determined by 3D image analysis based on SR- $\mu$ -CT images. The orange gridlines and the right ordinate show the mean biomass (solid line) and glucose (dotted line) concentration in medium of flasks A and B. Biomass and glucose concentrations were experimentally determined and taken from Müller et al. (2022). The functions for biomass concentration  $X(t)$  and hyphal volume of pellets  $V(t)$  depending on time were used to fit the growth rate of biomass  $\mu_X$  and hyphal volume of pellets  $\mu_V$ . SR- $\mu$ -CT, synchrotron radiation-based microcomputed tomography.



After 32–48 h, a decrease of the mean equivalent diameter and the number of spores can be observed in Figures 3 and 4. The decreased mean number of spores per pellet from 974 after 32 h to 793 after 48 h supports the hypothesis in Müller et al. (2022) that pellets may break completely or partially at their spore core, supposedly because of glucose depletion in the medium (Figure 5). Parts breaking out from the spore core of pellets were reported by Buffo et al. (2020).

### 3.2 | Global morphology development of pellets

Figure 5 provides an overview of the development of the mean hyphal volume of pellets from cultivation flasks A and B (left ordinate)

over time (abscissa). Furthermore, the mean biomass and glucose concentration from flasks A and B (right ordinate) is shown over time replicated from Müller et al. (2022). In contrast to the linear increase of the equivalent diameter (Figure 3), the hyphal volume of the pellets and the biomass of the culture increases exponentially in the early growth phase when no substrate limitations occur (Wucherpfennig et al., 2010). Based on the hyphal volume data from the 3D image analysis, we calculated a growth rate of pellets  $\mu_V$  of  $0.09 \text{ h}^{-1}$  after 9–22 h within a 95% CI ranging from  $0.08 \text{ h}^{-1}$  to  $0.11 \text{ h}^{-1}$ . From the experimentally determined biomass (Müller et al., 2022), a growth rate  $\mu_X$  of  $0.12 \text{ h}^{-1}$  was calculated for the same cultivation period within a 95% CI ranging from  $0.11$  to  $0.14 \text{ h}^{-1}$ . It must be noted that the shown biomass data were determined with the dry weight of the complete culture including

dispersed mycelia (Müller et al., 2022). The hyphal volume in Figure 5 was calculated using pellets only. Therefore, we assume that the difference between the calculated growth rates is due to the growth of dispersed mycelia, which usually increases after early cultivation times with a higher growth rate compared to pellets (Kurt et al., 2018; Papagianni & Matthey, 2006; Veiter et al., 2018). After 32–48 h, a reduced increase of the biomass can be observed due to glucose limitation, which is in accordance with the analyzed hyphal volume from the 3D image analysis.

Figure 6a shows the mean total hyphal length of pellets from flasks A and B over time which increases from 35.36 to 169.12 mm after 9–32 h. Since the total hyphal length for each pellet is calculated based on the total hyphal volume and the average hyphal diameter for each pellet, it is slightly overestimated, since the spores within pellets are included in the hyphal volume for each pellet. However, the size of the spore core remains relatively constant over

cultivation time and has almost no influence on the obtained apical growth velocity of hyphal tips. Based on the proposed model of Schuhmann and Bergter (1976), we calculated an apical growth velocity  $\alpha$  per hyphal tip of  $9.3 \mu\text{m h}^{-1}$  after 9–22 h within a 95% CI ranging from 7.9 to  $10.6 \mu\text{m h}^{-1}$ . Since hyphae do not grow straight, but extend curved, we obtained a smaller increase of the mean equivalent radius per pellet (see the previous section), which is also assumed in modeling approaches of fungal pellets. For example, the change of the pellet radius is usually modeled as  $r_{\text{Pellet}}(t) = \gamma \cdot \alpha \cdot \psi_{\text{Tip}} \cdot t + r_0$ , where  $\gamma$  is a factor, taking into account that hyphae grow curved, and  $\psi_{\text{Tip}}$  is the growth activity, which describes the saturation kinetics related to the substrate supply (similar to Michaelis–Menten kinetics) (Buschulte, 1992; King, 1998). Using the increase of the mean equivalent radius, which was calculated to be  $14.06 \mu\text{m h}^{-1} \cdot 0.5$ , we calculated  $\gamma$  as the ratio between the equivalent radius and the apical growth velocity, which is 0.76. Buschulte (1992)

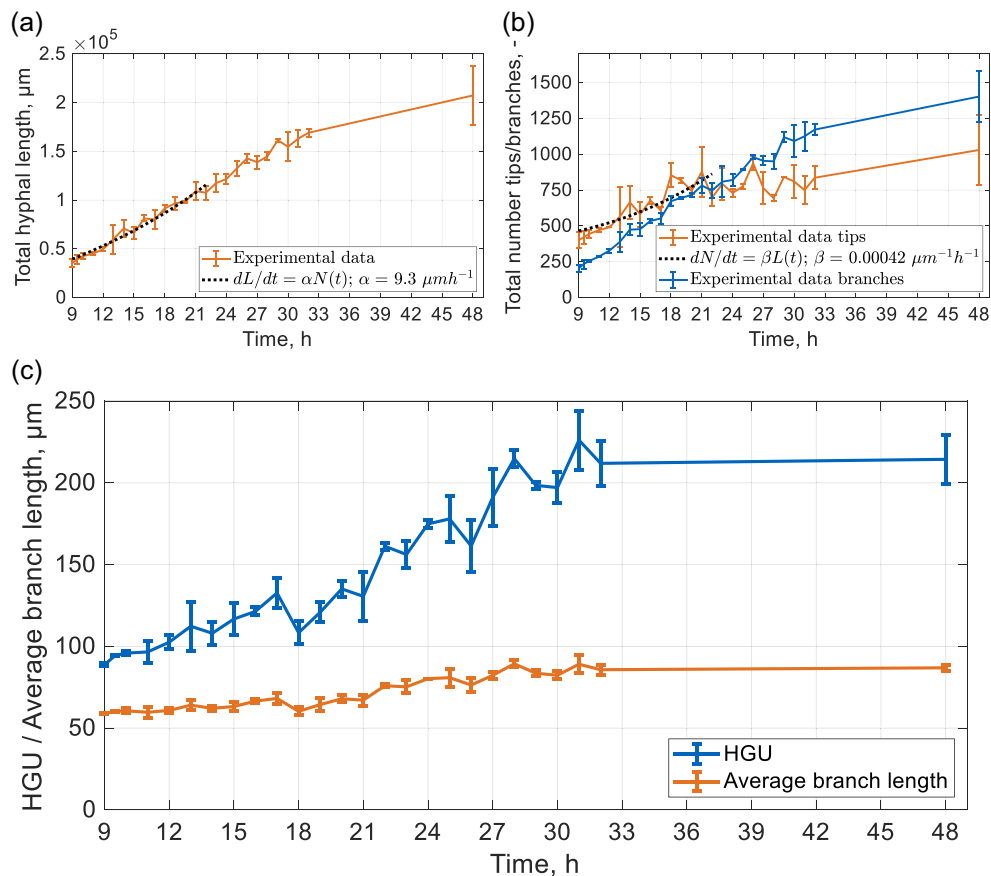


**FIGURE 6** Mean total hyphal length, number of tips, and branching points of pellets as a function of cultivation time, which were used to calculate the hyphal growth unit (HGU) and average branch length. (a) Mean total hyphal length of pellets as a function of cultivation time for flask A and B. The error bars indicate the standard deviations between flasks A and B. The total hyphal length was calculated based on the total hyphal volume  $V_{\text{Hyphae}}$  and the hyphal diameter  $d_{\text{Hyphae}}$  for each pellet as  $L_{\text{Hyphae}} = \frac{4 \cdot V_{\text{Hyphae}}}{\pi \cdot d_{\text{Hyphae}}^2}$ . The total hyphal volume and the hyphal diameter were determined by 3D image analysis based on SR- $\mu$ -CT images. The differential equation  $\frac{dL}{dt} = \alpha N(t)$  was used to fit the apical growth velocity of tips  $\alpha$ . (b) Mean total number of tips (orange) and branching points (blue) of pellets as a function of cultivation time for flask A and B. The error bars indicate the standard deviations between flasks A and B. The differential equation  $\frac{dN}{dt} = \beta L(t)$  depending on  $L(t)$  was used to fit the branching rate  $\beta$ . The total number of tips and branching points for each pellet were determined by 3D image analysis based on SR- $\mu$ -CT images. (c) Mean (blue) and mean average branch length (orange) of pellets as a function of cultivation time for flasks A and B. The error bars indicate the standard deviations between flasks A and B. The HGU was calculated as  $\frac{\text{Total hyphal length}}{\text{Total number of tips} + \text{Total number of branching points}}$  for each pellet. The average branch length was calculated as  $\frac{\text{Total hyphal length}}{\text{Total number of tips}}$  for each pellet. SR- $\mu$ -CT, synchrotron radiation-based microcomputed tomography.

estimated a value of 0.8 for *Streptomyces tendae* within his modeling approach. The comparison between the growth velocity of the equivalent pellet radius derived from 2D image analysis and the apical growth velocity of the tips based on 3D image analysis indicates that these values were calculated in a correct range.

The calculated average diameters of hyphae per pellet, which also influence the calculated total hyphal length, are in accordance with manually measured hyphal diameters. After, 9, 24, and 48 h, the average hyphal diameters and standard deviations from the 3D image analysis of all analyzed pellets (flasks A and B) were calculated at  $3.9 \pm 0.22$ ,  $4.6 \pm 0.49$ , and  $4.4 \pm 0.56$   $\mu\text{m}$ , respectively. The standard deviations indicate the differences between the analyzed pellets. 100 manually measured hyphal diameters of pellets were determined in differential interference contrast images (DIC) for selected cultivation times resulting in mean values of  $4.4 \pm 0.46$ ,  $4.4 \pm 0.52$ , and  $4.0 \pm 0.53$  after 9, 24, and 48 h, respectively. The DIC images were generated in Müller et al. (2022). Furthermore, Colin et al. (2013) measured hyphal diameters of *A. niger* ranging from 2.5 to 4.5  $\mu\text{m}$ , depending on cultivation conditions, indicating that our calculated hyphal diameters from the 3D image analysis are within a sufficiently precise range.

Figure 6b shows the mean number of tips and branching points of pellets from cultivation flasks A and B over time. After 9–18 h, the number of tips and branching points increased from 400 to 853 and from 202 to 672, respectively. Contrary to the branching points, the tips show higher variations in the mean values and between flasks A and B, expressed by the standard deviations. Since tips move and do not remain stable in pellets compared to branching points, they are detected mainly in the outermost parts of the pellet, where different factors can influence the tip detection by 3D image analysis. For example, tips can touch other hyphae resulting in the detection of a branching point instead of a tip. Furthermore, remaining freeze-dried impurities from the medium can cause hyphae to stick together, making tip detection less technically reproducible. However, the course of the tips and branching points shows a similar behavior until 21 h. After 22 h, the number of branching points overrules the number of tips pointing toward hyphal anastomosis, a well described phenomenon occurring in filamentous fungi including species of the genus *Aspergillus*. Hyphae not only grow by hyphal extension and branching but can also fuse with other hyphae in the older part of the mycelium, thus forming an interconnected mycelium that can distribute nutrients much more easily (Glass, 2004). Based on the model of Schuhmann and Bergter (1976) and the detected tips, we calculated a branching rate  $\beta$  of  $0.00042 \mu\text{m}^{-1} \text{h}^{-1}$  within a 95% CI ranging from  $0.00029$  to  $0.00054 \mu\text{m}^{-1} \text{h}^{-1}$ .

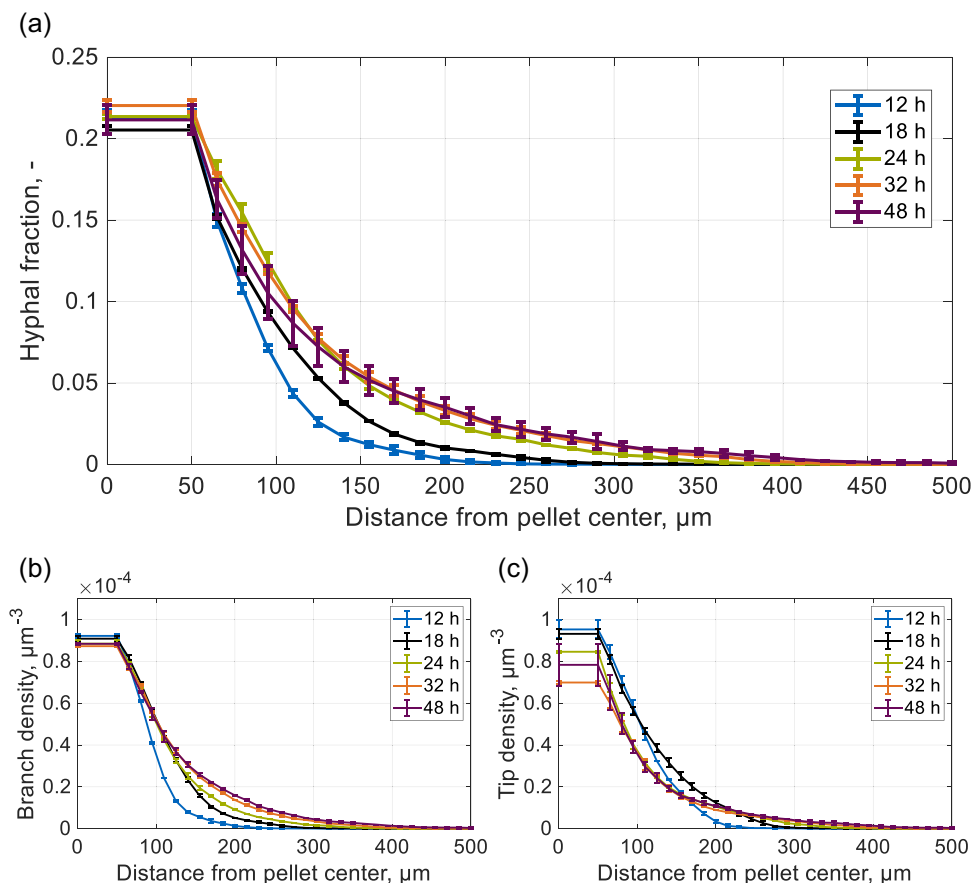
Figure 6c shows the mean HGU and the mean average branch length, which is the average length between two branching points or a branching point and a tip. The HGU, originally defined by Caldwell and Trinci (1973), expresses the mean hyphal length available per tip of a pellet. Experiments for young mycelium have shown that the HGU remains constant if the number of tips/branching points and consequently the total hyphal length increases exponentially (Dynesen & Nielsen, 2003; Trinci, 1974). If the HGU becomes

constant for a growing mycelium, the average branch length is also constant. In Figure 6c, contrary to the HGU, the mean average branch length remains almost constant at around 63  $\mu\text{m}$  until 21 h and subsequently increases to about 86  $\mu\text{m}$  after 32 h. Since the average branch length takes both parameters into account, the number of tips and branching points taken into account softens the effect of possibly underestimated tips by means of the image analysis. Furthermore, during the constant exponential growth phase of a pellet, the average branch length can be easily interpreted as the length between two branching points or a branching point and a tip. We therefore recommend introducing the average branch length as a parameter to characterize the growth of fungal pellets by means of 3D image analysis. In the literature, an HGU of 108  $\mu\text{m}$  for young mycelium of *A. niger* can be found, which corresponds to our analyzed values after 14 and 18 h (Colin et al., 2013).

### 3.3 | Local morphology development of pellets

To our knowledge, this study is the first to measure an incomparable high number of fungal pellets three-dimensionally over several cultivation time steps. Therefore, especially the data in Figure 7a,c cannot be verified with data from the literature.

Figure 7a,c show the mean hyphal fraction, branching point, and tip density of pellets from cultivation flasks A and B over the distance from the pellet center, which is defined as the center of mass of the spore core. The small standard deviations indicate a high reproducibility of the developed method inclusive of the sampling of the cultivation flasks, the transfer into the sample holder for 3D imaging, and the developed image analysis. In Figure 7a, the hyphal fraction in the outer pellet regions increases with time. Since the spore core defines the pellet center and has an equivalent diameter of about 146  $\mu\text{m}$  after 12 h (Figure 3), the hyphal fraction up to 50  $\mu\text{m}$  from the pellet center represents mainly the solid fraction of the spore core, ranging from 20.5% after 18 h to 22% after 32 h, and is also the densest part of a pellet. After 48 h, it can be observed that the hyphal fraction within inner pellet regions decreased compared to after 24 and 32 h. Since the detected mean number of spores per pellet also decreased after 32–48 h from about 1000 to 800, we are assuming that parts from the spore core are breaking out from the pellet and lead to a reduced hyphal fraction. However, the hyphal fractions after 48 h show the highest standard deviations, possibly pointing at autophagic processes reported for later stages of *A. niger* batch cultivations, which are associated with cell death (Nitsche et al., 2013). Various biological effects including breakage of pellets or lysis effects due to changes in carbon source or limitation can lead to a higher population heterogeneity (Tegelaar et al., 2020), which was observed in Müller et al. (2022) after 48 h under glucose limitation (Figure 5). Figure 7b,c indicate the branching point and tip density. Contrary to tips, branching points do not move during pellet growth. This can clearly be seen in Figure 7b, where the branching point density remains constant in the inner pellet regions, but increases in the outer regions over time. Contrarily, the tip density in



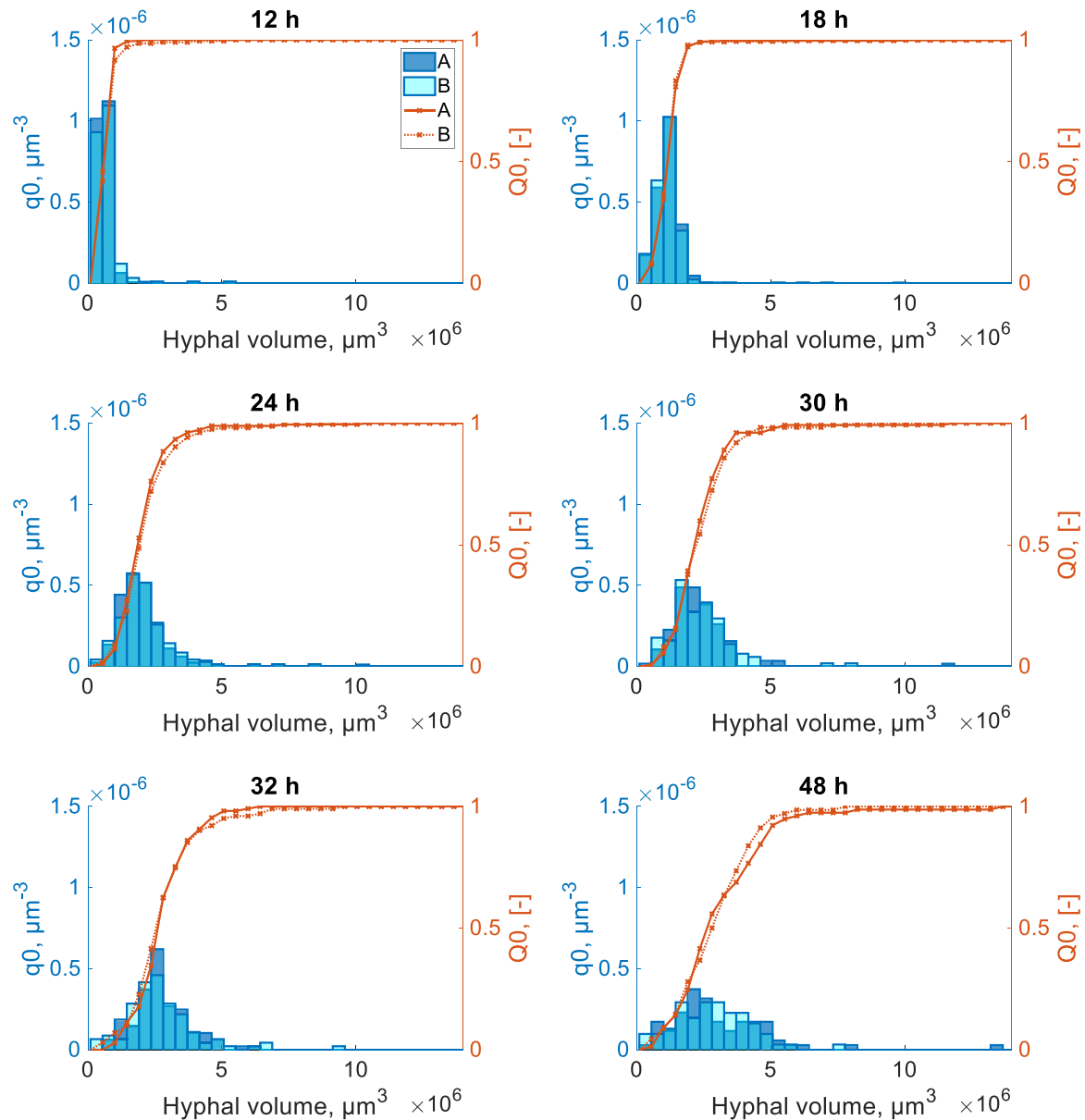
**FIGURE 7** Mean hyphal fractions as well as branching point and tip densities of pellets over the distance from pellet center for selected cultivation times. The hyphal fractions, tip, and branching point densities were determined in spherical shells or intersections between the convex hull of a pellet and the corresponding shell with a certain distance from pellet center. The processed image data were generated from SR- $\mu$ -CT measurements. The shown data are mean values, calculated with the mean for flasks A and B. The error bars indicate the standard deviation between flasks A and B. (a) Mean hyphal fractions; (b) mean branching point densities; (c) mean tip densities. SR- $\mu$ -CT, synchrotron radiation-based microcomputed tomography.

Figure 7c decreases in the inner and increases in the outer regions over time. The cultivation time after 48 h shows an exception. Here, the tip densities increase up to 80  $\mu\text{m}$  from the pellet center compared to the tip densities after 32 h. The highest standard deviations between flask A and B can be observed after 48 h due to a low sampling number and high population heterogeneity, showing the uncertainty in the data.

### 3.4 | Critical evaluation of the developed method

By using SR- $\mu$ -CT and an automatic image processing and data analysis pipeline, we overcame the limitation of a low sample throughput for  $\mu$ -CT measurements and could analyze a statistically representative number of pellets for multiple sampling times in three-dimensions. However, the preparation of this high number of pellets entails certain risks of sample damage during preparation and artefactual image processing (see Section 2.1.1), which cannot be completely eliminated. We therefore decided to cluster the pellets in artifacts and regular pellets. Forty-four percent or 8783 of the

19,940 potential pellet objects were clustered as artifacts, which is a high percentage, but the remaining 11,157 regular pellets are still the highest number of fungal pellets ever analyzed in three dimensions. Details of the cluster result are shown and described in Supporting information: Figure S2 and Table S1 in the Supporting information Materials. Furthermore, in this first case study analyzing the 3D growth of *A. niger*, we focused on simple pellet growth, which has the potential disadvantage of neglecting the study of other effects such as pellet breakage resulting in an increasing population heterogeneity. However, analysis of the number density distributions of the hyphal volume of pellets from the 3D image analysis per cultivation time depicted in Figure 8 shows that population heterogeneity is increasing toward 48 h which was also observed in Müller et al. (2022), as indicated by the broader size distributions after later cultivation times. Furthermore, a reduced mean equivalent diameter of the spore cores after 48 h was indicated by the 2D as well as by the 3D image analysis (Figure 3) and was additionally confirmed by a reduced number of detected spores per pellet (Figure 4). This indicates that the soft clustering by GMM classifies only very “unusual” pellets as artifacts. A potential drawback of the developed



**FIGURE 8** Normalized number-density-distribution  $q_0$  (left ordinate, blue) and cumulative size distributions  $Q_0$  (right ordinate, orange) as a function of the hyphal volume of pellets at different sampling times for flasks A and B. To generate the distributions, the values of the hyphal volumes of pellets were divided into 70 equidistant size classes between the minimal and maximal hyphal volume. The data were determined by 3D image analysis based on SR- $\mu$ -CT images. SR- $\mu$ -CT, synchrotron radiation-based microcomputed tomography.

method based on SR- $\mu$ -CT is the limited accessibility of synchrotrons. However, we strongly anticipate that rapid developments in the field of 3D imaging techniques will lower the barriers to entry for 3D measuring of complete fungal cultures.

#### 4 | CONCLUSION

The present study describes SR- $\mu$ -CT of a high amount (19,940) of *A. niger* pellets after multiple cultivation times. For this purpose, a standardized sample holder was developed and SR- $\mu$ -CT measurements were performed with the DESY imaging beamline P05. To

quantify and describe the 3D growth of fungal pellets over time, an image and data processing pipeline was set up based on: (1) the automatic segmentation of individual pellets from the sample holder; (2) the determination of global and local pellet parameters including the quantity and densities of spores, tips, branching points, and hyphal material for each pellet; (3) the GMM clustering of the data in artifacts and regular “normally” grown pellets; (4) the analysis and interpretation of the final data from 3D image analysis and GMM clustering. In addition, parameters such as the hyphal diameter, the total hyphal length, the average branch length, and the HGU of pellets were obtained for all cultivation times. The development over time of the equivalent diameters of spore cores and pellets analyzed

with 2D image analysis is in accordance with our developed 3D image analysis. In addition, 3D pellet growth was monitored by locally resolved hyphal fractions, and tip and branching point densities at multiple time steps. Furthermore, the time course of the data allowed us to analyze the growth rate, apical growth velocity, and branching rate for pellets, which to our knowledge is the first time this has been done for complete fungal pellets. The proposed methodology can be used to gain mechanistic insights into the evolution of fungal morphologies as a function of genetic, metabolic, and process factors (Meyer et al., 2021). With this approach, it now becomes feasible to quantitatively assess and study the dynamics of mycelial pellet formation as well as pellet heterogeneity within filamentous cultures and their dependence on spore inoculum, shear stress and nutrient availability, and other environmental factors. In addition, this first study of a 3D growth analysis of fungal pellets from a 48 h *A. niger* cultivation can pave the way to handle, process, and present high amounts of 3D data from fungal cultivations. Synchrotrons all over the world offer free beamtimes for scientists, companies can easily access synchrotrons with a paid industrial beamtime (Thiry et al., 2021), moreover the development of compact synchrotrons (Günther et al., 2020), and more powerful laboratory  $\mu$ -CTs will boost 3D measurements of complete fungal cultivations. An approaching vision is to set up a 3D database from multiple fungal species under different process conditions. This database can serve to gain mechanistic insights into the development of fungal morphologies and for the validation/development of modeling approaches, which predict the growth and substrate supply of filamentous pellets in submerged cultures (Buschulte, 1992; Celler et al., 2012; King, 2015; Lejeune & Baron, 1997; Nielsen, 1996; Schmideder et al., 2020).

#### AUTHOR CONTRIBUTIONS

Henri Müller did the conception and design of the study. Henri Müller and Charlotte Deffur wrote the manuscript, which was edited and approved by all authors. All authors interpreted the data. Heiko Briesen and Vera Meyer supervised the study. Lars Barthel, Henri Müller, and Stefan Schmideder cultivated filamentous fungi and prepared pellets for microcomputed tomography (SR- $\mu$ -CT) measurements. Lars Barthel developed the applied cultivation conditions. Jörg Hammel, Henri Müller, Stefan Schmideder, and Lars Barthel performed SR- $\mu$ -CT measurements of pellets. Jörg Hammel and Henri Müller reconstructed the image data. Henri Müller, Stefan Schmideder, Tiaan Friedrich, and Lukas Mirlach created the code for image analysis. Charlotte Deffur created the code for modeling the growth parameters. Henri Müller and Tiaan Friedrich created the code for clustering the pellets with GMM. Henri Müller performed the image and data processing and analyzed the results.

#### ACKNOWLEDGMENTS

We acknowledge DESY (Hamburg, Germany), a member of the Helmholtz Association HGF, for the provision of experimental facilities. We acknowledge provision of beamtime, related to the proposals I-20211150 and I-20200214 at the Imaging Beamline P05 at PETRA III at DESY, a member of the Helmholtz Association (HGF).

This research was supported in part by the Maxwell computational resources operated at Deutsches Elektronen-Synchrotron DESY, Hamburg, Germany. Furthermore, the authors thank Domenic Trinkl, Kilian Lupp, and Diana Kellhammer for preliminary studies on image analysis and data processing. The authors thank the Deutsche Forschungsgemeinschaft for financial support for this study within the SPP 1934 DiSPBiotech-315384307 and 315305620 and SPP2170 InterZell-427889137. Open Access funding enabled and organized by Projekt DEAL.

#### CONFLICT OF INTEREST STATEMENT

The authors declare no conflict of interest.

#### DATA AVAILABILITY STATEMENT

The data that support the findings of this study are openly available in <https://mediatum.ub.tum.de/> at <https://doi.org/10.14459/2023mp1700656>. All segmented 16-bit gray level and binarized 3D images of potential pellet objects can be downloaded there. Additional data and the image analysis scripts are available upon request.

#### ORCID

Henri Müller  <http://orcid.org/0000-0002-4831-0003>  
 Charlotte Deffur  <http://orcid.org/0000-0002-3902-0602>  
 Stefan Schmideder  <http://orcid.org/0000-0003-4328-9724>  
 Lars Barthel  <http://orcid.org/0000-0001-8951-5614>  
 Tiaan Friedrich  <http://orcid.org/0000-0001-8346-4908>  
 Lukas Mirlach  <http://orcid.org/0000-0002-8106-6049>  
 Jörg U. Hammel  <http://orcid.org/0000-0002-6744-6811>  
 Vera Meyer  <http://orcid.org/0000-0002-2298-2258>  
 Heiko Briesen  <http://orcid.org/0000-0001-7725-5907>

#### REFERENCES

- Antimonov, M., Khounsary, A., Weigand, S., Rix, J., Keane, D., Grudzinski, J. J., & Jansma, W. (2015). *Large-area Kapton X-ray windows* (pp. 62–71). SPIE. <https://doi.org/10.1117/12.2193680>
- Bishop, C. M. (2009). Pattern recognition and machine learning (Corrected at 8th printing 2009), *Information science and statistics*. Springer.
- Buffo, M. M., Esperança, M. N., Farinas, C. S., & Badino, A. C. (2020). Relation between pellet fragmentation kinetics and cellulolytic enzymes production by *Aspergillus niger* in conventional bioreactor with different impellers. *Enzyme and Microbial Technology*, 139, 109587. <https://doi.org/10.1016/j.enzmictec.2020.109587>
- Buschulte, T. C. (1992). Mathematische Modellbildung und Simulation von Zellwachstum, Stofftransport und Stoffwechsel in Pellets aus Streptomyceten (PhD thesis). Fakultät Verfahrenstechnik der Universität Stuttgart.
- Cairns, T. C., Feurstein, C., Zheng, X., Zheng, P., Sun, J., & Meyer, V. (2019). A quantitative image analysis pipeline for the characterization of filamentous fungal morphologies as a tool to uncover targets for morphology engineering: A case study using apID in *Aspergillus niger*. *Biotechnology for Biofuels*, 12, 149. <https://doi.org/10.1186/s13068-019-1473-0>
- Cairns, T. C., Nai, C., & Meyer, V. (2018). How a fungus shapes biotechnology: 100 years of *Aspergillus niger* research. *Fungal Biology and Biotechnology*, 5, 13. <https://doi.org/10.1186/s40694-018-0054-5>

- Cairns, T. C., Zheng, X., Zheng, P., Sun, J., & Meyer, V. (2019). Moulding the mould: Understanding and reprogramming filamentous fungal growth and morphogenesis for next generation cell factories. *Biotechnology for Biofuels*, 12, 77. <https://doi.org/10.1186/s13068-019-1400-4>
- Caldwell, I. Y., & Trinci, A. P. J. (1973). The growth unit of the mould *Geotrichum candidum*. *Archiv für Mikrobiologie*, 88(1), 1–10.
- Celler, K., Picioreanu, C., van Loosdrecht, M. C. M., & van Wezel, G. P. (2012). Structured morphological modeling as a framework for rational strain design of *Streptomyces* species. *Antonie Van Leeuwenhoek*, 102(3, SI), 409–423.
- Colin, V. L., Baigorí, M. D., & Pera, L. M. (2013). Tailoring fungal morphology of *Aspergillus niger* MYA 135 by altering the hyphal morphology and the conidia adhesion capacity: Biotechnological applications. *AMB Express*, 3, 27.
- Cui, Y. Q., Okkerse, W. J., van der Lans, R. G. J. M., & Luyben, K. C. A. M. (1998). Modeling and measurements of fungal growth and morphology in submerged fermentations. *Biotechnology and Bioengineering*, 60(2), 216–229.
- Dynesen, J., & Nielsen, J. (2003). Branching is coordinated with mitosis in growing hyphae of *Aspergillus nidulans*. *Fungal Genetics and Biology*, 40(1), 15–24. [https://doi.org/10.1016/S1087-1845\(03\)00053-7](https://doi.org/10.1016/S1087-1845(03)00053-7)
- Ehgartner, D., Herwig, C., & Fricke, J. (2017). Morphological analysis of the filamentous fungus *Penicillium chrysogenum* using flow cytometry—the fast alternative to microscopic image analysis. *Applied Microbiology and Biotechnology*, 101(20), 7675–7688.
- El-Enshasy, H. A. (2011). Filamentous fungal cultures—Process characteristics, products, and applications. In S.-T. Yang (Ed.), *Bioprocessing for value-added products from renewable resources: New technologies and applications* (pp. 225–261). Elsevier Science. <https://doi.org/10.1016/B978-044452114-9/50010-4>
- Ester, M., Kriegel, H.-P., Sander, J., & Xu, X. (1996). A density-based algorithm for discovering clusters in large spatial databases with noise. In *Proceedings of the 2nd International conference on knowledge discovery and data mining*, (Vol. 96, pp. 226–231).
- Fiedler, M. R. M., Barthel, L., Kubisch, C., Nai, C., & Meyer, V. (2018). Construction of an improved *Aspergillus niger* platform for enhanced glucoamylase secretion. *Microbial Cell Factories*, 17(1), 95. <https://doi.org/10.1186/s12934-018-0941-8>
- Füting, P., Barthel, L., Cairns, T. C., Briesen, H., & Schmideder, S. (2021). Filamentous fungal applications in biotechnology: A combined bibliometric and patentometric assessment. *Fungal Biology and Biotechnology*, 8(1), 23. <https://doi.org/10.1186/s40694-021-00131-6>
- Glass, N. (2004). Hyphal homing, fusion and mycelial interconnectedness. *Trends in Microbiology*, 12(3), 135–141. <https://doi.org/10.1016/j.tim.2004.01.007>
- Greving, I., Wilde, F., Ogurreck, M., Herzen, J., Hammel, J. U., Hipp, A., & Beckmann, F. (2014). P05 imaging beamline at PETRA III: First results. In S. R. Stock, (Ed.), *SPIE proceedings, developments in X-ray tomography IX (92120O)*. SPIE. <https://doi.org/10.1117/12.2061768>
- Günther, B., Gradl, R., Jud, C., Egg, E., Huang, J., Kulpe, S., Achterhold, K., Gleich, B., Dierolf, M., & Pfeiffer, F. (2020). The versatile X-ray beamline of the Munich compact light source: Design, instrumentation and applications. *Journal of Synchrotron Radiation*, 27(5), 1395–1414. <https://doi.org/10.1107/S1600577520008309>
- Haibel, A., Ogurreck, M., Beckmann, F., Dose, T., Wilde, F., Herzen, J., & Mohr, J. (2010). Micro- and nano-tomography at the GKSS Imaging Beamline at PETRA III. In S. R. Stock, (Ed.), *SPIE proceedings, developments in X-ray tomography VII (78040B)*. SPIE. <https://doi.org/10.1117/12.860852>
- Haralick, R. M., & Shapiro, L. G. (1992). *Computer and robot vision (II)*. Addison-Wesley.
- Hille, A., Neu, T. R., Hempel, D. C., & Horn, H. (2009). Effective diffusivities and mass fluxes in fungal biopellets. *Biotechnology and Bioengineering*, 103(6), 1202–1213.
- Jacobson, A., & Panozzo, D. (2018). *libigl: A simple C++ geometry processing library*.
- Kerschnitzki, M., Kollmannsberger, P., Burghammer, M., Duda, G. N., Weinkamer, R., Wagermaier, W., & Fratzl, P. (2013). Architecture of the osteocyte network correlates with bone material quality. *Journal of Bone and Mineral Research*, 28(8), 1837–1845. <https://doi.org/10.1002/jbmr.1927>
- King, R. (1998). Mathematical modelling of the morphology of streptomyces species: Relation between morphology and process performances. In K. Schügerl, (Ed.), *Relation between morphology and process performances* (pp. 95–124). Springer Berlin Heidelberg.
- King, R. (2015). A framework for an organelle-based mathematical modeling of hyphae. *Fungal Biology and Biotechnology*, 2(1), 5. <https://doi.org/10.1186/s40694-015-0014-2>
- Kurt, T., Marbà-Ardébol, A.-M., Turan, Z., Neubauer, P., Junne, S., & Meyer, V. (2018). Rocking *Aspergillus*: Morphology-controlled cultivation of *Aspergillus niger* in a wave-mixed bioreactor for the production of secondary metabolites. *Microbial Cell Factories*, 17(1), 128. <https://doi.org/10.1186/s12934-018-0975-y>
- Kurtz, S. M. (2012). *PEEK biomaterials handbook*. William Andrew Publishing.
- Kwon, M. J., Nitsche, B. M., Arentshorst, M., Jørgensen, T. R., Ram, A. F. J., & Meyer, V. (2013). The transcriptomic signature of RacA activation and inactivation provides new insights into the morphogenetic network of *Aspergillus niger*. *PLoS One*, 8(7), e68946.
- Lee, T. C., Kashyap, R. L., & Chu, C. N. (1994). Building skeleton models via 3-D medial surface axis thinning algorithms. *CVGIP: Graphical Models and Image Processing*, 56(6), 462–478. <https://doi.org/10.1006/cgip.1994.1042>
- Lejeune, R., & Baron, G. V. (1997). Simulation of growth of a filamentous fungus in 3 dimensions. *Biotechnology and Bioengineering*, 53(2), 139–150.
- Lewis, J. P. (1995). Fast normalized cross-correlation. In *Vision Interface*, 120–123.
- Lytaev, P., Hipp, A., Lottemoser, L., Herzen, J., Greving, I., Khokhriakov, I., & Beckmann, F. (2014). Characterization of the CCD and CMOS cameras for grating-based phase-contrast tomography. In S. R. Stock, (Ed.), *SPIE proceedings, developments in X-ray tomography IX (p. 921218)*. SPIE. <https://doi.org/10.1117/12.2061389>
- Lyu, J., Tegelaar, M., Post, H., Moran Torres, J., Torchia, C., Altelaar, A. F. M., Bleichrodt, R. J., de Cock, H., Lugones, L. G., & Wösten, H. A. B. (2023). Heterogeneity in spore aggregation and germination results in different sized, cooperative microcolonies in an *Aspergillus niger* culture. *mBio*, 14(1), e0087022. <https://doi.org/10.1128/mbio.00870-22>
- Maurer, C. R., Qi, R., & Raghavan, V. (2003). A linear time algorithm for computing exact Euclidean distance transforms of binary images in arbitrary dimensions. *IEEE Transactions on Pattern Analysis and Machine Intelligence*, 25(2), 265–270. <https://doi.org/10.1109/TPAMI.2003.1177156>
- Meyer, F. (1994). Topographic distance and watershed lines. *Signal processing*, 38(1), 113–125. [https://doi.org/10.1016/0165-1684\(94\)90060-4](https://doi.org/10.1016/0165-1684(94)90060-4)
- Meyer, V., Basenko, E. Y., Benz, J. P., Braus, G. H., Caddick, M. X., Csukai, M., de Vries, R. P., Endy, D., Frisvad, J. C., Gunde-Cimerman, N., Haarmann, T., Hadar, Y., Hansen, K., Johnson, R. I., Keller, N. P., Kraševc, N., Mortensen, U. H., Perez, R., Ram, A. F. J., ... Wösten, H. A. B. (2020). Growing a circular economy with fungal biotechnology: A white paper. *Fungal Biology and Biotechnology*, 7(1), 5. <https://doi.org/10.1186/s40694-020-00095-z>

- Meyer, V., Cairns, T., Barthel, L., King, R., Kunz, P., Schmideder, S., Müller, H., Briesen, H., Dinius, A., & Krull, R. (2021). Understanding and controlling filamentous growth of fungal cell factories: Novel tools and opportunities for targeted morphology engineering. *Fungal Biology and Biotechnology*, 8(1), 8. <https://doi.org/10.1186/s40694-021-00115-6>
- Meyer, V., Ram, A. F. J., & Punt, P. J. (2010). Genetics, genetic manipulation, and approaches to strain improvement of filamentous fungi. In R. H. Baltz, J. E. Davies, & A. L. Demain (Eds.), *Reference manual, ASM Press. Manual of industrial microbiology and biotechnology* (3rd ed., pp. 318–329). ASM Press. <https://doi.org/10.1128/9781555816827.ch22>
- Moosmann, J., Ershov, A., Weinhardt, V., Baumbach, T., Prasad, M. S., LaBonne, C., Xiao, X., Kashef, J., & Hofmann, R. (2014). Time-lapse X-ray phase-contrast microtomography for in vivo imaging and analysis of morphogenesis. *Nature Protocols*, 9(2), 294–304. <https://doi.org/10.1038/nprot.2014.033>
- Müller, H., Barthel, L., Schmideder, S., Schütze, T., Meyer, V., & Briesen, H. (2022). From spores to fungal pellets: A new high-throughput image analysis highlights the structural development of *Aspergillus niger*. *Biotechnology and Bioengineering*, 119(8), 2182–2195. <https://doi.org/10.1002/bit.28124>
- Nielsen, J. (1996). Modelling the morphology of filamentous microorganisms. *Trends in Biotechnology*, 14(11), 438–443. [https://doi.org/10.1016/0167-7799\(96\)10055-X](https://doi.org/10.1016/0167-7799(96)10055-X)
- Nitsche, B. M., Burggraaf-van Welzen, A.-M., Lamers, G., Meyer, V., & Ram, A. F. J. (2013). Autophagy promotes survival in aging submerged cultures of the filamentous fungus *Aspergillus niger*. *Applied Microbiology and Biotechnology*, 97(18), 8205–8218. <https://doi.org/10.1007/s00253-013-4971-1>
- Otsu, N. (1979). A threshold selection method from gray-level histograms. *IEEE Transactions on Systems, Man and Cybernetics*, 9, 62–66.
- Palenstijn, W. J., Batenburg, K. J., & Sijbers, J. (2011). Performance improvements for iterative electron tomography reconstruction using graphics processing units (GPUs). *Journal of Structural Biology*, 176(2), 250–253. <https://doi.org/10.1016/j.jsb.2011.07.017>
- Papagianni, M. (2004). Fungal morphology and metabolite production in submerged mycelial processes. *Biotechnology Advances*, 22(3), 189–259.
- Papagianni, M., & Mattey, M. (2006). Morphological development of *Aspergillus niger* in submerged citric acid fermentation as a function of the spore inoculum level. Application of neural network and cluster analysis for characterization of mycelial morphology. *Microbial Cell Factories*, 5. <https://doi.org/10.1186/1475-2859-5-3>
- Posch, A. E., Spadiut, O., & Herwig, C. (2012). A novel method for fast and statistically verified morphological characterization of filamentous fungi. *Fungal Genetics and Biology*, 49(7), 499–510.
- Schmideder, S., Barthel, L., Friedrich, T., Thalhammer, M., Kovačević, T., Niessen, L., Meyer, V., & Briesen, H. (2019). An X-ray microtomography-based method for detailed analysis of the three-dimensional morphology of fungal pellets. *Biotechnology and Bioengineering*, 116(6), 1355–1365. <https://doi.org/10.1002/bit.26956>
- Schmideder, S., Barthel, L., Müller, H., Meyer, V., & Briesen, H. (2019). From three-dimensional morphology to effective diffusivity in filamentous fungal pellets. *Biotechnology and Bioengineering*, 116(12), 3360–3371. <https://doi.org/10.1002/bit.27166>
- Schmideder, S., Müller, H., Barthel, L., Friedrich, T., Niessen, L., Meyer, V., & Briesen, H. (2020). Universal law for diffusive mass transport through mycelial networks. *Biotechnology and Bioengineering*, 118(2), 930–943. <https://doi.org/10.1002/bit.27622>
- Schuhmann, E., & Bergter, F. (1976). [Microscopic studies of *Streptomyces hygroscopicus* growth kinetics]. *Zeitschrift für Allgemeine Mikrobiologie*, 16(3), 201–205. <https://doi.org/10.1002/jobm.19760160305>
- Tegelaar, M., Aerts, D., Teertstra, W. R., & Wösten, H. A. B. (2020). Spatial induction of genes encoding secreted proteins in micro-colonies of *Aspergillus niger*. *Scientific Reports*, 10(1), 1536. <https://doi.org/10.1038/s41598-020-58535-0>
- Thiry, M., Beckmann, F., Hammel, J. U., Moosmann, J. P., & Wilde, F. (2021). Brilliant light for materials science: Industrial applications of the high energy microtomography at beamline HEMS/P07 at PETRA III. In B. Müller & G. Wang, (Eds.), *Proceedings of SPIE: Volume 11840, developments in X-ray tomography XIII: 1-5 August 2021, San Diego, California, United States* (p. 20). SPIE. <https://doi.org/10.1117/12.2596669>
- Trinci, A. P. (1974). A study of the kinetics of hyphal extension and branch initiation of fungal mycelia. *Journal of General Microbiology*, 81(1), 225–236.
- Van Aarle, W., Palenstijn, W. J., De Beenhouwer, J., Altantzis, T., Bals, S., Batenburg, K. J., & Sijbers, J. (2015). The ASTRA toolbox: A platform for advanced algorithm development in electron tomography. *Ultramicroscopy*, 157, 35–47. <https://doi.org/10.1016/j.ultramic.2015.05.002>
- Van Aarle, W., Palenstijn, W. J., Cant, J., Janssens, E., Bleichrodt, F., Dabrovolski, A., De Beenhouwer, J., Joost Batenburg, K., & Sijbers, J. (2016). Fast and flexible X-ray tomography using the ASTRA toolbox. *Optics Express*, 24(22), 25129–25147. <https://doi.org/10.1364/OE.24.025129>
- Veiter, L., Kubicek, M., Hutter, H., Pittenauer, E., Herwig, C., & Slouka, C. (2020). Study of metabolism and identification of productive regions in filamentous fungi via spatially resolved time-of-flight secondary ion mass spectrometry. *Analytical and Bioanalytical Chemistry*, 412(9), 2081–2088. <https://doi.org/10.1007/s00216-019-01980-2>
- Veiter, L., Rajamanickam, V., & Herwig, C. (2018). The filamentous fungal pellet-relationship between morphology and productivity. *Applied Microbiology and Biotechnology*, 102(7), 2997–3006.
- Ward, O. P. (2012). Production of recombinant proteins by filamentous fungi. *Biotechnology Advances*, 30(5), 1119–1139. <https://doi.org/10.1016/j.biotechadv.2011.09.012>
- Wilde, F., Ogurreck, M., Greving, I., Hammel, J. U., Beckmann, F., Hipp, A., & Schreyer, A. (2016). Micro-CT at the imaging beamline P05 at PETRA III O30035. In *AIP Conference Proceedings 1741* (p. 30035). <https://doi.org/10.1063/1.4952858>
- Willemsse, J., Büke, F., van Dissel, D., Grevink, S., Claessen, D., & van Wezel, G. P. (2018). Sparticle, an algorithm for the analysis of filamentous microorganisms in submerged cultures. *Antonie Van Leeuwenhoek*, 111(2), 171–182. <https://doi.org/10.1007/s10482-017-0939-y>
- Wittier, R., Baumgartl, H., Lübbers, D. W., & Schügerl, K. (1986). Investigations of oxygen transfer into *Penicillium chrysogenum* pellets by microprobe measurements. *Biotechnology and Bioengineering*, 28(7), 1024–1036. <https://doi.org/10.1002/bit.260280713>
- Wongwicharn, A., McNeil, B., & Harvey, L. M. (1999). Effect of oxygen enrichment on morphology, growth, and heterologous protein production in chemostat cultures of *Aspergillus niger* B1-D. *Biotechnology and Bioengineering*, 65(4), 416–424.
- Wösten, H. A. B. (2019). Filamentous fungi for the production of enzymes, chemicals and materials. *Current Opinion in Biotechnology*, 59, 65–70. <https://doi.org/10.1016/j.copbio.2019.02.010>
- Wucherpennig, T., Kiep, K. A., Driouch, H., Wittmann, C., & Krull, R. (2010). Morphology and rheology in filamentous cultivations.

*Advances in Applied Microbiology*, 72, 89–136. [https://doi.org/10.1016/S0065-2164\(10\)72004-9](https://doi.org/10.1016/S0065-2164(10)72004-9)

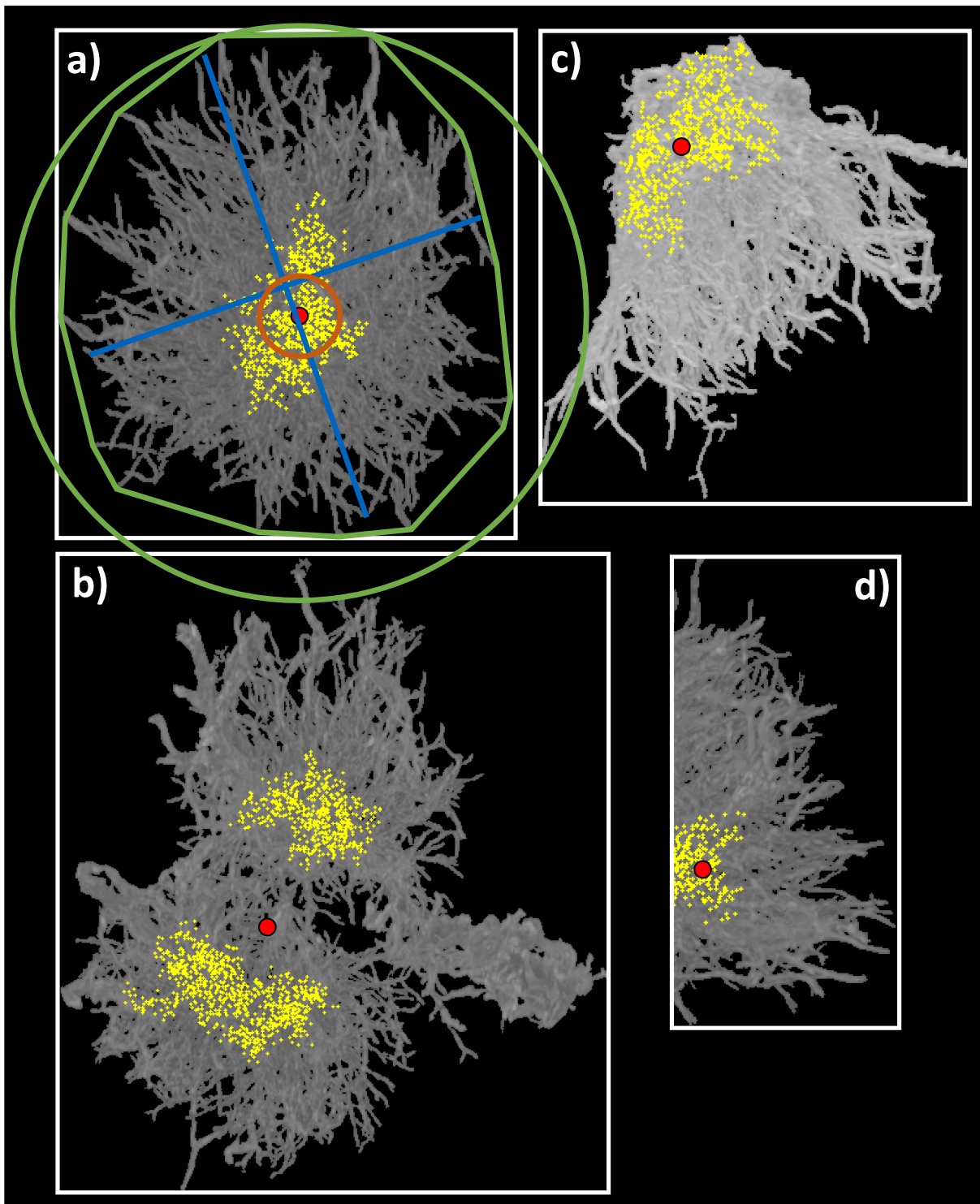
Zhang, J., & Zhang, J. (2016). The filamentous fungal pellet and forces driving its formation. *Critical Reviews in Biotechnology*, 36(6), 1066–1077.

#### SUPPORTING INFORMATION

Additional supporting information can be found online in the Supporting Information section at the end of this article.

**How to cite this article:** Müller, H., Deffur, C., Schmideder, S., Barthel, L., Friedrich, T., Mirlach, L., Hammel, J. U., Meyer, V., & Briesen, H. (2023). Synchrotron radiation-based microcomputed tomography for three-dimensional growth analysis of *Aspergillus niger* pellets. *Biotechnology and Bioengineering*, 1–17. <https://doi.org/10.1002/bit.28506>

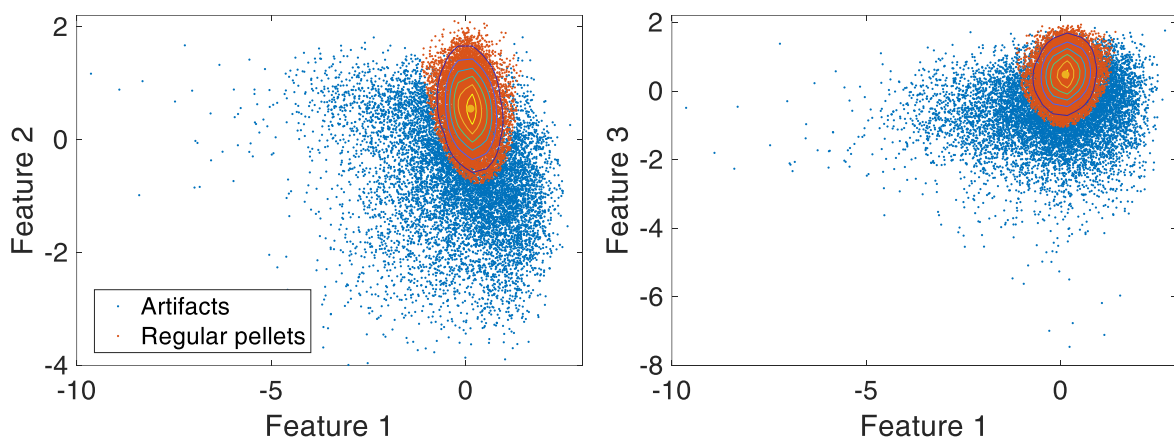
1 **Supplementary Figures**



2  
3 **Figure S1: Visualization of the three features used for the Gaussian mixture model (a) and**  
4 **potential pellets clustered as artifacts (b-d).**

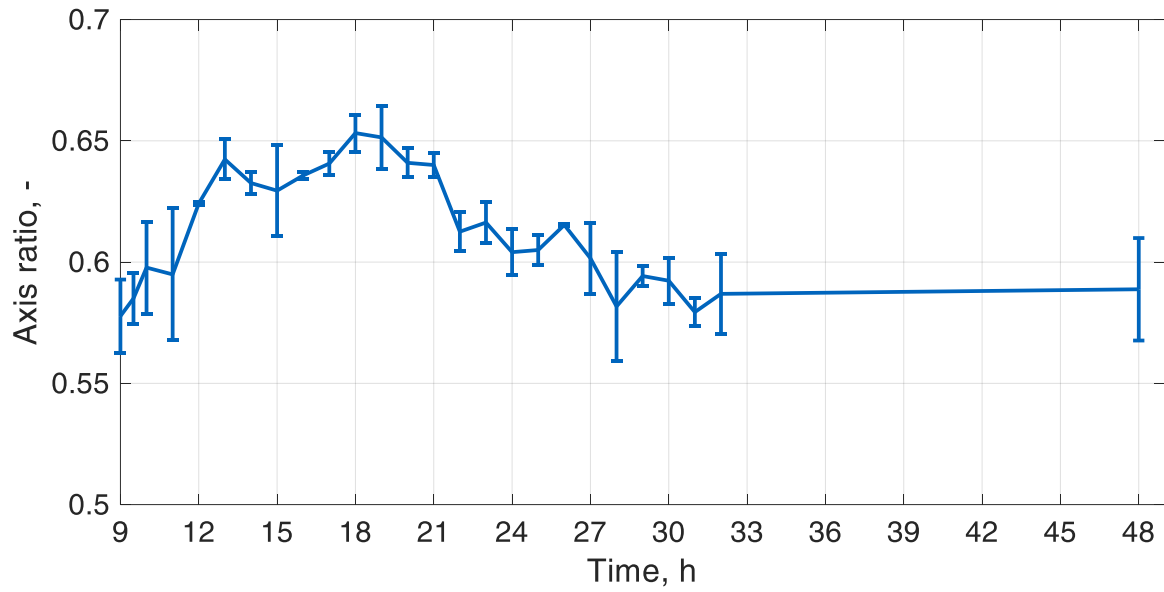
5 a) Sketch of the three features used for the Gaussian mixture model, shown on a pellet clustered as  
6 regular pellet. The orange object represents feature 1 (F1), the calculated hyphal fraction within the

7 inner sphere of radius 50  $\mu\text{m}$ . The green objects represent feature 2 (F2), the volume ratio between the  
 8 convex hull of a potential pellet object and the volume of the circumscribed sphere of potential pellet  
 9 objects centered on the center of mass of the spore core (red dot). The yellow dots indicate the centroids  
 10 of the detected spores. The blue lines represents feature 3 (F3), the axis ratio of the shortest and longest  
 11 major axes of a potential pellet object. The regular pellet has the following feature values. F1: 0.24; F2:  
 12 0.47; F3: 0.8; b) Entangled pellet clustered as artifact (F1: 0.06; F2: 0.34; F3: 0.44); c) Broken pellet  
 13 clustered as artifact (F1: 0.26; F2: 0.23; F3: 0.71); d) Cropped pellet clustered as artifact (F1: 0.13; F2:  
 14 0.25; F3: 0.44).



15  
 16 **Figure S2: Cluster result of Gaussian mixture model.**

17 All 19,940 potential pellet objects were clustered in artifacts (blue) and regular pellets (orange). Every  
 18 dot shows a single segmented potential pellet object depending on its features. Feature 1 represents the  
 19 calculated hyphal fraction within the inner sphere of radius 50  $\mu\text{m}$  of potential pellet objects. Feature 2  
 20 represents the volume ratio between the convex hull of a potential pellet object and the volume of the  
 21 circumscribed sphere of potential pellet objects centered on the spore core centroid. Feature 3 represents  
 22 the axis ratio of the shortest and longest major axes of a potential pellet object. All features were  
 23 logarithmized and standardized to have a mean of zero and standard deviation of one. The contour lines  
 24 indicate the Gaussian distribution of the model for the regular pellets. 44 % or 8,783 potential pellet  
 25 objects were clustered as artifacts and 56 % or 11,157 were clustered as regular pellets.



26

27 **Figure S3: Mean axis ratio of pellets as a function of cultivation time.**

28 The mean axis ratio of pellets were calculated with the mean axis ratio of flasks A and B. The error bars  
 29 indicate the standard deviations between flasks A and B. The axis ratios per pellet were determined by  
 30 the 3D image analysis based on SR- $\mu$ -CT images.

1 **Tables**

2 **Table S1: Artifacts, regular pellets and total number of potential pellet objects for each**  
3 **cultivation time.**

4 The numbers indicate the amount of SR- $\mu$ -CT analyzed pellets from flasks A and B clustered as artifacts  
5 or regular pellets by the applied Gaussian mixture model.

<b>Time, h</b>	9	9.5	10	11	12	13	14	15	16	17	18	19	20
<b>Artifacts</b>	89	124	114	48	238	138	333	107	365	340	279	293	330
<b>Regular pellets</b>	116	226	208	125	693	348	785	240	665	735	989	845	624
<b>Total</b>	205	350	322	173	931	486	1118	347	1030	1075	1268	1138	954

<b>Time, h</b>	21	22	23	24	25	26	27	28	29	30	31	32	48
<b>Artifacts</b>	502	429	456	455	515	576	452	725	331	340	397	376	431
<b>Regular pellets</b>	775	511	520	334	374	445	329	205	279	239	194	208	145
<b>Total</b>	1277	940	976	789	889	1021	781	930	610	579	591	584	576

6

**C. Unpublished and not peer-reviewed  
Article I**

# Generalized morphology modeling of aggregating, filamentous microorganisms

Henri Müller, Stefan Schmideder, Heiko Briesen

Process Systems Engineering, Technical University of Munich, 85350 Freising, Germany

## Abstract

Widely used in industrial biotechnology, filamentous fungi produce chemicals, enzymes, acids, antibiotics, and further lifesaving pharmaceuticals. Due to a strong relation between fungal morphology, process conditions, and productivity, targeted morphology engineering techniques aim to improve fungal morphology in terms of process behavior and productivity. However, the exact impact of such genetic and process modification methods are often unknown. The reason for this is the lack of appropriate analytical methods and models that correlate the fungal morphology to substrate supply. In this chapter, we present a method based on X-ray micro-computed tomography and image processing for detailed analysis of three-dimensional fungal morphology. This method has been extended in terms of sample throughput and, in combination with an additionally developed 2D image analysis method, allows the description of the micro- and macro-morphological development of complete fungal cultures. Furthermore, we used Monte Carlo growth simulations to expand the database of experimentally 3D-imaged fungal pellets by 3125 in-silico generated, morphologically different fungal structures. This database was used to perform diffusion computations through the 3D images, revealing a universal correlation between the structure and diffusivity through hyphal networks. The developed methods and results eventually contribute to targeted morphology engineering and improved control of filamentous fungal bioprocesses, leading to increased productivity.

## Introduction

Filamentous fungi are an integral part of industrial biotechnology. They are masters of biosynthesis, producing chemicals, enzymes, acids, antibiotics, and further lifesaving pharmaceuticals in bioreactors with several hundred cubic meters capacity [1–5]. Features such as their potential to build various bioactive molecules [6–8], their highly expanded protein secretion apparatus [9], and their ability to perform complex post-translational modifications [10] make them these efficient cell factories. Filamentous fungi are also capable of completely degrading lignocellulosic biomass into a variety of useful and sustainable products, making them unique as microorganisms [11].

When cultivated under industrially relevant submerged conditions, filamentous fungi adopt different morphologies. The developed morphology strongly influences the productivity of the bioprocess [12–14]. In general, filamentous fungi consist of branched hyphae that may be loosely packed, which corresponds to the morphology of dispersed mycelia, or very dense and highly branched, which is referred to as pellets [12, 15]. These two forms of morphology each bring advantages and disadvantages. Dispersed mycelia grow rapidly, but cause a non-Newtonian behavior and high viscosity of the cultivation broth, and thus, reduce the nutrient supply due to insufficient mixing [13, 16]. Contrary, cultivation broths with pellets as predominant macromorphology show low viscosities, but the transport of nutrients and oxygen into pellets is diffusion-limited by the dense structure [17, 18], reducing growth and growth-associated product

---

Henri Müller • Stefan Schmideder • Heiko Briesen  
Process Systems Engineering, Technical University of Munich, Munich, Germany  
e-mail: heiko.briesen@tum.de

formation [12, 13, 19]. This clearly indicates that the morphology and inner structure of pellets, e.g., the spatial distribution of tips and hyphal material, affects their productivity. Thus, various strategies have been developed to modify fungal morphology. These strategies include the variation of titre, vitality and hydrophobicity of the spore inoculum [20, 21] and cultivation conditions, including medium composition, temperature, shear stress [15, 22], and the addition of microparticles [14, 23–25], as well as genetic modifications of the fungus [19, 26, 27]. However, the mode of action of such strategies is often unknown, limiting targeted morphology engineering of filamentous fungi for increased productivity. These knowledge gaps are due the lack of experimental methods and mathematical models to (1) study the micromorphology within whole intact pellets [28], (2) correlate the three-dimensional (3D) structure and diffusive mass transport of oxygen and nutrients within pellets [29, 30], and (3) analyze the morphological evolution of complete cultivations holistically with a statistically representative number of samples, starting from single spores, through spore agglomeration, to final heterogeneous pellet populations.

In context of the priority program DiSPBiotech of the German Science Foundation (DFG SPP 1934), 3D image analysis methods based on X-ray micro-computed tomography ( $\mu$ -CT) were developed to determine the micromorphology of whole pellets [28]. Furthermore, diffusion computations through 3D images of pellets from  $\mu$ -CT measurements and in-silico generated filamentous fungi from 3D Monte Carlo growth simulations revealed a universal correlation between the structure and diffusivity through hyphal networks [29, 30]. Moreover, high-throughput 2D and 3D image and data processing methods based on stereomicroscopy and synchrotron radiation based micro-computed tomography (SR- $\mu$ -CT) were developed to track the macro- and micro-morphological development of complete cultivations [31, 32]. Such methods and models can serve to generate a database providing mechanistic insights into the development of fungal morphologies including growth, breakage, and aggregation processes. In addition, modeling approaches can be validated/developed to predict the evolution of fungal morphology, for which suitable experimental data on the internal structure and diffusivity of pellets have been lacking [33–36]. Eventually, the results generated during the research project DFG SPP 1934 may contribute to targeted morphology engineering and increased control of filamentous fungal bioprocesses resulting in enhanced productivities.

Since important parameters for model development are missing in the literature, e.g. local hyphal densities of pellets, we set ourselves the task of detailed characterization of fungal morphology by 2D and 3D image analysis. This topic has received an unexpected higher momentum in the project due to the collaborative opportunities within the SPP and successful exploratory tests to characterize pellet structures with X-ray  $\mu$ -CT in an instrument that became available in our group (Major Research Instrumentation Grant DFG INST 95/1111-1). Therefore, our overall project title of this report could be misleading with respect to the weighting between modeling and image analysis content.

## Material and Methods

### Cultivation, sampling, and preparation of pellets

To obtain pellet structures for method development and analysis, the following industrially relevant fungal species/strains were cultivated: *Penicillium chrysogenum* strain MUM17.85 (Micoteca da Universidade do Minho, Braga, Portugal), *Aspergillus niger* strain MF22.4 [27] and its parental strain MF19.5 [37], *Rhizopus stolonifer* (isolated organisms), *Rhizopus oryzae* CBS 607.68 (unknown source). *Aspergillus niger* and *Rhizopus stolonifer* were cultivated at the TU Berlin in cooperation with the SPP working group of Prof. Meyer. Sporangiospores (*Rhizopus* spp.) and conidiospores (*A. niger* and *P. chrysogenum*) of all strains

were received from agar plate cultures [38]. Erlenmeyer flasks with liquid media were inoculated with the spores and pellets were grown by submerged cultivation [28, 30, 31].

For  $\mu$ -CT measurements, a stable and dried state of the pellet samples is required. Therefore, we developed a protocol to generate freeze-dried fungal pellets [28]. Following our protocol, a culture sample with pellets was carefully pipetted into an Eppendorf tube (Eppendorf SE), washed three times with sterile tap water to remove impurities from the medium, and deep frozen in liquid nitrogen while pellets were floating in water. Subsequently, the frozen pellet sample was freeze-dried, resulting in one Eppendorf tube containing several dried pellets with preserved structure. Figure 1 indicates the preserved structure.

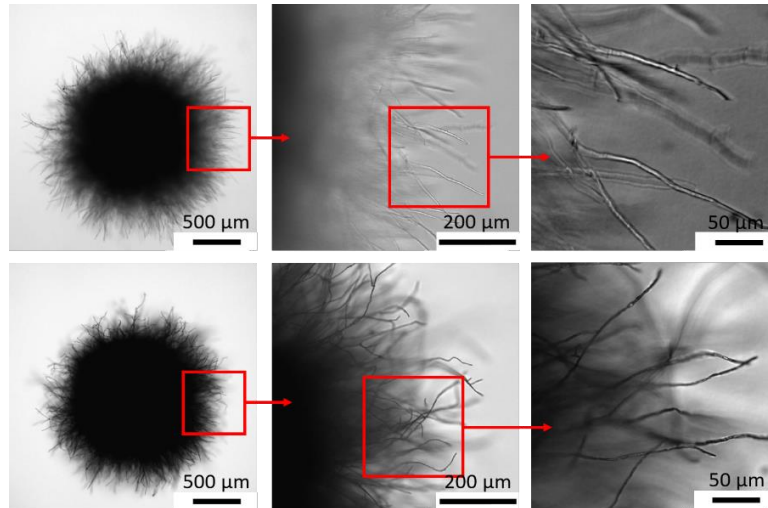


**Figure 1:** Light microscope images of a *P. chrysogenum* pellet. The upper row shows the “wet” state of the pellet, whereas the lower row shows the freeze-dried state. (Reprinted with permission from [28], Copyright (2019) John Wiley and Sons)

### Micro-computed tomography

To generate 3D images of the freeze-dried filamentous pellets using laboratory-scale  $\mu$ -CT [28–30] and SR- $\mu$ -CT [32], the freeze-dried pellets were placed on specially designed sample holders which were mounted on a sample pin that fit into the sample rotation stage between the X-ray source and the camera. The generated 2D projections from different angles taken during  $\mu$ -CT measurements were reconstructed into a 3D image by the filtered back projection algorithm.

In case of the laboratory-scale  $\mu$ -CT (XCT-1600HR; Matrix Technologies, Feldkirchen, Germany), measurements were performed inhouse with a cone X-ray beam generated at an energy of 60 kV. The exposure time was between 5-6 s per projection. At least 2000 projections were acquired per CT scan using a 10.8 MP CCD camera system. A custom-designed software (Matrix Technologies, Feldkirchen, Germany) that uses CERA (Siemens, Munich, Germany) was used for 3D image reconstruction. The final reconstructed 3D gray level image had a size of 2000×2000×1225 voxel with a voxel size of 1  $\mu$ m.

SR- $\mu$ -CT was realized at the Imaging Beamline P05 [39–41] at the storage ring PETRA III (Deutsches Elektronen-Synchrotron - DESY, Hamburg, Germany). Imaging was performed at a photon energy of 18 keV and 30 ms exposure time per projection. Per tomographic scan, 2401 projections were recorded using a 20 MP CMOS camera system. Two scans per measured sample holder were performed to increase the

field of view in the vertical direction. The volumes were reconstructed with a custom reconstruction pipeline [42] based on MATLAB (MathWorks) and the Astra Toolbox [43–45]. The reconstructed bottom and upper volumes of a sample were stitched together, resulting in a final 3D gray level image with  $2595 \times 2595 \times 3718$  voxel with a voxel size of  $1.28 \mu\text{m}$ . It must be mentioned, that the high brilliance of synchrotron radiation enables a higher signal to noise radiation and thus better image contrast compared to a laboratory  $\mu\text{-CT}$ .

### **3D image segmentation of multiple pellets**

Within the project, several steps were developed and iteratively refined for processing the 3D gray level images showing pellets, parts of the sample holder, and background. During this development period, parts of the image processing were performed with different software, e.g., MAVI (version 1.4.1; Fraunhofer ITWM, Kaiserslautern, Germany), VGSTUDIO MAX (version 3.2, Volume Graphics GmbH, Heidelberg, Germany), and FIJI/ImageJ. These processing parts were finally transferred completely and identically to MATLAB (MathWorks). The following description therefore concentrates on the image processing steps that were established in MATLAB. Furthermore, for the first  $\mu\text{-CT}$  based study, fungal pellets were segmented manually from the 3D grayscale images and subsequently post-processed for detailed and accurate determination of micromorphological parameters, e.g., the locally resolved branch and tip density of pellets [28]. The manual segmentation of pellets was replaced by an automated method to increase sample throughput in  $\mu\text{-CT}$  measurements and image processing for statistically meaningful results, and to cope with the large amount of 3D image data from SR- $\mu\text{-CT}$  measurements [30, 32]. The developed automated method enabled the segmentation and processing of up to 579 pellets from a single SR- $\mu\text{-CT}$  image. In the following, this method is presented.

For  $\mu\text{CT}$  measurements, several freeze-dried fungal pellets were transferred into a specially designed sample holder consisting of a polyether ether ketone (PEEK) base, a Kapton tube, and a PEEK cap. PEEK and Kapton ensure high X-ray resistance and transparency (Figure 2a). Figure 2b shows a microtomography from SR- $\mu\text{-CT}$  measurements depicting a sample holder filled with several pellets. To enable the analysis of the micromorphology of individual pellets described in the next section, pellets need to be segmented out of this pellet stack. Before segmentation, the complete gray level tomography was binarized with Otsu's method [46]. Subsequently, the sample holder was removed based on a normalized cross-correlation [47, 48] between a template of the Kapton tube and the tomography. Labeling and segmentation into individual pellets were established by a marker-controlled watershed segmentation. Here, pellets were dilated with a spherical structured element and remaining holes within the dilated pellets were filled. Based on the dilated and filled pellets a distance transformation was performed. Using the resulting distance image, markers representing the inner part of the pellet spheres were determined by masking voxels that were a certain distance from the background with zero. For each marker, a pellet was labeled and segmented by the watershed segmentation (Figure 2c). Each grayscale image, representing only a single pellet, was obtained by masking all voxels on the original grayscale tomography with zero except the corresponding segmented pellet. The resulting gray level pellet images were binarized (Figure 2d) and further processed for tip and branching point detection as well as for diffusion computations of the filamentous structures.

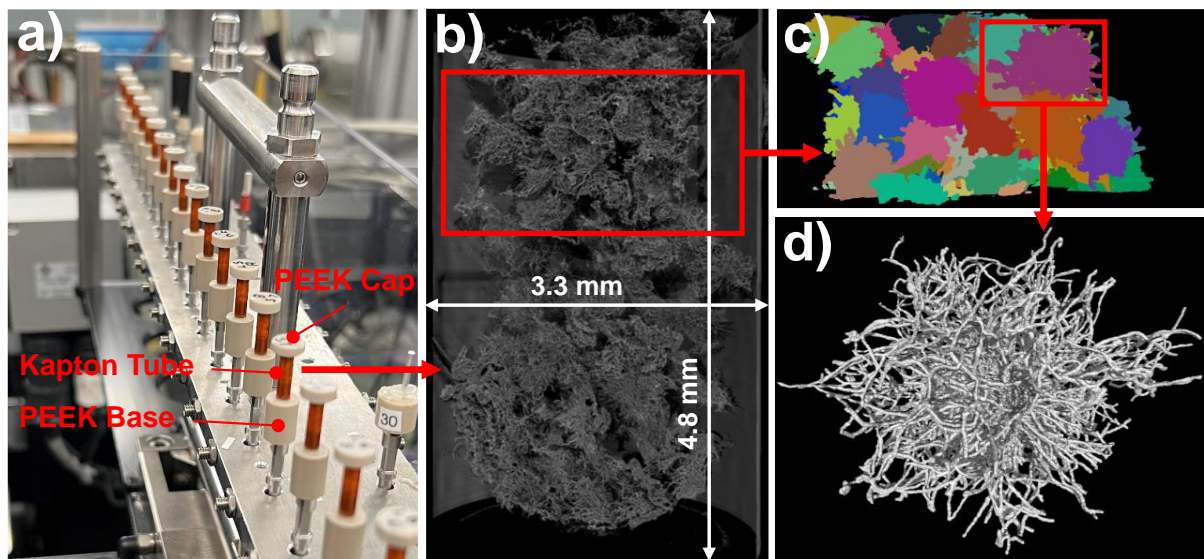


**Figure 2:** Sample preparation, microtomography, and image processing. a) Sample holders with freeze dried pellets at the P05 beamline; b) Synchrotron radiation based X-ray microtomography with a voxel size of  $1.28 \mu\text{m}$ ; c) Segmented and labeled pellets; d) Segmented and binarized pellet with an equivalent diameter of  $557 \mu\text{m}$ . (Reprinted with permission from [32], Copyright (2023) John Wiley and Sons)

### Post-processing of segmented 3D pellets

Following the developed automatic segmentation method (previous section) [30, 32], the segmented 3D gray level images depicting only the pellet were binarized by setting a global threshold using Otsu's method [46]. Subsequently, remaining small connected objects that were not part of the pellet were deleted (Figure 3a-b). Using the processed and binarized image, the skeleton of the pellet representing the centerline of hyphae was calculated by an iterative thinning algorithm [49, 50] (Figure 3c). Based on the skeleton, tips, and branching point voxels were computed (Figure 3d). Branching point voxels are characterized by at least three neighboring voxels. Contrary, tips have only one neighbor and represent the endpoints of the skeleton. "Normal" hyphae voxels, are those with two neighboring voxels. When detecting tips and branching points based on the skeleton, errors may occur that lead to artefactual detection of individual tips and branching points. Thus, postprocessing steps were performed to correct the skeleton. The first step eliminates falsely detected tips due to short branches caused by surface roughness of hyphae (Figure 4a-b). Here, the Euclidean length of each branch was calculated. If this length was shorter than  $4 \mu\text{m}$ , which is close to the hyphal diameter of the used strains, the branch and thus the tip was eliminated. In the second step, wrongly detected branching points, caused by overlapping hyphae were corrected (Figure 4c-d). Since true hyphal branching points connect only three branches, the number of branches was determined for each branching point. If the number was greater than three, the branching point was falsely detected and consequently deleted. In the third postprocessing step, the branching points were corrected, which result from parallel and closely spaced hyphae due to small bridges between hyphae (Figure 4e-f). These connections can result from the limited spatial resolution, making it impossible to distinguish between background and hyphae if the distance between two hyphae is too small. To correct this issue, the distance between two branching points must be

at least 6.5  $\mu\text{m}$ , otherwise the branching points are deleted and recognized as “normal” voxels of the skeleton. For a more detailed description of the developed postprocessing steps, we refer to [28].

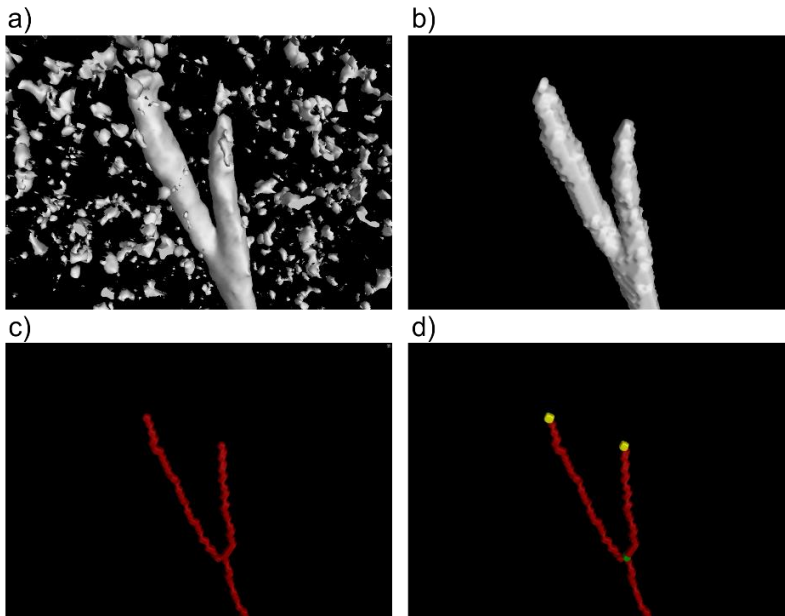


**Figure 3:** Image processing steps for a small region of a *P. chrysogenum* pellet; images are rendered with VGSTUDIO MAX. (a) Raw image: CT data with remaining image noise and small connected objects. (b) Preprocessed and binarized image with deleted small connected objects (c) Skeletonized image. (d) Analyzed image: analysis of the skeleton; tips are marked yellow and branches green. (Reprinted with permission from [28], Copyright (2019) John Wiley and Sons)

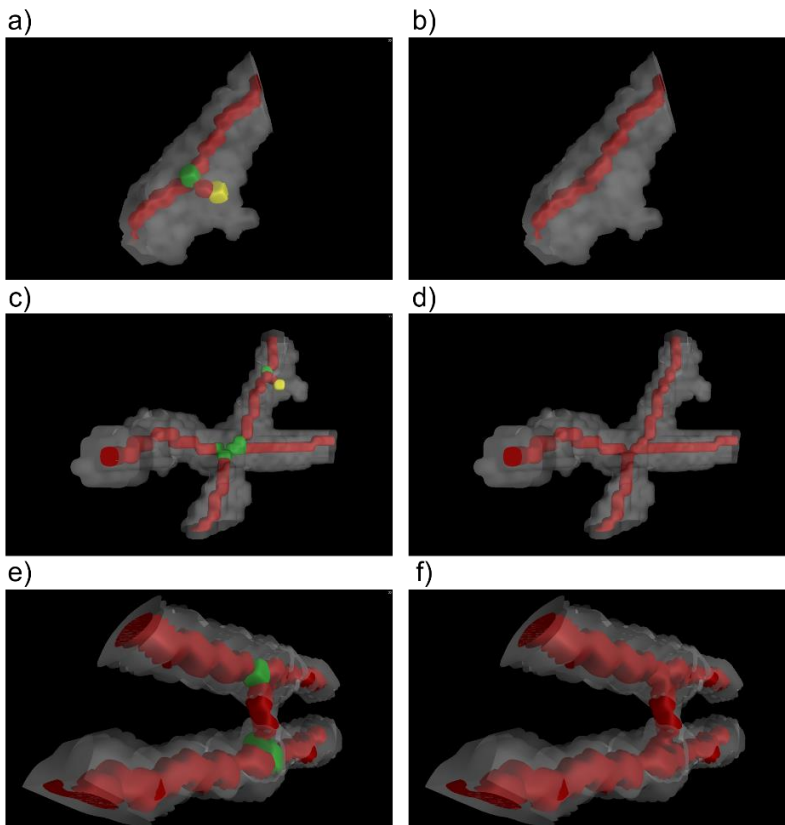


**Figure 4:** Post-processing steps for small regions of *P. chrysogenum* pellet; transparent grey objects illustrate the binarized 3D data, red objects the skeleton, yellow markers the tips, and green markers the branches. (a) Rough surface of binarized hyphae result in a short junction. (b) Post-processing: short junction from rough surface is deleted. (c) Overlapping hyphae result in a branch. (d) Post-processing: incorrect branch is deleted. (e) Close parallel hyphae result in bridges imitating branches. (f) Post-processing: incorrect branches are deleted. (Reprinted with permission from [25], Copyright (2019) John Wiley and Sons)

## Global and local morphology properties of $\mu$ -CT pellets

Based on the full 3D pellet structure from  $\mu$ -CT measurements and image processing the following global morphology features were determined within the studies [28] and [32]: total tip number, total branch number, total hyphal volume, total hyphal fraction, pellet equivalent diameter, total hyphal length, average hyphal diameter, hyphal growth unit (HGU), and average branch length.

The total number of tips  $N_{Tips}$  and branching points  $N_{Branches}$ , were obtained by counting the corresponding segmented object voxels of the pellet. To calculate the total hyphal volume  $V_{Hyphae}$ , all hyphal voxel of the binarized pellet were summarized and multiplied with the voxel volume. The convex hull, extending over the outermost tips of the pellet, was used to calculate the total volume of the pellet  $V_{Pellet}$ . The ratio between  $V_{Hyphae}$  and  $V_{Pellet}$  defined the total hyphal fraction of a pellet. The total pellet volume was further used for the calculation of the equivalent spherical diameter of the pellet as

$d_{Pellet} = \sqrt[3]{\frac{6 \cdot V_{Pellet}}{\pi}}$  [28]. Similarly, the equivalent spherical diameter of the spore core, which is the spore agglomerate within a pellet, was calculated [32]. During the project, different calculation methods for the average hyphal diameter and total hyphal length were applied. To process a high number of fungal pellets without further input from different software, we calculated the total hyphal length as  $L_{Hyphae} = \frac{4 \cdot V_{Hyphae}}{\pi \cdot d_{Hyphae}^2}$ ,

where  $d_{Hyphae}$  is the average hyphal diameter.  $d_{Hyphae}$  was calculated by masking all voxels of the distance image of the binarized pellet with zero, except for those representing the skeleton of the pellet and thus the regional radii of the pellet. The regional radii were used to calculate the arithmetic mean of the hyphal diameter [32]. Furthermore, the HGU was calculated as  $\frac{L_{Hyphae}}{N_{Tips}}$  [51]. Complementary, the average branch length  $L_{Branch}$  for pellets, which is the length between two branching points or a branching point and a tip, was estimated as  $L_{Branch} = \frac{L_{Hyphae}}{N_{Tips} + N_{Branches}}$  [32].

The analyzed pellets had a spherical structure, which allowed quantifying the morphological properties distributed along their radii. For this, the number densities of tips, branches, and the hyphal fractions of a pellet were determined in shells along its distance from the pellet center. The width of the shells was at least 15  $\mu\text{m}$  and 50  $\mu\text{m}$  for the central sphere. The pellet center was defined as the mass center of the pellet [28] and in a later study as the mass center of the determined spore agglomerate within pellets, the spore core of a pellet [32]. The hyphal fraction of a shell was determined by dividing the hyphal volume of the shell by the total volume of the shell. Accordingly, to calculate the number densities, the number of tips and branches for the shell was divided by the volume of the corresponding shell.

## Three-dimensional growth simulation of filamentous fungal pellets

To generate nature-like 3D images of filamentous fungal pellets in-silico, a microscopic modeling approach was adopted. This allowed the calculation of the entire micromorphological 3D structure of pellets including the exact positions of hyphae, branches, and tips. Furthermore, the modeling approach enabled the voxel-based generation of 3125 morphologically different fungal structures covering a broad range of fungal morphologies. The simulated pellets increased the database of pellet structures to be analyzed with respect to diffusion properties as will be presented and discussed in the following section.

The morphological simulations were implemented using MATLAB and based on stochastic growth models for filamentous microorganisms [34, 52]. Compared to Celler et al. [34], we neglected oxygen limitation

and cross wall-formation during growth. Furthermore, we introduced the pellet formation from spore agglomerates to generate coagulative type pellet structures in addition to non-coagulative ones. A voxel-based output of the pellet structures was introduced to compare the simulated data with the  $\mu$ CT data. The developed model includes 3 main parts: (1) spore aggregation, (2) growth, and (3) generation of voxel-based 3D structure (Figure 5). In order to simulate morphologically different pellets, the following parameters were varied in the corresponding main steps: number of initial spores, branching interval, branching angle, maximum growth angle, and the hyphal diameter. For each parameter five values were varied to generate  $5^5 = 3125$  morphologically different structures. Figure 6 summarizes the varied parameters which were estimated based on values for filamentous fungi from literature [11, 53, 54]. Spore aggregation to produce the initial spore agglomerates that grow into the pellet structure was estimated using the diffusion-limited-limited aggregation (DLA) method [55]. The spore agglomerate was initialized with a first seed spore and iteratively enlarged by further spores, which performed a random walk until they came into contact with the first spore or the already formed spore agglomerate. This process was terminated, if the desired number of spores was reached (Figure 5, top section). The second main step, growth, began with germination, where random orientated segments of the length  $l_{germ}$  developed from the spores. In this process, collisions of the formed segments with other germlings were prevented. After germination, tip extension and branching of the hyphae began. These two operations were repeated at each time step  $\Delta t$  until the end of the growth simulation. For tip extension, a segment with the length  $l_{segment}$ , which is the product of  $\Delta t$  and the tip extension rate  $\alpha_t$ , was attached to the previous segment at a random growth angle  $\theta_g$  between  $0^\circ$  and the desired maximum growth angle (Figure 5, middle section). Overlapping and collisions between new segments and already simulated hyphal material was prevented with closest-point computations [56]. New possible branching points (node between two segments) were computed in subapical regions of hyphae, which were defined by the length  $l_{subapical}$  beginning from the tip, if three conditions were fulfilled: (1) location of branching point in subapical region, (2) no branches in the neighboring four nodes, (3) current number of branches of the hyphae was lower than the possible number of branches, calculated by dividing the length of the hyphae by the minimum mean distance between two branches  $d_{b,min}$ . If these three conditions were met, a new possible branch with the desired branching angle  $\theta_b$  was calculated, checked for collisions with already simulated hyphal material [56], and rejected if a collision was detected (Figure 5, middle section).

The output of the growth section includes the morphological data of the locations and connections of nodes, hyphal segments, and spores, which were converted to the final 3D voxel-based output. Within this last main step (Figure 5, bottom section), the locations were scaled with the factor  $f_{scale} = \frac{d_{h,vx}}{d_h}$  to represent the hyphae with the desired hyphal diameter in  $\mu\text{m}$   $d_h$  and resolution depending on the hyphal diameter in voxels  $d_{h,vx}$ . Subsequently, the connections between nodes were discretized with Bresenham's line algorithm [57] to compute skeletons of pellets. Finally, the skeletons were dilated with a spherical structuring element resulting in voxel-based 3D pellet images with the desired hyphal diameter. For a more detailed description of the Monte Carlo growth model, we refer to [30].

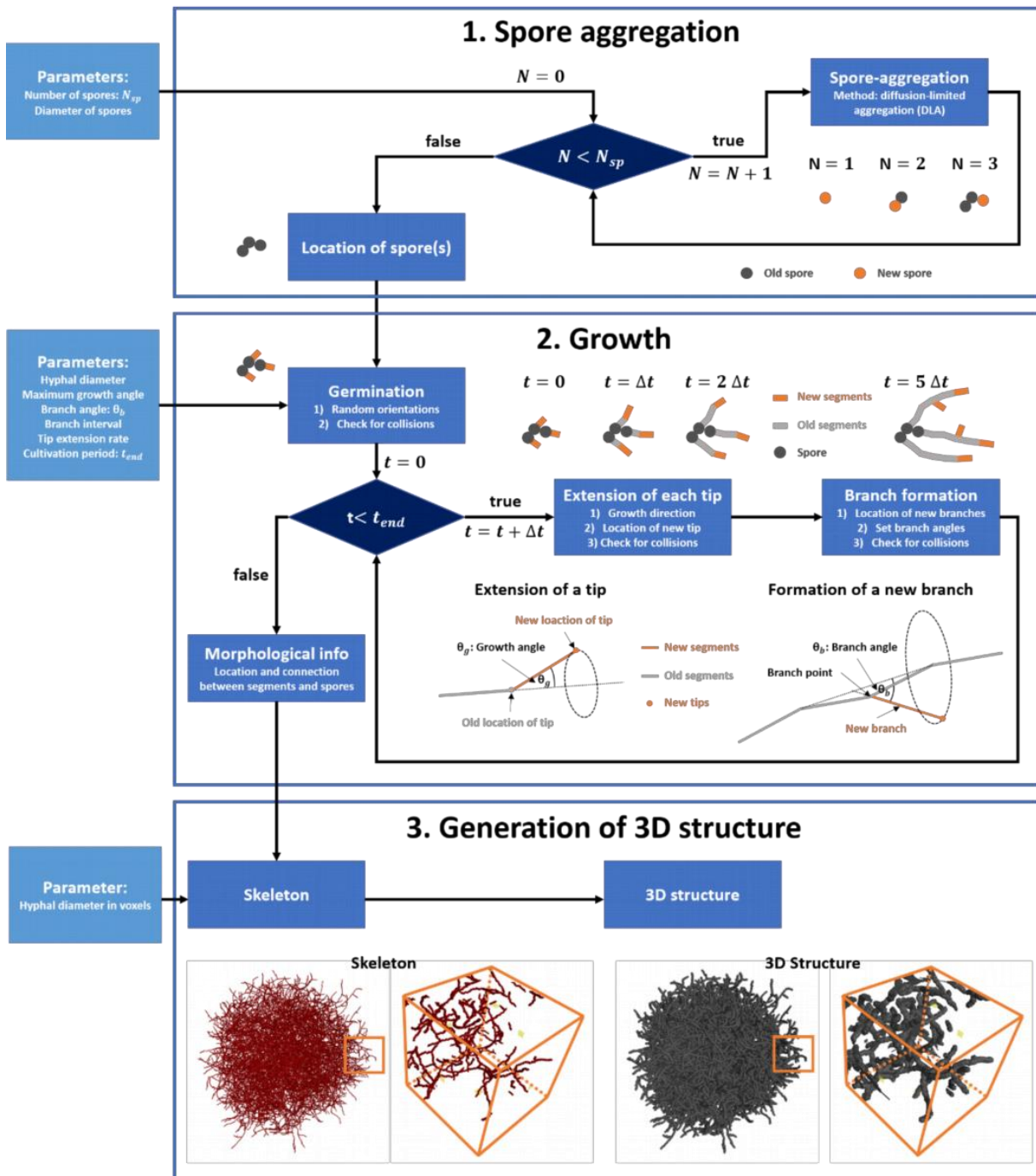


**Figure 5:** Overview of the algorithm of morphological growth simulations. (Reprinted with permission from [30], Copyright (2020) John Wiley and Sons)

	Value 1	Value 2	Value 3	Value 4	Value 5
Maximum growth angle	0°	12°	24°	36°	48°
Branch angle	20°	55°	90°	125°	160°
Hypal diameter	0.5 μm	3.4 μm	6.3 μm	9.1 μm	12 μm
Branch interval	3	11	19	27	35
Number of spores	1	10	100	1000	10000

**Figure 6:** Applied morphological parameters and values for simulations of filamentous structures. Each of these parameters was varied to five values resulting in a total of  $5^5 = 3125$  simulations performed with the Monte Carlo method. (Reprinted with permission from [30], Copyright (2020) John Wiley and Sons)

### Diffusion computations within fungal pellets

Dense hyphal networks can limit mass transport resulting in oxygen/nutrient starvation [17, 18, 58, 59] and morphological heterogeneity [60] inside fungal pellets. To predict the concentration of substrates inside pellets, it is necessary to know the metabolic rate and diffusive mass transfer through hyphal networks, which is considered the main transport phenomenon inside submerged cultivated pellets [34, 36, 61, 62]. To calculate the diffusive mass transport, the effective diffusion coefficient  $D_{i,eff}$  of the diffusing component  $i$  (e.g. oxygen or a nutrient) is required, which is defined as [63]

$$D_{i,eff} = D_{i,bulk} \cdot k_{eff}, \quad (1)$$

where  $D_{i,bulk}$  is the diffusion coefficient of the diffusing component  $i$  in the bulk medium and  $k_{eff}$  the effective diffusion factor.  $k_{eff}$  should be independent of the diffusing substance and describes the geometrical diffusion hindrance due to the pore geometry. Thus, it reduces the free bulk diffusion  $D_{i,bulk}$  to the effective diffusion coefficient  $D_{i,eff}$  in the pore network. Since  $D_{i,bulk}$  can be estimated from the medium condition [64],  $k_{eff}$  is the only unknown variable to determine  $D_{i,eff}$  and thus the effective diffusivity inside pellets. The diffusion factor  $k_{eff}$  is defined as [65]

$$k_{eff} = \frac{\epsilon}{\tau^2}, \quad (2)$$

where  $\epsilon$  is the porosity and  $\tau$  the tortuosity of the porous medium. The tortuosity  $\tau$  can be described as the ratio of the average pore length to the length of the porous medium along the major flow or diffusion axis. The definition of the effective diffusion factor and the tortuosity implies that the detailed 3D micro-structure of the analyzed porous medium has to be known to determine these parameters. In the absence of suitable models and experimental methods for predicting the effective diffusion factor and thus the effective diffusivity inside whole non-destructive fungal pellets [29], we harnessed  $\mu$ -CT and 3D image analysis to resolve the 3D micro-structure of whole pellets and computed locally resolved effective diffusion factors. To compute the spatially resolved effective diffusivity inside filamentous fungal pellet structures gained from  $\mu$ -CT measurements as well as from Monte Carlo growth simulations, several representative cubic sub-volumes were cropped out of each voxel-based 3D pellet image. Within each representative elementary volume (REV), diffusion computation were performed with the module DiffuDict of the commercial software GeoDict (Math2Market GmbH) [63, 66, 67].

Using MATLAB, the REVs were extracted along the three main axis originating from the calculated mass center of the 3D pellet structures (Figure 7). The distance between the centers of cubic REVs along the main axis was set at 25  $\mu\text{m}$ , resulting in 50-150 single REVs per pellet depending on the pellet size. In our studies [29, 30], we proved that an edge length of at least six times the hyphal diameter of the analyzed fungal species and strains was sufficient as REV to investigate the hyphal fraction and diffusivity.

Since DiffuDict enables the voxel-based solution of transport equations, the cubic REVs could directly be processed. Diffusion computations were performed in the radial direction, pointing to the mass center of the pellet, and two tangential directions (perpendicular to the radial direction) for each cube to compute the effective diffusion factor for the corresponding direction. The diffusion was computed in the space/liquid between the hyphae, the porous medium. We applied pure bulk diffusion which was modeled by the Laplace equation with Neumann boundary conditions on the pores-to-solids boundaries and a concentration drop of the diffusing component in the diffusion direction [63]. For the in- and outlet, we used Dirichlet boundary conditions and symmetric boundary conditions on the other four faces. Pure bulk diffusion is the predominant diffusion regime in liquids [63, 68] and was therefore the method of choice. Surface effects on the solid-liquid interface that could affect diffusion were neglected [29]. In addition to the diffusion computations, the porosity  $\epsilon$  and the hyphal fraction  $c_h = 1 - \epsilon$  were determined of each REV.

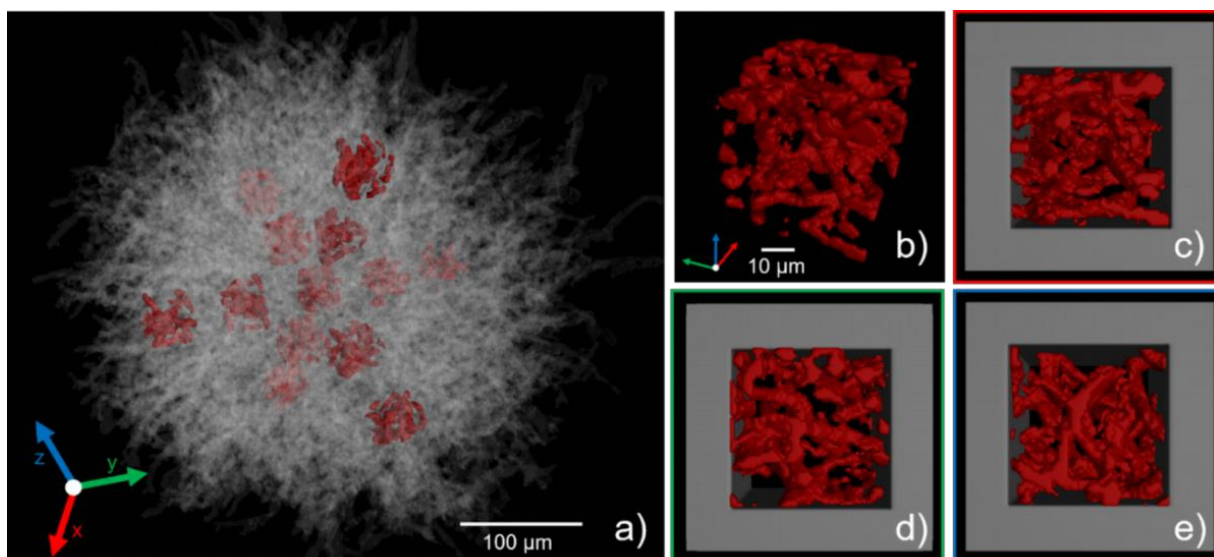


**Figure 7:** Binarized and processed 3D  $\mu$ -CT image of an *Aspergillus niger* pellet and cropped cubes for the diffusion computations: (a) Transparent: projection of a whole pellet; red: exemplary cubes used for diffusion computations. (b–e) Morphology of a single cube from different viewing directions; the gray boundaries in (c–e) illustrate the boundaries parallel to the diffusion computation. (Reprinted with permission from [29], Copyright (2019) John Wiley and Sons)

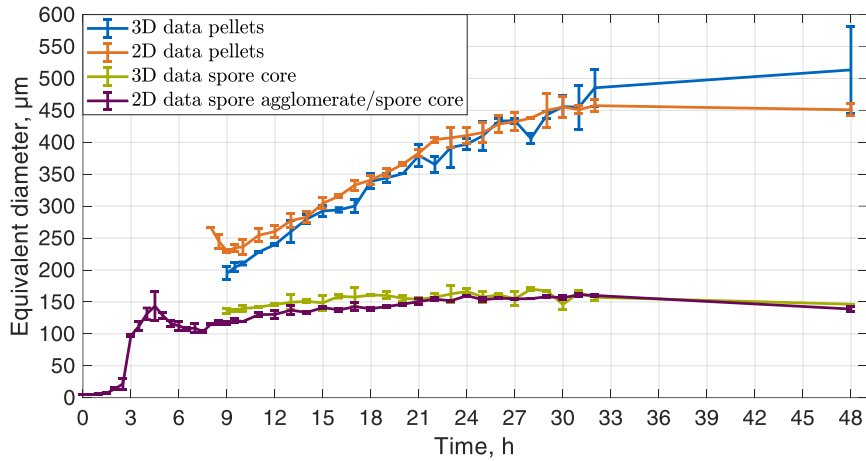
## Results and Discussion

### Morphological development of pellets based on 2D and 3D imaging

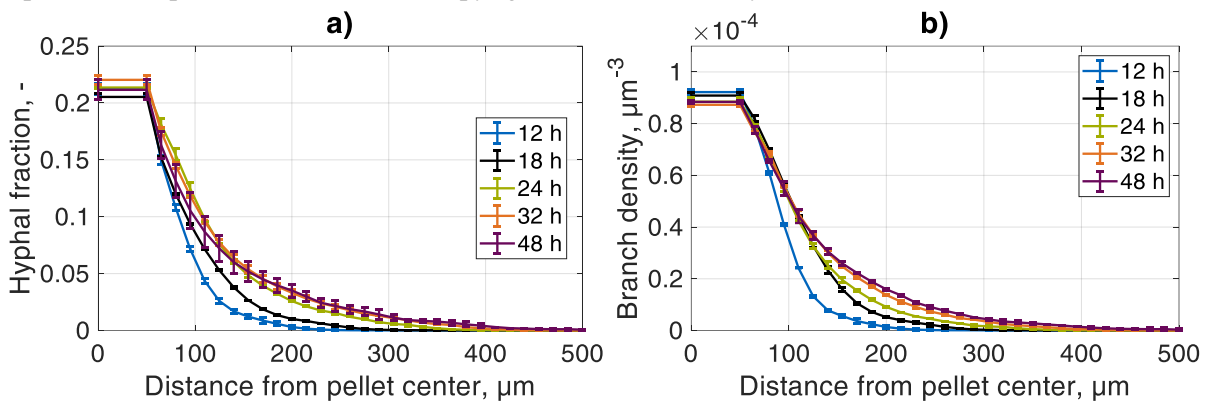
The  $\mu$ -CT measurements and developed image analysis revealed micromorphological properties of whole filamentous fungal pellets [28, 32]. Due to the lack of measurement techniques, most of these properties had not been determined for pellets before [69]. Moreover, properties such as the number density of tips, branches, and the hyphal fraction were locally resolved enabling a comprehensive analysis of the pellets' morphology [28]. Furthermore, the development of a high-throughput 2D image analysis method enabled the tracking of macromorphological pellet growth and population heterogeneity based on size distributions of spore agglomerates and pellets. For the sake of brevity we did not include any information on the 2D image analysis in the in Method Section but instead refer to [31]. In addition, SR- $\mu$ -CT allowed the three-dimensional resolution of large volumes of pellet samples from multiple time steps revealing the micromorphological development during pellet growth [32].

Figure 8 shows the size evolution of spore agglomerates evolving into spore cores and of pellets in an *A. niger* cultivation. The data show good agreement between the developed 2D [31] and 3D [32] image analysis and thus a correct segmentation of single pellets from a large volume with multiple pellets. With the 2D analysis it is possible to track the spore agglomeration and pellet growth with one reproducible method. Contrary, the developed 3D image analysis does not provide information on spore agglomeration. However, it provides much more detailed data, which can be locally resolved as exemplarily indicated in Figure 9. Here, an increase of the hyphal fraction in outer pellet regions can be observed during the cultivation (Figure 9a). The hyphal fraction up to 50  $\mu$ m ranges between 20.5% (18 h) to 22% (32 h) representing mainly the solid fraction of the spores/spore agglomerate which are embedded in the pellet center. Since branching points remain constant at their place of origin, the branch density increases in outer pellet parts but remains

constant in inner parts with cultivation time (Figure 9b). For a more detailed interpretation of these results we refer to our publications [31, 32].



**Figure 8:** Mean equivalent diameters of pellets and spore cores over cultivation time using 2D and 3D  $\mu$ -CT image data. Spore cores are detected spore agglomerates within pellets that are detected from 8 h. The error bars indicate the standard deviation between replicated (flask A and B) cultivations. (Adapted and reprinted with permission from [32], Copyright (2023) John Wiley and Sons)



**Figure 9:** Hyphal fractions and branch densities over the distance from the pellet center. The error bars indicate the standard deviation between replicated cultures. a) Mean hyphal fractions; b) Mean branch densities; (Adapted and reprinted with permission from [32], Copyright (2023) John Wiley and Sons)

### Effective diffusivity through mycelial networks

As a main result of the project, a law for predicting the effective diffusion factor as a function of the hyphal fraction was found [29]. This law was shown to be applicable to all experimentally measured and in-silico generated filamentous fungi [30].

In a first diffusion study [29], the radial effective diffusion factors from five *A. niger* pellets of  $\mu$ -CT measurements were plotted over the hyphal fractions of the corresponding representative elementary volumes (REVs, Figure 10). Furthermore, existing models from the literature predicting the diffusion factor depending on the hyphal fraction/porosity ( $\epsilon = 1 - c_h$ ) of filamentous microorganisms (Figure 10a) and fibers (Figure 10b) were compared to the experimental diffusion data of *A. niger*. The linear assumption

$k_{eff} = \epsilon$  applied in simulation studies for filamentous microorganisms by Celler et al. [34], Cui et al. [61], and Buschulte [33] overestimates the effective diffusion factors compared to the experimental data. This model ( $k_{eff} = \epsilon$ ) is also known as the “law of mixtures” [70], which was developed for flow along parallel fibers and does not take into account the tortuosity of the filamentous network resulting in an increased diffusion factor. In contrast, Lejeune and Baron [36] assumed a constant tortuosity of two ( $k_{eff} = \epsilon/2$ ). Thus, their model would result in a reduced, geometrically hindered diffusion for a hyphal fraction of zero making their model not applicable. The non-linear model of Meyerhoff et al. [62] satisfies the mandatory condition of an effective diffusion factor of one and zero for a hyphal fraction of zero and one, respectively. However, the proposed model overestimates the experimental effective diffusion factors. Buschulte [33] used a second model ( $k_{eff} = e^{-2.8c_h}$ ) that best fits the experimental data compared to other models for filamentous fungi in the literature. This model underestimates our experimental data and also does not meet the condition of an effective diffusion factor of zero for a hyphal fraction of one. Figure 10b shows the “law of mixtures” and correlations for 3D random distributed overlapping fibers. Compared to the models formulated for filamentous microorganisms (Figure 10a), our experimental data were fitted better by the non-linear models of Tomadakis and Sotirchos [71] and He et al. [72] for overlapping non-parallel fibers (Figure 10b). Both models include a power function of porosity, which is often used to estimate the effective diffusion factor of isotropic structures [73]. However, additional parameters are needed in these models: the percolation porosity [71] or a further fitting parameter [72]. Since the existing assumptions in the literature for modeling diffusion in filamentous microorganisms inaccurately correlated the effective diffusion factor with the porosity/hyphal fraction, and in order to obtain a relation with only one fitting parameter, we proposed a new non-linear correlation:

$$k_{eff} = (1 - c_h)^a, \quad (3)$$

with a fitting parameter  $a$  of  $2.02 \pm 0.02$  within 95% confidence bounds, this model fitted the experimental diffusion factors of the five investigated *A. niger* pellets very well. Furthermore, our simple equation is theory-consistent with the condition of a diffusion factor of one and zero for a hyphal fraction of zero and one, respectively [29].

To get closer to a generally applicable correlation for filamentous fungi, we performed diffusion computations with REVs of additional strains of industrial-relevant fungal species including *P. chrysogenum* (penicillin producer), *R. stolonifer* (fumaric acid), and *R. oryzae* (enzymes, tempeh) [30]. Subsequently, we fitted the parameter  $a$  of the developed correlation (Equation 3) based on the computed diffusion factors and hyphal fractions of 66  $\mu$ CT analyzed Pellets (Figure 11). Although the pellet morphologies of the strains studied differed significantly, the fitting parameter  $a$  was similar for all strains.

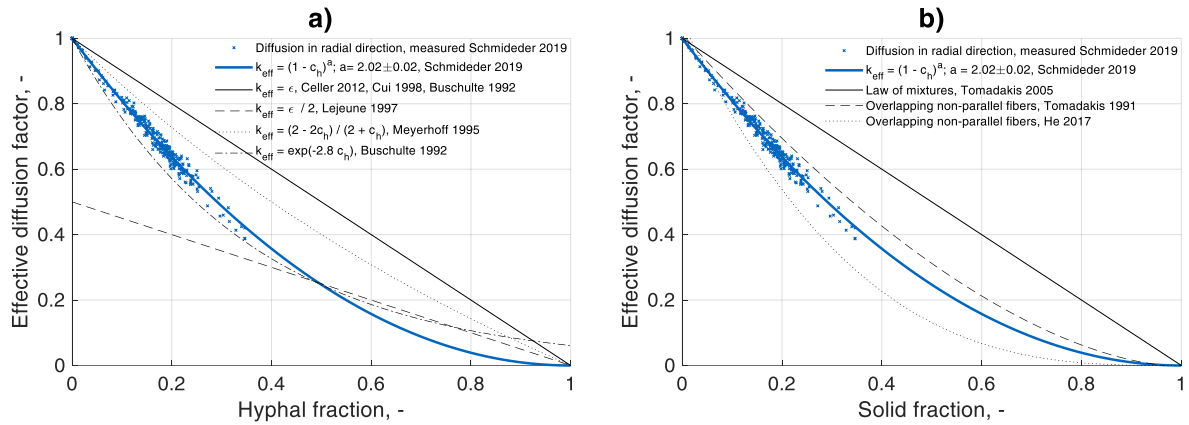


**Figure 10:** Correlations between hyphal fraction  $c_h$ / porosity ( $\epsilon = 1 - c_h$ ) and effective diffusion factor  $k_{eff}$ . The blue data points correspond to the computed effective diffusion factors of five *A. niger* pellets in the radial direction. The solid bold blue line shows the new correlation between the hyphal fraction and the effective diffusion factor; the black lines represent existing correlations in the literature for (a) filamentous microorganisms and (b) 3D random distributed overlapping fibers. (Reprinted with permission from [29], Copyright (2019) John Wiley and Sons)

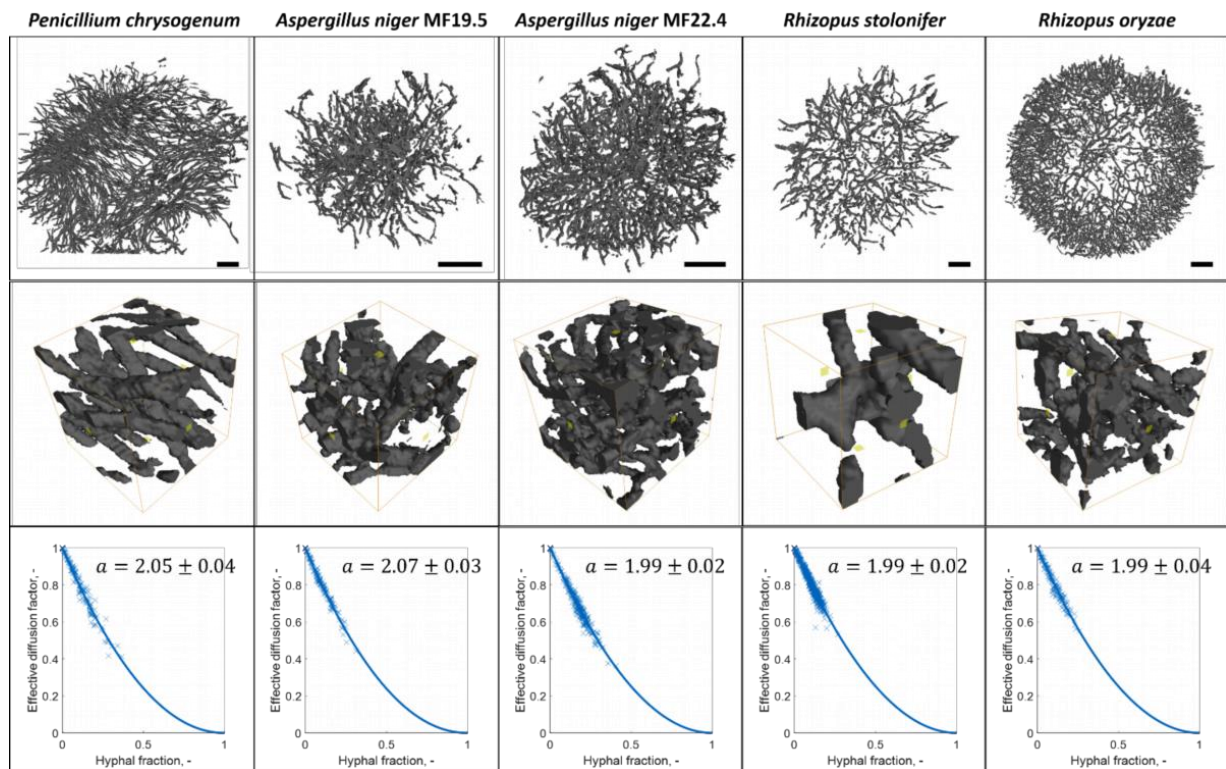


**Figure 11:** Morphology and diffusivity of experimentally investigated pellets. Upper two rows: Projections of processed  $\mu$ -CT images. Cubes are  $50 \times 50 \times 50 \mu\text{m}$ . Bottom row: correlation between hyphal fraction ( $c_h$ ) and effective diffusion factor ( $k_{eff}$ ). Each blue data point corresponds to one cube applied for diffusion computations. The solid blue line shows the new correlation  $k_{eff} = (1 - c_h)^a$ , resulting in the fitted

exponent  $a$ .  $\pm$  specifies the 95% confidence interval. (Reprinted with permission from [30], Copyright (2019) John Wiley and Sons)

To cover the wide variety of fungal morphologies, we performed further diffusion computation within 3125 morphological different simulated filamentous structures using a Monte Carlo growth model (see Materials and Methods) and fitted the parameter  $a$  (Figure 12) [30]. Since we observed a dependence between image resolution and the fitted parameter  $a$ , we simulated pellets with an image resolution representing hyphae with 5 (Figure 12a) and 13 voxels (Figure 12b) in diameter. By the variation of growth parameters, the Monte Carlo growth simulations also computed very loose structures with a mean hyphal fraction of the respective cubes less than 0.05 and pellet structures with very unlikely morphological parameters, e.g., straight hyphae or extreme branch angles ( $20^\circ$  and  $180^\circ$ ). We discarded these simulated structures and fitted the parameter  $a$  for the remaining 898 and 712 pellets with hyphae represented by 5 and 13 voxels, respectively. As a result, a mean correlation factor with a narrow distribution of  $a = 2.072 \pm 0.025$  and  $a = 1.760 \pm 0.023$  was obtained. In Figure 12a,  $\mu$ -CT pellets were also included, indicating a fitting parameter  $a$  in the range of simulated pellets for the comparable resolution, where hyphae are represented with a diameter of 5 voxels. The narrow range of the fitting parameter  $a$  indicated a universal application of the diffusion law. Since we showed, that the fitting parameter  $a$  converges to  $1.6 < a < 1.8$  with increasing resolution, we proposed the law for high resolutions as universal applicable law to calculate the diffusivity through fungal pellets [30]:

$$k_{eff} = (1 - c_h)^{1.76}, \quad (4)$$

where the fitting parameter  $a$  was calculated based on 712 morphologically different pellet structures and hyphae were represented with a resolution of 13 voxel in diameter.

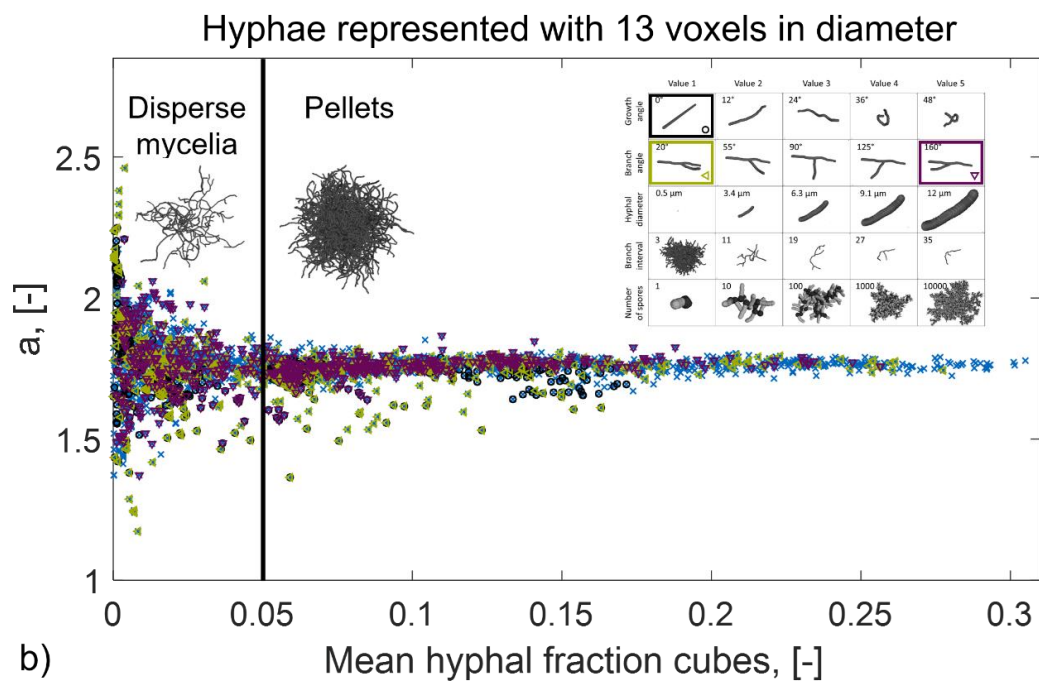
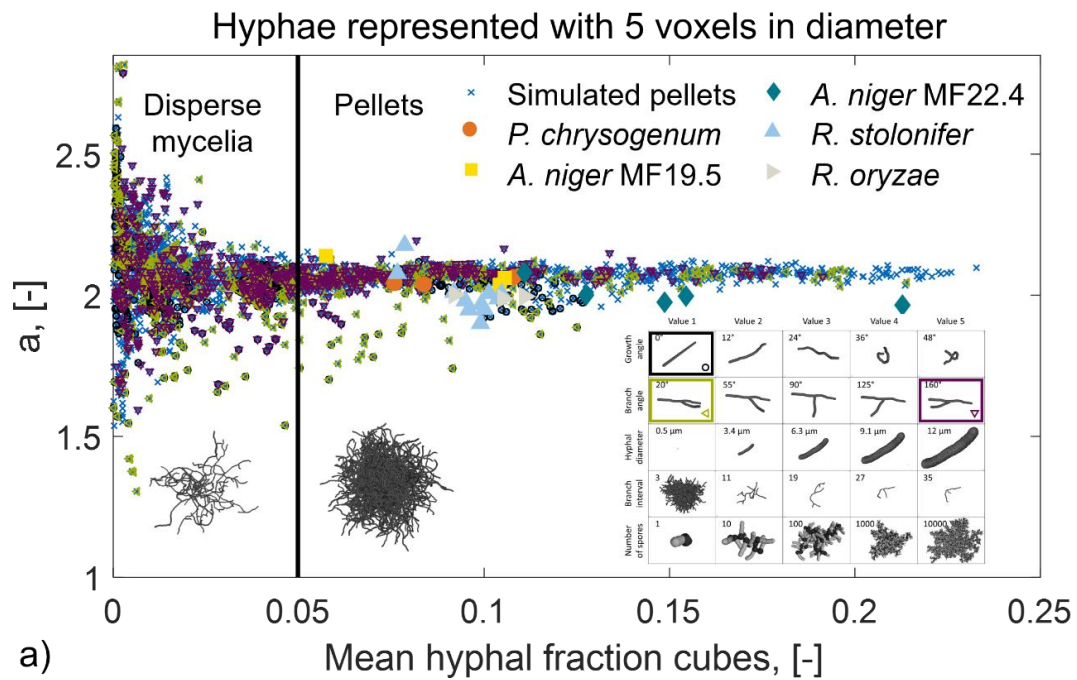


**Figure 12:** Correlation factor  $a$  for simulated and experimentally determined pellets. Each data point corresponds to the correlation ( $k_{eff} = (1 - c_h)^a$ ) between the hyphal fraction  $c_h$  and the effective diffusion factor  $k_{eff}$  of one pellet, resulting in the fitted exponent  $a$ . For each pellet, the fit is based on diffusion computations through several cubes. Hyphae of simulated pellets are represented with a “resolution” of five (top) and 13 (bottom) voxels in diameter. (Reprinted with permission from [30], Copyright (2020) John Wiley and Sons)

## Conclusion

In our project within the priority program DiSPBiotech funded by the German Science Foundation (DFG SPP 1934), three main methods/results were elaborated: (1) a method based on  $\mu$ -CT measurements and image analysis was developed to quantify the three-dimensional morphology of whole intact pellets [28]; (2) the developed 3D analysis method was significantly improved in terms of sample throughput and allows in combination with an additionally developed 2D image analysis method the description of the micro- and macro-morphological evolution of complete fungal cultures [31, 32]; (3) based on diffusion computations through  $\mu$ -CT measured and simulated pellets, a universal correlation between micromorphology and effective diffusivity was found, allowing the diffusive transport of nutrients and oxygen in filamentous fungi to be calculated [29, 30].

It is well known, that the supply of oxygen and nutrients strongly affects the growth and productivity of fungal pellets [12, 13, 19]. Morphology engineering therefore aims to create idealized structures that allow the desired nutrient supply of the whole pellet [26]. The concentration of nutrients inside pellets depends on the metabolic consumption rate of the fungus and the transport through the filamentous network, which is mainly driven by diffusion [34, 36, 61, 62]. Our generated methods and findings make it now feasible to compute the concentration profile of nutrients within a pellet making targeted morphology engineering possible. For this objective, we propose the following procedure:

1. Using  $\mu$ -CT measurements and 3D image analysis, a morphology database of fungal cultivations with different strains or at modified process conditions can be generated. Furthermore, growth simulations allow to extend this database by the variation of reasonable growth parameters.
2. The diffusive mass transport within each pellet can be solved using the generated diffusion law ( $k_{eff} = (1 - c_h)^{1.76}$ ) and the database including the local hyphal fractions. The concentration profile of nutrients inside pellets can be calculated with modeling approaches based on partial differential diffusion-reaction equations [33, 34, 74]. The micromorphology required for these models, e.g., number of tips and branches, can in turn be derived from the morphology database. Furthermore, the reaction term within these models requires the substrate consumption rate of the fungus which can be acquired from literature or additional experiments.
3. The calculated nutrient concentration profiles enable to determine substrate-limited and substrate-saturated areas within each pellet. Based on the requirements for the product of interest, e.g., limitation or saturation needed, a suitable pellet structure can be selected from the database.
4. Using process and/or genetic engineering approaches, the upscaling of the cultivation with the desired pellet structure to the size of industrially relevant bioreactors could be realized.

Some steps of this proposed procedure are still lacking detailed elaboration. However, in addition to modeling/simulation approaches even the pure data from synchrotron radiation based  $\mu$ -computed tomography and subsequent high-throughput 3D image analysis will lead to a holistic understanding of the morphological development of pellets. This will open new opportunities for morphological engineering towards enhanced process control and productivity.

## References

1. Hoffmeister, D., Keller, N.P.: Natural products of filamentous fungi: enzymes, genes, and their regulation. *Natural product reports* (2007). <https://doi.org/10.1039/b603084j>
2. Vera Meyer: Genetic engineering of filamentous fungi — Progress, obstacles and future trends. *Biotechnology Advances* **26**, 177–185 (2008)
3. Punt, P.J., van Biezen, N., Conesa, A., Albers, A., Mangnus, J., van den Hondel, C.: Filamentous fungi as cell factories for heterologous protein production. *Trends in Biotechnology* (2002). [https://doi.org/10.1016/s0167-7799\(02\)01933-9](https://doi.org/10.1016/s0167-7799(02)01933-9)
4. Cairns, T.C., Nai, C., Meyer, V.: How a fungus shapes biotechnology: 100 years of *Aspergillus niger* research. *Fungal biology and biotechnology* (2018). <https://doi.org/10.1186/s40694-018-0054-5>
5. Fütting, P., Barthel, L., Cairns, T.C., Briesen, H., Schmieder, S.: Filamentous fungal applications in biotechnology: a combined bibliometric and patentometric assessment. *Fungal biology and biotechnology* (2021). <https://doi.org/10.1186/s40694-021-00131-6>
6. Brakhage, A.A.: Regulation of fungal secondary metabolism. *Nature reviews. Microbiology* (2013). <https://doi.org/10.1038/nrmicro2916>
7. Keller, N.P.: Fungal secondary metabolism: regulation, function and drug discovery. *Nature reviews. Microbiology* (2019). <https://doi.org/10.1038/s41579-018-0121-1>
8. Nielsen, J.C., Grijseels, S., Prigent, S., Ji, B., Dainat, J., Nielsen, K.F., Frisvad, J.C., Workman, M., Nielsen, J.: Global analysis of biosynthetic gene clusters reveals vast potential of secondary metabolite production in *Penicillium* species. *Nature microbiology* (2017). <https://doi.org/10.1038/nmicrobiol.2017.44>
9. Ward, O.P.: Production of recombinant proteins by filamentous fungi. *Biotechnology Advances* (2012). <https://doi.org/10.1016/j.biotechadv.2011.09.012>
10. Wang, Q., Zhong, C., Xiao, H.: Genetic Engineering of Filamentous Fungi for Efficient Protein Expression and Secretion. *Frontiers in bioengineering and biotechnology* (2020). <https://doi.org/10.3389/fbioe.2020.00293>
11. Meyer, V., Basenko, E.Y., Benz, J.P., Braus, G.H., Caddick, M.X., Csukai, M., Vries, R.P. de, Endy, D., Frisvad, J.C., Gunde-Cimerman, N., Haarmann, T., Hadar, Y., Hansen, K., Johnson, R.I., Keller, N.P., Kraševc, N., Mortensen, U.H., Perez, R., Ram, A.F.J., Record, E., Ross, P., Shapaval, V., Steiniger, C., van den Brink, H., van Munster, J., Yarden, O., Wösten, H.A.B.: Growing a circular economy with fungal biotechnology: a white paper. *Fungal Biol Biotechnol* (2020). <https://doi.org/10.1186/s40694-020-00095-z>
12. Veiter, L., Rajamanickam, V., Herwig, C.: The filamentous fungal pellet-relationship between morphology and productivity. *Applied Microbiology and Biotechnology* **102**, 2997–3006 (2018)
13. Krull, R., Wucherpfennig, T., Esfandabadi, M.E., Walisko, R., Melzer, G., Hempel, D.C., Kampen, I., Kwade, A., Wittmann, C.: Characterization and control of fungal morphology for improved production performance in biotechnology. *Journal of Biotechnology* **163**, 112–123 (2013)
14. Böl, M., Schrunner, K., Tesche, S., Krull, R.: Challenges of influencing cellular morphology by morphology engineering techniques and mechanical induced stress on filamentous pellet systems-A critical review. *Eng. Life Sci.* (2021). <https://doi.org/10.1002/elsc.202000060>
15. Papagianni, M.: Fungal morphology and metabolite production in submerged mycelial processes. *Biotechnology Advances* **22**, 189–259 (2004)

16. Krull, R., Cordes, C., Horn, H., Kampen, I., Kwade, A., Neu, T.R., Nörtemann, B.: Morphology of Filamentous Fungi: Linking Cellular Biology to Process Engineering Using *Aspergillus niger*. In: Wittmann, C., Krull, R. (eds.) *Biosystems Engineering II: Linking Cellular Networks and Bioprocesses*, pp. 1–21. Springer Berlin Heidelberg, Berlin, Heidelberg (2010)
17. Hille, A., Neu, T.R., Hempel, D.C., Horn, H.: Oxygen profiles and biomass distribution in biopellets of *Aspergillus niger*. *Biotechnology and Bioengineering* **92**, 614–623 (2005)
18. Hille, A., Neu, T.R., Hempel, D.C., Horn, H.: Effective Diffusivities and Mass Fluxes in Fungal Biopellets. *Biotechnology and Bioengineering* **103**, 1202–1213 (2009)
19. Cairns, T.C., Zheng, X., Zheng, P., Sun, J., Meyer, V.: Moulding the mould: understanding and reprogramming filamentous fungal growth and morphogenesis for next generation cell factories. *Biotechnology for biofuels* (2019). <https://doi.org/10.1186/s13068-019-1400-4>
20. Papagianni, M., Matthey, M.: Morphological development of *Aspergillus niger* in submerged citric acid fermentation as a function of the spore inoculum level. Application of neural network and cluster analysis for characterization of mycelial morphology. *Microbial cell factories* **5** (2006)
21. Dynesen, J., Nielsen, J.: Surface hydrophobicity of *Aspergillus nidulans* conidiospores and its role in pellet formation. *Biotechnology Progress* (2003). <https://doi.org/10.1021/bp0340032>
22. Wucherpfennig, T., Kiep, K.A., Driouch, H., Wittmann, C., Krull, R.: Morphology and rheology in filamentous cultivations. *Advances in applied microbiology* (2010). [https://doi.org/10.1016/S0065-2164\(10\)72004-9](https://doi.org/10.1016/S0065-2164(10)72004-9)
23. Laible, A.R., Dinius, A., Schrader, M., Krull, R., Kwade, A., Briesen, H., Schmideder, S.: Effects and Interactions of Metal Oxides in Microparticle-enhanced Cultivation of Filamentous Fungi and Bacteria. *Eng. Life Sci.* (2021). <https://doi.org/10.1002/elsc.202100075>
24. Driouch, H., Sommer, B., Wittmann, C.: Morphology Engineering of *Aspergillus niger* for Improved Enzyme Production. *Biotechnology and Bioengineering* **105**, 1058–1068 (2010)
25. Kaup, J.-A., Ehrich, K., Pescheck, M., Schrader, J.: Microparticle-enhanced cultivation of filamentous microorganisms: Increased chloroperoxidase formation by *Caldariomyces fumago* as an example. *Biotechnology and Bioengineering* **99**, 491–498 (2008)
26. Meyer, V., Cairns, T., Barthel, L., King, R., Kunz, P., Schmideder, S., Müller, H., Briesen, H., Dinius, A., Krull, R.: Understanding and controlling filamentous growth of fungal cell factories: novel tools and opportunities for targeted morphology engineering. *Fungal Biol Biotechnol* (2021). <https://doi.org/10.1186/s40694-021-00115-6>
27. Fiedler, M.R.M., Barthel, L., Kubisch, C., Nai, C., Meyer, V.: Construction of an improved *Aspergillus niger* platform for enhanced glucoamylase secretion. *Microbial cell factories* (2018). <https://doi.org/10.1186/s12934-018-0941-8>
28. Schmideder, S., Barthel, L., Friedrich, T., Thalhammer, M., Kovačević, T., Niessen, L., Meyer, V., Briesen, H.: An X-ray microtomography-based method for detailed analysis of the three-dimensional morphology of fungal pellets. *Biotechnology and Bioengineering* (2019). <https://doi.org/10.1002/bit.26956>
29. Schmideder, S., Barthel, L., Müller, H., Meyer, V., Briesen, H.: From three-dimensional morphology to effective diffusivity in filamentous fungal pellets. *Biotechnology and Bioengineering* (2019). <https://doi.org/10.1002/bit.27166>

30. Schmideder, S., Müller, H., Barthel, L., Friedrich, T., Niessen, L., Meyer, V., Briesen, H.: Universal law for diffusive mass transport through mycelial networks. *Biotechnology and Bioengineering* (2020). <https://doi.org/10.1002/bit.27622>
31. Müller, H., Barthel, L., Schmideder, S., Schütze, T., Meyer, V., Briesen, H.: From spores to fungal pellets: A new high-throughput image analysis highlights the structural development of *Aspergillus niger*. *Biotechnology and Bioengineering* (2022). <https://doi.org/10.1002/bit.28124>
32. Müller, H., Deffur, C., Schmideder, S., Barthel, L., Friedrich, T., Hammel, J., Meyer, V., Briesen, H.: Synchrotron radiation based micro-computed tomography for three-dimensional growth analysis of *Aspergillus niger* pellets. *Biotechnology and Bioengineering* (In Preparation)
33. Buschulte, T.C.: *Mathematische Modellbildung und Simulation von Zellwachstum, Stofftransport und Stoffwechsel in Pellets aus Streptomycceten* (PhD thesis), Stuttgart, Germany: Fakultät Verfahrenstechnik der Universität Stuttgart (1992)
34. Celler, K., Picioreanu, C., van Loosdrecht, Mark C. M., van Wezel, G.P.: Structured morphological modeling as a framework for rational strain design of *Streptomyces* species. *Antonie van Leeuwenhoek International Journal of General and Molecular Microbiology* **102**, 409–423 (2012)
35. King, R.: A framework for an organelle-based mathematical modeling of hyphae. *Fungal Biol Biotechnol* (2015). <https://doi.org/10.1186/s40694-015-0014-2>
36. Lejeune, R., Baron, G.V.: Simulation of growth of a filamentous fungus in 3 dimensions. *Biotechnology and Bioengineering* **53**, 139–150 (1997)
37. Kwon, M.J., Arentshorst, M., Roos, E.D., van den Hondel, C.A.M.J.J., Meyer, V., Ram, A.F.J.: Functional characterization of Rho GTPases in *Aspergillus niger* uncovers conserved and diverged roles of Rho proteins within filamentous fungi. *Molecular microbiology* (2011). <https://doi.org/10.1111/j.1365-2958.2010.07524.x>
38. J. W. Bennet, L. L. Lasure: *More gene manipulations in fungi*. Academic Press (1991)
39. Greving, I., Wilde, F., Ogurreck, M., Herzen, J., Hammel, J.U., Hipp, A., Friedrich, F., Lottermoser, L., Dose, T., Burmester, H., Müller, M., Beckmann, F.: P05 imaging beamline at PETRA III: first results. In: Stock, S.R. (ed.) *Developments in X-Ray Tomography IX*. SPIE Optical Engineering + Applications, San Diego, California, United States, Sunday 17 August 2014, 92120O. SPIE (2014). <https://doi.org/10.1117/12.2061768>
40. Haibel, A., Ogurreck, M., Beckmann, F., Dose, T., Wilde, F., Herzen, J., Müller, M., Schreyer, A., Nazmov, V., Simon, M., Last, A., Mohr, J.: Micro- and nano-tomography at the GKSS Imaging Beamline at PETRA III. In: Stock, S.R. (ed.) *Developments in X-Ray Tomography VII*. SPIE Optical Engineering + Applications, San Diego, California, USA, Sunday 1 August 2010, 78040B. SPIE (2010). <https://doi.org/10.1117/12.860852>
41. Wilde, F., Ogurreck, M., Greving, I., Hammel, J.U., Beckmann, F., Hipp, A., Lottermoser, L., Khokhriakov, I., Lytaev, P., Dose, T., Burmester, H., Müller, M., Schreyer, A.: Micro-CT at the imaging beamline P05 at PETRA III. In: *AIP Conference Proceedings* 1741, 030035 (2016), p. 30035
42. Moosmann, J., Ershov, A., Weinhardt, V., Baumbach, T., Prasad, M.S., LaBonne, C., Xiao, X., Kashef, J., Hofmann, R.: Time-lapse X-ray phase-contrast microtomography for in vivo imaging and analysis of morphogenesis. *Nature protocols* (2014). <https://doi.org/10.1038/nprot.2014.033>
43. Palenstijn, W.J., Batenburg, K.J., Sijbers, J.: Performance improvements for iterative electron tomography reconstruction using graphics processing units (GPUs). *Journal of structural biology* (2011). <https://doi.org/10.1016/j.jsb.2011.07.017>

44. van Aarle, W., Palenstijn, W.J., Beenhouwer, J. de, Altantzis, T., Bals, S., Batenburg, K.J., Sijbers, J.: The ASTRA Toolbox: A platform for advanced algorithm development in electron tomography. *Ultramicroscopy* (2015). <https://doi.org/10.1016/j.ultramic.2015.05.002>
45. van Aarle, W., Palenstijn, W.J., Cant, J., Janssens, E., Bleichrodt, F., Dabravolski, A., Beenhouwer, J. de, Joost Batenburg, K., Sijbers, J.: Fast and flexible X-ray tomography using the ASTRA toolbox. *Optics express* (2016). <https://doi.org/10.1364/OE.24.025129>
46. Otsu, N.: A Threshold Selection Method from Gray-Level Histograms. *Systems, Man and Cybernetics, IEEE Transactions on* **9**, 62–66 (1979)
47. Haralick, Robert M., and Linda G. Shapiro: *Computer and robot vision*. Addison-Wesley, Boston, MA (1992)
48. Lewis, J.P.: *Fast Normalized Cross-Correlation*. Industrial Light & Magic. <http://scribblethink.org/Work/nvisionInterface/nip.pdf>. (1995)
49. Kerschnitzki, M., Kollmannsberger, P., Burghammer, M., Duda, G.N., Weinkamer, R., Wagermaier, W., Fratzl, P.: Architecture of the osteocyte network correlates with bone material quality. *Journal of bone and mineral research : the official journal of the American Society for Bone and Mineral Research* (2013). <https://doi.org/10.1002/jbmr.1927>
50. Lee, T.C., Kashyap, R.L., Chu, C.N.: Building Skeleton Models via 3-D Medial Surface Axis Thinning Algorithms. *CVGIP: Graphical Models and Image Processing* (1994). <https://doi.org/10.1006/cgip.1994.1042>
51. Caldwell, I.Y., Trinci, A.P.J.: The growth unit of the mould *Geotrichum candidum*. *Archiv für Mikrobiologie* **88**, 1–10 (1973)
52. Yang, H., Reichl, U., King, R., Gilles, E.D.: Measurement and simulation of the morphological development of filamentous microorganisms. *Biotechnology and Bioengineering* (1992). <https://doi.org/10.1002/bit.260390108>
53. Zacchetti, B., Andrianos, A., van Dissel, D., Ruiter, E. de, van Wezel, G.P., Claessen, D.: Microencapsulation extends mycelial viability of *Streptomyces lividans* 66 and increases enzyme production. *BMC biotechnology* (2018). <https://doi.org/10.1186/s12896-018-0425-2>
54. Lehmann, A., Zheng, W., Soutschek, K., Roy, J., Yurkov, A.M., Rillig, M.C.: Tradeoffs in hyphal traits determine mycelium architecture in saprobic fungi. *Scientific reports* (2019). <https://doi.org/10.1038/s41598-019-50565-7>
55. Witten, T.A., Sander, L.M.: Diffusion-Limited Aggregation, a Kinetic Critical Phenomenon. *Phys. Rev. Lett.* (1981). <https://doi.org/10.1103/PhysRevLett.47.1400>
56. Ericson, C.: *Real-Time Collision Detection*. CRC Press (2004)
57. Bresenham, J.E.: Algorithm for computer control of a digital plotter. *IBM Syst. J.* (1965). <https://doi.org/10.1147/sj.41.0025>
58. Veiter, L., Kubicek, M., Hutter, H., Pittenauer, E., Herwig, C., Slouka, C.: Study of metabolism and identification of productive regions in filamentous fungi via spatially resolved time-of-flight secondary ion mass spectrometry. *Analytical and bioanalytical chemistry* (2020). <https://doi.org/10.1007/s00216-019-01980-2>
59. Rüdiger Wittier, Horst Baumgartl, Dietrich Werner Lübbers, Karl Schügerl: Investigations of oxygen transfer into *Penicillium chrysogenum* pellets by microprobe measurements. *Biotechnology and Bioengineering* (1986). <https://doi.org/10.1002/bit.260280713>

60. Zaccetti, B., Wösten, H.A.B., Claessen, D.: Multiscale heterogeneity in filamentous microbes. *Biotechnology Advances* (2018). <https://doi.org/10.1016/j.biotechadv.2018.10.002>
61. Cui, Y.Q., van der Lans, R., Luyben, K.: Effects of dissolved oxygen tension and mechanical forces on fungal morphology in submerged fermentation. *Biotechnology and Bioengineering* **57**, 409–419 (1998)
62. Meyerhoff, J., Tiller, V., Bellgardt, K.-H.: Two mathematical models for the development of a single microbial pellet. *Bioprocess Engineering* (1995). <https://doi.org/10.1007/BF00369507>
63. Becker, J., Wieser, C., Fell, S., Steiner, K.: A multi-scale approach to material modeling of fuel cell diffusion media. *International Journal of Heat and Mass Transfer* (2011). <https://doi.org/10.1016/j.ijheatmasstransfer.2010.12.003>
64. Yaws, C.L.: *Transport Properties of Chemicals and Hydrocarbons*. William Andrew (2014)
65. Norman Epstein: On tortuosity and the tortuosity factor in flow and diffusion through porous media. *Chemical Engineering Science* **44**, 777–779 (1989)
66. Velichko, A., Wiegmann, A., Mücklich, F.: Estimation of the effective conductivities of complex cast iron microstructures using FIB-tomographic analysis. *Acta Materialia* (2009). <https://doi.org/10.1016/j.actamat.2009.07.004>
67. Wiegmann, A., Zemitis, A.: EJ-HEAT: A Fast Explicit Jump Harmonic Averaging Solver for the Effective Heat Conductivity of Composite Materials. *Berichte des Fraunhofer-Instituts für Techno- und Wirtschaftsmathematik (ITWM Report)*, vol. 94. Fraunhofer-Institut für Techno- und Wirtschaftsmathematik, Fraunhofer (ITWM), Kaiserslautern (2006)
68. Panerai, F., Ferguson, J.C., Lachaud, J., Martin, A., Gasch, M.J., Mansour, N.N.: Micro-tomography based analysis of thermal conductivity, diffusivity and oxidation behavior of rigid and flexible fibrous insulators. *International Journal of Heat and Mass Transfer* (2017). <https://doi.org/10.1016/j.ijheatmasstransfer.2016.12.048>
69. Schmideder, S.: Following fungal features - micromorphology and diffusivity of filamentous fungal pellets revealed by three-dimensional imaging and simulation. *Universitätsbibliothek der TU München, München* (2022)
70. Tomadakis, M.M., Robertson, T.J.: Viscous Permeability of Random Fiber Structures: Comparison of Electrical and Diffusional Estimates with Experimental and Analytical Results. *Journal of Composite Materials* (2005). <https://doi.org/10.1177/0021998305046438>
71. Tomadakis, M.M., Sotirchos, S.V.: Effects of Fiber Orientation and Overlapping on Knudsen, Transition, and Ordinary Regime Diffusion in Fibrous Substrates. *MRS Proc.* (1991). <https://doi.org/10.1557/PROC-250-221>
72. He, X., Guo, Y., Li, M., Pan, N., Wang, M.: Effective gas diffusion coefficient in fibrous materials by mesoscopic modeling. *International Journal of Heat and Mass Transfer* (2017). <https://doi.org/10.1016/j.ijheatmasstransfer.2016.11.097>
73. Nam, J.H., Kaviany, M.: Effective diffusivity and water-saturation distribution in single- and two-layer PEMFC diffusion medium. *International Journal of Heat and Mass Transfer* (2003). [https://doi.org/10.1016/S0017-9310\(03\)00305-3](https://doi.org/10.1016/S0017-9310(03)00305-3)
74. King, R.: Mathematical modelling of the morphology of streptomyces species. Relation Between Morphology and Process Performances. In: Schügerl, K. (ed.) *Relation Between Morphology and Process Performances*, pp. 95–124. Springer Berlin Heidelberg, Berlin, Heidelberg (1998)